

**Modeling the Molecular Spectra of Selected Peptides
and
Development of an Optical Trapping Raman System**

BY

ANJAN ROY

B.Sc.(University of Delhi) 2002

M.Sc.(University of Delhi) 2004

M.S. (University of Illinois at Chicago) 2009

THESIS

Submitted as partial fulfillment of the requirements
for the degree of Doctor of Philosophy in Chemistry
in the Graduate College of the
University of Illinois at Chicago, 2014

Chicago, Illinois

Defense Committee:

Prof. Timothy A. Keiderling, Chair and Advisor

Prof. Luke Hanley

Prof. Preston T. Snee

Prof. Michael Trenary

Prof. Anjum Ansari, Physics

UMI Number: 3668630

All rights reserved

INFORMATION TO ALL USERS

The quality of this reproduction is dependent upon the quality of the copy submitted.

In the unlikely event that the author did not send a complete manuscript and there are missing pages, these will be noted. Also, if material had to be removed, a note will indicate the deletion.



UMI 3668630

Published by ProQuest LLC (2014). Copyright in the Dissertation held by the Author.

Microform Edition © ProQuest LLC.

All rights reserved. This work is protected against unauthorized copying under Title 17, United States Code



ProQuest LLC.
789 East Eisenhower Parkway
P.O. Box 1346
Ann Arbor, MI 48106 - 1346

*To my parents, Animesh and Anita Roy. . .
. . . for showing me the big picture.*

ACKNOWLEDGMENT

While the rest of this acknowledgment is more or less in chronological order, I would like to start by thanking my thesis advisor Prof. Timothy Keiderling for all his support and infinite patience and for letting me pursue many different research ideas.

For my fascination with the physical and natural world I would like to credit my mother. Without the seed of intrigue that she sowed, this journey wouldn't have begun. For my interest in all things engineering and applied, I credit my father who has always been inquisitive and passed on his knowledge with much fervor. I would also like to thank my sister, Antara, for filling in for me.

Ram Vishwakarma for giving me my first break in real science. Joohyun Kim for kindling my interest in theoretical aspects of chemistry. Petr Bour for solutions to computational problems and for inspiring me to walk fast and talk slow. Pat Ratacyzck for making graduate life much easier.

These years would never have been possible without my partner, Chhavi Bhardwaj. She has been the key factor in every aspect of my doctoral student life, calculus homework, laser alignment, cell growth and most importantly, for comforting food when all else failed. Molecular discussions with Sachin Tyagi were very stimulating and I thank him even more for being the best support we could have had in Chicago. I should also thank Chicago, for being such a supportive city.

Frank Tobias, Kevin Lynch, Joe Dublin and Richard Freuh for machining parts, often at short notice, and Don Rippon for help with electronics design and repair.

I thank Marcelo Nakaema, his hands-on approach made the prototype instrument a reality and has motivated me all along. I am thankful to Yang Cui, the instrument has taken its final form because of his expertise in software interfacing and for our fruitful discussions. I would like to thank George Papadontanakis for his constant encouragement and exciting conversations.

ACKNOWLEDGMENT (Continued)

I would like to thank my committee members Professors, Luke Hanley, Preston Snee, Michael Trenary and Anjum Ansari for their time.

I thank members of the Keiderling group, both past and present for a pleasant work atmosphere.

I would like to thank everyone who helped me on online forums and via email. I salute this spirit of sharing information, my research and instrument exist largely due to this spirit.

Finally, I would like to thank my peers, and students I taught at UIC, who asked me questions. Had they not asked, I would not have known.

AR

TABLE OF CONTENTS

<u>CHAPTER</u>		<u>PAGE</u>
1	INTRODUCTION	1
1.1	Overview	1
1.2	Peptides and proteins	1
1.2.1	The peptide bond	2
1.2.2	Ramachandran plot	4
1.2.3	Helical types	7
1.2.3.1	Helices and hydrogen bonding	7
1.2.3.2	The elusive 3_{10} - helix	7
1.2.3.3	Poly proline-II helices	10
1.2.4	β -hairpins	10
1.3	Molecular vibrations	11
1.3.1	Normal modes	11
1.3.2	The amide mode(s)	12
1.3.3	Deuteration	14
1.4	Spectroscopy	15
1.4.1	Infrared (IR)	15
1.4.2	Vibrational circular dichroism (VCD)	15
1.4.3	Raman Scattering	16
1.4.4	Electronic circular dichroism (ECD)	16
1.5	Theory: The role of computations	18
2	COMPUTATIONAL METHODOLOGY	20
2.1	Overview	20
2.2	Hierarchy of approximations	21
2.3	Energy calculations	22
2.3.1	Hartree Fock	22
2.3.2	Density Functional Theory	25
2.3.3	DFT: Choice of parameters	26
2.4	Harmonic approximation and normal modes	28
2.4.1	Harmonic approximation	28
2.5	Calculation of spectral properties	29
2.5.1	Infrared absorption	30
2.5.2	Vibrational circular dichroism	32
2.5.3	Raman Scattering	35
2.6	The effect of solvation	37
2.7	Scaling up: Transfer of spectral properties	38
2.8	Calculation of vibrational coupling constants	39
2.9	Excited states: electronic CD	42
2.10	Conclusion	44

TABLE OF CONTENTS (Continued)

<u>CHAPTER</u>	<u>PAGE</u>
3 MOLECULAR VIBRATIONS IN PEPTIDES : SPECTROSCOPIC SIMULATIONS	45
3.1 Overview	45
3.2 Vibrational coupling in 3_{10} -helical peptides	46
3.2.1 Scheme	46
3.2.2 Establishing isotope effects with single labeled peptides	48
3.2.3 Site specific coupling: double labeled peptides	51
3.2.4 Coupling analysis	55
3.2.5 Modified force field analyses	61
3.3 Inter-residue coupling of polyproline II helical peptides.	65
3.3.1 Scheme	65
3.3.2 Coupling analysis: all proline model	68
3.3.3 The effect of proline side chain	71
3.4 β -strands in β -hairpins	73
3.4.1 Scheme	74
3.4.2 Single labeling on the beta-strand	76
3.4.3 Computational interpretation	83
3.4.4 Summary	88
3.5 Two strands and a turn: Cross strand coupling in β -hairpins	88
3.5.1 Scheme	89
3.5.2 Spectral simulation results	89
3.5.3 The spliced fragment approach	92
3.5.4 Complete hairpin approach	94
3.5.5 Site-specific vibrational coupling	95
3.6 Overall summary of vibrational simulations	97
4 MODELING OF THE CIRCULAR DICHROISM FOR A TRYPTOPHAN ZIPPER PEPTIDE WITH TDDFT OF COUPLED AROMATIC RESIDUES	100
4.1 Introduction	100
4.2 Scheme	103
4.2.1 TDDFT calculation	103
4.2.2 Dipole coupling	105
4.3 Results	107
4.3.1 Single indole	107
4.3.2 Two coupled tryptophan models	112
4.3.3 Trpzip2: four coupled indoles model	116
4.4 Coupling analysis	117
4.4.1 TDDFT vs TDC results	122
4.5 Tyrosine and tryptophan coupling : TDDFT	124
4.6 Conclusion	127
5 OPTICAL TRAPPING AND RAMAN SPECTROSCOPY	129
5.1 Motivation	129
5.2 Raman Spectroscopy	130

TABLE OF CONTENTS (Continued)

<u>CHAPTER</u>		<u>PAGE</u>
	5.2.1 Chemical information from Raman	130
	5.2.2 The Raman effect	131
	5.2.3 Infra-red vs. Raman	134
	5.2.4 Fluorescence interference in Raman	136
	5.2.5 Raman microscopy	136
5.3	Optical Trapping Principle	138
	5.3.1 Ray optics approach	139
	5.3.2 Rayleigh approach	140
	5.3.3 Trap details	143
5.4	Quantitative measurements	145
	5.4.1 Position detection	145
	5.4.2 Force calibration	146
5.5	Optical Trapping Raman Spectrometry (OTRS)	149
6	DESIGN AND CONSTRUCTION OF A FORCE SENSING OPTICAL TRAPPING RA- MAN SPECTROMETER (OTRS)	151
6.1	Objective	151
6.2	Design	151
6.3	Construction	153
	6.3.1 Microscope	153
	6.3.2 Raman Channel	157
	6.3.3 Illumination and Imaging Channel	159
	6.3.4 Lasing Channel: Trapping and Raman Excitation	160
	6.3.4.1 785 nm Laser	160
	6.3.4.2 532 nm Laser	161
	6.3.5 Force Detection	162
	6.3.6 Data Acquisition and Instrument Control	162
	6.3.7 Sample chamber	163
6.4	Alignment	164
	6.4.1 Laser	165
	6.4.2 Raman	165
	6.4.3 Confocal Raman	166
	6.4.4 Force detection	168
	6.4.5 Force calibration	168
6.5	Calibration	168
	6.5.1 Spectral calibration	168
	6.5.2 Spectral imaging	170
	6.5.3 Image magnification	170
	6.5.4 Choice of immersion oil	171
6.6	Conclusion	171

TABLE OF CONTENTS (Continued)

<u>CHAPTER</u>	<u>PAGE</u>
7 TESTING AND APPLICATIONS OF THE OTRS	173
7.1 Polystyrene beads	174
7.1.1 Raman spectrum	174
7.2 Single cells	178
7.3 Metal nanoparticles	181
7.4 Possible improvements in the OTRS	183
7.5 Future goals	186
CITED LITERATURE	187
APPENDICES	206
Appendix A	207
VITA	213

LIST OF TABLES

<u>TABLE</u>	<u>PAGE</u>
I Summary of various helical structures for a deca-alanine model.	8
II Summary of the amide modes observed in experiment.	13
III Summary of molecular spectroscopy methods computed.	17
IV Molecular properties as derivatives of energy	36
V Amino acid sequences and labelling patterns of the peptides used in the study of 3_{10} helices	47
VI DFT computed frequency values (normal modes) for ideal 3_{10} -helices and fits to IR simulation	55
VII Experimental and theoretical band fitted values for the amide peak positions for the 3_{10} -helical peptides investigated	56
VIII Variation in double label positions with ϕ ψ angles, both with PCM correction for CHCl_3 solvent	64
IX Sequences and labeling pattern of peptides used in the PPII helix study	66
X Variation in double label positions and splitting using different simulation models	71
XI Definition of the Trpzip sequences and labeling positions in the peptide sequence along with their abbreviations. The labeled residues are highlighted.	74
XII Comparison of experimental and simulated amide I' IR frequencies (cm^{-1}) for labeled TZ2C variants.	79
XIII Comparison of amide I' frequencies calculated with hybrid B3PW91 functional and simple BPW91 functional (both 6-31G** in vacuum).	82
XIV Outer residue calculated amide I' frequencies calculated for the TZ2C model . . .	85
XV Comparison of maxima and dispersion for solvent corrected amide I with single and double labels.	86
XVI Single strand calculations comparing PPII structure (unfolded model) with β -strand amide I frequencies, with and without solvent correction	87
XVII Comparison of experimental and simulated $^{13}\text{C}=\text{O}$ labeled amide I IR frequencies for an all alanine variant of the TZ2C NMR structure.	93

LIST OF TABLES (Continued)

<u>TABLE</u>		<u>PAGE</u>
XVIII	Transition dipole moments of 3-methyl indole and corresponding energies calculated at B3LYP/6-311++G** level of theory	109
XIX	Comparison of transition energies and oscillator strengths (OS) of the S1,S2 and S3 transitions for indole and 3-methyl indole calculated using various geometries and basis sets	110
XX	Comparison of simulated CD spectra with experimental results for TD-DFT and TDC-CO models.	126
XXI	Transition cross sections of various processes	134
XXII	Refractive index of materials used in our studies.	144
XXIII	List of parts used in the construction of the OTRS	155
XXIV	Characteristic Raman peaks of polystyrene	175
XXV	Tentative assignments for the Raman spectrum of a single <i>E. coli</i> cell	181
XXVI	Tentative assignments for the Raman spectrum of a single <i>S. cerevisiae</i> cell	182

LIST OF FIGURES

<u>FIGURE</u>	<u>PAGE</u>
1 Peptide formation	3
2 The hierarchical building up of structural complexity in proteins	5
3 A sketch of a Ramachandran plot highlighting some of the secondary structures that are sterically allowed.	6
4 Outline of the steps involved in the modeling of theoretical spectra starting from the initial peptide structure.	40
5 Experimental and simulated vibrational spectra of UH, A4, and A5	49
6 Experimental and simulated vibrational spectra of spectra of A4A5H and A4A5O	53
7 Experimental and simulated vibrational spectra of spectra of A2A4H and A2A5H	54
8 Frequency variation for a single label ^{13}C position in the 3_{10} -peptide sequence.	60
9 Simulated IR and VCD of UH, A4A5H, A3A4H and A2A5H with solvent correction for CDCl_3	63
10 Structural models used for computations in the polyproline II study.	67
11 Simulated amide I' FTIR, VCD and Raman spectra for the unlabeled Ac-P $_{13}$ -NH $_2$ compared to the sequential and alternate doubly labeled ones adopting polyproline II conformation	69
12 Simulated amide I' FTIR, VCD and Raman spectra for the unlabeled Ac-A $_{22}$ -NHCH $_3$ compared to the sequential and alternate doubly labeled ones adopting polyproline II conformation	72
13 Representative trpzip conformation taken from 20 best NMR structures determined for TZ2C.	75
14 Single isotope labeled variants of TZ2C used for this study	76
15 Experimental and simulated amide I' absorption spectra of unlabeled TZ2C, A1 , A3 and A10	78
16 Comparison of calculated amide I' with PCM solvent correction and vacuum	80
17 Double isotope labeled variants of trpzip2C used for this study	90

LIST OF FIGURES (Continued)

<u>FIGURE</u>		<u>PAGE</u>
18	Comparison of simulated and experimental IR spectra for TZ2C , A1A10, A3A8 and A3A10	91
19	The Trpzip2 peptide indicating the sequential positions of the four tryptophans involved	104
20	Calculated in-plane transition dipole moments for 3MI used in the TDC computations	107
21	Calculated UV absorbance spectra for 3 methyl indol (3MI) and indole	111
22	UV absorption and CD spectra computed for all the two-indole pairs studied . . .	114
23	Calculated CD spectra for the selected pairs of indoles	115
24	Comparison of the calculated CD spectra for two tryptophans, four tryptophans, and the summation of all the double mutant calculations.	121
25	Orbital analysis of the transitions corresponding to the observed transitions	123
26	TDC-DCO modeled UV and ECD spectra for the tetramer, W2W11 and W4W9. . .	125
27	Calculated CD spectra for the selected pairs of tyrosines and tryptophans in WYYW, modeled using 3MI and p-cresol.	128
28	Common Raman shift regions for organic molecules	131
29	Energy levels associated with scattering and fluorescence	133
30	Basic Raman spectroscopy experimental design	134
31	Two common experimental geometries	138
32	A ray optics picture of optical trapping	140
33	Cross section of an optical trap and a trapped particle.	141
34	Illustrative principle of optical trapping.	146
35	Schematic of the force detection method.	148
36	Outline of the basic building blocks of the OTRS.	152
37	Detailed schematic of the OTRS.	154
38	Exploded view of the OTRS core.	158
39	Cross section of the sample chamber.	164
40	Confocal Raman microscopy	167

LIST OF FIGURES (Continued)

<u>FIGURE</u>		<u>PAGE</u>
41	The quadrant position sensitive detector.	169
42	Reflection of a well aligned 785 nm trapping laser.	173
43	Confocal mode Raman spectrum of trapped polystyrene beads.	175
44	Plot of the intensity of the 1000 cm^{-1} peak of polystyrene	176
45	Power spectral density of a trapped polystyrene bead.	177
46	Raman spectra from L-B media	179
47	Raman spectra from a single <i>E. coli</i> cell	180
48	Raman spectra from a single yeast <i>S. cerevisiae</i> cell	182
49	UV-Vis absorption spectrum of bare gold nanorods	184

LIST OF ABBREVIATIONS

3MI	3-Methyl Indole
AAT	Atomic Axial Tensor
APT	Atomic Polar Tensor
B3	Becke 3 parameter
CCD	Charge Coupled Device
CD	Circular Dichroism
COSMO	Conductor Like Screening Model
DAQ	Data Acquisition
DCO	Degenerate Coupled Oscillator
DFT	Density Functional Theory
DPSS	Diode Pumped Solid State
ECD	Electronic Circular Dichroism
FTIR	Fourier Transform Infrared
FWHM	Full Width At Half Maximum
GGA	Generalized Gradient Approximation
GNR	Gold Nano Rods
GTO	Gaussian Type Orbitals
IR	Infra Red
LB	Luria Bertani
LDA	Local Density Approximation
LED	Light Emitting Diode
LYP	Lee Yang Parr
NA	Numerical Aperture
NDF	Neutral Density Filter
OD	Optical Density
OTRS	Optical Trapping Raman Spectrometer
PCM	Polarizable Continuum Model
PDB	Protein Data Bank
PP II	Poly Proline II
PSD	Position Sensitive Detector
PW91	Perdew-Wang 91
QPD	Quadrant Photodiode
RMS	Royal Microscopical Society
SERS	Surface Enhanced Raman Spectroscopy
STO	Slater Type Orbitals
TDC	Transition Dipole Coupling
TDDFT	Time Dependent Density Functional Theory
UV	Ultraviolet
VCD	Vibrational Circular Dichroism

SUMMARY

This is a thesis in two parts. The first part (A), comprising Chapters 1 through 4, details the modeling of molecular spectra of various peptide secondary structures using ab-initio quantum mechanical (QM) calculations. Molecular spectroscopy, both vibrational and electronic, can be used as a sensitive tool to study molecular structure but since it is an inherently low resolution method, theoretical calculations are essential for a complete understanding of vibrational and electronic spectra.

Chapter 1 is an introduction to peptide structure, and also introduces vibrational spectroscopy as a general phenomena. The chapter then progresses to describe aspects of vibrational spectral signatures that can probe peptide structure. Since the first part of this thesis is modeling spectra using computational methods, the chapter ends by highlighting the importance of modeling in molecular spectroscopy.

Chapter 2 is a review of the theory behind the computational tools required to model IR spectra. The approximations that are assumed in the theoretical model that we choose are highlighted. Two primary methods that are used to calculate the energy in molecular systems, Hartree-Fock and density functional theory (DFT) are then introduced. It is then shown that spectral properties are derivatives of the energy of the molecular structure. The chapter closes with a brief description of the transfer of force field and spectral properties from short peptide systems to longer peptide chains.

Chapter 3 is a discussion of calculation of ground state spectral properties of various peptide secondary structures. Helical structures are the most common type of secondary structure of which the most popular, α helix has been previously studied in the Keiderling research group in detail. The

SUMMARY (Continued)

chapter begins with a study of the molecular spectra of other kinds of helices: 3_{10} and polyproline II helices. The latter part of the chapter is related to the spectral study of β -hairpins. In this study the transfer method is not used, rather calculations are performed on the β -hairpin structure in its entirety. This proves to be a better description of the experimental spectrum of β -hairpins.

Chapter 4 moves away from secondary structure and vibrational spectroscopy. While Chapter 3 focused on the backbone structure of β -hairpins studied, in Chapter 4 the interaction of the side chain of tryptophans (Trp) is the focus. The interaction of these Trp can be studied by modeling their electronic circular dichroism (ECD) spectra. Since electronic states are not accessible using ground state methods such as DFT, other computational methods need to be resorted to. One of the newer QM methods that includes excited states is time dependent DFT (TDDFT). Using TDDFT the ECD spectra of various Trp interactions has been modeled and compared to experiment.

Chapters 5 to 7 comprise the second part (B) of this thesis. The second part of this thesis is an exploration of the use of optical trapping methods in studying the experimental Raman spectra of microbes and vesicles. Chapter 5 introduces optical trapping as a method that allows for the manipulation of sub-micron scale objects, using tightly focused laser light. Next the experimental aspects of Raman spectroscopy are discussed. The chapter also discusses of the prospects coupling of a Raman microscope with an optical tweezer as a novel method that might give insight into the relationship between mechanical forces acting upon cells and their molecular structure.

Chapter 6 details the actual construction an instrument that implements the method introduced in Chapter 5. This instrument is referred to as an optical trapping Raman spectrometer (OTRS). In this chapter, the technical aspects of the successful coupling of the various components of the OTRS are discussed in detail.

SUMMARY (Continued)

Chapter 7 discusses the potential applications of the OTRS to test systems, and, as an example, Raman spectra for two single cell systems using the OTRS is discussed. Finally, shortcomings of the OTRS and modifications that may improve its performance are discussed.

CHAPTER 1

INTRODUCTION

1.1 Overview

The first half of this thesis centers on theoretical calculations of the spectroscopic signatures of peptides. This introduction deals with some preliminaries of peptide structure and their spectroscopy. Section 1.2 introduces peptides as a subclass of biomolecules, describes their characteristics and justifies their study. Section 1.3 discusses concepts behind the spectroscopies (specifics of the computational method are presented in Chapter 2). The last section is an overview of the importance of theoretical calculations in successful analysis of the experimental spectra.

1.2 Peptides and proteins

Biomolecules, or more specifically biogenic molecules, are macromolecules produced by life processes. Proteins, lipids, polysaccharides and nucleic acids constitute the “big four” biomolecules, i.e. they are the four most commonly occurring in nature (1). With the exception of lipids, they are all polymerized chains of a basic structural unit (monomer). Although lipids are macromolecules, they are not true polymers as they lack covalent bonding between the individual monomers.

In both proteins and peptides, the monomeric unit is an amino acid that contains two functional groups, an amine and a carboxylic acid. Two such units can undergo a condensation reaction (the elimination of water) and form an amide bond, otherwise known as a peptide bond. Further amide condensation reactions lead to the formation of a polypeptide.

The distinction between protein and polypeptides is an ambiguous one and can be attributed to a multitude of criteria viz. size, function, composition, source, etc. The United States Food and Drug

Administration bases its distinction on size, citing the Biologics Price Competition and Innovation (BPCI) Act of 2009. According to the BPCI act, any alpha amino acid polymer with a specific defined sequence that is greater than 40 amino acids in size is a protein and less than 40 is an peptide. In addition, according to the BPCI, a “chemically synthesized polypeptide” might have anywhere between 2 to 99 amino acids.

Another definition based on composition is more consistent and defines a protein as a polypeptide composed solely of proteinogenic amino acids. Proteinogenic amino acids are those which are coded for in the genetic code of an organism, and a characteristic among them is that the amino group is bound to the α -carbon and their chirality is always L (except for glycine which is achiral).

1.2.1 The peptide bond

Figure 1 illustrates a dipeptide formed by two units of a chiral amino acid. If the side chain is methyl ($R=CH_3$), then the *primary structure*, which is merely the sequence of the covalently bonded monomeric subunits, would be alanyl-alanine. Looking closer, the $C=O$ double bond is delocalized, giving the $C-N$ bond a partial double bond character and hindering the rotation around the $C-N$ bond. The amide $O=C'-N-H$ atoms therefore lie in one plane, shown as a yellow shaded plane in the bottom scheme in Figure 1. The torsional rotation angle around the $C'-N$ bond is labeled ω and is usually 180° for trans peptide bonds. Rotation of the $C-N-C_\alpha-C$ (ϕ) and $N-C_\alpha-C-N$ (ψ) dihedral angles are still possible. Specific values of ϕ, ψ when repeated along the peptide sequence give rise to protein secondary structures like α -helices and β -sheets (2).

Beyond the secondary structure is the tertiary structure, in which, other interactions of the side chain functional groups of the residues in a single polypeptide chain determine the final geometry of the polypeptide. Inclusion of a folded polypeptide chain with other (non covalently bound) polypeptide chains leads to what is called the quaternary structure. Figure 2 summarizes these levels

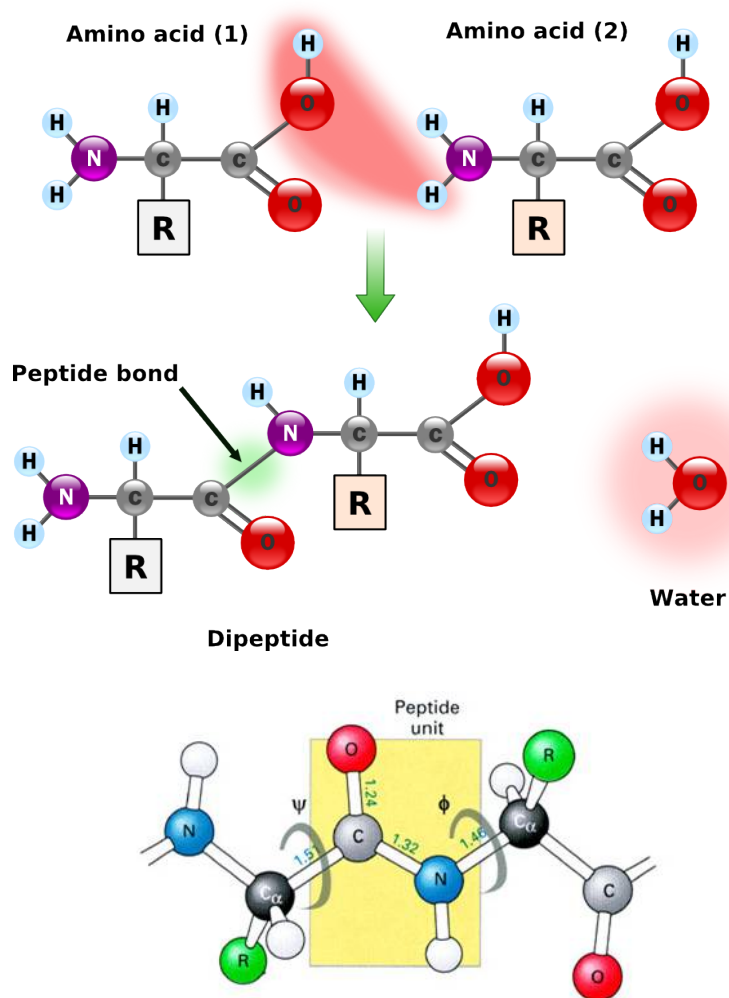


Figure 1: (Top) Shows peptide formation by condensation of amino acids with the elimination of a water molecule. “R” might be any side chain group of the amino acid. (Bottom) Highlights the two dihedral angles that eventually define secondary structure. Adapted version of original illustration released into the public domain by Yassine Mrabet.

of structure. For small peptide systems, without side chain interactions, the secondary structure dominates the structural characterization.

1.2.2 Ramachandran plot

Due to the steric effects of the C_α substituents, some values of ϕ , ψ are energetically more favorable than others. The Ramachandran plot(3) is a convenient way to visualize these torsional angles in a structure. It is most often a two dimensional plot, with the abscissa and ordinate being the ϕ and ψ torsional angles, respectively. Each point on this plot represents torsional angles for a single peptide bond in a peptide sequence. Ramachandran and coworkers showed using simple alanyl-alanine models that while some regions of this " ϕ, ψ -space" are highly likely to be populated, others (almost 70%) are not. Although these regions were based solely on steric effects (avoidance of steric clashes between the C_α and amide group), a study of the protein data bank (PDB) (4) confirms that a majority of proteins listed there lie in the allowed regions.

The main regions of Ramachandran space are the α -helices, 3_{10} - helices, polyproline helices, β -sheets and α_L -helices (proline and glycine are exceptions due to their high rigidity and high flexibility, respectively). It is important to mention that other secondary structures might be defined but these either have a low frequency of occurrence or have minor structural variation from major structures. As an example, 3_{10} -helices are not always explicitly shown in illustrations and are considered part of the broad family of right-handed helices. α_L -helices have a left handed twist, which is not energetically favored by peptide bonds that are formed between L-amino acids. In addition the side chains are not aligned well enough to allow energetically favorable interactions; these factors make α_L -helices rare. On the other hand, right handed helices are commonly found in proteins and have considerable structural variation amongst them. Since they are of primary interest in this thesis, they will be elaborated upon in the next section.

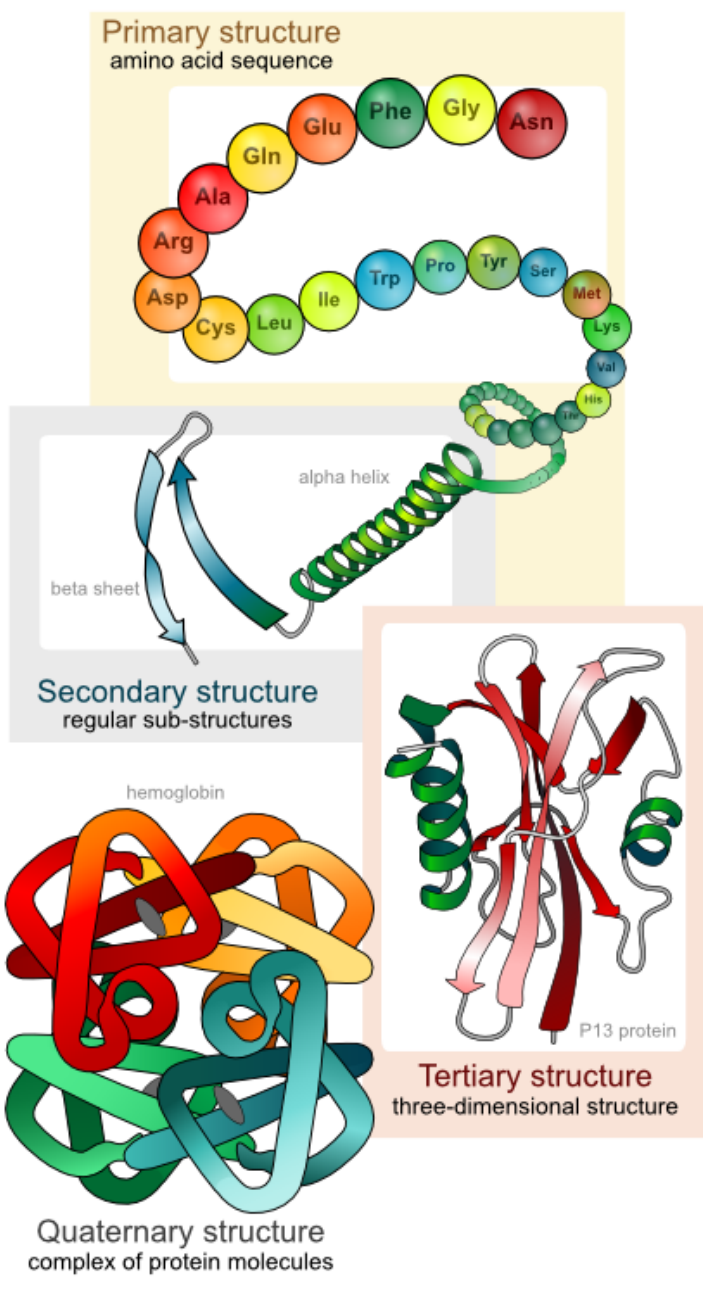


Figure 2: The hierarchical building up of structural complexity in proteins as explained in the text. Adapted version of original illustration released into the public domain by Mariana Ruiz Villarreal.

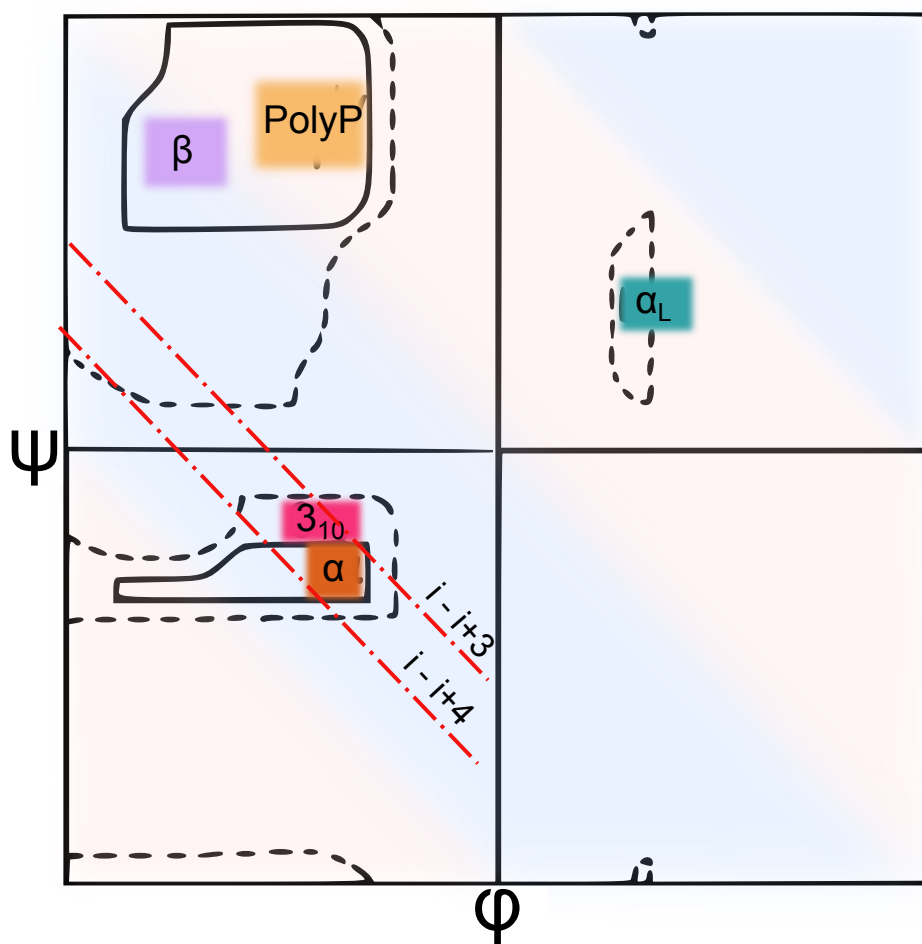


Figure 3: A sketch of a Ramachandran plot highlighting some of the secondary structures that are sterically allowed. The red dash-dotted line illustrates ϕ, ψ angles which allow for $i \rightarrow i + 3$ or $i \rightarrow i + 4$ hydrogen bonding. The pink and blue shaded regions roughly indicate the regions of left-handed and right-handed helices respectively. The dashed line contains allowed regions of ϕ, ψ with τ angle($NC_{\alpha}C$) of $\approx 110^{\circ}$ (5). Adapted version of original illustration by Jane Richardson, Duke university and used under a Creative Commons Attribution-ShareAlike license.

1.2.3 Helical types

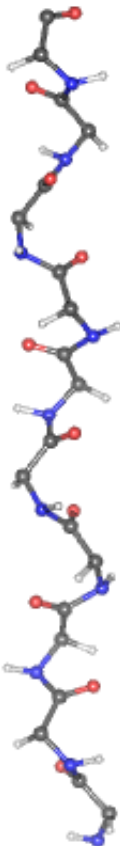
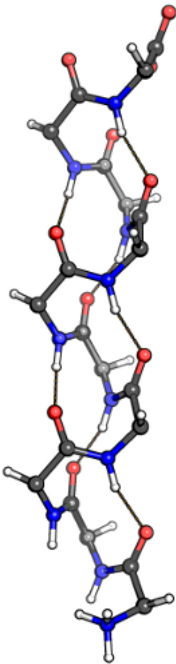
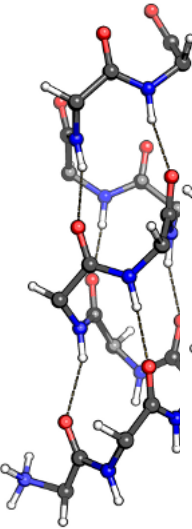
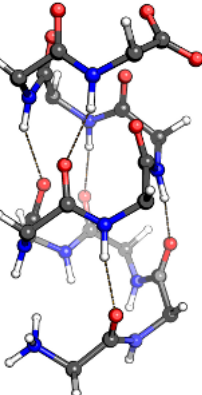
1.2.3.1 Helices and hydrogen bonding

Primary factors affecting helix stability are conformational entropy, hydrophobic effects, and hydrogen bonding. Conformational entropy always favors the unfolded state while hydrophobic effects favor the compact state so that hydrophobic residues are less exposed to solvent. Hydrogen bonding is now accepted as the stabilizing force forming the folded helical state (6). The energy of a single hydrogen bond is in the 2-8 kcal/mol range in isolated molecules but for peptides that are in an aqueous environment, it is estimated to be 1-2 kcal/mol (7). The driving force for secondary structure stability is that all hydrogen bond donors and acceptors in the peptide backbone should be saturated (8). In a protic environment this can mean hydrogen bonding to the solvent. This can be achieved in various ways and the backbone dihedral variations among the helices are due to internal hydrogen bonding pattern in the helices. The helix structures and parameters are summarized in Table I. α helices have been well studied in the Keiderling group (9; 10) and by others (11; 12; 13) in the past.

1.2.3.2 The elusive 3_{10} -helix

Table I shows that for the same number of residues a 3_{10} -helix is more tightly wound, longer, and thinner than an α -helix. 3_{10} -helices make up $\approx 4\%$ of all protein secondary structures (14) (alternatively stated, 10% of helical structures are 3_{10} -helical) and they are usually not more than 5 residues long (15). 3_{10} -helices are often found at the terminus of an α -helix and show a higher variation in their backbone dihedral angles than do α -helices (16). Additionally, it has been recently shown that in membrane bound helices the probability of occurrence of longer 3_{10} -helices is substantially higher (17).

TABLE I: Summary of various helical structures for a deca-alanine model.

Structure	PP II-helix	3_{10} -helix	α -helix	π -helix
deca-alanine				
ϕ, ψ -angles ($^\circ$)	-75,145	-60,-30	-57,-47	-85,-70
H-bonding	none	$i \rightarrow i + 3$	$i \rightarrow i + 4$	$i \rightarrow i + 5$
Helical-Pitch ^a (\AA)	9.3	6	5.4	1.7
Handedness	Left	Right	Right	Right

^a Helical pitch is the rise along the helical axis per one complete turn

Besides their probability of occurrence, 3_{10} -helices also have a functional role. Millhauser and coworkers have proposed that the 3_{10} -helix is an intermediate along the helix-coil folding pathway (18). Bezanilla and coworkers suggest an $\alpha \rightarrow 3_{10}$ transition to be the key factor for the voltage sensing domain of sodium channels in neurons (19; 20). Moreover, their association with membranes might be due to lower solvation (21) and a higher electric potential near the membrane (20; 22; 23).

In solution, α -helices usually require a longer sequence to become stabilized via intra-molecular hydrogen bonding (24). 3_{10} -helices on the other hand can tend to form helical structures with just six amino acids (25; 26; 27). The critical length for transition from the 3_{10} - to α -helix is eight residues (21). Due to competitive stabilities, isolated 3_{10} - helices are in equilibrium with α -helices. This equilibrium can be shifting either by changing solvent polarity (28) or by application of an external electric field (29).

One of the ways to study the 3_{10} -helical structure exclusively is the introduction of amino-isobutyric acid (Aib) as a residue in the peptide sequence. Addition of a non-proteinogenic amino acid, which has steric hindrance due to a second methyl substitution at the α -position, favors the 3_{10} conformation even for short trimeric peptides (30; 31). This is because in an α - helix the i^{th} Aib methyl group unfavorably interacts with a residue present at the $(i+3)^{th}$ position (32) making the 3_{10} -helix more stable in vacuum calculations (12). Due to the minor variation in structural parameters between α and 3_{10} helices, they are not easy to distinguish in solution. In Chapter 3, I further explore the differences in the vibrational spectra and vibrational coupling in α - and 3_{10} -helices.

1.2.3.3 Poly proline-II helices

Proline (Pro) does not have a hydrogen atom at its amino group, therefore it cannot form a hydrogen bond to stabilize an α -helix or a β -sheet. Proline's presence in a helix often leads to a kink in the helix and is a helix breaker in solution (33), however Pro can lead to helix stabilization in membrane environments (34; 35) where the cis-trans isomerization can act as a gating mechanism (36). Longer sections of Pro residues, with trans amide couplings form a left handed helical structure known as the polyproline- II (PPII) helix (Table I), an example of which is a single strand in the collagen triple helix (PDB ID:1CAG). Due to the lack of an internal C=O...H-N hydrogen bond, stability in these structures is attributed to the increased rigidity of the pyrrolidine ring in proline. A recent study showed that the $n \rightarrow \pi^*$ electronic interaction from the oxygen of the peptide bond and the subsequent carbonyl carbon in the polypeptide have been shown to contribute to polyproline stability (37; 38; 39; 40).

Since a proline peptide bond can also exist in a cis conformation, two conformations of PP helices, I and II, are possible (37). The polyproline-II (PP-II) helix ($\phi, \psi = -78, +146$), due to the trans X-Pro bond (where X is any amino acid), is energetically more stable and is the more populated conformation. What makes the PP-II conformation interesting is that it is the predominant conformation of all types of residues in unstructured regions of proteins. This unstructured region, known as a random coil, turns out to be not as random as once thought but is rather confined to a broad PPII region of the Ramachandran plot (41; 42; 43).

1.2.4 β -hairpins

The two most common structures found in the PDB after helices are β -sheets (2) and turns. β -sheets are formed by hydrogen bonding between chains of polypeptides that are in a near extended conformation ($\phi, \psi = -135, +135$). A single unpaired chain would be termed a β -strand. A common

definition of a turn requires the C_α of two non adjacent residues (usually, from one to five residues apart) to be closer than 7\AA and not be part of a helical or sheet secondary structure (44). While short stable helices are relatively easy to prepare, the nature of hydrogen bonding in β -sheets makes it hard to model using short sequences.

A good model for tight turns and β -sheet (anti-parallel) interactions is the β -hairpin motif (45). A motif is a super-secondary structure which is comprised of a combination of secondary structure elements that are frequently repeated in proteins. The β -hairpin is a special class of a turn where there is an additional interaction (attractive) between the two anti-parallel β strands that can stabilize a turn (46). The β in β -hairpin signifies the beta sheet interaction and the turn may be of any type, not necessarily a β -turn which contains three peptide bonds.

Isolated β -hairpins in solution can be further stabilized by adding pairs of tryptophan (Trp) residues on opposite strands of the hairpins (47). Interaction between the tryptophans can stabilize tertiary structure in a protein and is further explored in Chapter 4.

1.3 Molecular vibrations

1.3.1 Normal modes

Molecules are constantly vibrating at a multitude of frequencies with complex and coupled equations of motion. One way to simplify analysis of this motion is by changing the representation of these motions from local spatial coordinates (Cartesian) to normal coordinates. Normal coordinates are linear combinations of Cartesian coordinates; motions along these normal coordinates are called normal modes. A normal mode combines all the motions that occur with the same frequency and phase. Normal modes are thus separated from one another, on the basis of energy which makes them a natural basis for vibrational spectroscopy.

At lower frequencies, normal modes can represent completely delocalized global motions (like librations), while at higher frequency, normal modes represent slightly more localized motions (like the stretching of the peptide C=O). These modes might be dominated by contributions from specific chemical sub-structures, but are delocalized over the entire molecule. The dominant local modes that contribute to normal modes are what give rise to characteristic group frequencies, like the amide I (see below) (48). In our calculations of vibrational spectra, the primary interest is in the information contained in these higher energy normal modes (higher than 1000 cm^{-1}), i.e. bond stretching and bending (49).

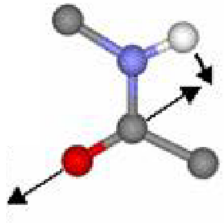
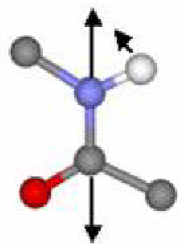
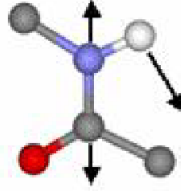
1.3.2 The amide mode(s)

The amide modes are the principal diagnostic probes for secondary structure in peptides in vibrational spectroscopy. The amide normal modes are so named since they primarily involve motion of the peptide amide bond. The modes that are of particular interest to my research and this thesis are listed in Table II.

The most widely used vibrational band is the amide I mode, which corresponds to the C=O stretching of the peptide bond (i.e. $\approx 80\%$ of the total energy in this mode) with minor mixing of the N-H bending and $C_{\alpha}H$ bending vibrations. Since the amide I lies in a frequency region that is devoid of other modes, it does not couple well with other modes. However, the amide I region is a broad band owing to vibrational coupling between the various individual C=O oscillators (50). This coupling depends upon the relative orientation of C=O to each other (ϕ, ψ angles), which in turn is governed by secondary structure. The C=O vibration is also dependent upon solvation as it can shift due to the formation of hydrogen bonds in protic environments (51; 52; 53).

The amide II mode is a combination of an N-H bend (60%) and a C-N stretch which are out-of-phase. Phase here corresponds to the relationship between the direction of the C-N stretch and N-H

TABLE II: Summary of the amide modes observed in experiment.

Mode	Motion	Contributing Motion	Frequency	2° Structure	Raman	IR
Amide I		C=O stretch	1645-1672	α -helix	s	s
			1660-1666	3_{10} -helix	s	s
			1665-1672	β -sheet	s	s
			1660-1670	PP-II coil	s	
Amide II		C-N stretch & N-H bend (out of phase)	1540-1560	α -helix	w	
			1530-1550	3_{10} -helix	w	
			1500-1550	β -sheet	w	
			1500-1550	PP-II coil	w	
Amide III		C-N stretch & N-H bend (in phase)	1270-1300	α -helix	w	w
			-	3_{10} -helix		
			1243-1253	β -sheet	s	w
			1229-1235	PP-II coil	m	w

s :strong

w :weak

m :medium

bend. In the out-of-phase case, while the C-N bond stretches outward, the N-H bends (in the peptide plane) away from the C-N bond. The amide II mode is either weak or absent in Raman (49). Due to a high contribution of the N-H bend to this mode, it is sensitive to deuteration of the peptide N-H unit (54; 55) which is discussed in the next section.

The amide III mode is also a combination of a N-H bend (30%) and a C-N stretch but in this case the motions are in-phase. This mode is also sensitive to deuteration but since the N-H contribution to this mode is lower, the shift in energy of this mode upon deuteration is not as large as is for the amide II. Additionally, the amide III is more than 10× weaker than the amide I in the IR (56), but is of similar magnitude to the amide I in Raman. Therefore, the amide III Raman has been used by others for secondary structure studies of peptides (57).

While they are the most exploited for analysis, the amide modes are not the only modes that are useful for conformational analysis. For example, Krimm and coworkers have shown that the C_α-H stretch is also sensitive to the secondary structure of peptides (58; 59).

1.3.3 Deuteration

Experimental IR and VCD spectra of peptides in water are often obtained in a deuterated solvent like D₂O since H₂O has a large absorption around the amide I peak ($\approx 1600 \text{ cm}^{-1}$). Raman spectra for the most part do not suffer from very large Raman scattering of water, although a non negligible scattering due to the H-O-H bending mode of water does occur at $\approx 1600 \text{ cm}^{-1}$, which needs to be subtracted.

Dissolving peptides in D₂O exchanges all the solvent exposed labile hydrogens with deuterium. This changes the reduced mass that is associated with the amide mode (going from N-H to N-D) and has an effect of red- shifting all the vibrational modes associated with the N-H bend. The shifts for the amide I, which is referred to as amide I', is negligible since the N-H contribution to this mode is

minor. However as mentioned above this shift can be $\approx 100 \text{ cm}^{-1}$ for an amide II mode, which is referred to as the amide II' mode after deuteration (55). All the computations done in this thesis are therefore corrected for H-D exchange.

1.4 Spectroscopy

1.4.1 Infrared (IR)

The frequency range of mid infrared radiation (mid-IR) is similar to the frequencies of molecular oscillations ($10^{12} - 10^{14}$ Hz). When a molecule interacts with IR radiation, its vibrational modes resonantly absorb IR light. In the harmonic approximation, the absorption only occurs at the frequencies of the normal mode oscillations. The absorption spectrum reflects not only the chemical composition (i.e. bonding and structure) of the system but can also be used to predict conformation based on the frequency variation of the normal modes. In the following chapters Fourier transform infrared (FTIR) will be used interchangeably with IR, since the FT part signifies only the instrumental design by which the IR spectrum is collected.

1.4.2 Vibrational circular dichroism (VCD)

VCD is the differential absorption of left circularly polarized (LCP) and right circularly polarized (RCP) IR radiation that only occurs if the molecule lacks axes of improper rotation, i.e. if it is chiral (60). The peptide amide I mode has a VCD band shape that is dependent on the local conformation of the molecule. It is especially sensitive to ϕ angle changes where it fares better than IR in distinguishing PP-II coils from α - helices (61; 62). In this thesis VCD spectra are calculated for helices in Chapter 3 and more background on the theoretical method is given in Chapter 2.

1.4.3 Raman Scattering

Raman spectroscopy also provides information on molecular vibrations. In IR spectroscopy, if the vibration is associated with a change in dipole moment, the mode will absorb IR radiation (i.e. is IR active). To be Raman active, a vibrational mode has to have a change in polarizability associated with a vibration. However Raman spectroscopy measures light that is scattered, not absorbed, which makes the Raman transition an intrinsically weak phenomena.

The advantage of Raman lies in the fact that peptides can be studied in water (as a natural environment, as opposed to D₂O) because water is a weak scatterer and does not usually interfere with Raman spectral analysis. Additionally, some amide modes like the amide III, that are useful for secondary structure analysis, show very weak IR activity but are stronger in Raman (63; 64; 57; 65). Raman spectroscopy also provides additional information about side chains especially with highly polarizable aromatic substituents. An example would be peptides with tryptophan residues (66), which were successfully measured in our group on an instrument that I had modified and reconfigured (67). Chapter 6 in this thesis provides a more in-depth look at theoretical aspects of Raman spectroscopy.

1.4.4 Electronic circular dichroism (ECD)

While IR light excites vibrational energy levels, UV light excites transitions between electronic energy levels in molecules with a chromophore. The chromophore (which is typically an unsaturated group) in peptides is the delocalized π system on the peptide amide bond. While the UV spectrum is sensitive to the presence of chromophores, it is not very sensitive to their relative orientation (secondary structure). However, if circularly polarized light is used to excite the transitions, the differential absorption of left and right circularly polarized light is sensitive to backbone secondary

structure. This difference is the electronic circular dichroism (ECD) and is a standard method for secondary structure determination.

However, in peptides where a substantial fraction of the side-chain substituents on the C_α are aromatic groups that are additionally conformationally constrained and interact with each other, the ECD method for structure determination fails. Aromatic groups have $\pi \rightarrow \pi^*$ transitions which can couple to each other, and if the relative conformation of the chromophore is fixed, then the coupled CD can easily overwhelm the ECD due to the amide bonds. The ECD spectrum then becomes diagnostic of the relative orientation of the aromatic rings. Chapter 4 in this thesis reports a computational study to interpret experimental ECD spectra of such coupled tryptophan side chains.

Table III gives an overview of the experimental methods that were simulated by theory in this thesis.

TABLE III: Summary of molecular spectroscopy methods computed.

Spectroscopic method	Light interaction process	Molecular phenomena	Chiral method?
Infrared	absorption	molecular vibration	No
Raman	scattering	molecular vibration	No
Vibrational CD	absorption	molecular vibration	Yes
Electronic CD	absorption	electronic excitation	Yes

1.5 Theory: The role of computations

Although vibrational spectroscopy does provide more detailed information than does electronic spectroscopy, molecular spectroscopy is in general an inherently low resolution method. Therefore other methods, like NMR and X-ray crystallography are used for structure determination. On direct comparison of IR and NMR, NMR is the clear winner in terms of spatial resolution whereas IR is better for time resolution. However, for a majority of experiments that our computations deconvolve, neither property is crucial. We seek to study the dependence of spectral variations and vibrational coupling on structural variations. A study of vibrational coupling, by definition, can only be done using vibrational spectroscopy. The choice of a specific method (IR, Raman, etc.) is subjective and depends on the system being studied.

In peptides, the amide I is a composite band of many amide C=O stretches of slightly different frequencies. The experimentally measured amide I is therefore a broad band, a convolution of the amide modes present in the peptide. To obtain residue specific information, an experimentalist can use isotope labeling of selected residues in a peptide. Labeling a residue's carbonyl with ^{13}C red-shifts the amide I band for that particular residue by $\approx 40\text{ cm}^{-1}$ to lie outside the normal bandwidth of the ^{12}C amide I, which means that a single residue or set of identical residues can be studied independently.

The amide I transition dipole moments are coupled to one another. While our primary interest was the fundamental study of spectral variation of this coupling phenomena in peptides (based on secondary structure), others have hypothesized that this coupling allows vibrational energy transfer in proteins (68; 69). To study the dependence of coupling on secondary structure, it is essential to know the individual uncoupled frequencies of the C=O oscillators. While isotopic labeling with ^{13}C might decouple the labeled oscillator from the rest of the C=O groups, it cannot discriminate two

labeled oscillators from each other. However, it can measure the shifts caused by coupling from the uncoupled positions if single and double labeled peptides are studied.

Accurate interpretation of the vibrational spectrum and its attribution to a specific conformation requires the support of computations. While classical calculations based on Wilson's empirical force field methods are possible (70), the lack of an objective force field parameters to use with that method motivates us to look to electronic structure based approaches to describe the spectra of the peptides. One such electronic method that we use is density functional theory (DFT) and its application is described in the next chapter.

For the research presented here either ideal structures (for helices) or NMR averaged structures (for hairpins) were used as a starting point to calculate spectra. Various isotopic labeling schemes were then used to study vibrational structure and coupling and the resultant simulated spectra were compared to the results of experimental studies performed by other members of the Keiderling group.

Electronic spectroscopy can also be greatly aided by computations. In Chapter 4, methods based on quantum mechanics are used to interpret the electronic spectra (ECD) of peptides containing tryptophan. Quantum mechanical calculations allow us to accurately model the properties of transitions between electronic states. In the next chapter I will elaborate on the specifics of our theoretical/computational approach.

CHAPTER 2

COMPUTATIONAL METHODOLOGY

2.1 Overview

This chapter will detail the methodology used to compute spectra for small peptide systems constrained to selected secondary structures. Since all the computational methods used herein are mature and well developed, I provide a conceptual overview of the methods that were used in the calculation of theoretical spectra, rather than details of their implementation. Emphasis is laid on the “tool chain” i.e. the flow of approximations, methods, algorithms, and methods used to perform the calculations feasibly.

The aim is to simulate molecular spectra and the way forward is to solve the Schrodinger equation (SE). For polyatomic systems, there exist far too many degrees of freedom for feasible calculation of large systems. Therefore, many theoretical approximations are needed to ensure that the problem is computationally feasible. Section 2.2 covers most of the approximations assumed in all the mainstream QM methods. Section 2.3 introduces Hartree-Fock (HF) and, our method of choice, density functional theory (DFT). In Section 2.4, normal modes are introduced, this time including some mathematical insight. Then briefly explained, in Section 2.5, are the spectral parameters we are trying to ascertain, followed by an overview of how solvation is introduced into these calculations in Section 2.6. In Section 2.7 the method that was used to calculate properties of larger structures from smaller ones is discussed. Section 2.9 introduces calculations to estimate excited state properties.

2.2 Hierarchy of approximations

Our calculations are performed on single isolated molecules for practicality with the immediate consequence that inter-molecular interactions are not taken into consideration. The molecular Hamiltonian can be written as

$$\hat{H}_{mol} = \overbrace{\hat{T}_N + \hat{T}_e}^{\text{Kinetic}} + \overbrace{\hat{V}_{ee} + \hat{V}_{eN} + \hat{V}_{NN}}^{\text{Coulomb Potential}} \quad (2.1)$$

where \hat{T}_N is the nuclear kinetic energy operator, \hat{T}_e is the kinetic energy of the electrons, \hat{V}_{ee} is the electron- electron repulsion term , \hat{V}_{eN} is the electron-nuclear attraction term and \hat{V}_{NN} is the nuclear-nuclear repulsion term.

The fact that a proton is approximately $2000\times$ heavier than an electron, generally means for any change in nuclear coordinates the electrons adjust instantaneously. Therefore, it is possible to separate the nuclear Hamiltonian from the electronic one and solve them independently. This is the Born-Oppenheimer approximation, which functionally assumes that the nuclei are fixed on the time scale of electronic events, so that the nuclear kinetic energy term (T_N) can be ignored for the electronic Hamiltonian and used for a separate SE describing nuclear motion. The solution of the electronic Hamiltonian is then added to the (\hat{V}_{NN}) term to create a potential energy for the nuclear motion. The electronic or clamped nuclei Hamiltonian can be written as,

$$\hat{H}_{elec} = \hat{T}_e + \hat{V}_{ee} + \hat{V}_{eN} \quad (2.2)$$

It would be expedient at this point to see the underlying structure of these operators (in atomic units):

$$\hat{H}_{elec} = \underbrace{\sum_i \frac{\hbar^2}{2m_e} \nabla_{\mathbf{r}_i}^2}_{\hat{T}_e} + \underbrace{\sum_i \sum_{j>i} \frac{1}{|\mathbf{r}_i - \mathbf{r}_j|}}_{\hat{V}_{ee}} + \underbrace{\sum_I \sum_j \frac{Z_I}{|\mathbf{R}_I - \mathbf{r}_j|}}_{\hat{V}_{eN}} \quad (2.3)$$

The electronic wavefunction can now be solved, with only a parametric dependence on the nuclear coordinates. These nuclear coordinates can be varied to calculate the energy as a function of all the degrees of freedom. A plot of the energy vs the various degrees of freedom is called a potential energy surface (PES). For a small semi-rigid molecule, the positional minimum energy on the PES is the equilibrium geometry and the search for this minimum is called geometry optimization, which will be explored more in 2.4. At each position of internuclear separation the total molecular energy needs to be calculated.

To make the system computable, a mean field theory like Hartree-Fock (HF) or density functional theory (DFT) might be used. DFT was preferred over HF since it is computationally more efficient. The computational codes used in this thesis implement DFT in its Kohn-Sham formulation (KS-DFT), and since KS-DFT is closely linked to Hartree-Fock, Hartree-Fock theory is briefly introduced.

2.3 Energy calculations

2.3.1 Hartree Fock

One approach to the many body problem is to assume that rather than each electron interacting with each other electron, each electron only “feels” an average potential of the rest of electrons in the molecule. This potential is the Hartree potential, an average Coulomb repulsion of all the other electrons. The single many- electron wave function (Ψ) can now be re-written as a product of many

one-electron wave functions, $\phi(r_n)$ (the molecular orbitals), also called the Hartree product, which is given as,

$$\Psi(r_1, r_2 \dots r_n) = \phi(r_1)\phi(r_2)\dots\phi(r_n) \quad (2.4)$$

However, electrons are Fermions and according to the Pauli principle, a Fermionic wave function must be anti-symmetric with respect to electron exchange. A Slater determinant (SD) provides a method of anti-symmetrizing, since exchanging any two columns in a Slater determinant flips the sign of the wave function. The SD is formulated as,

$$\Psi(r_1, r_2 \dots r_n) = \frac{1}{\sqrt{n!}} \begin{vmatrix} \phi_1(r_1) & \phi_2(r_1) & \dots & \phi_n(r_1) \\ \phi_1(r_2) & \phi_2(r_2) & \dots & \phi_n(r_2) \\ \vdots & \vdots & \ddots & \vdots \\ \phi_1(r_n) & \phi_2(r_n) & \dots & \phi_n(r_n) \end{vmatrix} \quad (2.5)$$

The SD, which is a form of the HF wave function, can be alternatively written as

$$\Psi_{SD} = \Psi_{HF} = \Psi(r_1, r_2 \dots r_n) = |\phi(r_1), \phi(r_2), \dots, \phi(r_n)\rangle \quad (2.6)$$

The Slater determinant makes every electron associated with every orbital. Minimization of the energy with respect to the SD gives rise to the Hartree- Fock equations. The idea in HF is to reformulate a single N-dimensional problem to N one-dimensional problems. In the next approximation each molecular orbital is written down as a linear combination of atomic orbitals

(AO). This is the linear combination of atomic orbitals (LCAO) ansatz, and for any matrix element in the RHS of Equation 2.5, the MO can be expanded as

$$\phi(r_i) = \sum_{\mu} C_{\mu i} \chi_{\mu}(r_i) \quad (2.7)$$

where χ_{μ} is an atomic orbital (AO) basis function and $C_{\mu i}$ is the MO coefficient, or the weight that a particular AO carries in the sum. To determine the value of the MO coefficients we use the variational principle and minimize the energy with respect to the coefficients.

$$E = \min_{\Psi} \langle \Psi_{SD} | \hat{H}_{HF} | \Psi_{SD} \rangle \quad (2.8)$$

Without going into detail, Equation 2.3 can be rearranged and condensed to

$$E_{HF} = \sum_i H_i + \frac{1}{2} \sum_{ij} (J_{ij} - K_{ij}) \quad (2.9)$$

where i and j are indexes for the i^{th} and j^{th} electrons. H_i is the one electron operator and contains the \hat{T}_e and \hat{V}_{eN} terms that only depend upon one electron. The Coulomb term J is due to the Coulombic electronic repulsion and the K term is due to electronic exchange. These are elements of the \hat{V}_{ee} term and are known as two electron integrals or electron repulsion integrals (ERI). These are the most computationally demanding part of the scheme. The two-electron terms constitute the Hartree-Fock repulsion potential that replaces the \hat{V}_{ee} term in Equation 2.3.

While electron exchange is accounted for by the HF formulation, electron correlation is still missing. Correlation effects can be introduced perturbatively using post-HF methods, but the computational cost is very high. To include correlation without this high computational cost we

focus on theories that are more tractable like DFT, which is formulated to compute the electron density.

2.3.2 Density Functional Theory

DFT is a standard theoretical model to calculate ground state properties for molecules. The basis for DFT are the Hohenberg-Kohn (H-K) theorems (71) which establish that the ground state electronic energy is determined completely by the electron density (ρ). Also, the true ground state ρ is the density that minimizes $E[\rho]$, which is the H-K variational theorem. The immediate advantage is that the density is a function of 3 variables (3-dimensional space) unlike the wave function that was $3N$ dimensional. Electron density as a concept is less esoteric than the notion of a wave function. An intuitive interpretation argues that the integral of the density defines the number of electrons and that the positions of the nuclei are the cusps in the density (72) .

The DFT energy is given as the sum of five components:

$$E_{DFT} = E_T + E_V + \underbrace{E_J + E_K + E_C}_{V_{ee}} \quad (2.10)$$

where E_T is kinetic energy, E_V is the potential energy, E_J is the coulomb term, E_K is the exchange term and E_C the correlation term. This is similar to Equation 2.2 except now we have an explicit correlation term, E_C . The Coulombic terms can be expressed exactly but the kinetic, exchange, and correlation term have no known exact expressions in terms of ρ . While the original H-K approach is orbital free there seems to be no prescription for the exact functional (a functional is a function that takes another function as its input). One way to move forward is the Kohn-Sham (KS) formulation of DFT, in which the orbitals are reintroduced. In the KS ansatz the original many body problem

is replaced with a fictitious system of non-interacting electrons that generate the same density as interacting ones (73).

Analogous to Equation 2.9 the Kohn-Sham operator is given as:

$$F^{KS} = H_{KS} + \int \frac{\rho}{r_{12}} dr + V_{XC} \quad (2.11)$$

The KS wave function is a KS Slater determinant and satisfies the non interacting Kohn-Sham Schroedinger equation:

$$\left[-\frac{1}{2}\nabla^2 + V_{eff} \right] \phi(r) = \epsilon_i \phi_i(r) \quad (2.12)$$

where $\phi_i(r)$ are the KS orbitals and ϵ_i are the KS eigenvalues. The energy of such a system in terms of KS quantities is

$$E = T_S + U + V + E_{XC} \quad (2.13)$$

where T_S , the KS kinetic energy, is the sum of the orbital contributions and U is the Hartree energy due to Coulombic interactions with a mean potential. V is the one body potential and E_{XC} is the exchange- correlation energy that has no definite form and needs to be given a functional form. This is the first approximation within the K-S formulation. The solution of Equation 2.12 parallels the solution for the HF theory, i.e the energy is minimized with respect to the KS orbital coefficients.

2.3.3 DFT: Choice of parameters

Traditionally, E_{XC} is broken to down into the exchange (X) and correlation (C) part. The XC energy density of a uniform electron gas can be used as a first approximation. This is called the local density approximation (LDA) and, while it works well, it does overestimate the binding energy by 1 eV per bond. A step up from LDA is the generalized gradient approximation (GGA), which includes

the dependence of E_{XC} on the gradient of density of electrons. Functional parameters can get more sophisticated if we fit them with some experimental reference data about atoms and molecules. In this thesis all vibrational calculations have been done with BPW91 (74) which is Becke's B88 GGA exchange (75) and Perdew-Wang's PW91 correlation functional (also GGA). This functional combination has been established in our research group to give best agreement with experiment for amide modes in peptides (76).

The correlation functional can also be fitted to experiment using the Lee- Yang-Parr functional (LYP) and H-F exchange can also be included (B3LYP). Some functionals perform very well, a prime example being B3LYP, which is ubiquitous in computational chemistry. The B3LYP is an amalgamate of B88 and LYP correlation, where H-F exchange is added on using three parameters. B3LYP has been established to be a standard for TDDFT calculations for the systems we study and consequently it is chosen for our excited state calculations

Similar to the HF-SCF method the KS orbitals are also expanded in an AO basis; the closest approximation to which are Slater type orbitals (STO). STO are computationally demanding to solve and Pople and coworkers first implemented the use of Gaussian type orbitals (GTO) to approximate the STO (77). GTO allow analytical integral evaluation and efficient pre-screening in polyatomic systems. The choice of basis set is usually a tradeoff between performance and computational time. Previously in our research group the 6-31G* basis set proved to be a suitable basis set (78; 79). The core electrons require a more detailed treatment since the density drops quickly near the nucleus. For calculations of force constants and normal mode frequencies it is important to add polarization to the basis sets.

Unfortunately, the XC functional doesn't have a closed form solution. DFT methods cannot be solved analytically and require numerical integration using grid methods. We select a fine pruned

grid for numerical quadrature, which is also the default in the Gaussian suite of programs. Pruned grids in Gaussian have asymmetric number of angular grids as the distance from nucleus increases. I will return to the topic of energy calculation in 2.9 but for now we will move on to calculating ground state molecular properties.

2.4 Harmonic approximation and normal modes

2.4.1 Harmonic approximation

In the vicinity of an equilibrium point, the internuclear potential can be modeled as being harmonic, i.e the restoring force is linearly proportional to the displacement from the equilibrium point. If these displacements are small, the harmonic approximation (mechanical harmonicity) is thought to be valid and the internuclear potential can be expanded as a Taylor series that has been truncated at the quadratic term:

$$\begin{aligned}
 E = E_0 + \sum_{i=1}^N & \left[\left(\frac{dE}{dx_i} \right)_0 y_i + \left(\frac{dE}{dy_i} \right)_0 y_i + \left(\frac{dE}{dz_i} \right)_0 z_i \right] \\
 + \frac{1}{2} \sum_{i=1}^N & \left[\left(\frac{d^2E}{dx_i^2} \right)_0 x_i^2 + \left(\frac{d^2E}{dy_i^2} \right)_0 y_i^2 + \left(\frac{d^2E}{dz_i^2} \right)_0 z_i^2 \right] \\
 + \frac{1}{2} \sum_{i,j=1}^N & \left[\left(\frac{d^2E}{dx_i dx_j} \right)_0 x_i x_j + \left(\frac{d^2E}{dy_i dz_j} \right)_0 y_i z_j + \left(\frac{d^2E}{dz_i dx_j} \right)_0 z_i x_j \right]
 \end{aligned} \tag{2.14}$$

where E_0 is the potential energy at the minimum, which can be taken to be zero, and the first summation term vanishes, since it is the first derivative of a function at a minimum. Equation 2.14 can be rewritten in matrix form (H^m in Equation 2.15), where the second and third summation terms of Equation 2.14 are the diagonal and off-diagonal (cross-terms) quadratic terms of H^m (Equation 2.15). The matrix of the second derivatives of the energy with respect to displacement is

called the Hessian. The Hessian, H^m , which is the Cartesian representation of the harmonic force field, is given as,

$$H^m = \begin{bmatrix} \frac{\partial^2 E}{\partial x_1^2} & \frac{\partial^2 E}{\partial x_1 \partial y_1} & \cdots & \frac{\partial^2 E}{\partial x_1 \partial z_2} \\ \frac{\partial^2 E}{\partial y_1 \partial x_1} & \frac{\partial^2 E}{\partial y_1^2} & \cdots & \vdots \\ \vdots & \vdots & \ddots & \vdots \\ \frac{\partial^2 E}{\partial z_2 \partial x_1} & \cdots & \cdots & \frac{\partial^2 E}{\partial z_2^2} \end{bmatrix} \xrightarrow[\text{Diagonalize}]{H^Q = Q^T H^m Q} H^Q = \begin{bmatrix} \frac{\partial^2 E}{\partial Q_1^2} & 0 & \cdots & 0 \\ 0 & \frac{\partial^2 E}{\partial Q_2^2} & \cdots & \vdots \\ \vdots & \vdots & \ddots & \vdots \\ 0 & \cdots & \cdots & \frac{\partial^2 E}{\partial Q_6^2} \end{bmatrix} \quad (2.15)$$

Off-diagonal terms in H^m make the Cartesian representation not very useful for describing molecular motions. To simplify the representation, a coordinate transformation from Cartesian coordinates to normal coordinates is performed by diagonalizing the Hessian \vec{H}^m from the Cartesian basis to a normal mode basis \vec{H}^q , which has no off-diagonal cross terms in the harmonic approximation (80). Normal coordinates are linear combinations of Cartesian coordinates and motions along these normal coordinates are called normal modes. Rotational and translational motion of a molecule do not change the geometry of the molecule and show up on the diagonal with zero energies and are separated out from the other $3N-6$ vibrational modes. After establishing that a geometry corresponds to the equilibrium point and having computed all the vibrational normal modes, spectral properties may be calculated.

2.5 Calculation of spectral properties

It is possible, in principle, to compute any spectroscopic property that can be measured using quantum mechanics, by computing the appropriate derivative of the energy. Different spectroscopies require different derivatives, and the ones of interest in this thesis are described below.

2.5.1 Infrared absorption

The integrated intensity of an isolated IR absorption band is directly proportional to the square of the dipole strength D_{if} , which can be evaluated via the extinction coefficient ϵ

$$D_{if} = 9.184 \times 10^{-39} \int_{band} \epsilon \frac{d\nu}{\nu} \quad (2.16)$$

where $\frac{d\nu}{\nu}$ is the frequency dispersion and D_{if} is the square of the electric dipole transition moment

$$D_{if} = |\langle \Psi_i | \mu | \Psi_f \rangle|^2 \quad (2.17)$$

and in which μ is the electric dipole moment operator and Ψ is the total molecular wave function. μ can be further split into its nuclear and electronic contributions:

$$\mu = \mu^{Electronic} + \mu^{Nuclear} \quad (2.18)$$

$$= -e \sum_i \vec{r}_i + e \sum_{\alpha} Z_{\alpha} \vec{R}_{\alpha} \quad (2.19)$$

where e is the charge on a single electron, r_i is the position of the i^{th} electron and Z_{α} and R_{α} are the sum and position of the α^{th} nucleus. The sums run over all electrons and nuclei respectively.

A fundamental transition is one from the ground to the first excited state ($|0\rangle \rightarrow |1\rangle$). For a fundamental IR transition in the i^{th} normal mode the transition moment integral is given by:

$$\langle 1 | \mu | 0 \rangle_i = \left[\frac{\partial \vec{\mu}}{\partial Q_i} \right]_0 \quad (2.20)$$

where Q are the normal mode coordinates. The component of μ in the Q_i direction is:

$$\mu(Q) = \mu(0) + \left(\frac{d\mu}{dQ_i} \right)_0 Q_i + \frac{1}{2} \left(\frac{d^2\mu}{dQ_i^2} \right)_0 Q_i^2 + \dots \quad (2.21)$$

where $\mu(0)$ is the permanent dipole moment and does not play a role in IR vibrational transitions. The first term to connect two vibrational levels is the linear term, $\left(\frac{d\mu}{dQ} \right)$. Terminating the above series at this linear term is also a harmonic approximation, which is called electrical harmonicity. All calculations done here are therefore done under the so called double harmonic approximation. A consequence of this approximation is that overtones and combination bands have zero intensity.

Thus the calculation of IR spectral intensities narrows down to the calculation of electric dipole moment derivatives. Since calculations are most often performed in Cartesian space we can rewrite Equation 2.20 as:

$$\langle 1 | \mu_{el} | 0 \rangle_i = \sum_{\lambda\alpha} P_{\alpha\beta}^\lambda S_{\lambda\alpha,i} \quad (2.22)$$

where,

$$P_{\alpha\beta}^\lambda = \left[\frac{\partial \mu_{el}}{\partial X_{\lambda\alpha}} \right]_0 \quad (2.23)$$

$$X_{\lambda\alpha} = \sum_i S_{\lambda\alpha,i} Q_i \quad (2.24)$$

The S-matrix defines the relation between the normal coordinates \vec{Q}_i and the Cartesian displacements \vec{X} . λ is the index of the nucleus being considered and α represents the x, y and z spatial coordinate indexes. The S-vectors provide a basis for visualizing the nuclear displacements associated with each normal mode. They are the vectors on each nucleus, the magnitude and direction of which depict how each nucleus moves in any given normal mode Q_i (81). The $P_{\alpha\beta}^\lambda$ tensor is termed as the

atomic polar tensor (APT) of nucleus λ and is the proportionality coefficient between the dipole moment and the atomic displacement. The APT has the dimensionality of a charge and it can be separated into contributions from the nuclear (N) and electronic parts (E),

$$\begin{aligned}
 P_{\alpha\beta}^{\lambda} &= E_{\alpha\beta}^{\lambda} + N_{\alpha\beta}^{\lambda} \\
 E_{\alpha\beta}^{\lambda} &= \left[\frac{\partial}{\partial X_{\lambda\alpha}} \langle \Psi | \mu_{el}^e | \Psi \rangle \right]_0 = 2 \left\langle \Psi^0 \left| \mu_{el}^e \left| \left(\frac{\partial \Psi}{\partial X_{\lambda\alpha}} \right)_0 \right. \right. \right\rangle \\
 N_{\alpha\beta}^{\lambda} &= (Z_{\lambda} e) \delta_{\alpha\beta}
 \end{aligned} \tag{2.25}$$

where μ_{el}^e is the electric dipole moment of the ground electronic state and $Z_{\lambda}e$ is the charge on the nucleus λ . Ψ is the unperturbed wave function and $\frac{\partial \Psi}{\partial X_{\lambda\alpha}}$ is the derivative of the wave function with respect to the Cartesian displacement coordinate. In the BO approximation, the nuclear positions are known and their contribution to the dipole are trivial to compute. The computational cost for the programs used for our calculations lies in the calculation of derivatives of the wave function for the electronic contribution to the APT.

2.5.2 Vibrational circular dichroism

The chiroptical analog to the dipole strength D in absorption is the rotatory strength, R ,

$$R_{if} = 2.296 \times 10^{-39} \int_{band} \Delta\epsilon \frac{d\nu}{\nu} \tag{2.26}$$

where $\Delta\epsilon$ is the difference in molar extinction coefficient for left and right circularly polarized light ($\Delta\epsilon = \epsilon_L - \epsilon_R$). Theoretically, for a fundamental excitation of the i^{th} normal mode in the electronic ground state ($|0\rangle_i \rightarrow |1\rangle_i$), R is given as (82)

$$R(0 \rightarrow 1)_i = Im \left[\langle 0 | \hat{\mu} | 1 \rangle_i \cdot \langle 1 | \hat{m} | 0 \rangle_i \right] \quad (2.27)$$

$$= |\vec{\mu}| \cdot |\vec{m}| \cdot \cos(\vec{\mu}, \vec{m}) \quad (2.28)$$

Equation 2.28 is the Rosenfeld equation (83), where $\mu = \langle \Psi_0 | \hat{\mu} | \Psi_1 \rangle$ is the electric dipole moment as in Equation 2.19 and $m = \langle \Psi_0 | \hat{m} | \Psi_1 \rangle$ is the magnetic dipole moment. The magnetic dipole moment operator \hat{m} , can again be separated into two components as:

$$m = m^{Electronic} + m^{Nuclear} \quad (2.29)$$

$$= \frac{e}{2m_e c} \sum_i \vec{r}_i \times \vec{p}_i + \frac{eZ_\alpha}{2M_\alpha c} \sum_\alpha \vec{R}_\alpha \times \vec{P}_\alpha \quad (2.30)$$

where e is the charge on a single electron, \vec{r}_i is the position of the i^{th} electron and Z_α and R_α are the sum and position of the α^{th} nucleus. \vec{p}_i is the electron angular momentum and \vec{P}_α is the momentum of the α^{th} nucleus. The mass of the electron is given as m_e , M_α is the mass of the α^{th} nucleus and c is the speed of light in atomic units.

Analyzing Equation 2.28 we can immediately put constraints on normal modes that will have any rotational strength. The mode must have a non zero electric dipole moment and a non zero magnetic moment. Additionally, \vec{m} and $\vec{\mu}$ must not be at right angles to each other. The electric dipole moment, $\vec{\mu}$, is calculated using the APT and the magnetic moments, \vec{m} , need to be calculated.

Within the BO approximation, for closed shell molecules, the electronic magnetic moment contribution to the VCD vanishes because $m_{el} = \langle \Psi_0^e | m_{el} | \Psi_0^e \rangle = 0$. VCD intensities were calculated using the magnetic field perturbation (MFP) method developed by Stephens (82). MFP provides a way to calculate VCD intensities within the BO approximation by perturbation of the ground states. The Stephens equation for the magnetic dipole transition moment of the fundamental transition of the i^{th} normal mode is (84) :

$$\langle 0 | m | 1 \rangle_i = \sum_{\lambda\alpha} \vec{M}_{\alpha\beta}^{\lambda} \vec{S}_{\lambda\alpha,i} \quad (2.31)$$

where $M_{\alpha\beta}^{\lambda}$ is an atomic tensor, termed atomic axial tensor (AAT) by Stephens. The AAT is given as:

$$M_{\alpha\beta}^{\lambda} = I_{\alpha\beta}^{\lambda} + J_{\alpha\beta}^{\lambda} \quad (2.32)$$

$$I_{\alpha\beta}^{\lambda} = \left\langle \left(\frac{\partial \Psi}{\partial \vec{X}_{\lambda\alpha}} \right) \left| \left(\frac{\partial \Psi}{\partial \vec{H}_{\beta}} \right) \right. \right\rangle \quad (2.33)$$

$$J_{\alpha\beta}^{\lambda} = (Z_{\lambda} e) R_{\lambda\gamma}^0 \epsilon_{\alpha\beta\gamma} \quad (2.34)$$

where $I_{\alpha\beta}^{\lambda}$ and $J_{\alpha\beta}^{\lambda}$ are the electronic and nuclear contributions to the AAT and $\left(\frac{\partial \Psi}{\partial \vec{H}_{\beta}} \right)$ is the derivative of the ground electronic wavefunction with respect to an external magnetic field perturbation \vec{H}_{β} . The factor $\epsilon_{\alpha\beta\gamma}$ is the Levi-Civita tensor with indices running over Cartesian components. The nuclear magnetic moment is straightforward to calculate, but the electronic part is not trivial. However it has been successfully implemented in the Gaussian program.

Computationally, the calculation of AAT is more involved than those of APT due to the additional calculation of magnetic field derivatives. Another complication in computing AATs is that of gauge origin. The magnitude of a physical observable should not depend on the choice of coordinate system. In the case of magnetic moments, it does. A remedy that is implemented in the Gaussian

programs (85) (and others) is the use of gauge including atomic orbitals (GIAO), wherein each AO centered on each atom is multiplied by a phase factor. This method removes origin dependence by including the gauge in the AO (86).

2.5.3 Raman Scattering

The intensity of scattered light is proportional to the square of the change of polarizability along a normal mode. The intensity can be defined as the ratio of the scattered radiation power per solid angle $\left(\frac{d\Phi}{d\omega}\right)$.

The polarizability (α) can be written as a Taylor-series expansion around a equilibrium point. In the far from resonance regime, we use the Placzek approximation by terminating the series at the linear term,

$$\alpha = \alpha(0) + \left(\frac{d\alpha}{dQ}\right)_0 Q \quad (2.35)$$

where Q is a geometry displacement along a normal mode. The static polarizability, $\alpha(0)$, leads to elastic Rayleigh scattering while the second term, with its dependence on molecular normal coordinates gives rise to inelastic Raman scattering. The Placzek approximation circumvents the need to sum over states and focuses on the nuclear coordinate dependence in the ground state (87).

Raman intensity is then,

$$\left(\frac{\partial \vec{\alpha}}{\partial \vec{Q}}\right)^2 \quad (2.36)$$

where polarizability, $\vec{\alpha}$, in the Harmonic approximation is given as

$$\alpha = \left(\frac{d^2 E}{d\epsilon_\alpha d\epsilon_\beta}\right) \quad (2.37)$$

where E is the total energy of the molecule and ϵ are the electric field components. The Raman intensities for the i^{th} mode is then given as:

$$P_i \propto \left(\frac{d^3 E}{dQ_i d\epsilon_\alpha d\epsilon_\beta} \right)_i \quad (2.38)$$

where Q_i is the displacement in the i^{th} normal mode. Similar to AATs, Raman intensities require the calculation of a mixed derivative. Raman intensities are effectively third order derivatives and very accurate calculations would be required to obtain reasonable results numerically. Analytical derivative methods are therefore preferred and implemented in Gaussian09.

Table IV summarizes the ground state properties that have been calculated in this thesis.

TABLE IV: Molecular properties as derivatives of energy

Derivative	Observable
$\frac{d^2 E}{dQ_i dQ_j}$	Hessian (FC) : Harmonic force constants
$\frac{d^2 E}{dQ_i d\epsilon_\alpha}$	APT: Dipole derivative, IR intensity
$\frac{d^3 E}{dQ_i d\epsilon_\alpha d\epsilon_\beta}$	Polarizability derivative, Raman intensity
$\frac{d^2 E}{dQ_i dB}$	Electronic part of the AAT ^a , VCD intensity

^a atomic axial tensor, see text for nuclear component.

2.6 The effect of solvation

The experimental spectra that these calculations are compared to are normally measured in solution. It is natural then to consider solvent effects in the calculation. In a QM calculation, both equilibrium geometries and vibrational frequencies are influenced by interaction with the solvent. One way to include solvation effects is to include solvent molecules with the solute in a larger DFT calculation. This super-molecular treatment is the explicit solvent model and has the inherent drawback of being computationally demanding and the more fundamental problem of localizing solvent molecules that are in constant motion with only weak attraction to the target molecule.

To alleviate the computational cost of adding atoms an alternative way is to look at an average effect of the solvent. One family of methods are the continuum solvation models, where the solvent is represented as a uniform polarizable medium with a dielectric constant of ϵ . The molecule is then placed in a cavity surrounded by this medium (72). The cavity in the medium costs energy, while the van der Waals interaction of the molecule with the medium usually adds stability. The solute polarizes the medium and the mirror charges in the dielectric provide a stabilizing electrostatic interaction. The free energy of solvation may therefore be written as:

$$\Delta G_{\text{solvation}} = \Delta G_{\text{cavity}} + \Delta G_{\text{repulsion/dispersion}} + \Delta G_{\text{elec}} \quad (2.39)$$

The default solvation model in Gaussian09 is the polarized continuum model (PCM) method (88). PCM creates the solute cavity via a set of overlapping spheres (tesserae). Unlike the Onsager case, which places the molecule in a spherical cavity, the form of this PCM cavity is dependent on molecular shape and the dielectric constant of this cavity is set to that of the solvent of interest. A variation to PCM is the conductor like screening model (COSMO). In the COSMO model the surrounding

medium is modeled as a conductor, rather than as a dielectric in order to establish the initial boundary conditions (89). When included in the PCM framework COSMO is called C-PCM and this method was chosen due to its better performance (90). A possibility not implemented in this work, but worth exploring are hybrid methods, where the molecule and some solvation shells form a super-molecule, the next few shells are calculated at the level of all atom molecular mechanics and the rest of the solvent is modeled as a continuum. These are sometimes called QM/MM (Quantum Mechanics/Molecular Mechanics) or ONIOM, depending on how they are implemented (91).

2.7 Scaling up: Transfer of spectral properties

The large size of some of the peptides studied experimentally made them too challenging for direct ab-initio calculations under our computational constraints. An alternate way to approach this problem is to perform calculations on smaller tractable systems and transfer the force field properties. Such transfers are routine in molecular mechanics and dynamics, where the force fields from experiment and theory are transferred from a database onto the molecules of interest (92).

A methodology developed previously by our collaborator Prof. Petr Bour, Academy of Science, Prague (93) was implemented as follows. First, a calculation is performed on a smaller model peptide system that had the important internal hydrogen bonding and structural elements of interest (backbone geometry). Then the Cartesian coordinates of the atoms in the smaller peptide (the “source”) were mapped onto the larger one (the “target”). This involved overlaying the source and target structure and mapping the force field and spectral properties (APT, AAT, etc.) from the source atoms to the corresponding target atoms, in terms of Cartesian tensor components. The source molecule was then translated along the longer target molecule, rotated for optimal overlap of atoms (the rotation axis was collinear with the direction of translation) and the procedure repeated until the source molecule had traversed the entire length of the target molecule. After transfer of the FF

for all atoms in the larger molecule are represented by local FF values from the smaller molecule which appear in the full FF matrix as a diagonal band with interaction elements extending out the equivalent of the length of the smaller source molecules.

The normal modes of the larger molecule were then determined by diagonalizing the entire FF matrix. To compare effects of isotopic substitutions, selected atoms were chosen and ^{13}C atomic mass was substituted into the inverse mass matrix before diagonalizing the FF. Either way, the vibrational normal modes were then calculated in Cartesian coordinates expressed as an S matrix and the frequencies were determined from the eigenvalues. The S-matrix was used with the APT, AAT and polarizability derivatives to generate the IR, VCD and Raman spectral intensities. The spectra generated were line spectra having no spectral width or shape. To be compared with experiment, these intensities were convoluted with a Gaussian bandshape function. A suitable FWHM for the Gaussian band was chosen empirically by comparison to experiment. The entire method was developed by Petr Bour and reimplemented in our lab by a set of programs provided by him that parse the Gaussian output and then do the selected spectral simulations. The protocol followed in our calculations is summarized in Figure 4, the individual steps of which are highlighted in the preceding sections.

2.8 Calculation of vibrational coupling constants

In Chapter 3 of this thesis, vibrational coupling between isotopically labeled amides is calculated using quantum calculations. Two amide groups in a peptide are selectively labeled with ^{13}C on the carbonyl carbon. The interaction or coupling of the two isotopically labeled amides is strongly dependent on the local secondary structure of the peptide. This coupling are also referred to as the off-diagonal elements of the Hessian. Quantum chemical calculations assume a harmonic potential and the resultant normal modes are delocalized modes with no coupling amongst the modes, i.e.

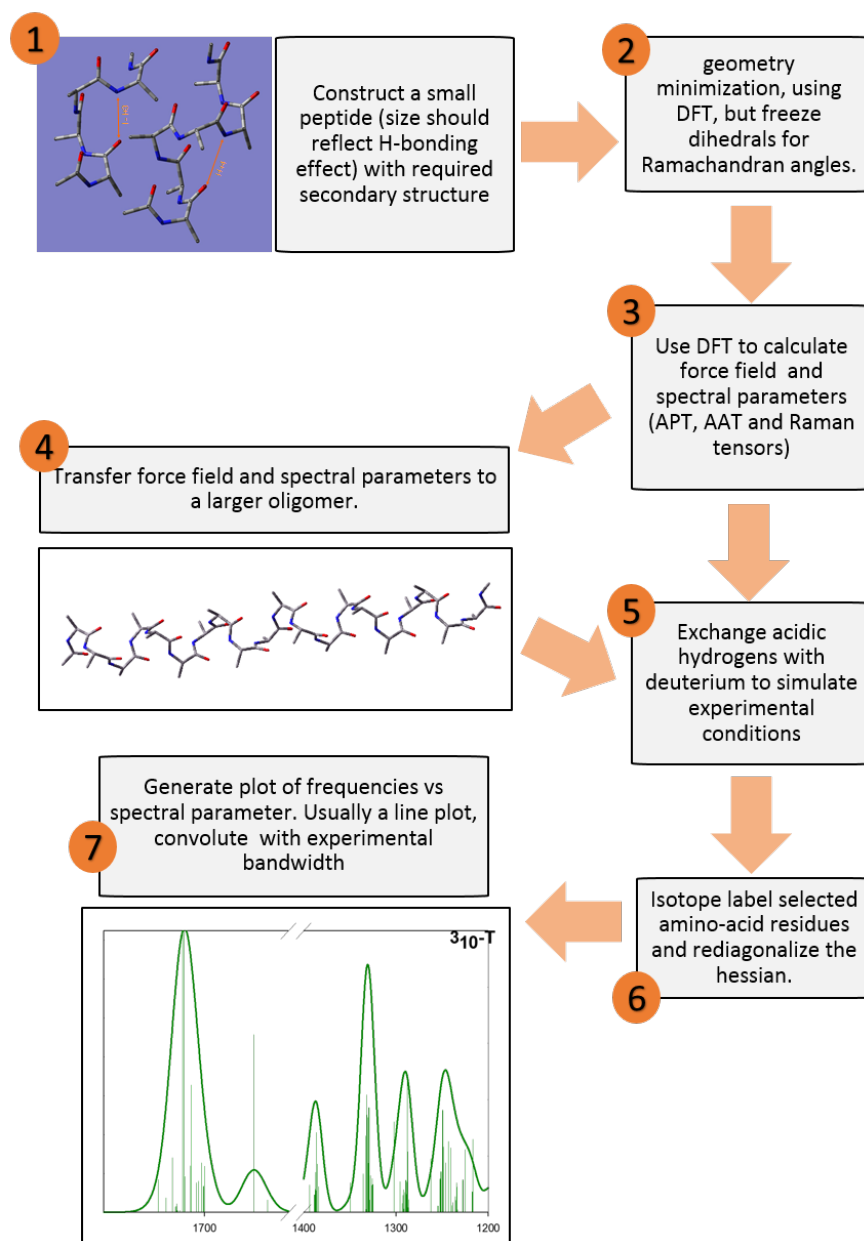


Figure 4: Outline of the steps involved in the modeling of theoretical spectra starting from the initial peptide structure.

there are no off-diagonal elements in the Hessian expressed in the normal coordinates. The amide I normal modes can also be analyzed as linear combinations of local amide I modes. Local modes, while unrealistic, provide a more intuitive picture of the interaction between two discrete local oscillators (94).

The local amide mode picture is based on the assumption that the amide I normal modes are not mixed to other normal modes. Furthermore, on isotope labeling selected amides in a peptide with ^{13}C , it is also assumed that ^{13}C isotope labeled amide I modes are not coupled to the rest of the ^{12}C amide modes. Thus, an isolated 2×2 Hessian $H^{Q,sub}$ is extracted from the complete Hessian H^Q . $H^{Q,sub}$ has two diagonal elements and no off-diagonal elements. The diagonal elements are eigenvalues for the symmetric (in-phase) and anti-symmetric (out-of-phase) amide I modes.

$H^{Q,sub}$, a 2×2 Hessian with respect to normal modes $H^{Q,sub}$ might be converted to a 2×2 Hessian with respect to localized (normally assumed to be degenerate) modes $H^{L,sub}$, by a unitary transformation to internal coordinates (94):

$$H^{L,sub} = U^T H^{Q,sub} U \quad (2.40)$$

where the diagonal elements of $H^{L,sub}$ are the force constants of the two local amide I modes and the off-diagonal elements are the vibrational coupling force constants between such local modes. In our model, the diagonal elements of the $H^{L,sub}$ are degenerate, suggesting that in the absence of coupling the local modes would appear in the spectrum at the same frequency. With this assumption the vibrational coupling can be calculated from the difference in the frequency of the two ^{13}C labeled amides, and the coupling constant is defined to be half of that difference. Thus, without explicitly

changing the coordinate system in our analysis, we are able to calculate the coupling constant from our spectral calculations, based on the assumption in this simple local mode coupling model.

2.9 Excited states: electronic CD

The simulation of electronic CD spectra requires the ab-initio calculation of the rotational strength R , which is the imaginary component of the scalar product of electronic dipole moment, μ and the electronic magnetic moment, m ,

$$R = \text{Im}[\mu \cdot m] \quad (2.41)$$

where R represents only the electronic component of Equation 2.28.

In the prior sections, the calculation of molecular properties by a perturbative treatment of the ground state was highlighted. Even for VCD, which in principle depends on vibronic coupling to other states, it was possible to calculate the magnetic vibrational transition dipole moment using the energy derivative methods, fully in the ground state, by using Stephen's magnetic field perturbation approach. However, electronic absorption and electronic circular dichroism (ECD) calculations involve transitions from the ground state to excited electronic states which must be explicitly evaluated and therefore usually require the inclusion of excited states in the calculation.

HF theory lacks treatment of electron correlation and is not suitable for excited state calculations. Post-HF methods might be used for excited states, but they scale unfavorably with size of the system and usually require very large basis sets for accurate results (95). While the H-K theorems in DFT are formulated for the ground electronic state, time dependent DFT (TDDFT) theory encompasses non-stationary states and states in external fields and provides access to excited state properties (96).

TDDFT is a relatively new tool and is computationally inexpensive (97), especially in contrast to other QM theories that incorporate excited states.

One approach to include time would be to start with a self-consistent Kohn- Sham state selected for the initial time and to let the system propagate in time. The time variation of the dipole moment could be recorded and Fourier transformed to obtain the dynamic polarizability, from which the the electronic absorption and ECD spectrum could be obtained. Such a real time method might be required to model a molecule that is exposed to a short, intense laser pulse (98).

For perturbation by weak fields, like in the case of ECD, there is another approach known as the linear response density functional theory (LR-TDDFT) approach (99; 100). The linear response approach assumes that the external perturbation does not destroy the ground state wavefunction. In this approach, instead of propagating the system explicitly in time, the ground state system is perturbed (V_0) with an applied time dependent electromagnetic field ($V_1(t)$) to give an effective external potential, V_{ext} :

$$V_{ext} = V_0 + V_1(t) \quad (2.42)$$

Since the perturbation ($V_1(t)$) is weak, there is only a small change in the electron density ($\rho_1(r, t)$) from the original time independent ground state electron density ($\rho_0(r)$) calculated with time independent DFT:

$$\rho(r, t) = \rho_0(r) + \rho_1(r, t) \quad (2.43)$$

The first order variation in the electron density can be determined from the the linear density response equation of the system (in frequency space):

$$\rho(r, \omega) = \int \chi(r, r', \omega) V_1(r', \omega) dr \quad (2.44)$$

where the susceptibility, χ , is the density response function and gives the density change at point r due to a change in applied potential at point r' . At the transition frequencies of the system, the change in the density is dramatic and the complex valued response function χ blows up, i.e. the response function has a pole. Gaussian09 implements the Casida linear response approach to calculate ECD intensities (101). Casida reformulated the calculation of the poles of the response function to a generalized Hermitian matrix eigenvalue problem. Eigenvectors of the Casida matrices are the exact vertical excitation energies and the dipole oscillator and rotational strengths can be calculated from the eigenvalues of the Casida matrices (100).

TDDFT also allows for the optimization of excited state geometries, which are of comparable computational cost to the ground state optimizations (102). In this thesis, we have calculated the vertical transitions from the ground state equilibrium geometries and thus avoid optimizing the excited state. These vertical transitions (or Frank Condon allowed transitions) are what we observe in our experiments.

2.10 Conclusion

Given that computations to calculate molecular properties can be executed with the click of a mouse button, it is thus easy to treat these programs as “black boxes”. The purpose of this chapter was to open that box a little and discuss how the molecular Hamiltonian is built for the various calculations performed. Even an intermediate understanding of the steps involved can lead to two positive outcomes. The first is gaining confidence in the reliability of the results. The other is developing a knowledge of the kind of questions that can be asked. This is what eventually led to Chapter 4.

CHAPTER 3

MOLECULAR VIBRATIONS IN PEPTIDES : SPECTROSCOPIC SIMULATIONS

The results of these studies were published. I performed the theoretical calculations in collaboration with other experimentalists which were published in:

- Lakhani A., Roy A., De Poli M., Nakaema M., Formaggio F., Toniolo C., and Keiderling T. A. (2011) Experimental and theoretical spectroscopic study of 3_{10} -helical peptides using isotopic labeling to evaluate vibrational coupling. *J. Phys. Chem. B* 115, 6252-64.
- Chi H., Lakhani A., Roy A., Nakaema M. and Keiderling, T. A. Inter- residue coupling and equilibrium unfolding of PPII helical peptides. Vibrational spectra enhanced with ^{13}C isotopic labeling. *J. Phys. Chem. B* 114, 12744-53 (2010).
- Hauser K., Ridderbusch O., Roy A., Hellerbach A., Huang R., and Keiderling T. A. (2010) Comparison of isotopic substitution methods for equilibrium and T-jump infrared studies of beta-hairpin peptide conformation. *J. Phys. Chem. B* 114, 11628-37.
- Huang R., Wu L., McElheny D., Bour P., Roy A., and Keiderling T. A. (2009) Cross-strand coupling and site-specific unfolding thermodynamics of a trpzip β -hairpin peptide using ^{13}C isotopic labeling and IR spectroscopy. *J. Phys. Chem. B* 113, 5661-74.

3.1 Overview

In the past, the Keiderling research group has used isotopic labeling to study vibrational coupling for conformationally stable peptide sequences in α -helical conformations (9; 103). This grew from a large number of studies of peptide spectral simulations for various conformations (104; 76), using computational strategies that were explained in Chapter 2. In this chapter, I extend the scope of our research to various other peptide secondary structures.

This chapter opens with a study of 3_{10} -helical peptides, where the ϕ, ψ dihedral angles are largely similar to those of α -helices. In the next section spectral signatures of polyproline II helices are explored which are very different in structure from α - and 3_{10} -helices. In the last two sections, vibrational spectra of β -hairpins are modeled, with both single and double cross-strand isotopic labels.

3.2 Vibrational coupling in 3_{10} -helical peptides

3.2.1 Scheme

The 3_{10} helix is characterized by a tighter twist of the backbone as compared to that of the α helix and its intramolecular C=O•••H-N hydrogen bonds (H-bonds) are oriented at a slightly larger angle to the helical axis. This latter property results in lower stability of the 3_{10} helix motif as compared to the α helix, which is evidenced primarily for longer peptides, particularly in H-bonding solvents. While the ideal experimental approach for determining the coupling between 3_{10} -helical residues might seem to involve preparation of very long 3_{10} -helical peptides with two central residues labeled with $^{13}\text{C}=\text{O}$, such an approach does not work in practice, since stabilized uniform 3_{10} helices cannot be obtained with longer sequences. For shorter structures, 3_{10} helix structure formation is favored by incorporation of residues having dialkyl substitution on the α carbon that restricts the rotational freedom of the backbone (ϕ, ψ) torsion angles (25; 105). Thus, incorporation of α, α -aminoisobutyric acid (Aib) residues and restriction to peptides of limited lengths can favor 3_{10} helix formation.

For convenience of isotopic labeling, our collaborators prepared a series of mixed Aib/Ala containing hexapeptide amides and an octapeptide ester. Previous studies by our research group indicated that a host Aib oligomer having up to three guest proteinic residues in a terminally protected (or blocked) hexapeptide amide or octapeptide ester could yield a 3_{10} -helical structure if dissolved in a solvent like CDCl_3 (106) (92). The use of such short lengths suggests questioning the conformational homogeneity, particularly at the ends, but obtaining a 3_{10} structure is the critical first step in such a targeted coupling study and correction for the design shortcomings must come second. Recently ^{13}C , ^{18}O , and ^{15}N isotopically labeled 3_{10} helical peptides have also been targets of

coherent 2D IR studies to observe cross-peaks between the amide I and amide II modes coupled through a C=O...H-N intramolecular H-bond (59).

TABLE V: Amino acid sequences and labelling patterns of the peptides used in the study of 3_{10} helices

Notation	Peptide Sequence
UH	iPrCO-Aib-Ala-Aib-Ala-Ala-Aib-NHiPr
A4H	iPrCO-Aib-Ala-Aib-Ala [*] -Ala-Aib-NHiPr
A5H	iPrCO-Aib-Ala-Aib-Ala-Ala [*] -Aib-NHiPr
A4A5H	iPrCO-Aib-Ala-Aib-Ala [*] -Ala [*] -Aib-NHiPr
A2A4H	iPrCO-Aib-Ala [*] -Aib-Ala [*] -Ala-Aib-NHiPr
A2A5H	iPrCO-Aib-Ala [*] -Aib-Ala-Ala [*] -Aib-NHiPr
A4O	Ac-Aib-Ala-Aib-Ala [*] -Ala-Aib-Aib-Aib-OMe
A5O	Ac-Aib-Ala-Aib-Ala-Ala [*] -Aib-Aib-Aib-OMe
A4A5O	Ac-Aib-Ala-Aib-Ala [*] -Ala [*] -Aib-Aib-Aib-OMe

In this study, IR absorption, VCD, and Raman spectra were calculated for several single- and double-labeled, terminally blocked peptides (Table V), which all had the same basic sequence, -Aib-Ala-Aib-Ala-Ala-Aib-, and these DFT simulations were compared to their experimental spectra. The double-labeled hexapeptides varied only in sequential position of the isotopic label ($^{13}\text{C}=\text{O}$) on two of the Ala residues to yield three different compounds, designated as **A4A5H**, **A2A4H**, and **A2A5H**. In addition, an octapeptide, -Aib-Ala-Aib-Ala-Ala-Aib-Aib-Aib-, was synthesized and calculated with double labels as **A4A5O** to avoid end effects on the Ala5 label position in the hexapeptides. Finally,

the unlabeled **UH** and the single labeled **A4H** and **A5H** hexapeptides were prepared to provide spectral references for adjusting our DFT force field.

The experimental spectra in this section were acquired in the Keiderling group by Ahmed Lakhani and Marcelo Nakaema, who also established the band fitting routine for both the experimental and simulated spectra. Peptides were synthesized by Matteo De Poli and Fernando Formaggio, in the lab of Claudio Toniolo, at the University of Padova. Experimental details regarding spectral acquisition and peptide synthesis have been published elsewhere (107; 108).

3.2.2 Establishing isotope effects with single labeled peptides

The IR absorption spectrum of the unlabeled peptide **UH** in the amide I region (Figure 5a) consists of a single band with slightly asymmetrical line shape to the lower energy side. This band can be fit into two Gaussian components, a large feature at $\sim 1660\text{ cm}^{-1}$ and a small feature at $\sim 1630\text{ cm}^{-1}$ which both probably result from exciton coupled $^{12}\text{C}=\text{O}$ local stretching modes that make up the amide I band plus possible deviation from the 3_{10} -helical frequency for terminal amides. The observed unlabeled hexapeptide amide I VCD spectra (Figure 5a) has a positive couplet shape, going positive to negative (from lower to higher frequency), indicative of right-handed helical formation. This couplet could be fit to three Gaussian components (Figure 5a).

For the single labeled **A4H** and **A5H** peptides an additional $^{13}\text{C}=\text{O}$ band appears in the IR absorption spectrum (Figure 5b and c) as a shoulder on the lower energy side of the amide I band. The **A5H** $^{13}\text{C}=\text{O}$ mode was fit to a band component at higher energy ($\sim 1626\text{ cm}^{-1}$) than that for **A4H** ($\sim 1621\text{ cm}^{-1}$). The difference arises because the Ala5 C=O group does not have a H-bond to another amide group, which results in that local mode having a higher energy than if it were intramolecularly H-bonded, as for Ala4. The significance of there not being a H-bond (end effect) at Ala5 will be addressed further with regard to comparisons of double labeled hexa- and octa- peptides.

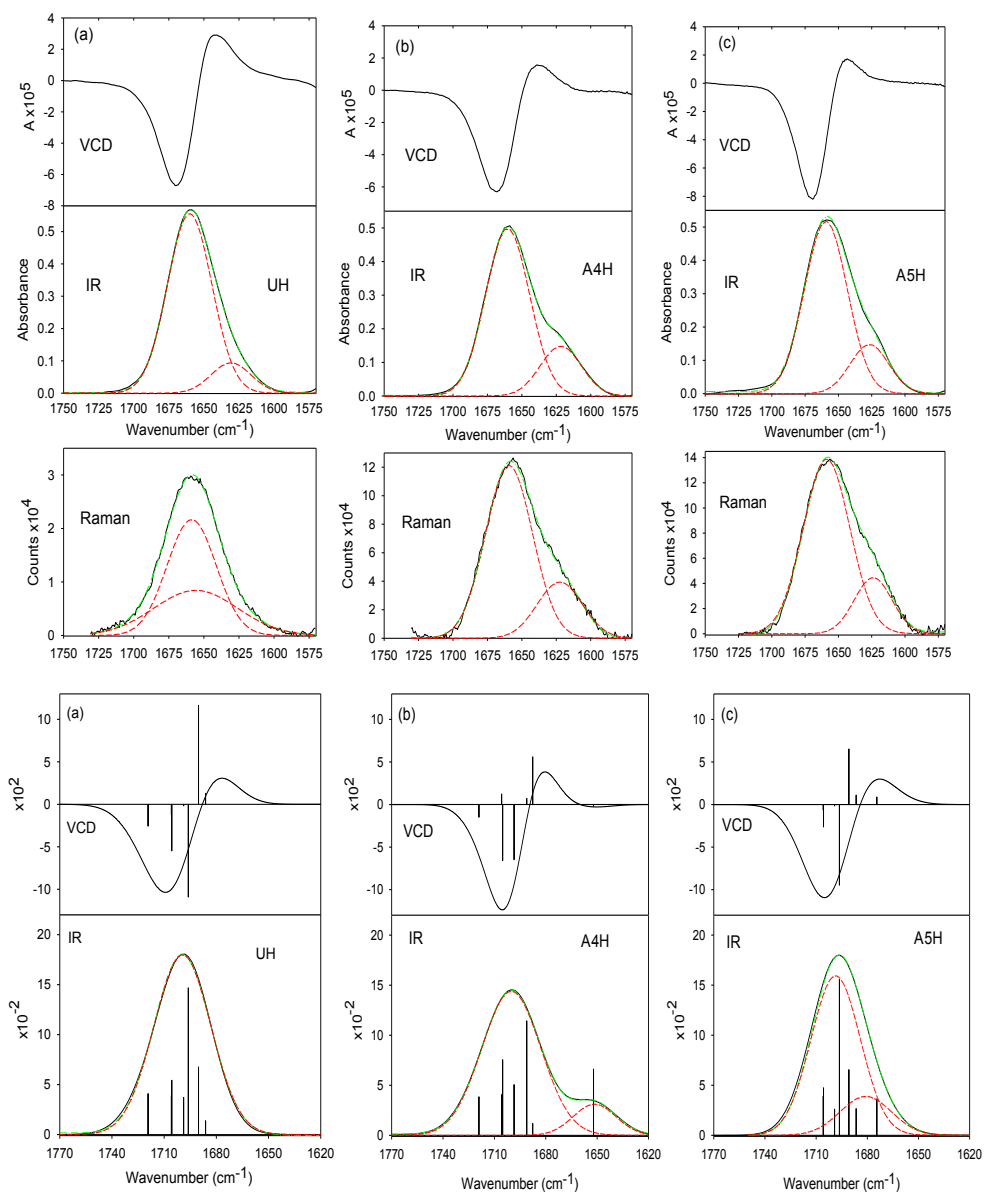


Figure 5: (Top) Experimental Amide I VCD (upper panel), IR absorption (middle panel), and Raman (bottom panel) spectra of (a) UH, (b) A4, and (c) A5 (in TFE/CHCl₃ (1:3 v/v)) and (Bottom) Simulated IR absorption (bottom panel) and VCD (upper panel) spectra of (a) UH, (b) A4, and (c) A5.

The measured **A4H** and **A5H** VCD, as shown in Figure 5b,c (upper panel), have somewhat reduced intensities and bandshapes that resemble those of UH, since no identifiable VCD features are seen due to the single $^{13}\text{C}=\text{O}$ label. This lack of $^{13}\text{C}=\text{O}$ VCD is a consequence of its reduced coupling with other ($^{12}\text{C}=\text{O}$) vibrations and offers graphic evidence of the importance of coupling in providing structural sensitivity to the spectral response. The lower VCD intensity for **A4H** and **A5H** is due to their having one less coupled $^{12}\text{C}=\text{O}$ oscillator and somewhat broader spectra. The broadening is probably due to the isotope labeling, causing a break in the degenerate exciton coupling. The shorter extent of identical oscillators in an exciton model disperses the intensity over more modes, instead of concentrating it in one or two coupled modes. This has been clearly demonstrated previously in simulations of IR spectra for isotopically labeled α -helical or β -sheet peptides (92).

The Raman spectra for UH, **A4H**, and **A5H** (Figure 5b and c) reflect the IR absorption result, showing just a weak shoulder to low frequency on the main Raman amide I band. In each case the IR absorption band ($^{12}\text{C}=\text{O}$) maximum is at $\sim 1660\text{ cm}^{-1}$, while that of the Raman band is at $\sim 1658\text{ cm}^{-1}$. This difference is due to the relative intensity distribution among the exciton split amide I modes.

The calculated IR absorption and VCD spectra for the idealized 3_{10} helix geometry qualitatively agree with the **UH** experimental spectra as shown for the amide I band in Figure 5a. The main differences are that the calculated amide I frequency is higher by $40\text{-}45\text{ cm}^{-1}$, as is normal for DFT generated force fields (FF), and the $^{12}\text{C}=\text{O}$ - $^{13}\text{C}=\text{O}$ separation is larger for **A4H** in comparison to the experimentally observed patterns. Compared to the experimental results, these calculated isotope shifts for **A4H** and **A5H** differ too greatly. The **A4H** simulation has qualitative agreement with experiment, but the isotope shift is too large, while for the **A5H** (Figure 5c) the computed $^{13}\text{C}=\text{O}$ mode is predicted at too high a frequency, due to lack of H-bond, and does not result in a

distinguishable shoulder on the $^{12}\text{C}=\text{O}$ amide I band. This difference between the Ala4 and Ala5 $\text{C}=\text{O}$ frequencies has two sources, the FF overestimation of both the end effect for Ala5 (frequency too high) and the isotope effect for Ala4 (frequency too low). The source of this error for Ala4 is tied to the partial disruption of the excitonic coupling as seen by the increased dispersion of the $^{12}\text{C}=\text{O}$ amide I mode intensities (and consequent loss of overall peak intensity) for **A4H**. Nonetheless, these effects (mostly H-bond formation differences plus neglect of helical fraying) clearly lead to a non-degeneracy in the two local oscillators (Ala4 and Ala5) which can be seen experimentally (but less often) and must be accounted for in order to analyze the coupling between pairs of $\text{C}=\text{O}$ groups on different sites. This phenomenon provided a continuing challenge in interpreting the theoretical simulation analyses of the experimental spectra.

3.2.3 Site specific coupling: double labeled peptides

Due to the anomalous structure (lack of H-bond) for the Ala5 position $^{13}\text{C}=\text{O}$ in the hexapeptide, the single mode frequencies were not well represented in the modeling of **A5H**. Even when a solvent correction for CDCl_3 (deuterated chloroform), using the PCM model, was added the results were fundamentally the same. The modes all shift down by $\sim 25\text{ cm}^{-1}$, but their relative separations and intensities remain unchanged. Consequently, the computed spectra for the double labeled **A4A5H** and **A2A5H** were expected to have difficulty reproducing the experimental results, so that their simulated bandshapes are most useful when viewed in terms of differences from predictions for peptides with single labels and each other. By contrast, the **A2A4H** and **A4A5O** peptides are labeled so as to minimize the end effects, and they provide useful references for the **A4A5H** and **A2A5H** experimental spectra. Consequently the spectral simulations for all the peptides are best discussed together, rather than individually with the spectral data. The amide I IR absorption bands for each of the double labeled peptides are predicted to have a resolved $^{13}\text{C}=\text{O}$ side band, but the relative

intensities match the experiment only for the **A2A4H** and **A4A5O**, which have internally H-bonded labeled C=O groups. The simulated $^{13}\text{C}=\text{O}$ IR bands for **A4A5H** and **A2A5H** are too weak because only one mode (computed at $\sim 1652\text{ cm}^{-1}$) contributes to it. The other $^{13}\text{C}=\text{O}$ mode appears as the lowest frequency component ($\sim 1674\text{ cm}^{-1}$) of the apparent exciton broadened $^{12}\text{C}=\text{O}$ band (the center of which fits to a broadened Gaussian at $\sim 1698\text{ cm}^{-1}$). The frequencies for the computed $^{13}\text{C}=\text{O}$ modes and the fitted intensity bandshapes (as shown in Figure 6, Figure 7) are listed in Table VI.

It is important to distinguish between mode and band profile positions, as the observed spectra reflect the latter and their shifts from the modes for $^{13}\text{C}=\text{O}$ are indicative of our ability to derive coupling constants from those spectra. The computed modes are all high by $\sim 50\text{ cm}^{-1}$ due to lack of correction for solvent effects and to normal DFT errors. These can be partially corrected by using the PCM solvation model for CDCl_3 , which results in similar, but slightly reduced mode separations, as also summarized in Table VI. The line widths used in the figures for the contributions of individual components are a compromise between mimicking overall absorbance shapes and preserving the fluctuations in the VCD band profile, despite the overestimated Ala4 and Ala5 frequency differences. As determined from our simulations, the IR absorption and Raman amide I spectra are predicted to have very similar intensity patterns, making their measurement only confirmatory for 3_{10} - helices, in contrast to the complementary isotope shifts found due to opposite relative intensity patterns for IR and Raman for other structures such as β -sheets or PPII helices (109).

The simulated **A4A5O** VCD spectrum has a clear positive couplet $^{12}\text{C}=\text{O}$ amide I, followed by a positive $^{13}\text{C}=\text{O}$ couplet (Figure 6) which is in qualitative agreement with the experimental results (Figure 6), but the computed $^{13}\text{C}=\text{O}$ component is too intense. Attempts to measure the spectrum with higher resolution, gave essentially the same spectral result as seen in Fig. 5. The simulated

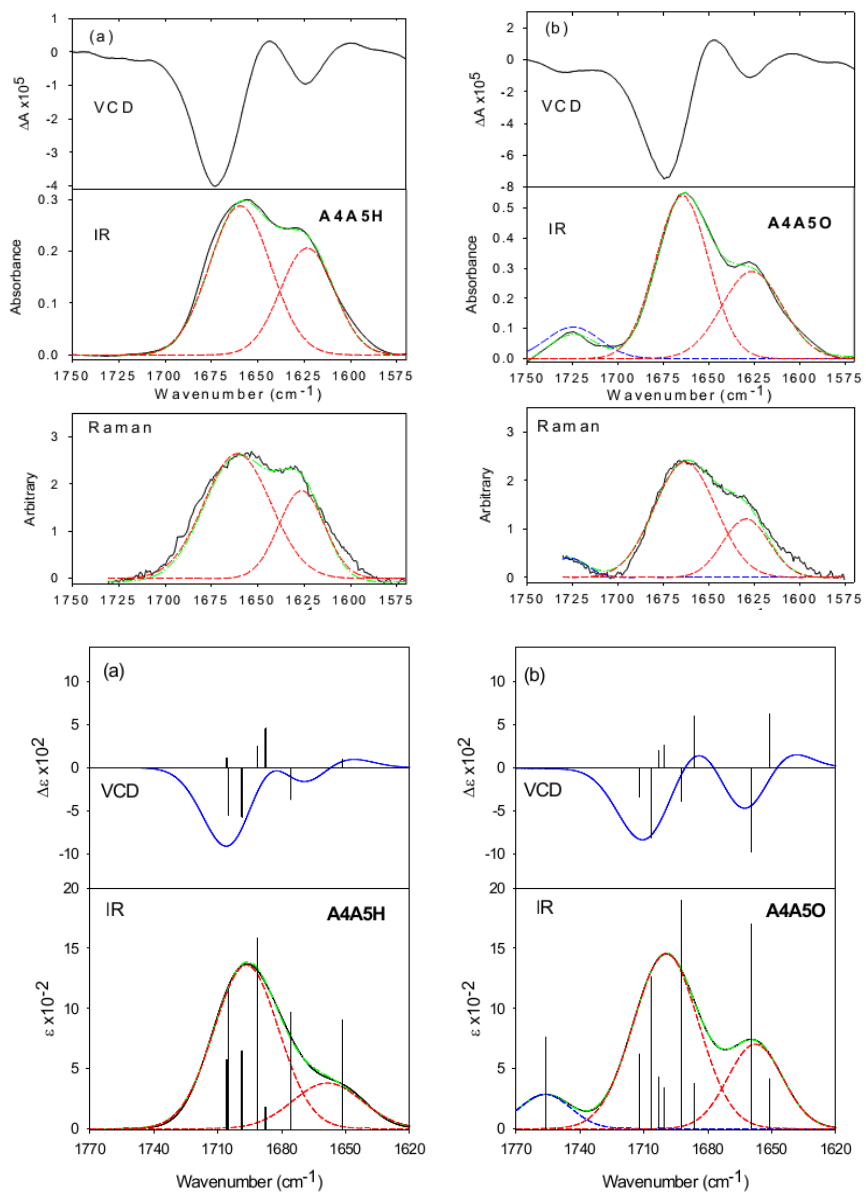


Figure 6: (Top) Experimental VCD (upper panel), IR absorption (middle panel), and Raman (lower panel) spectra of (a) A4A5H and (b) A4A5O, measured and fit to Gaussian components as in Figure 5. A4A5O has an ester C=O stretch, due to the C-terminal (OMe) cap, near 1725 cm⁻¹. (Bottom) Simulated IR absorption (bottom panel) and VCD (upper panel) spectra of (a) A4A5H and (b) A4A5O.

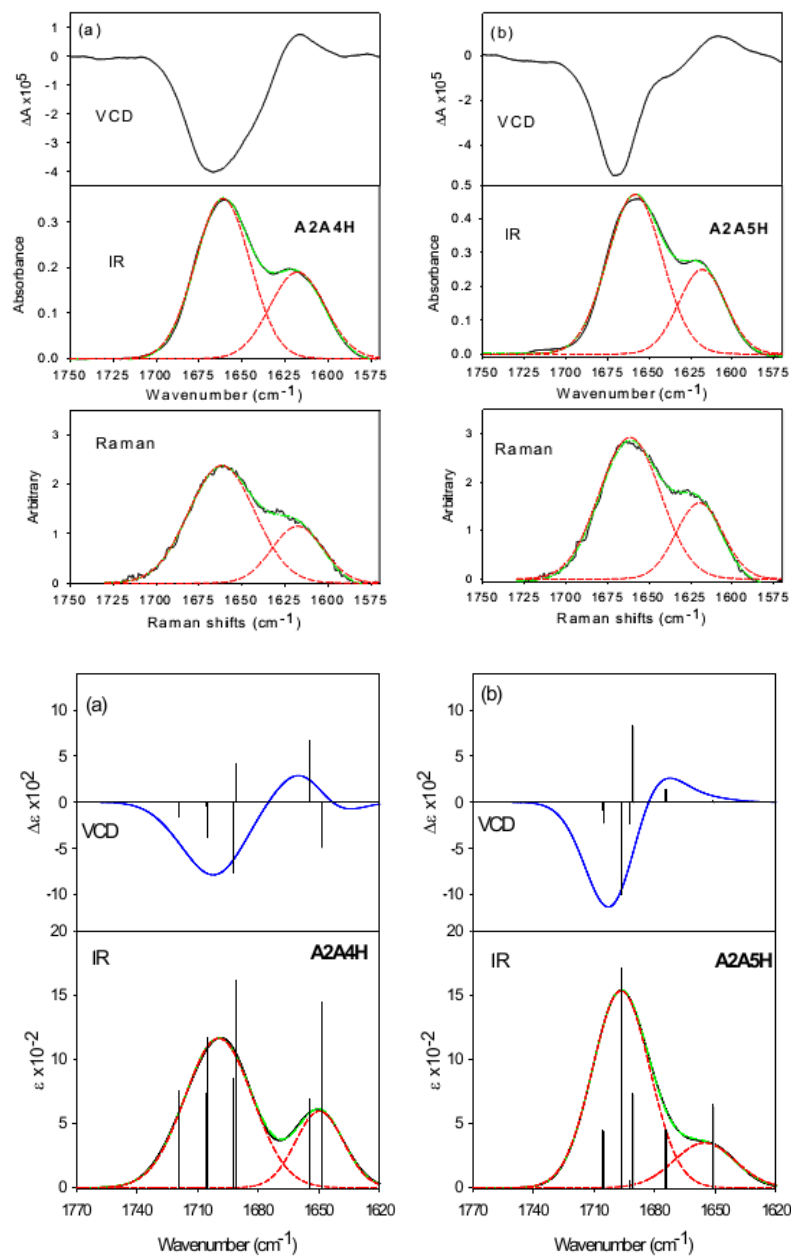


Figure 7: (Top) Experimental VCD (upper panel), IR absorption (middle panel) and Raman (lower panel) spectra of (a) A2A4H and (b) A2A5H, measured and fit to Gaussian components as in Figure 5. (Bottom) Simulated IR absorption (bottom panel) and VCD (upper panel) spectra of (a) A2A4H and (b) A2A5H, plotted and fit as in Figure 5.

TABLE VI: DFT computed frequency values (normal modes) for ideal 3_{10} -helices and fits to IR simulation

Notation	^{13}C mode frequency (cm^{-1})						Intensity fit ^a
	vacuum			PCM- CHCl_3			
	modes	splitting		modes	splitting		
A4H	1652			1627			1651
A5H	1674			1651			1675
A4O	1657			-			1655
A5O	1652			-			1652
A4A5H	1675	1652	23	1652	1627	25	1659
A4A5O	1659	1651	8	-	-	-	1658
A2A4H	1654	1648	6	1629	1625	4	1650
A2A5H	1674	1651	23	1652	1627	25	1655

^a The intensity fit was obtained by first applying a convolution to the DFT computed (vacuum) line spectra. The broadened peak was then fit to a single Gaussian.

VCD spectra (Figure 6) for **A4A5H** also qualitatively agree with the experimental spectra (Figure 6), but the $^{13}\text{C}=\text{O}$ contribution to the VCD is weak, which is discussed in the next section.

3.2.4 Coupling analysis

To better analyze and compare these overlapping contributions between different labeling patterns, all the IR absorption spectra were fit to a minimal number of Gaussian band components to give the same type of fit pattern to each spectrum, experimental and simulated, even if use of more components might have reduced the overall fitting error. From this point of view, the IR and Raman fits are quite acceptable and virtually the same in terms of components (see Figure 5, Figure 6, Figure 7), a systematic variation develops with isotope substitution pattern, and the

comparison of experiment and theory are qualitatively correct (Figure 6, Figure 7). The largest errors in the calculations for single label species regarding the $^{12}\text{C}=\text{O}$ to $^{13}\text{C}=\text{O}$ differences are for **A4H** calculated too large ($^{13}\text{C}=\text{O}$ low), and **A5H**, too small ($^{13}\text{C}=\text{O}$ high). The fit bands for the computed $^{13}\text{C}=\text{O}$ IR absorption components in **A4A5H** and **A2A5H** are $\sim 6\text{-}8\text{ cm}^{-1}$ higher in frequency than for **A2A4H**, which is in qualitative agreement with the **A4A5H** fitted experimental $^{13}\text{C}=\text{O}$ band being $\sim 6\text{ cm}^{-1}$ higher than that for **A2A4H**, as summarized in Table VII. The **A4A5O** and **A4A5H** experimental and theoretical fit band positions have roughly the same $^{12}\text{C}=\text{O}$ to $^{13}\text{C}=\text{O}$ separation ($\sim 42\text{ cm}^{-1}$), but the source of this apparent agreement is more complex due to the impact of the high-frequency Ala5 mode.

TABLE VII: Experimental and theoretical band fitted values for the amide peak positions for the 3_{10} -helical peptides investigated

Notation	$^{12}\text{C}/^{13}\text{C}$ Gaussian fit peak positions (cm^{-1})					
	Experimental				Theoretical	
	IR		Raman		IR	
	^{12}C	^{13}C	^{12}C	^{13}C	^{12}C	^{13}C
UH	1660	-	1659	-	1698	-
A4H	1660	1622	1659	1622	1700	1651
A5H	1659	1627	1659	1624	1697	1675
A4A5H	1660	1623	1661	1626	1697	1659
A2A4H	1661	1618	1662	1618	1700	1650
A2A5H	1659	1618	1662	1620	1697	1655
A4A5O	1665	1626	1663	1629	1700	1658

The quality of the simulated VCD patterns in both **A4A5H** and **A4A5O**, as shown in Figure 6, appear to be surprisingly good given the impact of end effects on the mode mixing for **A4A5H**. Presumably, this is because the primary criterion determining the $^{13}\text{C}=\text{O}$ VCD pattern is the sign of the coupling constant between the two labeled residues. This sign (positive) is correctly predicted (which is easiest to see in the VCD pattern) and is the same in both of these sequentially labeled peptides, although the splitting is larger for **A4A5H** due to the end effect. Thus, the experimental IR absorption frequency is higher (overlaps the $^{12}\text{C}=\text{O}$ more) and the relative VCD contribution is larger for **A4A5H** as well, due to effects of the local Ala5 and Ala4 mode (diagonal FF) differences. The simulations appear to overestimate the impact of internal H-bonding, resulting in too large a difference in diagonal FF for Ala4 and Ala5, as seen in the **A4H** and **A5H** mode positions in Table VI. However, there is another contribution, since the Ala4 substitution in **A4H** causes disruption in the amide I exciton coupling (evidenced as increased intensity dispersion, see Figure 5) that is less evident in **A5H**, which complicates the analysis. The impact of this error on the position of the fitted Gaussian components in **A4A5H** and **A4A5O** is small for the IR, due to convolution of multiple overlapping broadened components. The computed $^{13}\text{C}=\text{O}$ VCD for the octapeptide is larger than for the hexapeptide, despite the smaller separation of the Ala4 and Ala5 modes in **A4A5O**, in contrast to the complex mode mixing in **A4A5H**. This affects the overlap of positive and negative $^{12}\text{C}=\text{O}$ VCD contributions in the middle of the amide I band, resulting in more cancellation between $^{12}\text{C}=\text{O}$ VCD components and a relatively intense $^{13}\text{C}=\text{O}$ contribution. The overestimation of the difference of the diagonal FF for Ala4 and Ala5 makes the sequential coupling (A4A5) analysis more complex than for the alternate positions as in **A2A4H**.

For the simulated **A2A4H** peptide spectra, as shown in Figure 7, the more intense, in-phase mode is computed at a lower frequency (1648 cm^{-1}) while the weaker, out-of-phase mode is at

a higher frequency (1654 cm^{-1}), with a mode splitting of 6 cm^{-1} (Table VI). The corresponding VCD components are opposite in sign (negative to low frequency) and roughly equal in magnitude, confirming the negative sign for the coupling. If we assume that the uncoupled, Ala2 and Ala4 amide I local modes were degenerate, then the coupling constant required to yield this splitting would be 3 cm^{-1} . This assumption is supported by the relatively large difference in Raman intensities computed for the two bands, implying strong mixing, and by the near degenerate computed frequencies obtained with test calculations isolating the Ala4 (1652 cm^{-1}) and Ala2 (1651 cm^{-1}) $^{13}\text{C}=\text{O}$ modes (If this calculation were corrected for a non-degeneracy of 1 cm^{-1} , the coupling would be $\sim 2.9\text{ cm}^{-1}$, see Figure 8). The virtue of this model is in its agreement with the IR experimental spectra (Figure 6, Figure 7, Table VII). The computed VCD also agrees with experiment, as it is dominated by a broad negative to high frequency and with the positive $^{13}\text{C}=\text{O}$ component higher in frequency than the corresponding IR absorption band and a weak negative VCD to lower frequency in both experiment and simulation. Higher resolution might better define the $^{13}\text{C}=\text{O}$ contributions to VCD, but the signals are predicted to be small and the preliminary higher resolution experimental VCD tests did not yield added bandshape variation. Thus, this comparison to the experimental spectra supports the validity of the computed $\leq 3\text{ cm}^{-1}$ coupling constant, which is comparable in sign and magnitude to the $i \rightarrow i+2$ coupling constant derived for α helices (103).

Such a simple approximation of directly using the mode splitting to determine the coupling constant for **A4A5H** can not work, due to the end effects on the Ala5 $^{13}\text{C}=\text{O}$ group. However, for **A4A5O**, the $^{13}\text{C}=\text{O}$ components are resolved from the $^{12}\text{C}=\text{O}$ band, and the two coupled modes have different IR and Raman intensities, with the more intense in-phase mode to higher frequency, indicating strong mixing. The corresponding VCD components are opposite in sign, negative to high frequency, and of equivalent magnitude. All of these $^{13}\text{C}=\text{O}$ spectral predictions are strongly

correlated to the experimental observations and suggest coupling of near degenerate modes, much as seen for **A2A4H** above, except that the coupling for **A4A5O** (and **A4A5H**) is positive. This **A4A5O** pattern agrees with that of **A4A5H**, but is less evident there (IR intensities are similar and VCD are different, both due to non-degeneracy), and both fit the patterns seen for sequential labeling in α helices due to the positive $i \rightarrow i+1$ coupling (103).

By parallel reasoning to **A2A4H**, we can analyze the **A4A5O** simulation to determine the adjacent residue amide I coupling by use of the degenerate coupled oscillator assumption. The computed splitting of $\sim 8 \text{ cm}^{-1}$ (Table VI) would then correspond to twice the coupling giving a coupling constant of $\sim 4 \text{ cm}^{-1}$, which is significantly weaker than that found for α helices ($\sim 7 \text{ cm}^{-1}$) (103). The computed frequencies for the Ala4 and Ala5 amide I modes (for simulations of labeled octapeptide species) are not degenerate (Table VI, Figure 8). This deviation is probably an overestimate, but if taken into account, the coupling would be reduced to $\sim 3.1 \text{ cm}^{-1}$. Similarly a coupling constant of $\sim 5 \text{ cm}^{-1}$ can be obtained from a non-degenerate analysis of the **A4A5H** spectrum, suggesting that our coupling constant determination for sequential labels in a 3_{10} helix lies in the range of $3\text{-}5 \text{ cm}^{-1}$.

Thus the more tightly wound 3_{10} helix maintains the same sign pattern as the α helix in terms of coupling constants and resultant spectral patterns for the $i \rightarrow i+1$ and $i \rightarrow i+2$ interactions, but the magnitude of the closer, adjacent sequential interaction is decreased. For the $i \rightarrow i+3$ interaction, the sign pattern is less clear, and the **A2A5H** data unfortunately do not provide sufficient data to sort it out. The coupling sign for **A2A5H** appears to be opposite that of **A2A4H**, as can be derived from the relative frequency patterns of the experimental IR and VCD; however, in this case the calculated patterns are unclear and do not support a confident analysis of a positive sign for the coupling. Due to the small coupling constant magnitude combined with large non-degenerate FF

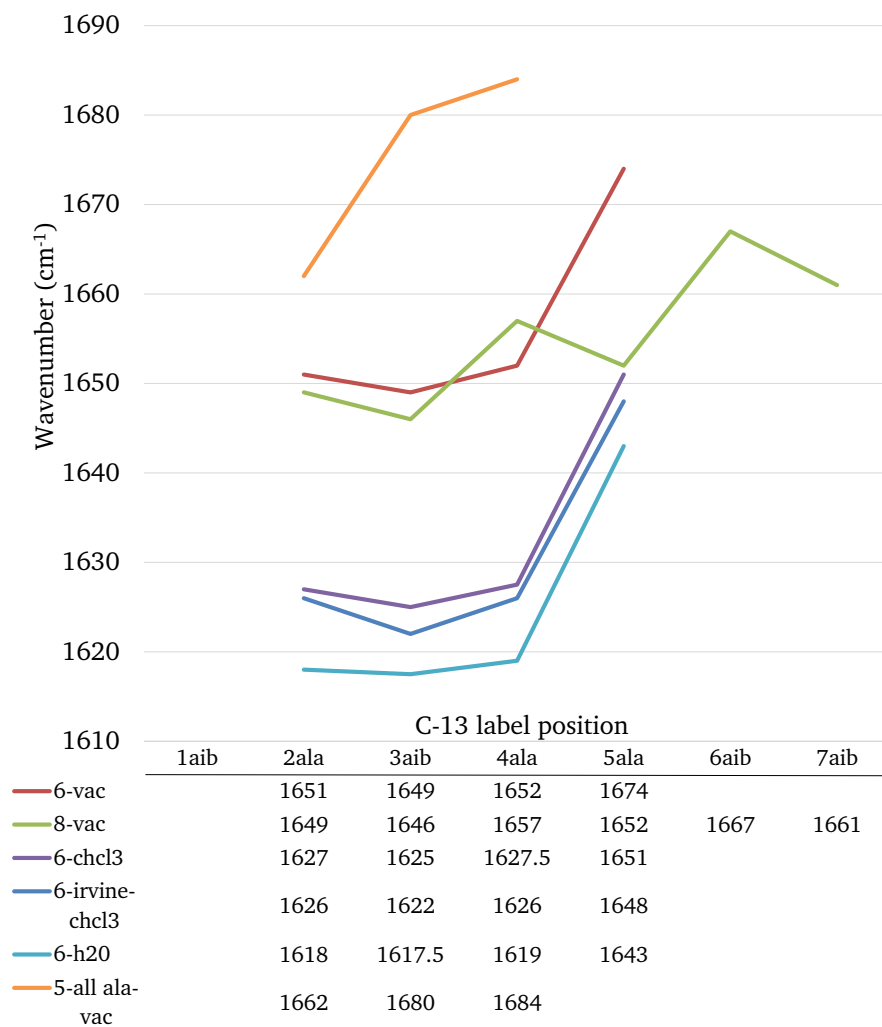


Figure 8: Frequency variation for a single label ^{13}C position in the 3_{10} -peptide sequence.

contributions (Ala5), it is not possible to derive an experimental or theoretical value for **A2A5H**. Despite the successes for **A2A4H** spectrum, and the **A4A5O** and **A4A5H** $^{13}\text{C}=\text{O}$ modes, in terms of coupling, there are difficulties in the intensity distributions for the latter. While the computed IR of **A4A5O** matches experiment well, its computed VCD is too intense for the $^{13}\text{C}=\text{O}$ band ($\Delta A/A$ is roughly twice the experimental value), and weak for the $^{12}\text{C}=\text{O}$ band (here $\Delta A/A$ is about half the experimental value).

3.2.5 Modified force field analyses

The methods above use simple two-state coupling models for the DFT determined modes and gain applicability by the match of experimental and simulated bandshapes for IR and VCD (and Raman by extension). The DFT FF calculations take into account all the modes of the molecule and are done at a relatively high level of theory. Also, they should reflect the impact of variation along the sequence. However, when compared to experiment, the Ala4 and Ala5 diagonal FF values are computed to be much lower and higher. This can dramatically impact comparison to experiment for **A4A5H**. The theoretical simulations are all in qualitative agreement with the amide I experimental IR absorption and VCD (as well as the Raman) results. However, the **A4A5H** $^{13}\text{C}=\text{O}$ IR absorption (and Raman) intensity is underestimated (in relation to the $^{12}\text{C}=\text{O}$ intensity) while the relative VCD for these modes is in good agreement with the experiment. By contrast, the **A4A5O** $^{13}\text{C}=\text{O}$ IR absorption contribution is computed in good agreement with the experimental $^{12}\text{C}=\text{O}$ - $^{13}\text{C}=\text{O}$ ratio, but its $^{13}\text{C}=\text{O}$ VCD contribution is too large. Also, the ester functional group resulting from the -OMe blocking group on the C-terminus has a band at $\sim 1725\text{ cm}^{-1}$ experimentally, which, accounting for the expected DFT error, is well predicted in the **A4A5O** simulation, but high in frequency, as usual, at $\sim 1757\text{ cm}^{-1}$. This mode may impact the $^{12}\text{C}=\text{O}$ mixing somewhat, as suggested by comparing detailed dipole and rotational strength dispersions for the simulations in Figure 6.

This variation in intensity patterns shows a limitation in our FF determination, which may be a consequence of solvation being left out of the model or a consequence of using the ideal 3_{10} helix structure ($\phi = -60^\circ$, $\psi = -30^\circ$) in creating the model. The simplest correction is to account for solvation by use of a PCM model. As seen in the values listed in Table VI, the inclusion of a dielectric corresponding to the CDCl_3 solvent shifts to the frequencies by $\sim 25 \text{ cm}^{-1}$ but has only small effects on the relative splittings of the $^{13}\text{C}=\text{O}$ band and the qualitative shapes of the simulated amide I spectra as shown in Figure 9. Other analyses have used or derived different torsional angle values ($\phi = -57^\circ$, $\psi = -30^\circ$), but our PCM calculations with this geometry give $^{13}\text{C}=\text{O}$ frequency values that are very similar to the PCM results for the ideal structure (Table VIII) (59).

Consequently, the local FF was corrected empirically for the Ala4 and Ala5 positions in the hexapeptide, to improve agreement with experimental $^{12}\text{C}=\text{O}$ shifts. By reducing the Ala5 C=O force constant so that its amide I mode moved to a position nearly degenerate with the Ala4, little change was seen in the IR absorption and VCD patterns. Both spectral simulations remain in qualitative agreement with the experiment, but the predicted $^{13}\text{C}=\text{O}$ IR absorption intensity is still very low. One can alternatively increase the diagonal FF for Ala4, but the two nearly equivalent bands seen in the experimental **A4A5H** IR absorption (and Raman) still fail to appear in our computations with a reasonable range of corrections.

Alternatively, the octapeptide FF was modified to attempt to obtain a better model of the VCD intensity, since its IR absorption was acceptably accurate. For the **A4A5O** FF, the Ala4 and Ala5 $^{13}\text{C}=\text{O}$ modes are still not degenerate, with Ala4 being computed 5 cm^{-1} higher than Ala5 (Table VI). This phenomenon impacts the splitting of the coupled $^{13}\text{C}=\text{O}$ modes and their simulated VCD intensity (by reducing overlap). This non-degeneracy could be removed by FF modification, and the coupled labeled modes would then show strong mixing (symmetric mode dominating the IR

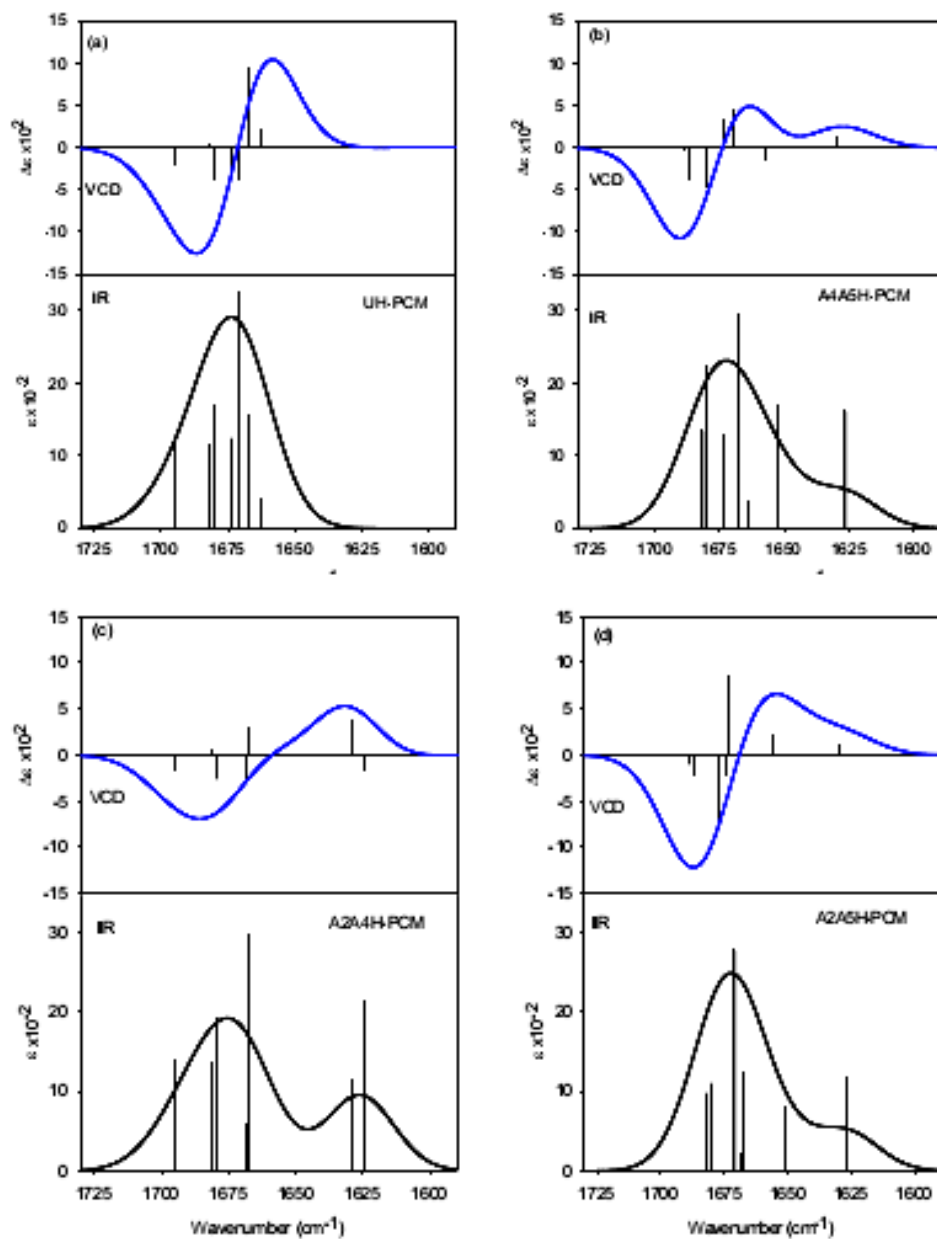


Figure 9: Simulated IR and VCD of (a) UH, (b) A4A5H, (c) A2A4H and (d) A2A5H with solvent correction for CDCl_3 .

TABLE VIII: Variation in double label positions with ϕ ψ angles, both with PCM correction for CHCl_3 solvent

Notation	^{13}C mode frequency (cm^{-1})					
	$\phi, \psi = -30, -60$			$\phi, \psi = -30, -57$		
	modes		splitting	modes		splitting
A2A4H	1624.5	1629	4.5	1623.5	1628.5	5
A2A5H	1627	1652	25	1626	1648.5	22.5
A4A5H	1627	1652	25	1625	1649	24

^a CHCl_3 is incorporated by choosing a solvent dielectric=4.81

intensity) for **A4A5O** with a splitting of $>7 \text{ cm}^{-1}$ or a coupling of $>3.5 \text{ cm}^{-1}$, in excellent agreement with the results following our degenerate and non-degenerate coupling analyses above. When Ala4 and Ala5 are made degenerate, the computed $^{13}\text{C}=\text{O}$ VCD decreased somewhat, but was still much more intense than that seen experimentally. This suggests that FF refinement can have an impact, but the FF changes we made are small compared to the probable impact of structure fluctuations on the dynamic peptide in solution.

Thus in both cases the simple local FF correction is not the dominant source of intensity overestimation for the $^{13}\text{C}=\text{O}$ **A4A5H** IR or **A4A5O** VCD. It can be noted that substitution of Ala4 vs. Ala5 with $^{13}\text{C}=\text{O}$ does impact the exciton coupling which effectively changes the local FF at those positions in the octapeptide. The effect of inserting one label is small but it varies for different sequential positions in the hexapeptide (Figure 5), which may explain why the **A4H** and **A5H** peptides differ so much in the simulations. At this level we must conclude that the mismatch of IR absorption and VCD intensities in **A4A5H** and **A4A5O** is due to more fundamental aspects of the

FF or due to non-uniform distortion of the experimental geometry from the ideal one used for the simulations discussed here.

The spectral characteristics of 3_{10} helix and α helix are not very different, which is due to minor differences in the structure of their peptide backbone. This originates from the fact that both 3_{10} and α helices are right-handed helices, which are stabilized by intra-helical hydrogen bonding. In the next section we progress to modeling helices with a left-handed twist that do not have such hydrogen bond stabilization.

3.3 Inter-residue coupling of polyproline II helical peptides.

Random coils are proteins, or parts of proteins, that completely lack secondary structure. Tiffany and Krimm originally proposed that the random coils were not as random as had been previously thought (110). They concluded that these coils contained a left handed turn character, by analogy of their CD spectra with that of polyproline II (PP II), which is a left-handed helical structure (41).

PP II helices lack intra-helical hydrogen bonding and they have an extended helical structure with a 9.3 Å rise per turn as opposed to 6 Å for the 3_{10} helix, and backbone dihedral angles of $\phi, \psi = -78^\circ, +145^\circ$, which result in a left handed twist. They lie in a region of Ramachandran space that is quite apart from the right handed helices. In conjunction with Heng Chi, a study was designed to extrude vibrational coupling information from PP II helical vibrational spectra using isotopically labeled peptides.

3.3.1 Scheme

To study coupling in PP II helices, a series of peptides were synthesized by Heng Chi as shown in Table IX. The two series of peptides that were computationally modeled were the A14 and the P14 series and are illustrated in Figure 10. The P14 series were all proline oligomers that were designed to yield a stable PPII conformer and the A14 series had four alanine residues in the center of the

peptide flanked by four proline residues on either side to enforce PP II helical structure. The label U (for unlabelled) refers to peptides that do not contain any ^{13}C isotopically labeled amides. The labels A and T correspond to ^{13}C isotopically labeled amides that are ^{13}C double labeled either one apart (A) or together/sequentially (T).

TABLE IX: Sequences and labeling pattern of peptides used in the PPII helix study

Notation	Length/Label position	Peptide Sequence ^a
P14U	14/none	P-P-P-P-P-P-P-P-P-P-P-P-NH ₂
P14T	14/ P7P8	P-P-P-P-P-P-P* ₇ -P* ₈ -P-P-P-P-P-NH ₂
P14A	14/P7P9	P-P-P-P-P-P* ₇ -P* ₉ -P-P-P-P-P-NH ₂
A14U	14/none	W-P-P-P-P-A-A-A-A-P-P-PK-NH ₂
A14T	14/A7A8	W-P-P-P-P-A-A* ₇ -A* ₈ -A-P-P-P-K-NH ₂
A14A	14/A7A9	W-P-P-P-P-A* ₇ -A* ₉ -A-P-P-P-K-NH ₂
K14U ^b	14/none	K-K-K-K-K-A-A-A-K-K-K-W-K-NH ₂
K14T ^b	14/A7A8	K-K-K-K-K-A* ₇ -A* ₈ -A-K-K-K-W-K-NH ₂
K14A ^b	14/A7A9	K-K-K-K-K-A* ₇ -A* ₉ -K-K-K-W-K-NH ₂

^a starred residues denote ^{13}C on the amide C=O

^b The K14 series were studied experimentally but not computationally modeled.

Full DFT computations for Pro₇ peptides (7-mer all proline) and Pro₁₅ (15-mer all proline) constrained in PPII conformations, were made to determine any impact of parameter transfer (mostly end effects). The Pro₇ parameters were transferred to a Pro₁₃ 13-mer model. Isotope effects were computed by changing the appropriate atomic masses (^{12}C to ^{13}C on amide carbonyls, plus

H to D where exchangeable) after transfer of spectral parameters and before diagonalization of the FF to get frequencies and intensities for comparison to experimental patterns. No transfer of parameters was required for the Pro₁₅ model.

To investigate if there is an effect of the proline side chain, spectral simulations were performed on model PPII peptide structures, which were constructed as relatively small (5-mer) all alanine oligomers, and whose backbone torsions were constrained to $\phi, \psi = -78^\circ, +145^\circ$ (appropriate for the PPII conformation). These were propagated onto a larger model Ala₂₂ peptide using the Bour CCT method (93).

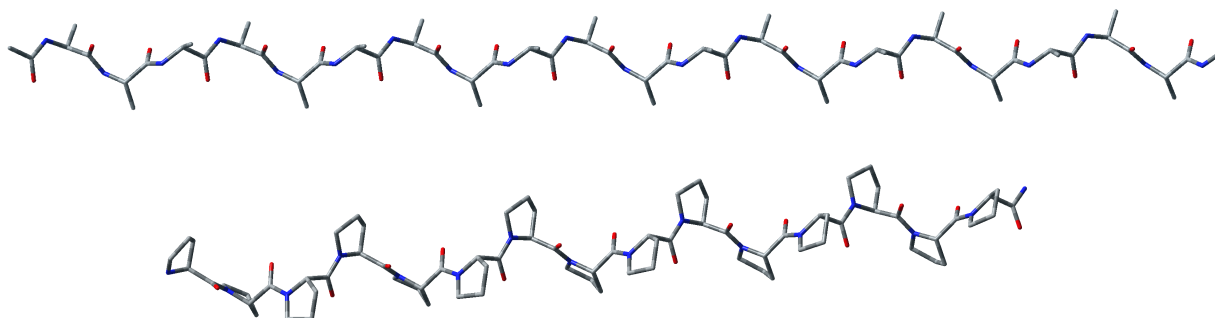


Figure 10: Shows the structural models used in the polyproline II study, for which spectra were generated. (Top) an alanine 22-mer and (Bottom) a proline 15-mer. Hydrogen atoms are not displayed for clarity.

The experimental spectra in this section were acquired by Heng Chi who also performed the band fits shown in Figure 11 and Figure 12. Experimental details regarding spectral acquisition and peptide synthesis have been published elsewhere (109).

3.3.2 Coupling analysis: all proline model

In Figure 11(a,d and g), the simulated amide I' IR, VCD and Raman spectra are compared for an Ac-Pro₁₃-NHCH₃ peptide constrained to the PPII conformation. These spectra are computed in vacuum and are not corrected for standard DFT FF error (which is mostly due to lack of H-bonding solvent) (78; 111), and hence the ¹²C-amide I' frequencies are $\approx 60 \text{ cm}^{-1}$ higher than experiment since all C=O groups are directed out from the helical axis and have no internal hydrogen bonding. These can be contrasted with computed spectra for the isotope substituted variants, which have two ¹³C=O labeled groups placed both sequentially (T, dashed line) and alternately (A, dotted line), in the center of the sequences. In the amide I' IR spectra, Figure 11a, the ¹²C band at $\approx 1685 \text{ cm}^{-1}$ loses intensity upon ¹³C substitution, and the resulting ¹³C band appears as a shoulder at $\approx 1640 \text{ cm}^{-1}$. Below these spectra are shown expansions of the ¹³C=O band to show the contributions of the coupled labeled modes in Figure 11(b, e, h) (T) and Figure 11(c, f, i) (A) for the IR, VCD and Raman, respectively. Due to the fact that comparable dipole strengths are computed for each split ¹³C component, of the in- and out-of-phase ¹³C=O coupled band, in P14T and the components are only weakly split in P14A, the sequentially and alternatively labeled peptides are predicted to have equivalent apparent spectral band shapes with only $\approx 1 \text{ cm}^{-1}$ difference in the peak maximum, which would make their experimental discrimination challenging.

While the dipole intensity distribution suggests that T should have a slightly lower frequency mode than A as shown in Figure 11b and c, respectively, for realistic bandwidths this may not be experimentally detectable. For two labels together, the splitting between the ¹³C modes is predicted to be 6 cm^{-1} indicating the coupling between them should be $\approx 3 \text{ cm}^{-1}$ with the lower frequency mode having a higher intensity, which should shift the apparent ¹³C band down from the average of the two modes. By contrast, the high frequency mode in the case of A is more intense, but is barely

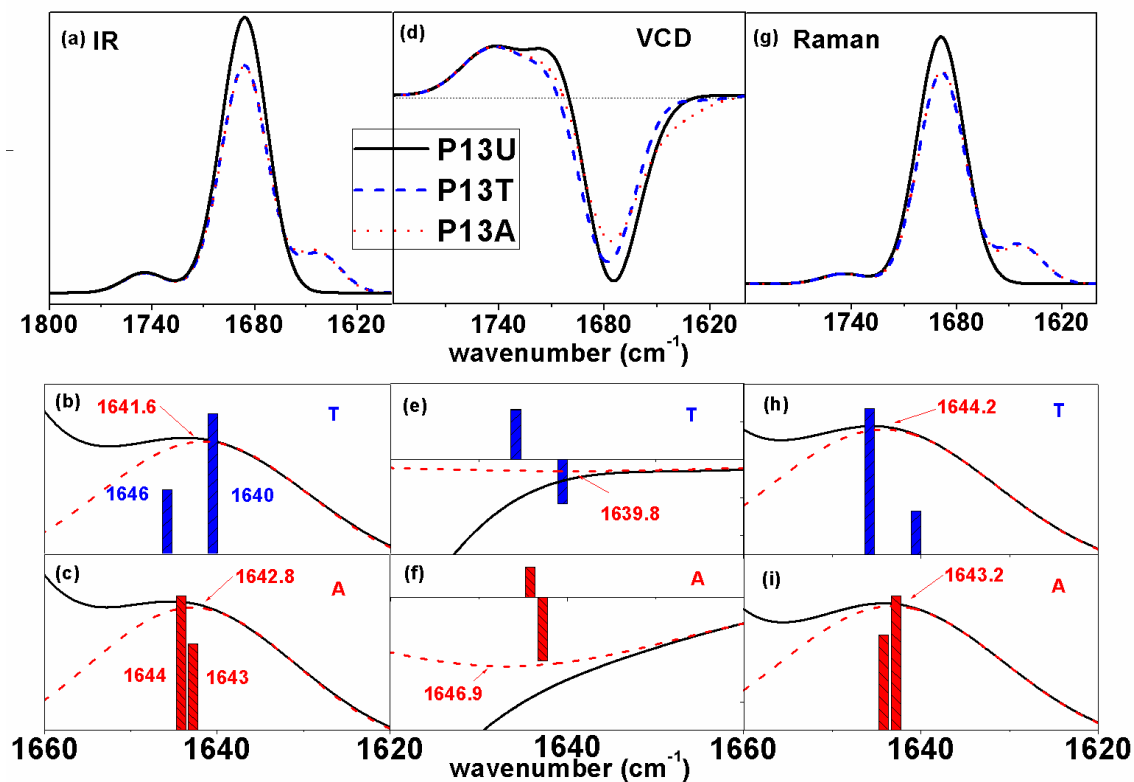


Figure 11: Simulated amide I' FTIR (a), VCD (d) and Raman (g) spectra for the unlabeled Ac-P₁₃-NH₂ (black solid line), compared to the sequential (blue dashed line) and alternate (red dotted line) doubly labeled ones adopting polyproline II conformation. Panels (b) and (c) are simulated ¹³C amide I' IR spectra and normal mode contributions for T (sequential labels) and A (alternate labels) double labeling patterns. Panels (e) and (f) are simulated ¹³C amide I' VCD spectra and normal mode contributions for T and A. Panels (h) and (i) are simulated ¹³C amide I' Raman spectra and normal mode contributions for T and A.

separated ($\approx 1 \text{ cm}^{-1}$) from the low frequency one, resulting in an overall band position close to that of the unperturbed ^{13}C mode. As indicated by the dashed traces in Figure 11b and c, if the summed bandshape is fit to a single Gaussian component, the ^{13}C band will appear at 1642 cm^{-1} for the T isomer and 1643 cm^{-1} for the A isomer. The 1 cm^{-1} difference between these two fitted bands would be less than the coupling between the two modes in T isomer and suggests that fitting the IR would at best only provide a lower bound to the coupling constant.

Although the VCD spectra computed for the same amide I' transitions of course have the same component peak resolution as the IR, a very different intensity distribution is obtained for the two labeling schemes due to the signed nature of the bands in VCD. As shown in Figure 11d, the broadened band shape still results in a single (negative) shoulder on the dominant negative VCD band. Due to the sign change, fitting a single Gaussian to the ^{13}C component for VCD results in a band at $\approx 1640 \text{ cm}^{-1}$ for T and $\approx 1647 \text{ cm}^{-1}$ for A. The difference, 7 cm^{-1} , is greater than the coupling constant and suggests VCD might provide an upper bound. Together fitting the experimental VCD and IR ^{13}C band components may provide a means of extracting a range of values of the underlying coupling in the T (adjacent labeling) case.

Raman modeling was done in a similar manner and the $^{13}\text{C}=\text{O}$ amide I' components are predicted to have the opposite relative intensity patterns compared to IR. Consequently our simulated Raman ^{13}C amide I' shoulder profiles are about the same as the IR ones for A, with small splitting and a component predicted at $\approx 1643 \text{ cm}^{-1}$ but for T are shifted up to $\approx 1644 \text{ cm}^{-1}$ and again would yield a lower bound (1 cm^{-1}) to the coupling. However if these patterns are impacted by variations in the sequence, particularly in the tertiary amide vs. secondary amide shifts of the diagonal FF or by added aromatic residues having significant side-chain contributions which are common in Raman, this would be difficult to resolve.

3.3.3 The effect of proline side chain

In our previous studies we have successfully simulated amide I vibrational spectra without the need to incorporate the side-chains in our computational models. The case of proline is different, since the peptide linkage is not the usual secondary amide peptide bond rather it is a tertiary amide bond (no labile hydrogens on the nitrogen). To investigate if the Pro residues had an impact on the theoretical modeling, an alanine 5-mer based calculation (in vacuum), which is constrained to the PPII geometry, was performed. This was propagated onto a 22 residue alanine model, using the CCT method (93) and the resultant spectra are shown in Figure 12.

Since the calculations are performed in vacuum, the ^{12}C -amide I frequencies are higher than the experiment by $\approx 100\text{ cm}^{-1}$. This is $\approx 40\text{ cm}^{-1}$ higher than the simulation using all proline residues, and shows that the inclusion of proline does have an impact on mode position. However, as Table X illustrates, the vibrational coupling between two labeled $^{13}\text{C}=\text{O}$ modes is predicted to be similar, albeit a bit larger coupling is observed in the Ac-A₂₂-NHCH₃ case. Table X also lists the vibrational coupling obtained from a simulation on a complete Pro₁₅ peptide (Ac-P₁₅-NH₂), which confirms that the transfer method does not affect the simulation results in this case.

TABLE X: Variation in double label positions and splitting using different simulation models

Notation	^{13}C mode frequency (cm^{-1})					
	Sequential (T)			1-Apart (A)		
	modes	splitting	modes	splitting		
Ac-P ₁₃ -NH ₂	1646	1640	6	1644	1643	1
Ac-A ₂₂ -NHCH ₃	1693	1685	8	1689.5	1688	1.5
Ac-P ₁₅ -NH ₂	1646.5	1641	5.5	1644.5	1643.5	1

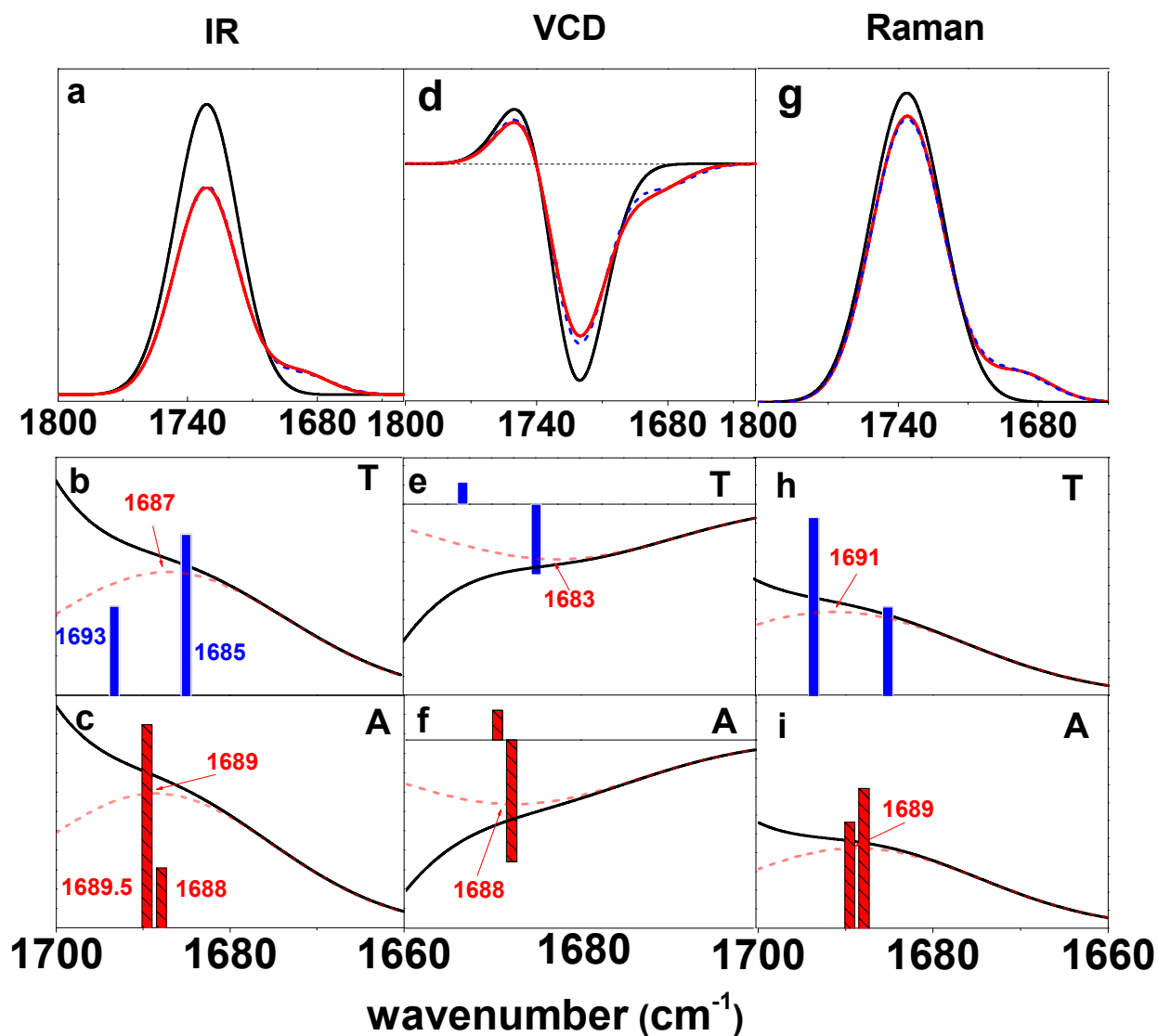


Figure 12: Simulated amide I' FTIR (a), VCD (d) and Raman (g) spectra for the unlabeled Ac-A₂₂-NHCH₃ (black solid line), compared to the sequential (blue dashed line) and alternate (red dotted line) doubly labeled ones adopting polyproline II conformation. Panels (b) and (c) are simulated ¹³C amide I' IR spectra and normal mode contributions for T (sequential labels) and A (alternate labels). (e) and (f) are simulated ¹³C amide I' VCD spectra and normal mode contributions for T and A. (h) and (i) are simulated ¹³C amide I' Raman spectra and normal mode contributions for T and A.

While experimental bandwidth limited the confirmation of the calculated vibrational splitting in these extended PP II helices, these simulations confirm that IR and VCD might be used to obtain lower and upper bounds to vibrational coupling in these helices.

3.4 β -strands in β -hairpins

With the selective isotope labeling of peptides, IR gains sensitivity to site-specific structural aspects of the peptide because of the vibrational coupling of the selected residues. Through-space and through-bond coupling of residues generate frequency shifts that contribute strongly to the characteristic IR and Raman frequencies and intensities, which are normally used for structural diagnoses. Hence, it is natural to choose to label structurally close-lying sites in peptide sequences to enhance their coupling. Observation of changes in their coupling during folding processes can be diagnostic of variations in local structure. However, other labeling schemes might also be useful, and have been utilized in previous IR studies (112; 113; 114). In particular, it is reasonable to ask what kind of information can be gained if only a single label is incorporated, since its location would be clearer than for multiple labels. Certainly single labels should sense local geometry or at least sequence variations through what might be termed the diagonal force-field components associated with that site. These are not easy to predict, since they are sensitive to residue type and local conformation, disorder and solvation. By contrast, the off-diagonal terms (corresponding to coupling between labeled residues) are relatively insensitive to these perturbations. The simplest β -sheet unit is a β -hairpin, in which two anti-parallel β -strands are connected by a reverse turn (usually 2-6 residues).

Among the many model β -hairpins that have been studied, the tryptophan zipper (or Trpzip) structures, which have four tryptophan residues forming a stable hydrophobic cluster in a sequence of 12-16 residues, has one of the most stable β -hairpin structures, particularly with a tight turn (47).

Consequently Trpzips have been the focus of a number of experimental and theoretical studies (115; 113; 116; 117). These hairpin peptides are monomeric, water-soluble, and have significant thermal stability in aqueous solution, due to cross-strand hydrophobic interactions between the tryptophan residues. Trpzip2 has been described as the smallest peptide sequence with proteinic residues that has a tertiary structure without aid from disulfide bonds or metal ion binding.

3.4.1 Scheme

In this study we focus on Trpzip2C hairpin (**TZ2C**, AWAWENKAWK-NH₂, where NG indicates the Asn-Gly residues in the tight β -turn), which is a slight modification of the original Trpzip2 sequence of Cochran et al (47). Substitution of Ala for residues 1, 3, and 10 was done for ease of labeling and the structures are shown in Figure 14.

TABLE XI: Definition of the Trpzip sequences and labeling positions in the peptide sequence along with their abbreviations. The labeled residues are highlighted.

Abbreviation	Peptide Sequence
TZ2C	A-W-A-W-E-N-G-K-W-A-W-K-NH ₂
A1	A*-W-A-W-E-N-G-K-W-A-W-K-NH ₂
A3	A-W-A*-W-E-N-G-K-W-A-W-K-NH ₂
A10	A-W-A-W-E-N-G-K-W-A*-W-K-NH ₂
A1A10	A*-W-A-W-E-N-G-K-W-A*-W-K-NH ₂
A3A10	A-W-A*-W-E-N-G-K-W-A*-W-K-NH ₂

These β -hairpin peptides were initially synthesized at the Protein Research Facility of the UIC Research Resources Center and the equilibrium infrared experiments were done by Rong Huang and

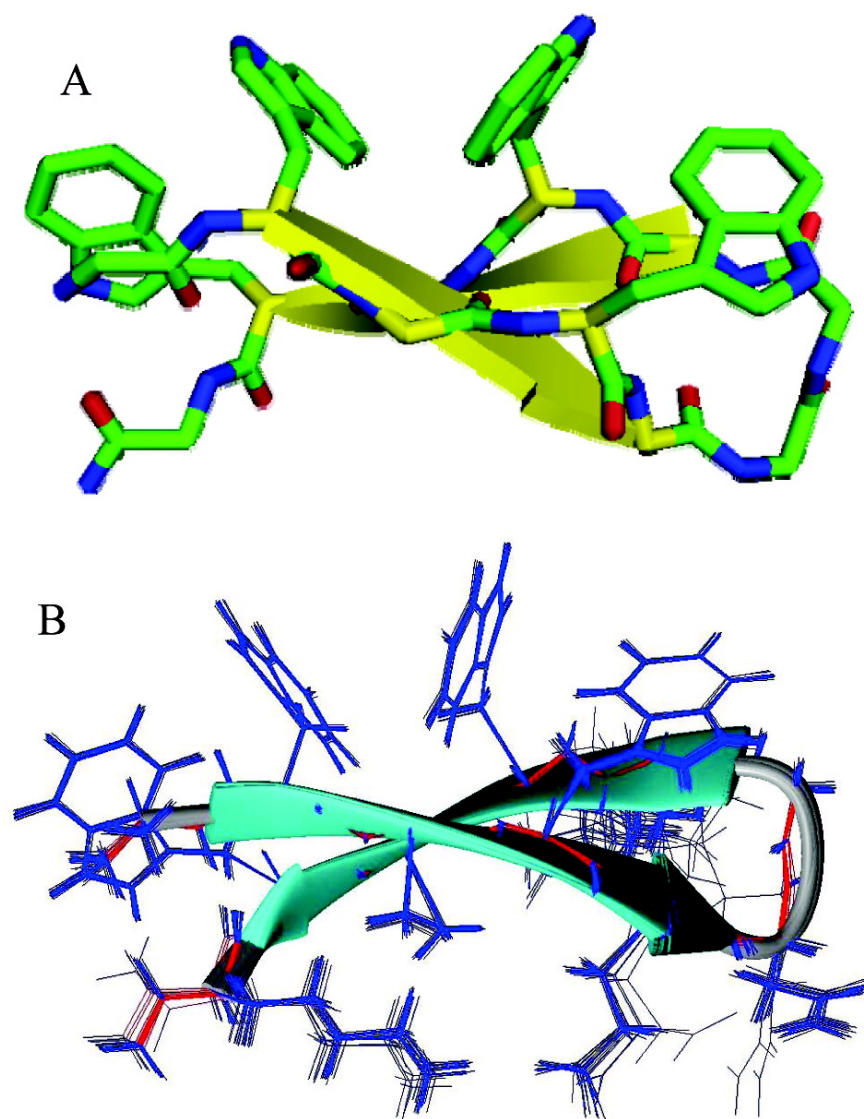


Figure 13: Representative trpzip conformation taken from 20 best NMR structures determined for TZ2C determined by Dan McElheny and Ling Wu at UIC.

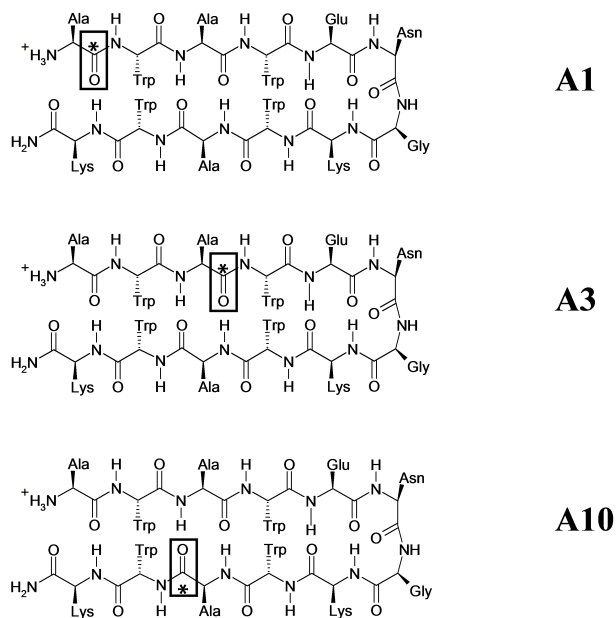


Figure 14: Single isotope labeled variants of TZ2C used for this study

Ling Wu. The experiments were further refined by Oliver Ridderbusch and Alexandra Hellerbach in the laboratory of Prof. Karin Hauser, which was originally at the University of Frankfurt and then at RWTH, Aachen. Experimental details may be found elsewhere (118).

3.4.2 Single labeling on the beta-strand

Using the NMR structure of Trpzip2C, an all-Ala peptide was constructed. It had the same ϕ, ψ angles and thus the same fold and cross-strand amide coupling and H-bonds as does the original hairpin. This reduced hairpin model was then used to calculate the vibrational force field after optimizing all geometrical parameters except the dihedral angles at the BPW91/6-31G** level (in vacuum and then again with implicit solvent correction) (119). The calculated IR spectra for the unlabeled peptide are in reasonable agreement with the experimental spectra (Figure 15). The

experimental amide I IR spectra are broader and have a more pronounced high frequency shoulder, the latter of which could possibly be due to TFA contamination. The peptide in solution has a dynamic structure with heterogeneously broadened spectra that is only approximately represented with the static approach implicit in the single structure QM simulation. This difference is illustrated by the overlap spectra in Figure 15 comparing the experimental and PCM corrected calculational results. As expected for DFT calculated FFs, the calculated amide frequencies are high, with maxima for the unlabeled variant at $\sim 1663\text{ cm}^{-1}$ and $\sim 1690\text{ cm}^{-1}$, for the solvent corrected and vacuum results, respectively, while the **TZ2C** experimental maximum is $\sim 1635\text{ cm}^{-1}$ (Table XII).

While frequency determination is important for interpreting single isotope labeled peptide spectra, the amide I' shift of the ^{13}C component from the ^{12}C main band is relatively independent of the general DFT error (compare vacuum and PCM results in Table XII) and can distinguish site variations in the diagonal FF predicted by our model. The band shapes for both calculations are similar, implying the off-diagonal terms are not very different, but the PCM correction leads to less dispersion of the amide I' and more resolution of the ^{13}C component (see Figure 16). This presumably arises from a relatively larger frequency reduction for those C=O groups pointed away from the other strand (hence out into vacuum), which can alter details of individual mode mixing.

To further test this concept, we empirically altered the FF for those C=O groups pointing out into solution to mimic H-bonds to the water solvent. The effect on the $^{13}\text{C}=\text{O}$ mode was not detectable for both the single- and double-labeled variants studied here. However, for the $^{12}\text{C}=\text{O}$ modes, the mode dispersion is further reduced and the frequency of the absorbance maximum slightly shifted down $\sim 2\text{ cm}^{-1}$, resulting in marginally smaller $^{13}\text{C} - ^{12}\text{C}$ splittings, which in principle are in better agreement with experiment but result in a more mismatched representation of the experimental

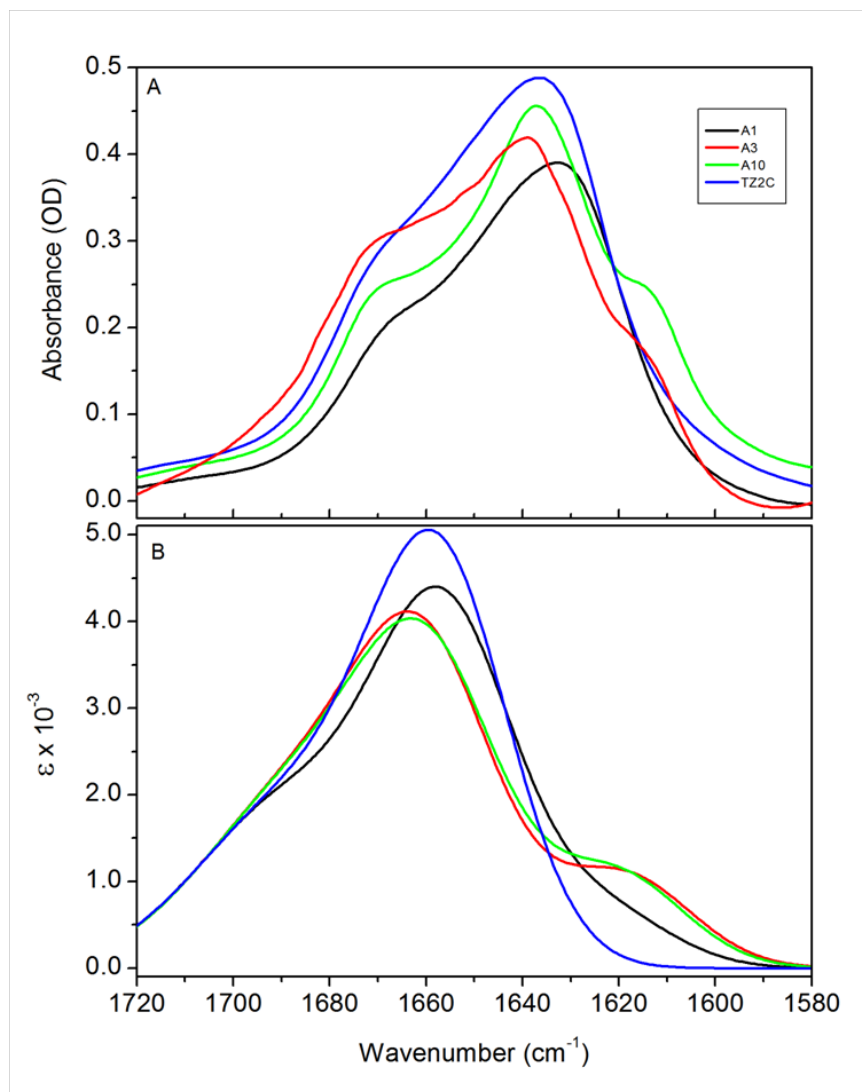


Figure 15: Experimental (A, top) and DFT simulated (B, bottom, with PCM solvent correction) amide I' absorption spectra of unlabeled TZ2C (blue) and labeled variants A1 (black), A3 (red) and A10 (green). There may be minor contribution at 1672 cm^{-1} from residual TFA in some of the experimental spectra.

TABLE XII: Comparison of experimental and simulated amide I' IR frequencies (cm^{-1}) for labeled TZ2C variants.

Notation	Experiment ^a				Simulation with TZ2C Model					
	¹³ C	¹² C	¹³ C- ¹² C	¹³ C	Vacuum			PCM(H ₂ O)		
					¹³ C	¹² C	¹³ C- ¹² C	¹³ C	¹² C	¹³ C- ¹² C
TZ2C		1635				1684				1658
A1	^b	1629	^b	1643	1687	44		1624	1656	32
A3		1615	23	1647	1688	41		1620	1661	41
A10		1614	22	1652	1687	35		1621	1660	39
E5^c				1650	1687	37		1620	1660	40
K8^c				1656	1686	30		1627	1659	32

^a Experimental frequency positions were determined by low pH difference spectra

^b No ¹³C band was observed for A1.

^c E5 and K8 isotope label models were calculated but not studied experimentally.

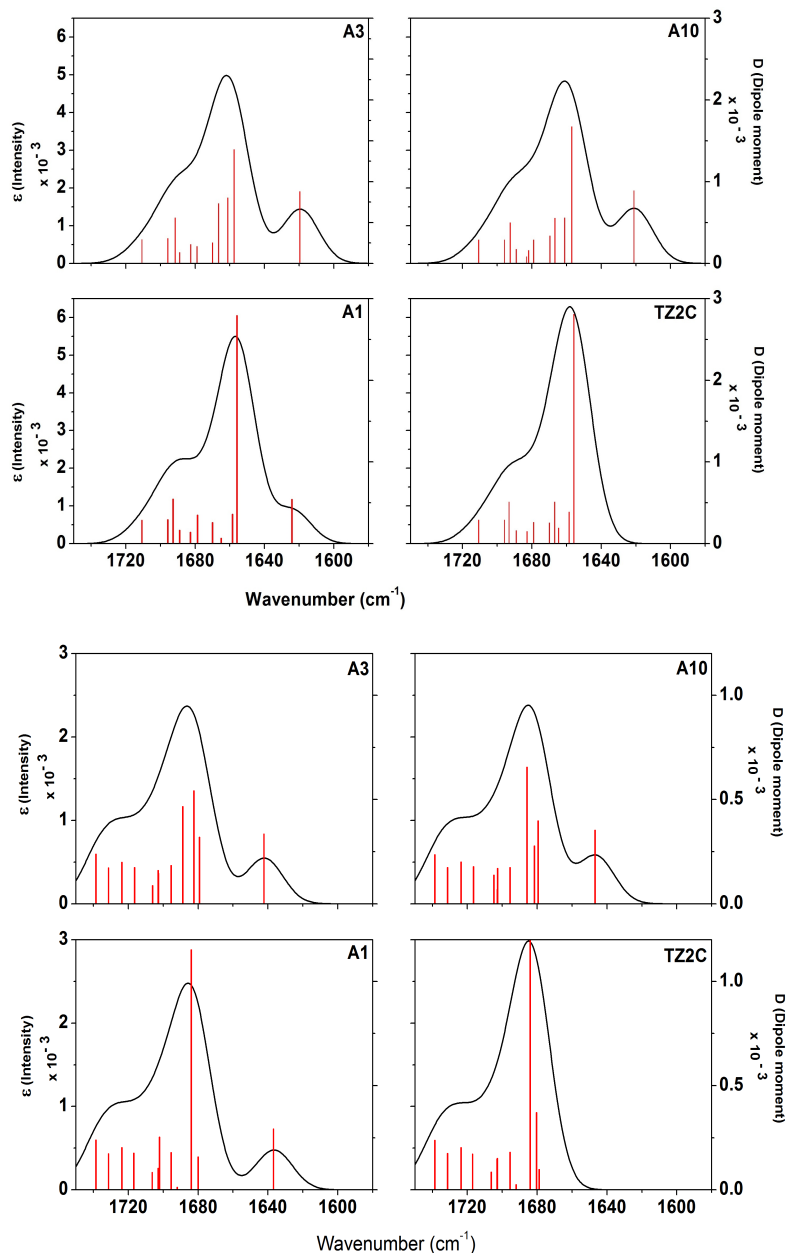


Figure 16: Comparison of calculated amide I' with PCM solvent correction (Top) and in vacuum (Bottom). The linewidths used for components are chosen at reduced width as compared to experiment to enhance distinguishability.

band width. This again suggests that conformational flexibility, or heterogeneous broadening due to an ensemble of structures, is the key missing component in simulating the observed bandwidth (79).

Our analyses focus on ^{12}C - ^{13}C shifts, assuming that the relative shift of $^{13}\text{C}=\text{O}$ modes for different substitution positions is fairly independent of the DFT errors. This assumption has been supported by previous work on labeled peptides with both helical and hairpin conformations (9; 103; 111; 120; 119). Labeling a residue in the middle of a β -strand tends to disrupt the exciton coupling, which leads to less intensity redistribution into the lowest energy mode, which is the most intense component in typical β -sheet structures (61). This exciton disruption is seen in our simulations, where there is more intensity in two modes adjacent to the strongest low frequency one causing the **A3** and **A10** $^{12}\text{C}=\text{O}$ band envelop maxima to shift up from the **A1** and **TZ2C** maxima, but this effect is less evident (smaller shift) in the experimental data (Figure 15). In summary, adding solvent effect corrections reduces the ^{12}C - ^{13}C shift values, by shifting the $^{12}\text{C}=\text{O}$ band down due to change in some diagonal FF elements, but does not alter their relative ordering for different substitution patterns (Table XII).

The values shown in Table XII summarize the frequencies for resultant bands corresponding to the ^{12}C and ^{13}C amide I' components as computed (DFT/BPW91/6-31G**) for the **TZ2C** NMR structure in vacuum and using the PCM solvent correction, along with experimental results for single labeled hairpins. As compared to experiment, these frequencies are systematically higher by 30 - 40 cm^{-1} and 40 - 50 cm^{-1} for the ^{13}C and ^{12}C maxima respectively, in vacuum, and by $<10 \text{ cm}^{-1}$ and 20-25 cm^{-1} for the PCM corrected ^{13}C and ^{12}C calculated band maxima. These results show that (except for **A1**) the $^{13}\text{C} - ^{12}\text{C}$ shift is about the same in vacuum and with solvent correction.

Although solvation corrections have a clear impact on DFT calculated frequencies, the amide I band shifts together. Thus, the relative shift ($^{13}\text{C}=\text{O}$ to $^{12}\text{C}=\text{O}$) does not significantly depend on

the solvent correction, even if we empirically correct for H-bonds to the outward oriented (solvated) C=O groups. For comparison, the hybrid semi-empirical B3PW91 (75; 74; 121) functional was used in lieu of BPW91. B3PW91 uses the PW91 correlation functional instead of LYP, but retains the three parameters derived for B3LYP. The related results obtained with B3PW91 were much higher yet, in error by $\sim 100 \text{ cm}^{-1}$ for the ^{13}C bands (vacuum) and $\sim 120\text{-}130 \text{ cm}^{-1}$ for the ^{12}C bands, but the $^{13}\text{C}\text{-}^{12}\text{C}$ split remained $\sim 45 \text{ cm}^{-1}$ (see Table XIII). This again is not very different from the other values we have calculated (Table XII), which shows the relative insensitivity of the off-diagonal FF to these DFT method variations, while the diagonal FF changes substantially.

TABLE XIII: Comparison of amide I' frequencies calculated with hybrid B3PW91 functional and simple BPW91 functional (both 6-31G** in vacuum).

Notation	B3PW91			BPW91		
	^{13}C	^{12}C	$^{13}\text{C}\text{-}^{12}\text{C}$	^{13}C	^{12}C	$^{13}\text{C}\text{-}^{12}\text{C}$
A1	1714	1762	48	1643	1687	44
A3	1718	1765	47	1647	1688	41
A10	1718	1762	44	1652	1687	35

Experimentally the **A3** and **A10** $^{13}\text{C}=\text{O}$ bands are quite similar, appearing at 1615 and 1614 cm^{-1} , respectively and have a $^{12}\text{C} - ^{13}\text{C}$ separation of 22-23 cm^{-1} . However, the corresponding **A1** $^{13}\text{C}=\text{O}$ band is not detectable, so no definitive conclusion can be drawn about its computed patterns, which for the solvent corrected calculations have a much smaller calculated frequency shift (32 cm^{-1}) than for **A3** (41 cm^{-1}) and **A10** (39 cm^{-1}). The difference in isotope substitution behavior

for **A1** is related to the terminal residue being disordered, so the representation of its $^{13}\text{C}=\text{O}$ mode with a single conformer simulation is measurably worse than that for **A3** and **A10**. The shift reflects a different diagonal FF component as compared to that for the **A3** and **A10** positions, which are in well-ordered parts of the β -strand and thus are subjected to stronger exciton coupling induced shifts.

3.4.3 Calculational interpretation

To evaluate the effects of stereochemistry on specific labels, our DFT calculations of the FF show that the sites **A3** and **A10** have equivalent frequency contributions to the ^{13}C amide I band. The mode structure and intensity distributions are almost identical (see Figure 16). On the other hand the solvent corrected calculations using PCM predict that **A1**, with the label on the terminal residue, has a different, higher frequency (Table XII). The **A3** and **A10** carbonyls are strongly H-bonded between the β strands, while the **A1** C=O is weakly H-bonded, and is partially solvated. Thus unfolding and breaking the **A3** and **A10** H-bonds are shown to yield a significant frequency shift. The calculations indicate that the labeled peptides (except **A1**) have amide I bands dominated by the ^{12}C components which have spectral overlap with the ^{13}C components Figure 15. **A1** and the unlabeled **TZ2C** have lower frequency amide I bands. The higher frequency ^{13}C and lower ^{12}C characteristic of **A1** combine to make the $^{12}\text{C} - ^{13}\text{C}$ shift $\sim 10 \text{ cm}^{-1}$ lower for **A1** than for **A3** and **A10**, which is the source of the overlap between the two contributions which is observed experimentally. If the **A1** were coupled to another labeled residue, such as in the double labeled **A1A10**, sensitivity to the local structure at the terminus would be preserved, but it is effectively lost in the single label case. The ^{12}C shift implies that elimination of an oscillator in the strand, e.g. by labeling **A3** or **A10** changes the exciton coupling that is the source of the characteristic intense, low frequency ^{12}C transitions. Theory seems to overestimate this effect, but since **A1** is labeled on the terminus, it does not impact the extent of exciton coupling very much.

Considering the ^{13}C components of **A3** and **A10**, the predicted relative displacements from the $^{12}\text{C}=\text{O}$ band are consistent with all the computed results, but the N-terminal labeled **A1** peptide has a higher wavenumber ^{13}C mode with PCM correction, and a lower value in vacuum, as compared to the **A3** and **A10**. This reversal of relative frequencies reflects the solvent exposure of the **A1** $\text{C}=\text{O}$ being greater than for the cross-strand H-bonded $\text{C}=\text{O}$ s in **A3** and **A10**. Consequently, **A1** is predicted to have a greater solvent effect and a less resolved ^{13}C sideband in the amide I' for the PCM calculation, which is qualitatively consistent with the pattern of experimental band shapes, even if it is not quantitatively in agreement.

All the above labeling discussion focuses on cross strand H-bonded $\text{C}=\text{O}$ groups, **A3** and **A10**. If instead those residues whose $\text{C}=\text{O}$ groups point out (for example any of the Trp residues, W) were labeled, our PCM based calculations still predict the frequencies to depend on the local conformation of single label residues. The amides in the center of the strand, W4 and W9, are computed to have ^{13}C amide I contributions whose difference from the maximum of the unlabeled **TZ2C** peptide are $\sim 5\text{ cm}^{-1}$ less than for those labeled at the terminus, W11 and W2. This difference from the unlabeled position is similar to what was predicted for **A1** vs. **A3**, **A10** and is summarized in Table XIV.

In other words, when residues in the center of the chain are labeled, they differ more from the unlabeled positions than do those on the termini. However, since the outer (W-associated) amide $^{13}\text{C}=\text{O}$ groups have no explicit H-bonds, their $^{13}\text{C}=\text{O}$ modes are higher in frequency ($\sim 12\text{ cm}^{-1}$) than the inner, cross-strand H-bonded (A3- and A10- associated) modes, so the ^{12}C - ^{13}C value is reduced in these simulated outer (W) labeled examples. Although the explicit H-bond caused by the cross strand interactions at **A3** and **A10** vs. only solvent dielectric for the $\text{C}=\text{O}$ s on the Trps (Ws) cause significant differences in $^{13}\text{C}=\text{O}$ frequencies, the outer (solvated) and inner (cross-

TABLE XIV: Outer residue calculated amide I' frequencies calculated for the TZ2C model, denoted W2,W11 for terminal residues, and W4,W9 for middle in-strand ones, as compared to middle cross-strand H-bonded residues, A3, A10

Notation	^{13}C	^{12}C	$^{13}\text{C}-^{12}\text{C}$
W2	1660	1640	20
W11	1657	1636	21
W4	1662	1633	29
W9	1663	1633	30
A1	1656	1624	32
A3	1620	1661	41
A10	1621	1660	39

strand H-bonded) carbonyls behave in a parallel manner, with the isotope effect being the dominant contributor.

All the above calculations use a PCM correction with an NMR determined, fully formed hairpin structure as a basis, with shielded (inner) C=O and exposed outer ones (on the W residues), but does not account for Trp shielding, which we have shown can be substantial (111) (119). These structures then unfold to an almost fully solvated sequence. Thus effects of changes in conformation and in solvation are mixed in the experimental situation, but can not be well represented in the single structure computations. Previous studies of solvation effects on spectra used helical models, which were similarly solvated in folded as in unfolded states, at least in terms of uniformity. These yielded fairly uniform spectral shifts, meaning that the solvent correction had little practical importance other than reducing the diagonal FF error, since the off-diagonal terms due to coupling were not greatly affected (111; 10). However for hairpins and other β -sheet models, the solvent correction is

more important because outer or “edge” C=O groups point out into either vacuum or solvent in the calculations, but are always directed at strongly interacting water molecules in the experiment. Our empirical tests of adding solvent H-bond corrections to the PCM based FF yielded less dispersion and a small shift down in wavenumber for the $^{12}\text{C}=\text{O}$ band and no detectable difference for the $^{13}\text{C}=\text{O}$ band (see Table XV). This did decrease the $^{13}\text{C}-^{12}\text{C}$ separation, making the calculated value approach the experimental one, but other than that there is little impact of change in the local FF for the solvated C=O groups.

TABLE XV: Comparison of maxima and dispersion for solvent corrected amide I with single and double labels.

	^{13}C	^{12}C	$^{13}\text{C}-^{12}\text{C}$	mode dispersion
A3	1620	1661	41	53
A10	1621	1660	39	54
A3A10	1617	1664	47	55
A3 ^t	1619	1659	40	45
A10 ^t	1621	1659	38	45
A3A10 ^t	1617	1662	45	45

^t FF empirical correction is added to the C=O for selected H-bonds.

In an attempt to decouple these effects, we simulated the amide I' of a 5-mer peptide in the strand conformation (thus no H-bonds) and in a “coil” or PPII like conformation, both using all Ala sequences. In these calculations, the frequency for a ^{13}C labeled residue in the middle of the

sequence (analogous to the local positions of labels in **A3** and **A10**) had a large shift on going from the vacuum to PCM result, as expected. It also sharply increased in relative intensity, which may be less expected. The solvent correction should enhance absolute intensity due to increased dipole moment in the imposed dielectric shell. However, this mode also had a substantial shift ($\sim 20 \text{ cm}^{-1}$ higher) in going from strand to coil, even in vacuum, which must be solely due to conformation, since no H-bonding or cross-strand interaction effects are included (see Table XVI).

TABLE XVI: Single strand calculations comparing PPII structure (unfolded model) with β -strand amide I frequencies, with and without solvent correction

	dielectric	^{12}C band	^{13}C band	^{13}C - ^{12}C
PPII	vacuum	1727	1686	41
	PCM ^a	1693	1655	38
β -strand	vacuum	1714	1665	49
	PCM ^a	1686	1638	48

^a The correction is implemented using an implicit solvent correction (PCM) with water as the solvent.

Thus the spectral impact of diagonal FF changes seen in thermal unfolding studies of the single label examples (118) are primarily due to conformational (ϕ, ψ) angle and not to H-bonding changes. This lower frequency comes from the enhanced dipole (exciton) coupling of parallel and anti-parallel oscillators in the strand, which transfers intensity to the lowest frequency mode, where local oscillations down the sequence are alternately out of phase (61).

3.4.4 Summary

Overall, the computed ^{12}C - ^{13}C separations (39 cm^{-1} and 41 cm^{-1} for **A10** and **A3**, respectively, with PCM) are much larger than the corresponding experimental values (24 and 22 cm^{-1}), which implies that in the experimental situation the hairpins have somewhat less coupling (exciton splitting) than for the computed models. The **A3** and **A10** results are very similar to each other, but going beyond these well ordered and experimentally studied positions, **K8** labeling is predicted to yield a different result, presumably due to the distortion at the turn, while the **E5** result was predicted much like **A3** and **A10** (Table XII). This reflects a pattern that was seen before with double labels (119) and is probably a consequence of our use of a specific, single structure for the computations. Development of a model to account for the ensemble of fluctuating molecules would be a challenge well beyond the scope of this chapter. Consequently, these computations may overemphasize the dipole strength of the lower frequency component of the $^{12}\text{C}=\text{O}$ amide I' exciton split band. Such small variations as those noted experimentally between **A3** and **A10** are unlikely to be significant, considering the ensemble of conformers contributing to the experimental results.

3.5 Two strands and a turn: Cross strand coupling in β -hairpins

In the previous section, the single isotope labeling on the beta strands of a TZ2C β -hairpin was discussed. A natural extension of that would be to explore the vibrational coupling across the two strands of a β -hairpin. In this section TZ2C is again selected as a model with a more extensive labeling scheme.

TZ2C has ϕ, ψ torsional angles of $50^\circ, 43^\circ$ for Asn and $72^\circ, 25^\circ$ for Gly, which can be viewed as being characteristic of a distorted type III' turn, where ideally ϕ is 60° and ψ is 30° for both residues. By contrast trpzip2 has a turn with (ϕ, ψ) values of $(71^\circ, 25^\circ)$ and $(82^\circ, -2^\circ)$, which is closer to a type I' turn where the ideal turn (ϕ, ψ) angles are $60^\circ, 30^\circ$ and $90^\circ, 0^\circ$.

3.5.1 Scheme

In addition to the peptides presented in the last section, this study had a series of peptides that had ^{13}C labels on amides that were on opposite strands of a β -hairpin (see Figure 17). All peptides in this study were synthesized at the Protein Research Facility of the UIC Research Resources Center and the experiments were done by Rong Huang and Ling Wu. Petr Bour performed the calculations using the transfer of spectral properties and FF from smaller fragments to a larger all alanine variant of TZ2C.

For more accurate calculations, The TZ2C NMR coordinates, provided by Dan McElheny, were substituted to have methyl side chains (all alanine representation) and optimized with constrained torsions. The result was used to directly compute spectral parameters (FF and APT) eliminating the need for fragment transfer. Solvent effects were incorporated by using an implicit solvation model (PCM).

3.5.2 Spectral simulation results

Figure 18 shows a comparison of some of these theoretical predictions for the amide I IR for the doubly labeled and unlabeled peptides with the ideal structure (Figure 18a) and **TZ2C** full DFT NMR structure (Figure 18b) as contrasted with the corresponding experimental results (Figure 18c).

As is typical for peptide DFT calculations, the computed amide I frequencies for both the ideal and NMR structure in vacuum are much higher ($\sim 50\text{ cm}^{-1}$) than seen in experiment. This is largely due to the lack of solvent effects in the computation, and in part is a consequence of the DFT-derived FF (10; 122; 61). The relative intensity and frequency patterns for the $^{13}\text{C}=\text{O}$ bands are primarily due to the coupling between residues (off-diagonal FF) and are mostly unaffected by this diagonal FF (frequency) error, resulting in good qualitative agreement with experiment for **A3A10** and **A3K8**, although the two low frequency features in **A1A10** are not reproduced in the computed spectra

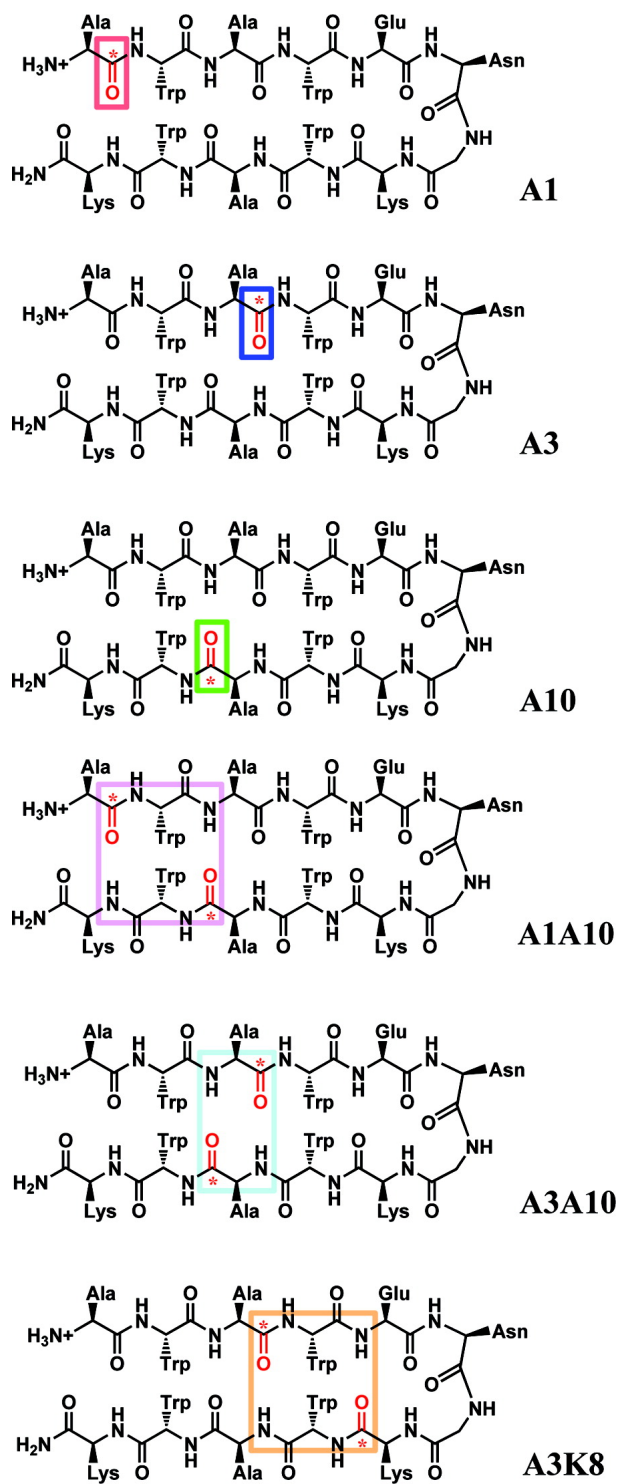


Figure 17: Double isotope labeled variants (^{13}C substituted $\text{C}=\text{O}$ indicated in red) of trpzp2C used for this study.

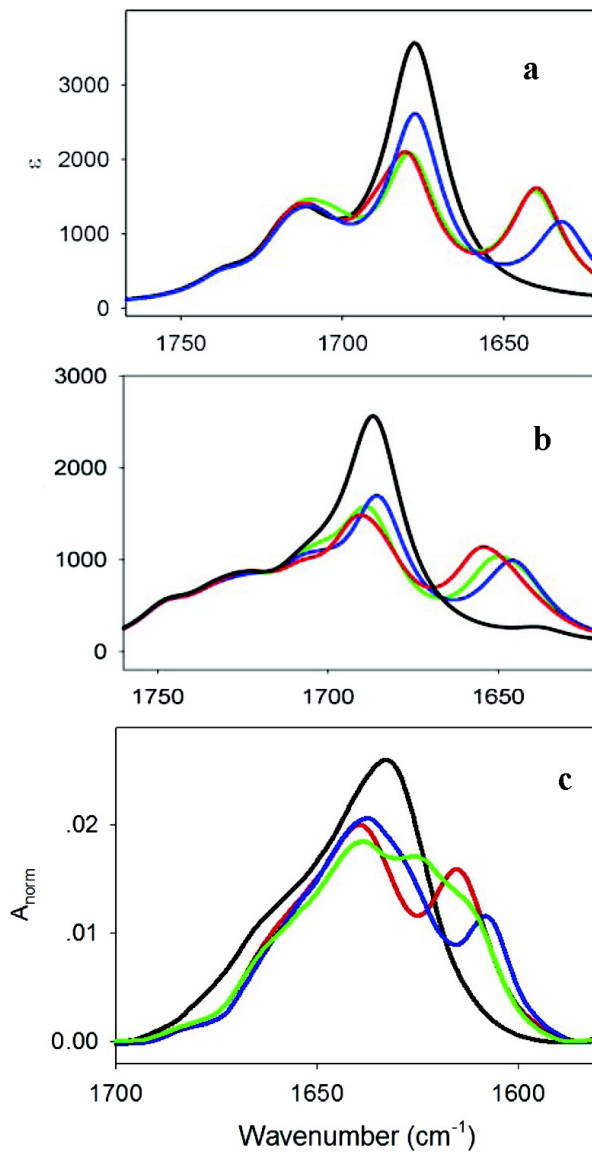


Figure 18: Comparison of (a,b) simulated IR spectra and (c) experimental IR spectra at 5°C for TZ2C (black), A1A10 (green), A3A8 (red) and A3A10 (blue). Simulations are presented for an all-Ala representation of the hairpin obtained from (a) a calculation for an ideal hairpin, using transfer from segments of a protein β -sheet (A3K8 and A3A10 predicted to overlap) and (b) a full DFT calculation of the Ala-substituted sequence constrained to the trpzip2C backbone NMR structure.

for either the ideal or NMR structures. The model structures have no fraying, since they are fully ordered in the ideal case and have a unique, although not fully regular, structure in the NMR case (Figure 13), which impacts the A1 position the most. The computed components of the $^{12}\text{C}=\text{O}$ bands for the ideal structure are also more resolved than seen experimentally for the same reason. In part, the difference between H-bonded C=O groups and those that are directed out into the vacuum in the calculation, but are H-bonded to D_2O in the experimental (solvated) conditions, leads to computational resolution of components. By necessity, these frozen structure calculations can not reflect the variations that characterize the ensemble of structures that exist for the real hairpins where the termini are partially unfolded, thereby sampling many local conformers, and where the turn is somewhat distorted and all residues are solvated. All that said, they do reproduce very well the qualitative patterns which are seen in experiment, especially for the labeled modes (see Table XVII).

3.5.3 The spliced fragment approach

As was previously demonstrated in the Keiderling group (122; 123; 124; 120), the labeling patterns used for **A3K8** and **A3A10**, forming larger (14-atom) and smaller (10-atom) cross-strand ^{13}C -labeled H-bonded rings, develop two distinct $^{13}\text{C}=\text{O}$ vibrational coupling patterns. In **A3K8** (large 14-atom ring), the ^{13}C peak appears at a higher frequency and with greater intensity than in **A3A10** (small 10-atom ring). This was seen for the **TZ2C** variants both in experiment and simulation, which clearly demonstrates that the vibrational coupling is different in these two cases and coincidentally proves that the TZ2 hairpin folds in-register as designed and as seen in the NMR structure. However, in contrast to the results for the idealized theoretical model of **A1A10**, two $^{13}\text{C}=\text{O}$ bands are observed when the labels are placed near the ends of the β -strands, as opposed to only one ^{13}C peak which primarily reflects the out-of-phase oscillation of the cross-strand coupled

TABLE XVII: Comparison of experimental and simulated $^{13}\text{C}=\text{O}$ labeled amide I IR frequencies for an all alanine variant of the TZ2C NMR structure.

		Experimental ^a			Theory		
		^{12}C	^{13}C	^{12}C - ^{13}C	Ideal structure		TZ2C NMR structure
					$^{13}\text{C}^b$	$^{13}\text{C}^b$	
					asym	sym ^d	splitting
						asym	sym ^d
							splitting
Trpzip2	1636						
TZ2C	1633						
A1	1630	n/a ^c			1636		1643
A3	1637	1615	22		1635		1647
A10	1637	1613	24		1637		1651
K8^e					1635		1655
A1A10	1638	1626/1613	12/25		1640	1632	1643
					(25/mix)	(1/mix)	(11/A1)
							(8/A10)
A3A10	1637	1608	29		1632	1640	1646
					(<1/mix)	(18/mix)	(13/mix)
							(1/mix)
A3K8	1639	1615	24		1640	1632	1647
					(25/mix)	(<1/mix)	(13/K8)
							(6/A3)

^a Frequencies, in cm^{-1} , are determined from original spectra

^b Individual normal mode frequencies (in cm^{-1}); numbers in parenthesis indicate relative mode intensity.

^c No obvious peak was observed.

^d The sym mode is weaker compared to the asym, since the cross-strand coupled dipoles oppose each other.

^e K8 was not synthesized but calculated for comparison to other double labeled peptides.

pair as seen for the others, where the labels are located in the center part of the peptide strands. The in-phase exciton component in a strongly coupled cross-strand pair would normally have very little intensity, since the dipoles would cancel. This means that in **A1A10**, the labeled residues are decoupled and significantly non-degenerate, which is a direct consequence of the ends being frayed and the **A1** position being a terminal residue. This prediction is supported by MD simulations of various hairpins, from which structures with varying degrees of frayed termini could be identified along a trajectory (125).

3.5.4 Complete hairpin approach

Computing the entire hairpin, all Ala, with the **TZ2C** conformation at the BPW91/6-31G** level in vacuum, without the need to splice fragments, results in predicted spectra that had better agreement with experiment, as can be seen in Figure 18b. In particular the variation in coupling constant and consequently the position of the peak of the $^{13}\text{C}=\text{O}$ absorbance for the **A3K8** and **A3A10** large and small rings is still well predicted. The distortion in the NMR structure causes the in-phase component to have about half the intensity of the out-of-phase component, so the $^{13}\text{C}=\text{O}$ bands tend to be broader and predicted with a shoulder. In most cases the $^{12}\text{C}=\text{O}$ modes reflect the pattern of the unlabeled species for the higher frequency amide I components, and the major variation in their pattern occurs for labels on **A3** and/or **A10** which are in the middle of the exciton coupled oscillators and thus disrupt the $^{12}\text{C}=\text{O}$ coupling. The dispersion of the $^{12}\text{C}=\text{O}$ modes in the full DFT NMR structure simulation is somewhat increased over that in the other calculations. Unlike the ideal case (Figure 18a), and in improved agreement with the experiment (Figure 18c), the **A1A10** $^{13}\text{C}=\text{O}$ band predicted with the NMR structure is different, lying between the two cross-strand coupled models, **A3K8** and **A3A10** (Figure 18c). The predicted **A1A10** IR still does

not exhibit the second band which is seen in experiment. However, since we computed a unique structure, rather than an ensemble, this is perhaps not surprising.

3.5.5 Site-specific vibrational coupling

As in previous reports for β -hairpin isotopic labeling (111) (123) (120), the **A3K8** and **A3A10** labeling patterns develop two distinct $^{13}\text{C}=\text{O}$ amide I band characteristics. Based on our calculational models and the similarity with labeled amide I results for previously studied hairpins, the differences can be assigned to a sign change in the site-specific vibrational coupling interactions. For the large ring, where labeled H-bonded C=O groups form a 14-atom ring, exemplified by **A3K8** (see Figure 17), the coupling constant is computed to be 4 cm^{-1} (half the splitting in Table XVII) resulting in the higher frequency component having a higher intensity, which for the less resolved experimental spectra would result in less apparent shift of the $^{13}\text{C}=\text{O}$ from the $^{12}\text{C}=\text{O}$ band but yield more intensity. For the small ring, where the labels form a 10-atom H-bonded ring, e.g. **A3A10** (see Figure 17) the opposite is true, the coupling being computed (ideal) as -4 cm^{-1} with the intense mode lower in wavenumber than the weak one, thus yielding a larger apparent isotope shift.

In the spectral calculations based on the NMR-structure, the local $^{13}\text{C}=\text{O}$ modes are somewhat less coupled due to non-degeneracy of the underlying oscillators (more so for the fragment calculation), resulting in double label coupling where both the components have intensity. Even so, the same relative intensity pattern and phase relationship is computed for these modes in **A3A10** and **A3K8**. Again the higher frequency component, is the more intense for **A3K8** (large ring), and the lower frequency ^{13}C component of the amide I' has greater intensity for **A3A10** (small ring), yielding agreement (more so for the full DFT calculation) with the experimental low temperature results (Figure 18c). The **A1A10** results are less coupled, more non-degenerate, but intermediate in predicted band position, which can also be seen to qualitatively agree with the experimental result.

The fragmentation may introduce end effects into the strand residues after transfer to the hairpin, which would distort the coupling in some pairs more than the others. The fact that the full peptide DFT calculation avoids this supports such an interpretation. DFT calculations are limited to smaller molecules, or to very large computational resources. From the fragmentation results, the PCM calculations are seen to have bandshapes for the $^{12}\text{C}=\text{O}$ amide I modes in better qualitative agreement with experiment as well as improved frequencies. Fragmentation calculations do not give the anomalous behavior for **A1A10**, which experimentally shows two non-degenerate $^{13}\text{C}=\text{O}$ peaks, although the full DFT calculation does predict the **A1A10** $^{13}\text{C}=\text{O}$ band to lie between the **A3A10** and **A3K8** results, as seen experimentally. This extra $^{13}\text{C}=\text{O}$ band in **A1A10** may be due to fraying of the hairpin termini, but these calculations are for a unique NMR structure, and even the ensemble of best structures does not deviate enough from regularity to bring out such a spectral deviation. It is possible that this is a problem of the NMR method which uses a specific force field to minimize the structure, but it is also a problem due to our use of just one structure.

The shift of the local modes by $\sim 40\text{ cm}^{-1}$ on ^{13}C substitution of the amide tends to decouple the labeled modes from the rest of the hairpin strand amide I vibrations, but some residual mixing does remain, which must be the source of the difference in intensity for the large and small ring variations. It is the sign change in the coupling constant that is the major, structure related consequence seen in the spectrum, as has been shown with other species (122; 123; 79; 120), and that sign pattern lets us confirm the alignment of the strands as well as provides a structurally sensitive probe of the unfolding as the temperature is increased. Although use of the NMR structure leads to more localized modes in our calculations, the coupling signs are the same as that evidenced by the intensity distribution, and they remain in overall agreement with experiment.

It is this real ensemble of structures, in a dynamic equilibrium, that probably lies at the basis for the ideal structure giving a qualitatively correct picture of the $^{13}\text{C}=\text{O}$ bands when the peptide is labeled mid-strand. For a fluctuating molecule, the contributions of the couplings to the termini and turn residues are averaged out so that the ideal picture retains interpretive value. Such a model for the dynamic hairpin structure was supported by MD simulations and is consistent with reported T-jump relaxation kinetics for these same isotopically substituted trpzip2C hairpins (126). Thus the oscillators in the center of the strands have less non-degeneracy than the model predicts, as can be seen by the well-resolved $^{13}\text{C}=\text{O}$ bands in **A3K8** and in **A3A10**, which are clearly offset from each other reflecting their oppositely signed coupling constants and a significant disparity in intensity for their in-phase (weak) and out-of-phase (intense) coupled modes than predicted with the NMR-structure based spectral calculations. However when labeled on the ends, the $^{13}\text{C}=\text{O}$ oscillator experiences an environment resulting in diagonal force field components which are not encompassed in the ideal model. Similarly, the $^{12}\text{C}=\text{O}$ modes always sample the termini and turn, so the replication of their spectra by single-structure based calculations is hindered.

3.6 Overall summary of vibrational simulations

Coupling between C=O groups on adjacent (T) and separated (A) residues in a series of 3_{10} helices were evaluated. Splitting for adjacent residues are determined to be 7 cm^{-1} , which is smaller than those found for α helices for adjacent residues, while that for separated (T) residues is the same for both α and 3_{10} helices (103). The sign coupling patterns are the same for α and 3_{10} helices where adjacent C=O groups have a positive coupling, yielding the same VCD sign pattern and a more intense IR component to higher energy (closer to the $^{12}\text{C}=\text{O}$ band). The C=O groups separated by one residue have negative coupling and the opposite VCD sign pattern. The computations support the observed isotopic shifts and splittings of coupled modes, and can be

analyzed to determine coupling constants. However, the details seem dependent on minor changes in the FF or geometry which were not included in the modeling, suggesting that the results should be treated as ranges. VCD for 3_{10} helices is weaker than for the corresponding α helices due to this weaker coupling. This reduced coupling appears to result from the different angle of the H-bonded C=O groups with respect to the helix axis in the 3_{10} helices as compared to the α helix H-bonding pattern.

Using the 14 residue proline oligomer, the coupling between sequential amide C=O's in a PPII helical structure was calculated to be in the range of 6-10 cm^{-1} and was verified by experiment. The coupling between alternative (A) labeled C=O's was predicted to be very weak (1 cm^{-1}). This low coupling might be attributed to the fact that the PP II is effectively an extended chain, differing from the fully extended flat β -strand by a 120° (in PPII) vs a 180° (in strand) twist. The C=O groups in PP II are further spread apart by the twist and the angle between individual amide dipoles reduces the coupling.

β -hairpins were successfully modeled with a DFT calculation of a complete all alanine variant of Trpzip2C. Adding a correction for the dynamics of the water environment and for the peptide itself and sampling an ensemble of related structures allowing for various distortions of the termini and the turn, would improve the spectral representation. However, it would also require a computational effort out of scale with the other approximations used in modeling the FF, such as ignoring the impact of side chains, a contribution that can lead to substantial shifts in the diagonal FF (A. Lakhani and G. Papadantonakis, unpublished results).

However, by consideration of structure variations and inclusion of the solvent effect, our ability to understand subtle spectral features improved. A key element of this improved understanding

came from the use of DFT based calculations of the vibrational spectra for the complete backbone of the peptide rather than the fragment based approach.

In this chapter, it has been demonstrated how DFT based calculations are crucial in interpreting the calculations of vibrational coupling. In some cases, like the 3_{10} helix octa-peptides, these calculations were instrumental in helping us decide the length of molecules that needed to be synthesized to experimentally obtain better results. The study started with examining intra-strand coupling in helices and evolved into exploring cross-strand coupling in β -hairpins (**TZ2C**). The cross-stranded coupling is a product of molecular conformation and geometry, and is therefore dependent on the tryptophan interaction in **TZ2C**. This interaction was clearly evident in the experimental far UV ECD spectra of **TZ2C** (127; 128; 67) and the chiral signature of tryptophans was intriguing. This chapter focused on molecular vibrations in the ground state. However, to fully understand the ECD signature of tryptophans and to model it, it is important to leave the ground state for a while as detailed in the next chapter.

CHAPTER 4

MODELING OF THE CIRCULAR DICHROISM FOR A TRYPTOPHAN ZIPPER PEPTIDE WITH TDDFT OF COUPLED AROMATIC RESIDUES

The results of these studies were published in :

- Roy, A., Bour, P., and Keiderling, T. A. (2009) TDDFT modeling of the circular dichroism for a tryptophan zipper peptide with coupled aromatic residues. *Chirality* 21, E163-71.

4.1 Introduction

Tryptophan (Trp) is a chiral amino acid with an aromatic side whose low lying electronic states are of critical value for fluorescence studies of proteins and peptides. Additionally, absorbance spectra to these states provide a useful marker for concentration determination. Consequently the electronic structure and excited state properties of tryptophan's side group, indole, have long been of wide interest.

From a chirality point of view, the associated electronic circular dichroism (ECD) of these transitions in an isolated amino acid is relatively weak due to the local planarity of the indole chromophore. On the other hand, in folded proteins or other stereochemically constrained environments, these Trp transitions yield useful, easily measured CD, typically detected in a region around 280 nm, whose presence or absence correlates with tertiary structure in the folded protein. If two or more Trp are in the protein sequence and have a fixed relative geometry, a particularly strong CD may be observed, as their transitions can couple and develop an exciton chirality whose distinctive shape and sign pattern could be used to determine the relative stereochemistry of the chromophores.

Recent studies of designed β -hairpin peptide structures, that are stabilized by hydrophobic interactions of various residues, have highlighted the special role of Trp (47; 129; 130). In particular, in a set of peptides denoted as tryptophan zippers (Trpzip) the Trp-Trp exciton coupled CD, which yields an intense couplet band shape in the far- ultraviolet (UV), was used to follow temperature induced unfolding of the hairpins (47; 127; 67; 119). The dominant bands seen in these peptides form a +/- couplet (with decreasing wavelength) that does not correspond to the Trp bands often used to monitor protein tertiary structure (at 280 nm) but rather to higher energy (electronic dipole allowed) transitions at 227(+) and 213(-). In these small peptide hairpins, the CD arising from the strong coupling of these Trp chromophores in the far UV region, due to their $\pi \rightarrow \pi^*$ transitions, completely overwhelms the traditionally studied amide CD often used for secondary structure analysis. The side chain CD also disappears for these peptides when they unfold at higher temperatures. The lower energy indole transition, which corresponds to that used in protein near-UV CD, can be detected as a single signed CD band, and its temperature dependence tracks that of the couplet (119).

Several mutants of these Trpzip peptides have been prepared with different residues substituted for the Trps in various pairs at cross-stranded positions (119; 126). These studies have shown that IR spectra can be used to follow secondary structure (β -strand) change in these peptides, while CD and fluorescence can follow tertiary structure (Trp-Trp interaction) change. Due to the central role of Trp CD in these important model systems as well as for proteins overall, it is important to develop a better understanding of their electronic spectra. In this chapter, the CD that can arise from stereochemical interactions of electronic (UV) excitations of two or more Trp residues is addressed, with a specific application of modeling one Trpzip system.

Recently, complete active space self consistent field (CASSCF) calculations have been used to successfully model excited state; however, their high computational cost favors their use for smaller molecular systems (131). The advent of widely accessible packages for time dependent density functional theory (TDDFT) method computations has allowed quantum mechanical calculation of properties of excited states with moderately sized computers at relatively low computational expense. Recent research on the electronic spectra of tryptophan using TDDFT (131; 132) has centered on the near UV transitions, i.e. those localized at the indole ring which are denoted as 1L_a and 1L_b in Platt's notation (133). These are the well studied $\pi \rightarrow \pi^*$ excitations from ground to the low lying excited (singlet) states and, according to Kasha's rule, are the source of the fluorescence emitting states for tryptophan (131; 134). There has been considerable debate over the relative ordering of these states and their detailed properties (131; 135; 136) but for our specific CD analyses, such issues are not critical, thus we will not comment on them directly. In this work, we instead focus on the more intense $\pi \rightarrow \pi^*$ transitions in the 190-230 nm region (1B states), which for Trpzip peptides dominate the far-UV CD spectrum and absorbance. In Trpzip, aromatic residues are designed to interact and thus occur in cross- stranded pairs.

The coupled oscillator (CO) model (137) can also help develop a qualitative understanding of the CD of these intense transitions, which depends on rotational strengths arising from dipole orientation and splitting from the dipolar interaction. Here we go beyond such a transition dipole coupling (TDC) based method by using ab-initio approaches based on the TDDFT methodology. To our knowledge, this is the first time TDDFT has been used to study the ECD of coupled tryptophans, although one of these computational results was reported in a previous article to explain the source of the UV CD in a Trpzip hairpin (119). TDDFT has been previously used for computing excited states of indoles and has been criticized with regard to its application for larger ring systems (135; 138),

however, our comparison of theoretical to experimental results for the 1B transitions in the Trp sidechain indole chromophore are satisfactory, and those of the 1L are also acceptable.

4.2 Scheme

4.2.1 TDDFT calculation

TDDFT calculations with a reasonable basis set for the excited states of a complete Trpzip2 molecule (209 atoms), the most stable small β -hairpin model available (47), would be computationally too expensive. Fortunately, because most of the observed electronic CD arises from the Trp side-chain and not the amide backbone, we could restrict ourselves to a series of excited state calculations on an isolated indole chromophore. For computing CD, chirality develops from coupling indole models whose relative geometries were fixed to correspond to those of the Trp side chains in Trpzip2. These local geometries are functionally the same in Trpzip1 and in the mutant structures we have prepared which have only two Trp residues (see Figure 19) (130; 127; 67; 119)

Transition energies and intensities were computed for isolated indole rings with different basis sets, and also for indoles with methyl substituents which represent the connection to the peptide backbone, at the β methylene carbon of Trp. The hybrid functional, B3LYP, was chosen because of its previous success with description of these excited states (139). To model the effect of solvation, we used the polarized continuum model (PCM) (140), which considers the solute to be in a dielectric cavity whose electrostatic potential is derived from the dielectric of the solvent, in our case water ($\epsilon_r=78.39$). All computations used either Gaussian 03 Rev D.0216 (141) or Turbomole ver. 5.1017 quantum chemical software (142).

The same kinds of B3LYP TDDFT electronic excitation computations, but including circular dichroism, were repeated using a 6-31++G** basis set for dimer models (and 6-31G** for tetramers) of indole rings that were constrained to selected relative orientations. These constrained indole

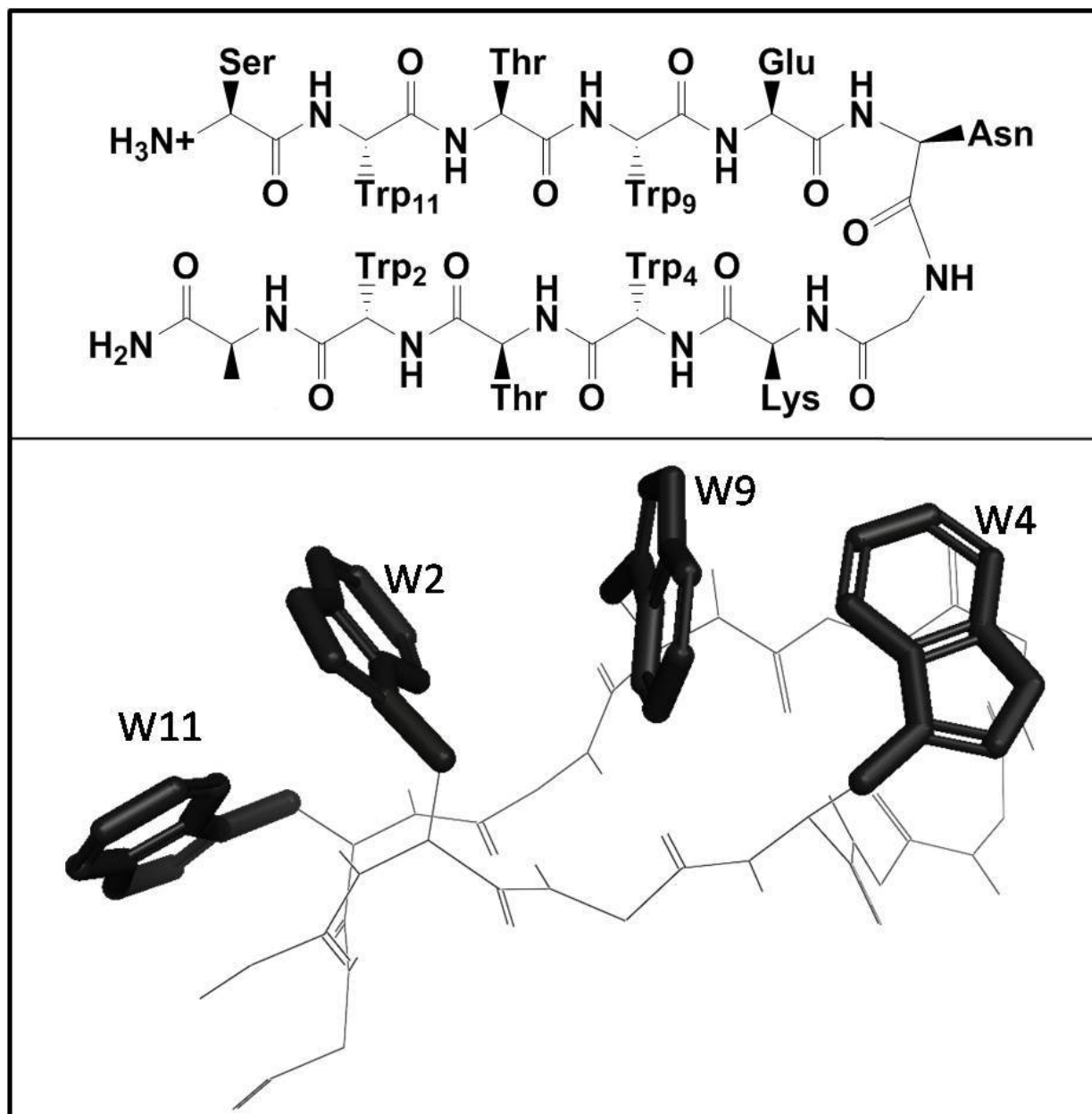


Figure 19: (Top) The Trpzip2 peptide indicating the sequential positions of the four tryptophans involved in the study (2, 4, 9 and 11), and (bottom) its three-dimensional representation showing the relative orientations of the Trps (PDB ID: 1LE1)(47). The backbone is represented using a line representation and the 3-methyl indole (3MI)-like side chains, which were used as a basis for further calculations, are highlighted using bold stick representation.

geometries model the conformations found for the Trp side-chains in the NMR-determined structure of a Trpzip2 (130), which was subsequently confirmed by Ling Wu and Dan McElheny, by NMR structure determination, to be functionally the same for mutated Trpzip2's that have only one pair of interacting Trps (119; 127). The rotational strengths were calculated with the dipole-velocity gauge formulation. In order to compare theory with experimental CD of the β -hairpins, Gaussian functions with a full width at half maximum (FWHM) of 20 nm were convoluted with each of the calculated rotational strengths. These when summed approximated the experimental band shapes but are simplified since they do not include vibronic effects. Experimental CD spectra, measured in our laboratory, are given in detail elsewhere in the literature (127; 67; 119) and results from those studies will be used here for comparison. Experimental absorbance is more difficult to determine due to the overlap of Trp transitions with those of other groups. Thus the computationally more reliable value of $\Delta A/A = \Delta\epsilon/\epsilon = 4R/D$ (i.e. the ratio of rotational (R) and dipole (D) strengths of a single transition) is not available from experiment for comparison with theory, which restricts quantitative evaluations of these computations in terms of experimental spectral results.

4.2.2 Dipole coupling

To estimate the role of the dipole coupling, the generalized transition dipole (coupled oscillator) model was used to compute dimer and tetramer CD employing ab initio computed monomer transition dipoles (μ_i) (143; 144). In this method, the interaction Hamiltonian containing only the

dipole-dipole interactions is diagonalized. From the eigenvectors c_{Ei} , dipolar (D) and rotational (R) strengths are obtained for each excited state (E) as

$$\langle D \rangle = \sum_i c_{Ei}^2 \mu_i^2 + 2 \sum_{i < j} c_{Ei} c_{Ej} \mu_i \cdot \mu_j \quad (4.1)$$

$$\langle R \rangle = \frac{-\omega}{2} \sum_{i < j} c_{Ei} c_{Ej} r_{ij} \cdot \mu_j \times \mu_i \quad (4.2)$$

where ω is light angular frequency, and r_{ij} the position vector of dipoles i and j .

The input electric transition dipole moments were obtained from the TDDFT (B3LYP/6-311++G**) computation (Table XVIII). Intrinsic magnetic moments were ignored; instead, the electric dipoles were placed close to the molecular center (the 4-atom average, as shown in Figure 20) where the magnetic moments (origin dependent) adopt small values. Electric dipoles computed by the velocity formalism were considered, to insure origin independence of the results. Interactions between all possible (20 lowest- energy) Trp transitions were considered, including the states polarized perpendicular to the tryptophan plane. Using NMR structures (47; 119) planes passing through the ring atoms were constructed and the angles between these were subsequently calculated for analysis of the relative geometries.

Grishna and Woody have previously used TDC to simulate Trp contribution to protein CD using semi-empirical parameters (137). Our adopted TDC model is similar to that used previously by Rogers and Hirst (145) where fewer tryptophan transitions (calculated at the CASSCF level) were used, but in their model, the Hamiltonian also included point charge interactions and interactions with the peptide chains.

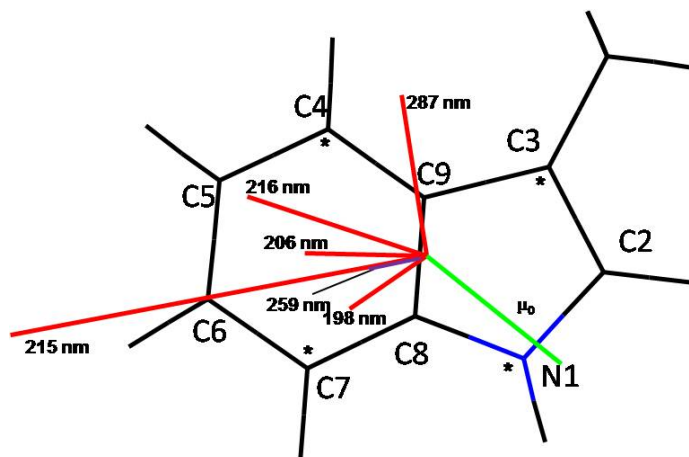


Figure 20: Calculated (B3LYP/6-311++G**) permanent (green, $|\mu_o|=2.02$ debye) and in plane transition dipole moments (red, wavelength indicated with energy in parentheses, in eV) for 3MI that were used in the TDC computations (z-polarized transitions are not shown). The dipoles were placed in the geometrical center of the atoms marked by the asterisk

The program that realizes this dipolar coupling was written by our collaborator, Dr. Petr Bour. Experimental data shown in this chapter were measured by Ling Wu and Rong Huang. Details for experiments are given elsewhere (127; 128; 119).

4.3 Results

4.3.1 Single indole

Geometry optimizations for indole and 3-methyl indole (3MI) were performed starting from a geometry derived from one Trp side-chain taken from the Trpzip2 NMR structure and energy minimizing the indole and related 3MI structures using DFT at the B3LYP/6-31G** level. The agreement between the experimental and calculated geometries was good, e.g., with less than 0.03 Å difference in C8-C9 bond length (similar for N1-C8). TDDFT calculations were then performed on both the geometry optimized and original structures, which proved to have qualitatively similar

transition energies and intensities, the two parameters important for the interpretation of our experiments. Indole and 3MI have a plane of symmetry and therefore have no rotational strength in isolation (no CD). We analyzed their computed oscillator strengths and energies as a test of our basis set selection and computational methods and to gain some insight into the most intense, lowest lying transitions observed in various indole calculations, as summarized in Table XIX and illustrated in Figure 21.

The unsubstituted indole ring is computed to have four relatively intense transitions in the UV, $S_1 - S_4$, where $S_1 - S_4$ indicate the four lower energy, intense singlet excitations from the ground (S_0) state. S_1 and S_2 , the near-UV $\pi \rightarrow \pi^*$ transitions, are calculated to be at 271 nm and that at 253 nm with the B3LYP/6-31++G** level of theory. Based on previous literature (136) and calculated dipole strengths, we attribute the 271 nm transition to the 1L_a and 253 nm to the 1L_b transition. Additionally, there is one strong $\pi \rightarrow \pi^*$ transition, S_3 , computed near 200 nm, which is more than 10 times stronger (oscillator strength, $f = 0.76$) than the 1L transitions ($f = 0.056$) and can be assigned to the 1B_b transition. Some weak transitions are also computed in this range and their number and distribution varies strongly with basis set. Several moderately strong transitions higher in energy than S_3 are seen with the polarized basis, 6-31G**, and they might be designated as S_4 , which may be the 1B_a transition. With diffuse functions added, as 6-31++G**, there are fewer of these intense, computed transitions, but the remaining ones are quite mixed in character and correspond to the excitations from the HOMO and HOMO-1 to the higher lying LUMO, LUMO+1 and LUMO+2 (146). This means the S_4 transition is not well characterized and will be consequently of less use in our analyses.

Addition of a methyl group on position 3 of the indole to form 3MI, shifts the 1L_a and 1L_b transitions down in energy and closer together for the 6-31++G** basis set (Figure 21b); but they

TABLE XVIII: Transition dipole moments of 3-methyl indole and corresponding energies calculated at B3LYP/6-311++G** level of theory

Transition number	Wavelength (nm)	Energy (eV)	Dipole (Debye)			Oscillator strength	
			x	y	z		
1 ^a	287	4.32	1.9	0.154	-0.692	0	0.053
2	279	4.44	0.12	0	0	-0.059	0
3 ^a	259	4.79	0.48	0.198	0.034	0	0.005
4	258	4.81	0.13	0	0	0.054	0
5	249	4.98	0.07	0	0	-0.031	0
6	236	5.25	0.45	0	0	-0.176	0.004
7	228	5.44	0.68	0	0	0.265	0.009
8	226	5.49	0.2	0	0	-0.081	0.001
9	220	5.64	0.24	0	0	-0.095	0.001
10 ^a	216	5.74	2.21	0.822	-0.282	0	0.106
11	216	5.74	0.12	0	0	0.047	0
12 ^a	215	5.77	4.98	1.952	0.364	0	0.558
13	209	5.93	0.64	0	0	-0.243	0.009
14 ^a	206	6.02	1.43	0.572	-0.01	0	0.048
15	201	6.17	0.42	0	0	0.159	0.004
16	199	6.23	0.13	0	0	-0.047	0
17 ^a	198	6.26	1.09	0.355	0.218	0	0.027
18	198	6.26	0.24	0	0	0.092	0.001
19	197	6.29	0.5	0	0	0.192	0.006
20	195	6.36	0.25	0	0	0.091	0.001

^a in-plane polarized transitions.

TABLE XIX: Comparison of transition energies and oscillator strengths (OS) of the S₁, S₂ and S₃ transitions for indole and 3-methyl indole calculated using various geometries and basis sets

model	basis set	S ₁			S ₂			S ₃		
		Energy (eV)	λ (nm)	OS ^a	Energy (eV)	λ (nm)	OS ^a	Energy (eV)	λ (nm)	OS ^a
indole										
vac ^b	6-31G**	4.730	262	0.050	5.020	247	0.020	6.350	198	0.156
vac	6-31G**	4.880	254	0.060	5.000	248	0.040	6.230	199	0.320
vac	6-31G**++	4.576	271	0.056	4.896	253	0.018	5.999	207	0.765
wat	6-31G**++	4.469	277	0.075	4.877	254	0.019	5.763	215	0.902
3MI										
vac ^b	6-31G**	4.540	273	0.050	4.960	250	0.005	6.120	203	0.615
vac	6-31G**	4.730	262	0.060	4.950	250	0.020	6.100	203	0.040
vac	6-31G**++	4.531	274	0.073	4.799	258	0.023	5.784	214	0.480
wat	6-31G**++	4.418	281	0.097	4.784	259	0.027	5.624	220	0.807

^a oscillator strength (OS) is a dimensionless quantity.

^b DFT calculation was performed on a molecular mechanics refined structure.

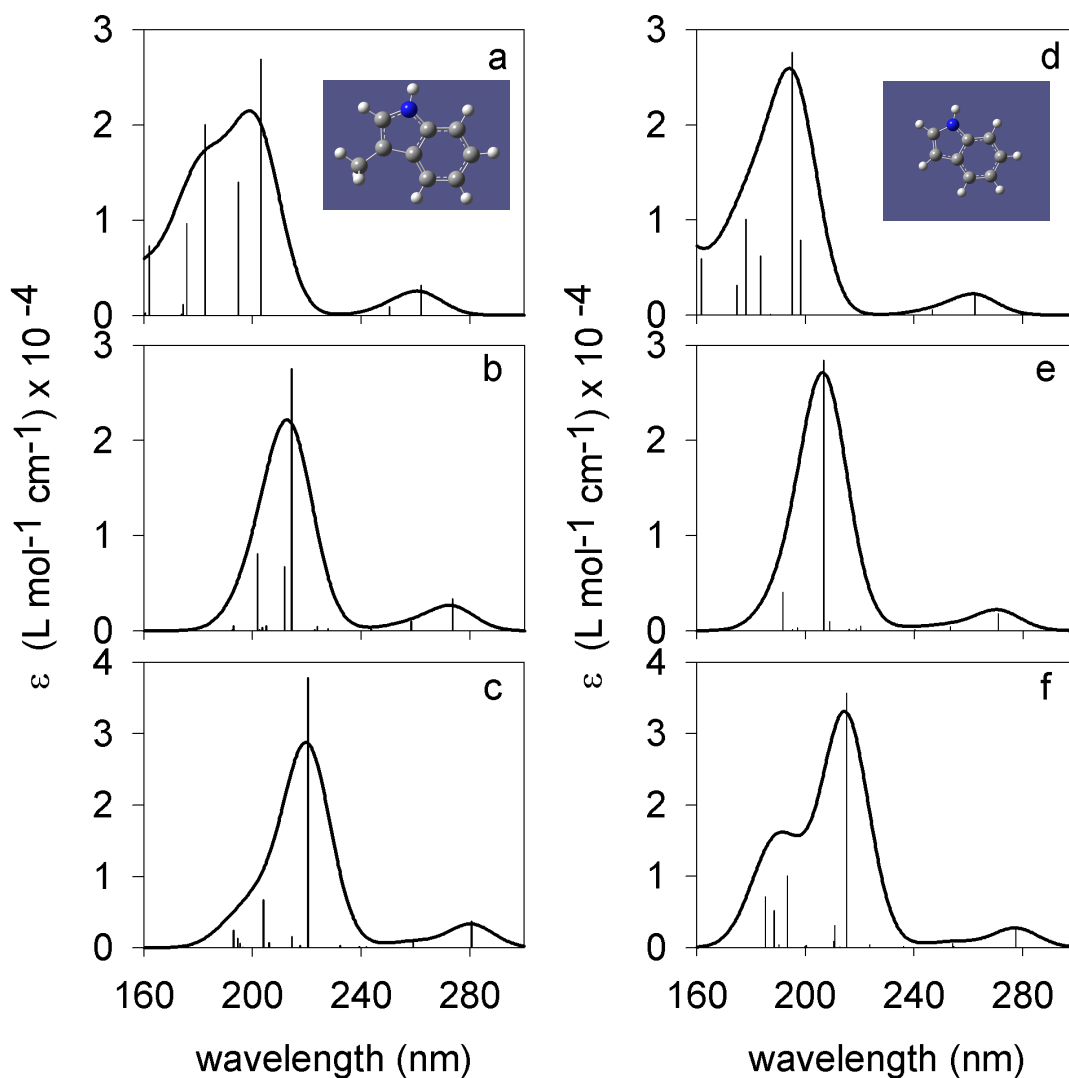


Figure 21: Calculated UV - absorbance spectra for 3 methyl indol (3MI) and indole. (a) 3MI in vacuum with a polarized basis set, 6-31G^{**}; (b) 3MI in vacuum with a diffuse basis set, 6-31++G^{**}; and (c) 3MI using a PCM model for water with a diffuse basis set, 6-31++G^{**}. (d) indole in vacuum with a polarized basis set, 6-31G^{**}; (e) indole in vacuum with a diffuse basis set, 6-31++G^{**}; and (f) indole using a PCM model for water with a diffuse basis set, 6-31++G^{**}. Vertical lines represent dipole strengths and solid curves the Gaussian convolutions of calculated bands using FWHM = 20 nm.

remain further apart for smaller basis set calculations (Figure 21a). S_3 , the 1B_b transition, is shifted down in energy from indole to 3MI (0.1 eV) and shifts even more using diffuse functions (0.2-0.3 eV) with 6-31++G**. Computation of the spectra for solvated indole or 3MI, using the PCM model and water parameters red shifts the entire UV spectrum, as expected. The 1L_a transition and the far-UV 1B_b transitions predicted to have large bathochromic shifts of 6-8 nm (0.1 eV), but the 1L_b transitions are much less affected, which is expected since the 1L_a and 1B states have a larger dipole moments than the 1L_b state and are stabilized by the dielectric environment imposed by the PCM model.

The geometry change has some impact on the 1L_a and 1B transitions but less on 1L_b , and the diffuse basis set, 6-31++G**, has a substantial effect on all the transitions, as does PCM. With diffuse functions, the transitions shift down in energy, by 0.25-0.3 eV, and become $\approx 50\%$ more intense, thereby enhancing dipole coupling. These behaviors with solvation and values for the transition energies are in good agreement with those reported earlier (131; 135).

4.3.2 Two coupled tryptophan models

Figure 19 shows a schematic representation of the Trpzip2 peptide with emphasis on the relative Trp geometries, as determined from its NMR structure. The tryptophans interact to stabilize the hairpin structure by forming a hydrophobic face on one side of the folded hairpin. Indole side chains were used to model relative interaction geometries for two and four Trp residues. Two 3MI molecules were fixed in space with relative geometries that were obtained from the Trpzip2 NMR structure by selecting pairs of cross-stranded interacting Trp side chains. Extending this procedure, using the full Trpzip NMR structure, provides the opportunity to create three combinations with two Trps, W2W11, W4W9, W2W9, that are designated as W(a)W(b), where a and b are the original Trp

positions in Trpzip2. A fourth possibility, W4W11, corresponds to the far separated pair of residues which are effectively not coupled, but its spectral parameters were computed for reference.

TDDFT calculations of the coupled excited states, UV absorbance and CD spectra were performed at the B3LYP/6-31++G**/PCM level. Since two planar rings can interact to form chiral pairs of chromophores, their computed CD is non-zero. The Trp side chains in the three examples studied were separated by 6.8-7.5 Å (measured between C9 positions on the Trp rings). In the case of W4W11 the tryptophans were 17 Å apart and, due to this long distance, did not couple strongly or show significant CD. The computed dipole and rotational strengths are plotted as vertical lines and the envelop corresponding to the sum of their overlapped band shape broadened components provide the absorbance and CD spectra as plotted for all interacting WW pairs in Figure 22. The basic features of most interest in the coupled CD spectrum are the negative couplet computed in the 190-230 nm region and the low energy negative peak in the 260-300 nm region. The intense couplet due to the coupling of the 1B_b transitions on each Trp is the important contribution in the former and in the latter the overlap of the 1L_a and 1L_b transitions dominate.

The W2W11 and W4W9 cases are similar (Figure 23) with both having a large -/+ couplet (with increasing wavelength) in the far UV and a weak negative band in the near UV, 260-300 nm region, as compared in Figure 23 (dash-dot red and solid black lines, respectively). This same spectral pattern probably arises because W2W11 and W4W9 each have indole moieties about the same distance apart with a relative angle of 80-90°, i.e. the rings are almost perpendicular.

The case of W2W9 is different (Figure 23). Two interesting features of the calculated spectra are the smaller 1B intensities in the far-UV CD, which are shifted to shorter wavelengths, and the positive CD computed for the near-UV 1L band. The distance between the indole rings in W2W9 is 7 Å and the angle between the planes is almost 50°, and the overlap is offset, being the largest

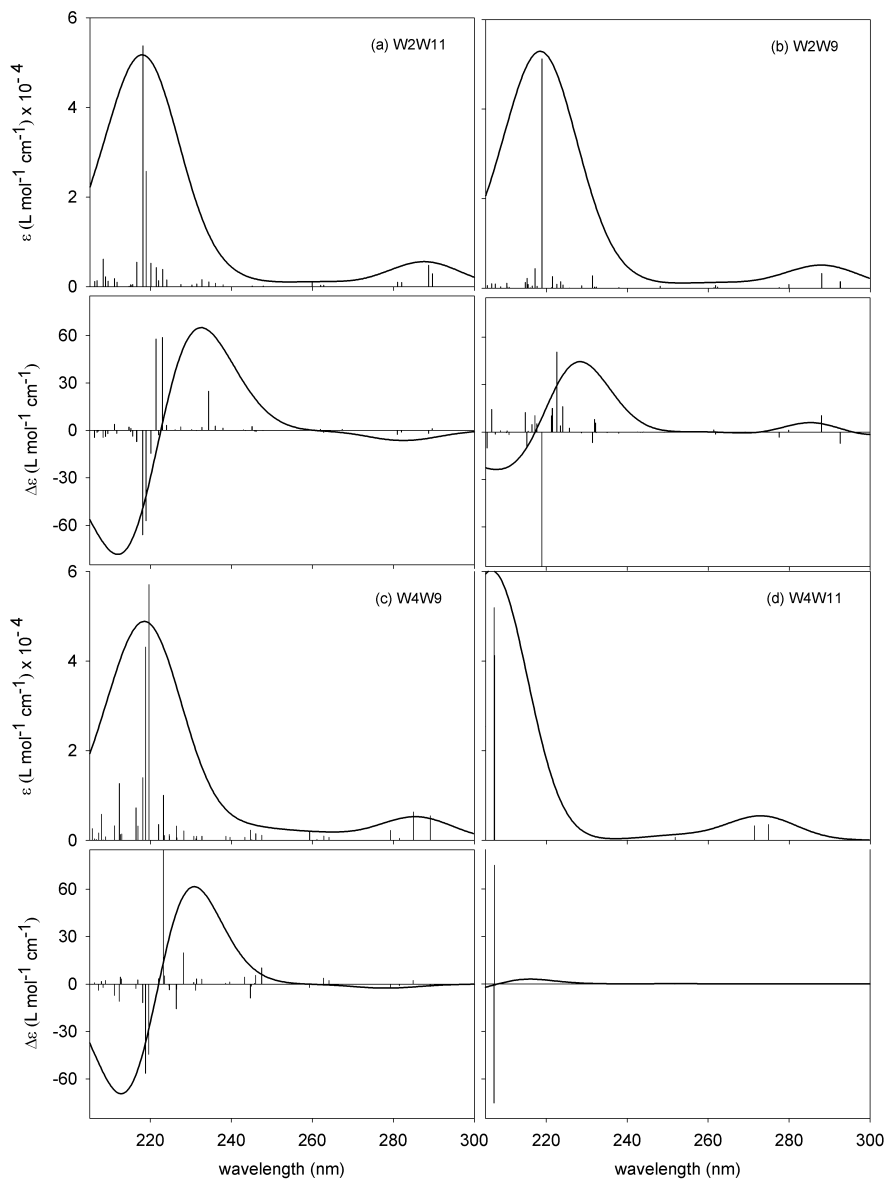


Figure 22: UV absorption and CD spectra computed for the all the two-indole pairs studied: vertical lines indicate the relative TDDFT/B3LYP/6-31++G** (W4W11 at B3LYP/6-31G**) computed dipole strengths (top panel) and rotational strengths (bottom panel) for (a) W2W11, (b) W2W9, (c) W4W9 and (d) W4W11.

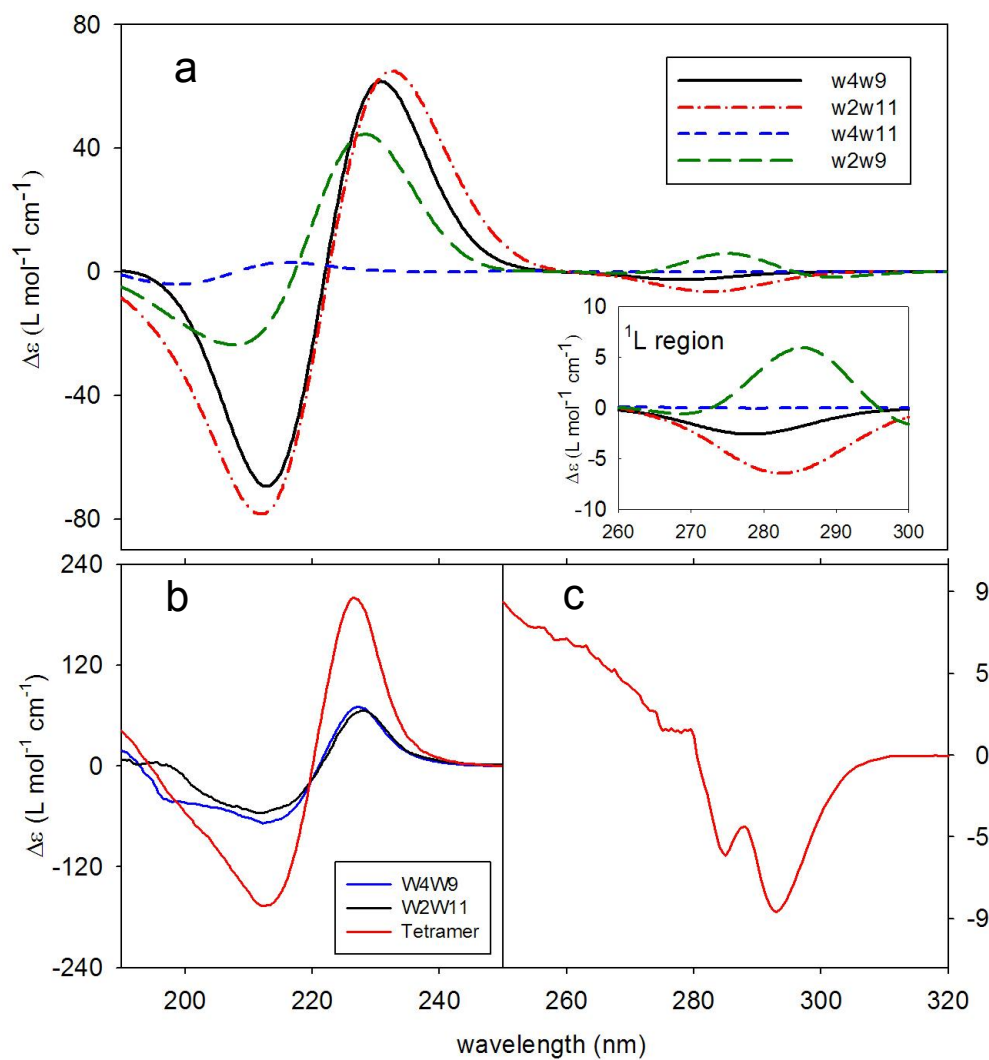


Figure 23: (a) Calculated CD spectra for the selected pairs of indoles: W4W9 (solid line), W2W11 (dot-dashed line), W2W9 (long dashed line), and W4W11 (short dashed line), plotted as the sum of components with FWHM=20 nm, computed at B3LYP/6-31++G**/PCM level (W4W11 at B3LYP/6-31G**). The inset shows a magnified view of the ¹L region. (b) Experimental far UV CD spectra for Trpzip1 (green dash) and Tyr substituted mutants containing two only Trps, data are replotted from Takekiyo et al (67) (note scale difference), and (c) for the near UV of Trpzip2, replotted from Huang et al(119).

between the five member rings on each indole rather than from the 6-member ring edge to the five member ring face as seen in W2W11 or W4W9.

For the far separated Trp pair, W4W11, the computed ECD was very weak with the 1B transition shifted up in energy, reflecting the monomer value. Separated by 17 Å, these indoles couple only poorly, so that transition energies are roughly equivalent to the indole values and weak CD is computed.

4.3.3 Trpzip2: four coupled indoles model

Finally, CD resulting from interactions of all four Trp side chains in the Trpzip2 NMR structure were simulated using four 3MI molecules, oriented as shown in Figure 19. The resulting geometry was used to calculate CD with Turbomole (which facilitated calculations on larger systems), and the molecule was modeled in vacuum for added computational stability. To compare these four Trp results more directly to the two Trp containing cases (Figure 23) we recalculated the spectra for the W2W11, W4W9, W2W9 and W4W11 pairs of indoles, this time also using Turbomole (B3LYP/6-31G**) and the vacuum approximation for consistency. Figure 24 shows the computed CD for four indoles interacting in the Trpzip2 geometry as compared with that for just two indoles (W2W11) and for the sum of the four pairs. The main features of the full four indole case are similar to those of the two indole W2W11 case, namely a weak negative band in the 260-300 nm region and intense 1B transitions forming a CD couplet in the far UV.

The computed bands are shifted up in frequency from those in Figure 23, due to the lack of solvent and diffuse functions (shown in Table XIX) and the sum of the four pairs has a larger intensity, particularly in the negative 1B_b band, than does the full calculation. The 1L bands in both cases have similar intensity negative CD, which might not be expected by simply adding the spectra in Figure 23. The W2W9 contribution in W2W4W9W11 must tend to cancel some of the negative CD

from the 1L transitions in W2W11 and W4W9, which explains the near agreement of all three near UVCD spectra in Figure 24. On the other hand, the 1B CD in the far UV is much stronger in the Trpzip case as all the indole 1B transitions have the same sign and the contributions of the various pairs tend to add up. The couplet shape is however different, being less conservative, since the lower energy positive band for four indoles is $\approx 2.5\times$ more intense than for W2W11 and shifted up in energy, while the higher energy negative band is only slightly more intense, but again is also higher in energy for W2W4W9W11. This is not a simple addition of four pairs overlapping as seen by the CD of the sum of pairs as compared to the Trpzip2 (four indole) case, but the sum does have a smaller negative than positive lobe for the 1B_b couplet. There is a positive CD band computed at ≈ 180 nm, which may be seen here due to a different cutoff in the excited state computations of the four indole calculation and which, by overlap of bandshape, could contribute to the lower intensity in the high frequency (low wavelength) component.

4.4 Coupling analysis

Tryptophan residues provide important probes of structure for various spectroscopic techniques including UV absorbance, fluorescence, IR, Raman and CD. In this work we have probed a set of structures and their electronic transitions that give rise to the characteristic ECD bands for coupled Trp side chains. This study has taken a focused point of view in using just the Trp side chain geometries, from a set of tryptophan zipper molecules because it was originally targeted at explaining a specific chiroptical observation, the large couplet CD in the far UV spectra of the Trpzip peptides. This was of interest, since the CD of these is available in the literature and has been an important part of using chirality to understand the peptide folding mechanisms for modeling β -structure formation mediated by hydrophobic collapse.

The calculations were initiated by focusing on a single indole, and extended to a methyl substituted indole (3MI) to develop an understanding of the impact of our computational schemes on the basic electronic $\pi \rightarrow \pi^*$ transitions and their spectral properties. Once established, we computed spectra for two coupled indoles constrained to various conformations found in Trpzip2 and finally we considered all four indole side chains corresponding to the full Trpzip2 aromatic residue structure, all computed at the TDDFT level.

While this approach was, of course, designed to refine our methods and provide an interpretive basis for the final model calculation results, it also has a firm relationship to experimental results. Several series of related Trpzip peptides with varying numbers of Trp residues have been synthesized. This was done for the purpose of developing improved understanding of aromatic vs. hydrophobic interactions in stabilizing these hairpin structures. In particular, Ling Wu, Rong Huang and Takahiro Takekiyo have previously prepared and discussed CD and IR spectra for a series of mutated Trpzip2 and Trpzip1 molecules that are substituted by either Val or Tyr for Trp to create structures with the substitution patterns represented here as W2W11 and W4W9 (127; 67; 119).

CD from all these mutated Trpzip hairpins showed similar qualitative patterns, four interacting Trp side chains in each case had far-UV CD that was much more intense than the CD for the two interacting side chains. All of these Trp containing, folded peptides gave the same couplet pattern in their far UV-CD, with a positive band that was lower in energy and more intense than the high frequency negative band. The quantitative aspects did vary depending on Tyr or Val substitution and did depend on the basic structure that was used: Trpzip2 or Trpzip1, but the qualitative pattern of the Trp transition CD was consistent.

After convolving the overlapped TDDFT transitions, the calculated magnitudes of the envelopes were in good agreement for W2W11 with the observed spectra (compare Figure 23a and Figure 23b)

with a peak to peak $\Delta\epsilon$ of $209 \text{ L mol}^{-1} \text{ cm}^{-1}$ for the vacuum calculations, $141 \text{ L mol}^{-1} \text{ cm}^{-1}$ for the PCM corrected ones and $48 \text{ L mol}^{-1} \text{ cm}^{-1}$ for the experiment. These values more than double for the Trpzip2 (four Trps) structure, as are compared in Figure 24. Obviously these values were very sensitive to bandwidths chosen, but the overall agreement is clear. Since the difference in the far UV CD between four and two Trps in a hairpin was greater than 2, both theoretically and experimentally, simple additivity was insufficient to explain the observed exciton chirality.

Where measured, the 1L transition in the near UV gave a weak negative CD that has some structure and collapsed upon unfolding with the same thermal behavior as characteristic of the collapse of the far-UV couplet at high temperatures (119). As shown in Figure 23c (in this case for Trpzip2), the 1L_a , 1L_b transitions yield negative CD of about $\Delta\epsilon = -8.5 \text{ L mol}^{-1} \text{ cm}^{-1}$ and in vacuum calculations were computed to overlap to yield $\Delta\epsilon \approx 216$ as shown in Figure 23 and Figure 24.

The TDDFT calculations presented here confirmed the origin of these observed CD in the coupling of the indole side chains of Trp. They further showed that the W2W11 and W4W9 coupled CD should be similar and overlapping in frequency, both being more intense than the W2W9 CD. However, computations indicate that the latter should not be particularly weak, which provides evidence that the W2W9 peptide studied experimentally lacks CD due to its being unfolded (disordered) and that its CD is not due to a lack of side chain interaction (if the folded W2W9 conformation were maintained). This also provides an explanation of why the Trpzip2 or Trpzip1 ECD spectra are more than twice as intense as that of either W2W11 or W4W9 (see Figure 23). In the stable folded Trpzip2 or Trpzip1, the W2W9 interaction would contribute with the same sign to the far UV ECD but with a weaker couplet shifted to higher frequency. This interaction contributes to the Trpzip2 intensity, resulting in more than a doubling over the two-Trp case, but also tends to make the shape less symmetric, have a broader and weaker high frequency negative component, which is seen in

our four-Trp calculations and is consistent with what is observed experimentally. On the other hand, our calculations indicate that the long range W4W11 interaction should have negligible contribution to the observed CD, even for the fully folded Trpzip2.

By contrast, the near UV situation is more complex, the W2W11 and W4W9 both have low energy negative contributions but the W2W9 interaction has the opposite sign due to the change in relative orientation of the two rings. This explains why the computed negative CDs for the four indole case and the two indole case (W2W11) are of about the same intensity (Figure 22). However they do remain quite sensitive to basis set and solvation model.

Ring orientation is the basic structural parameter explored by exciton coupled CD. Our calculations showed that when the Trp rings were held at predetermined inter-planar angles, the CD obtained varied both in amplitude and in sign. These computations are difficult to quantify, since variation in the relative twist of the rings, as well as inter-planar angle can change the coupling distance and are not independently controlled. However, the results do show that both the peak position and the peak intensity are quite angle sensitive.

The orbitals were analyzed to interpret the basic features of the states contributing to the CD spectra (Figure 25). The negative band in the 270-300 nm region is due to the 1L_a $\pi \rightarrow \pi^*$ transition, as would be seen in polar solvents (modeled here implicitly), and 1L_a is more intense than 1L_b . Although the experimental 1L_a appears to have fine structure, this would not be seen in the calculated spectra which do not include any vibronic coupling (146). The negative-positive couplet in the 190-230 nm region can be interpreted in terms of coupling between the 1B_b transitions on each indole (146). These are $\pi \rightarrow \pi^{**}$ transitions from the HOMO and HOMO-1 to higher unoccupied orbitals. The rotational strengths for the 1B transitions are calculated to be an order of magnitude more intense than for the 1L transitions, since the dipole strength of B transitions are

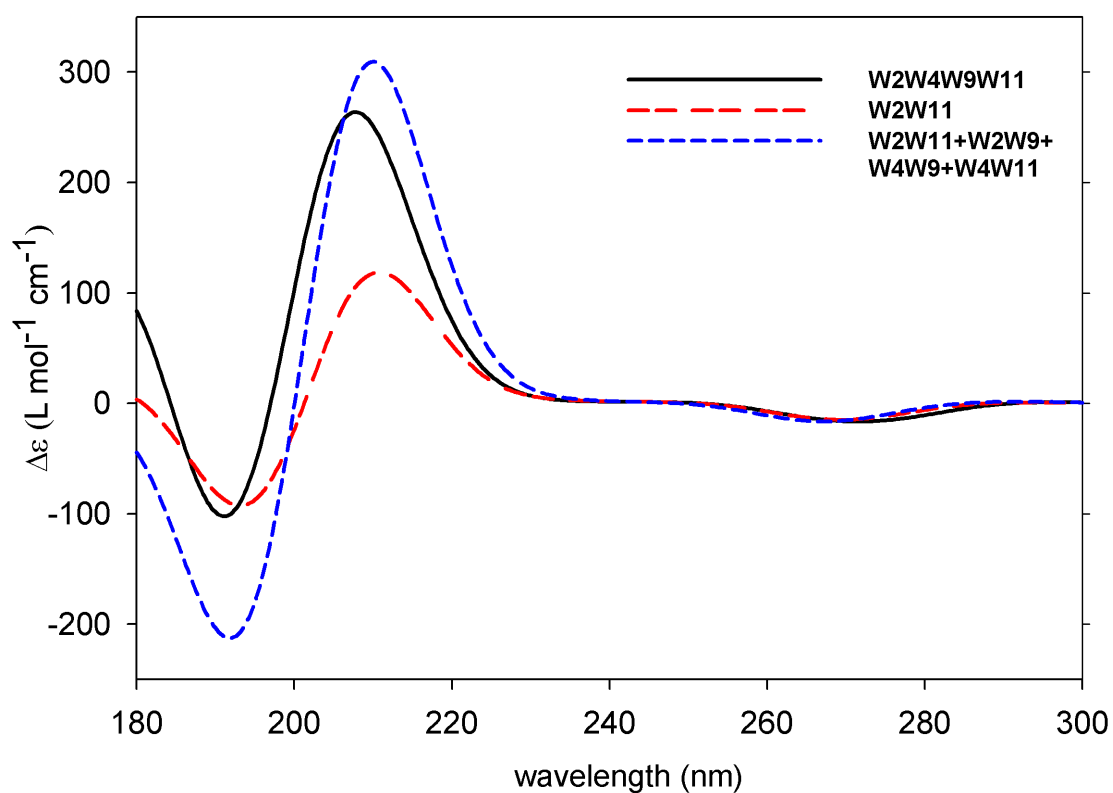


Figure 24: Comparison of the calculated CD spectra for two (W2W11, red, dashed line) and four tryptophans (W2W4W9W11, black, solid line), and the summation of all four of the double mutant calculations (W2W11+W2W9+W4W9+W4W11, blue, short- dashed line). Calculations were done using the B3LYP/6-31G** level (smaller basis set and no solvent correction), which results in a blue shift as compared to Figure 23.

much greater than those of L transitions (see Table XVIII and Equation 4.2) . For a single indole, even if it were in a chiral environment, the 1B_b would give a relatively weak CD response, although the 1L transitions do couple to their environment and yield diagnostically useful CD (126).

It is important to recognize that these calculations have a primarily qualitative value. In this case the frequencies observed for the near- and far-UV transitions are in exceptionally good agreement with the calculational results but the quantitative aspects are quite dependent on the basis set and functional used, as shown in Table XIX. The basis set effect is especially evident in comparing the computed spectra in Figure 23, where W2W11 has a positive band at 235 nm (negative at 215 nm), with those in Figure 24, where this W2W11 band appears at 212 nm (negative at 190 nm). The latter was calculated for a molecule in vacuum with a simpler polarized basis set, while the former is corrected for solvent (PCM) and used a diffuse basis set. Experimentally these transitions are found at 227 (+) and 213 (-) nm in Trpzip2 and W2W11 and W4W9, suggesting the 6-31++G**/PCM approach is a much better choice for our computations.

4.4.1 TDDFT vs TDC results

The qualitative pattern for the far-UV exciton coupled CD can also be modeled using semi-classical transition dipole coupling (TDC) for the component splitting and degenerate coupled oscillator (DCO) methods for their rotational strengths. As has been noted by others, the strong 1B_b transition has a dipole moment located along the long axis (passing through C2 and bisecting the bond between C5 and C6) of the indole moiety and the 1L_a and 1L_b transition dipoles are oriented roughly 45° off that direction as shown in Figure 20 (135; 136; 147). To model this interaction more completely, we chose a multidipole coupling method, summarized above in the Methods section, making use of our TDDFT computed dipole moments for the indole (3MI) monomer transitions as given in Table XVIII. Figure 26 shows that this classically modeled far UV CD provided the same

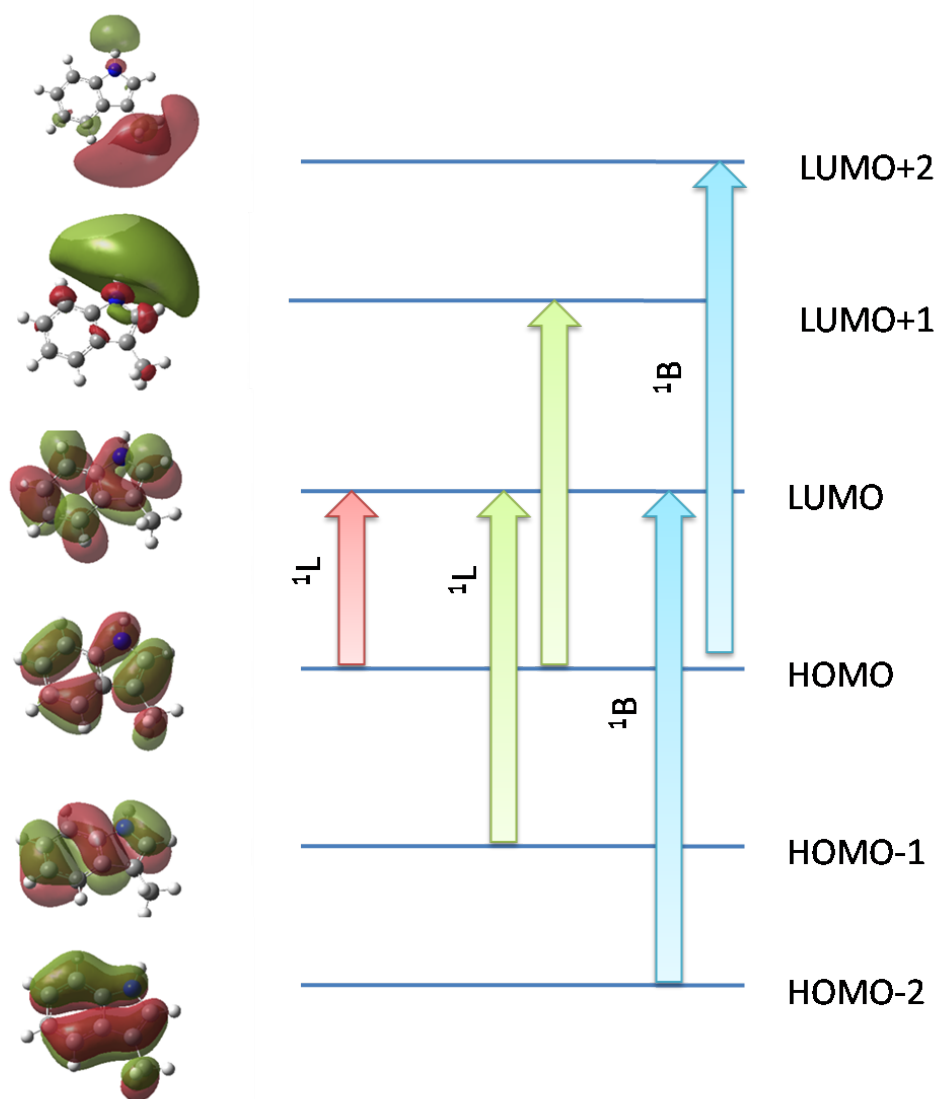


Figure 25: Orbital analysis of the transitions corresponding to the observed transitions

qualitative sign pattern for W2W11 and W4W9 as well as for W2W4W9W11. The near-UV CD of the 1L transitions is computed to be weak in the TDC-CO model, particularly with respect to the 1B_b couplet, and changes by a factor of about two from W2W11 to W2W4W9W11 but still are comparable to our experimentally observed value (119). On the other hand, the 1B couplet results with the TDC-CO model yield CD bands about twice as intense as those calculated with the TDDFT method and similarly much larger than seen experimentally, particularly for the four-Trp, Trpzip2 model as shown in Table XX. This may be due to a different dispersion with just dipole coupling or to other factors. However, it is clear that the couplet results primarily from coupling of the 1B transition dipole on each chromophore through the characteristic Trpzip2 edge-to-face indole geometry. If the angles are distorted from perpendicular, the CD magnitudes decrease.

4.5 Tyrosine and tryptophan coupling : TDDFT

This study was largely confined to studying the CD spectra due to the coupling of degenerate transitions on Trp molecules (modeled by 3MI). To extend that to non-degenerate transitions, I modeled Tyr-Tyr and Trp-Tyr calculations using TDDFT following a series of molecules that were experimentally studied by Ling Wu (128). Selected tryptophans on Trpzip2C were mutated to Tyr. For the computational study the Tyr side chains were represented by p-cresol, paralleling the method described above of using 3MI as a model for Tryptophan. In one mutant where the Trps on position 2 and 9 (Figure 19) are mutated to Tyr the peptide is notated as WYYW. The CD spectra for each pair of interactions $W2 \leftrightarrow W11$, $W2 \leftrightarrow Y9$, $Y4 \leftrightarrow Y9$ is calculated using TDDFT and is shown in Figure 27. W2W11 is a Trp-Trp interaction with the aromatic ring planes intersecting at 90° and consequently the calculated CD intensity is high, while for W2Y9 the Trp-Tyr results in a much smaller interaction. The Tyr-Tyr interaction in Y4Y9 displays a weak positive/negative couplet (going from lower to higher energy). While this may explain the a extra negative band observed at 185-190 nm in the

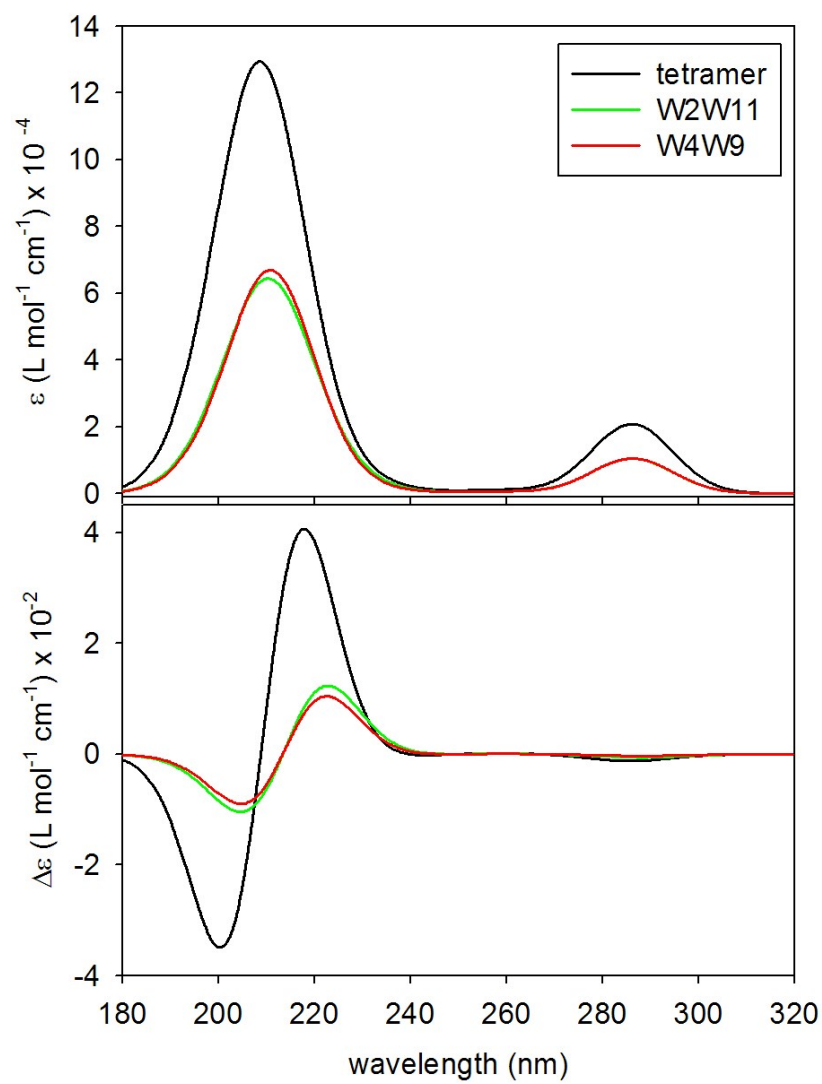


Figure 26: TDC-DCO modeled UV and ECD spectra for the tetramer, W2W11 and W4W9.

TABLE XX: Comparison of simulated CD spectra with experimental results for TD-DFT and TDC-CO models.

		TDDFT/6-31G**		TDC-CO		Experiment	
model	transition	wavelength nm	$\Delta\epsilon^a$ $\frac{L}{mol\ cm}$	wavelength nm	$\Delta\epsilon^a$ $\frac{L}{mol\ cm}$	wavelength nm	$\Delta\epsilon^a$ $\frac{L}{mol\ cm}$
W2W11	B	192	-92	203	-101	214	-72
	B	209	117	221	121	228	76
	L	270	-16	286	-5.5	-	-
Trpzip	B	190	-99	198	-337	212	-165
	B	206	261	217	406	220	226
	L	272	-16	285	-12	293	8.5

^a $\Delta\epsilon$ is the rotational strength of the transition.

experimental CD spectrum for WYYW (where this feature is observed at 195-200 nm) (128), the sum of the three modeled spectra (W2W11+W2Y9+Y4Y9) shows a positive feature instead. It is plausible that this error is due to the inability of the TDDFT calculation to accurately calculate the W2 \leftrightarrow Y9 interaction or more likely to correctly compute the relative energies of the indole and phenol excited states. Since this coupling analysis is credible only when supported by experiment, CD due to Trp-Tyr was not explored further.

4.6 Conclusion

The electronic circular dichroism of tryptophan side chains in a Trpzip peptide was modeled by TDDFT calculations for alkyl substituted indole rings. For a pair of indoles, the CD in the far-UV region, 190-230 nm, arises due to the coupling of the $\pi \rightarrow \pi^*$ (1B_b) transitions, which arise primarily from the HOMO, HOMO-1 to LUMO+1 and the LUMO+2 transitions. The simulated CD reproduces the intense negative-positive couplet in the far UV and the negative band in the near-UV region that were observed experimentally. This confirms that the intense far-UV CD in Trp-rich beta hairpins such as Trpzip are dominated by interactions of the Trp sidechain transitions without a significant contribution from the amide backbone transitions. Simpler dipole coupling models provide a similar qualitative picture for the electric dipole allowed 1B_b transitions, but magnitudes were not as directly comparable to the experiment and the CD arising from the 1L_a and 1L_b transitions are not predicted well with such classical models.

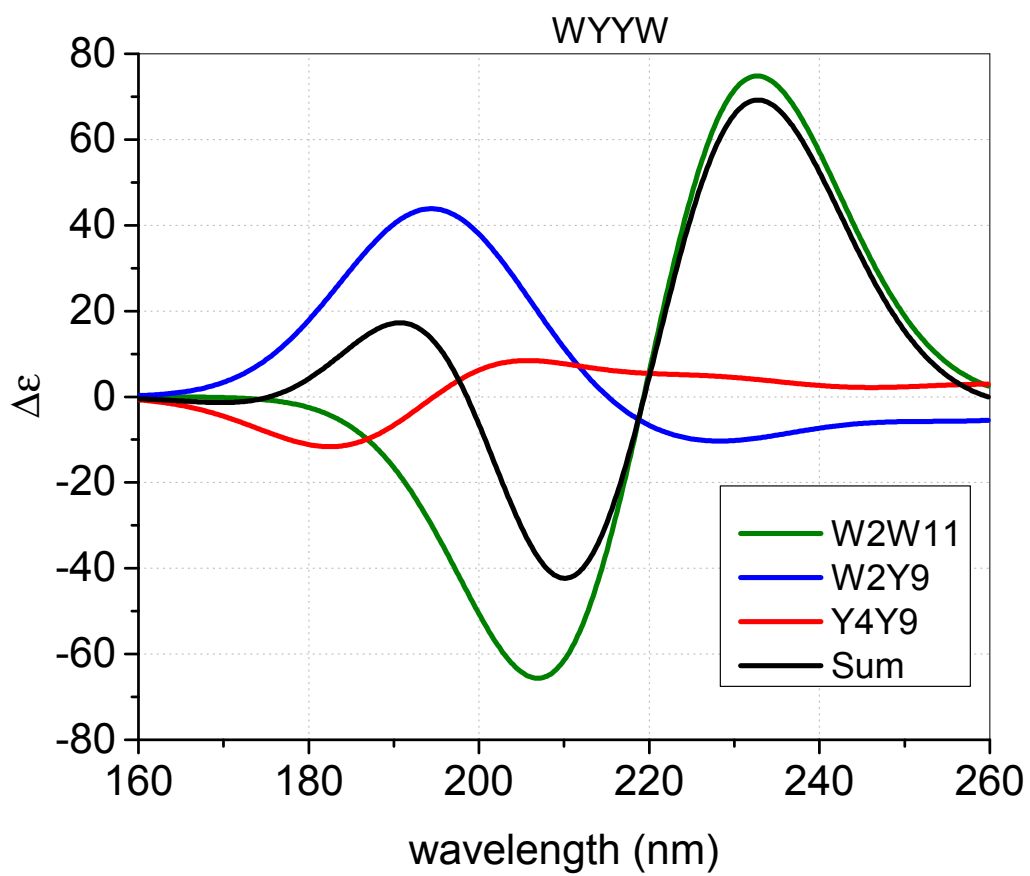


Figure 27: Calculated CD spectra for the selected pairs of tyrosines and tryptophans in WYYW, modeled using 3MI and p-cresol.

CHAPTER 5

OPTICAL TRAPPING AND RAMAN SPECTROSCOPY

5.1 Motivation

Raman activity was introduced in Chapter 1 and its theoretical prediction using quantum chemical computations was further discussed in Chapters 2 and 3. This Chapter expands on experimental aspects of Raman spectroscopy, focusing on a new technique that we have established in our group to study molecular vibrations in single cells, μm and sub- μm particles. We use the term Optical Trapping Raman Spectroscopy (OTRS) (148) for our design, however it is a nascent field and consequently the technique is also referred to by other acronyms viz. Laser Tweezer Raman Spectroscopy (LTRS) (149), Raman Activated Cell Sorting (RACS) (150) and Single Cell Raman Spectroscopy (SCRS) (151).

Our motivation for this project has three aspects. The primary motive is to use Raman spectroscopy to study conformational changes in proteins in single vesicles or cells. Another is to reduce the amount of analyte required to collect spectra. The last motive is to explore the possibility of protein conformational changes while applying mechanical forces to cells.

The chapter opens with an overview of Raman spectroscopy and why it is amenable to coupling with microscopy and hence also couples well with optical traps. Next, I introduce the phenomena of optical tweezing and in the last section deal with aspects regarding quantification of the trapping force.

5.2 Raman Spectroscopy

When interacting with matter, light may be absorbed, reflected or scattered. While scattering phenomena are of various types, most of any scattered light is scattered without any change in its energy (elastic scattering). Examples of this are Mie and Rayleigh scattering, which are sensitive to particle size and shape, but not to molecular structure. Inelastically scattered light is also of two types, Brillouin and Raman, and of these only Raman gives insight into molecular vibrations.

5.2.1 Chemical information from Raman

Prior to reviewing the principles of Raman spectroscopy, it is useful to review a few applications of Raman. Raman yields a molecular fingerprint of the intrinsic composition of the sample being studied. Its simplicity and portability give rise to many applications: some exotic, like mechanical stress in silicon integrated circuits (152), temperature monitoring of the upper atmosphere (153) and detecting counterfeit art (154; 155) to name a few.

When the chemical composition of the excited molecule changes, its Raman spectra changes too. To exemplify, Figure 28 shows characteristic Raman shifts for various organic chemical moieties. Most of the useful chemical information lies in the 1000 to 2000 cm^{-1} region, also known as the fingerprint region.

Our interest is in biological molecules like proteins and lipids. These large molecules are comprised of smaller moieties as shown in Figure 28 and conformational changes of the larger biomolecule results in changes in Raman shifts or changes in the band shape. Raman spectroscopy is sensitive to conformational changes in proteins (157) and lipids (158). In Chapter 3, calculations of amide band shapes associated with peptide secondary structure were shown to be in good agreement with experimental data. This also brings us to an important aspect of vibrational and Raman spectroscopy: The spectral signature can be computationally predicted with quantum chemical

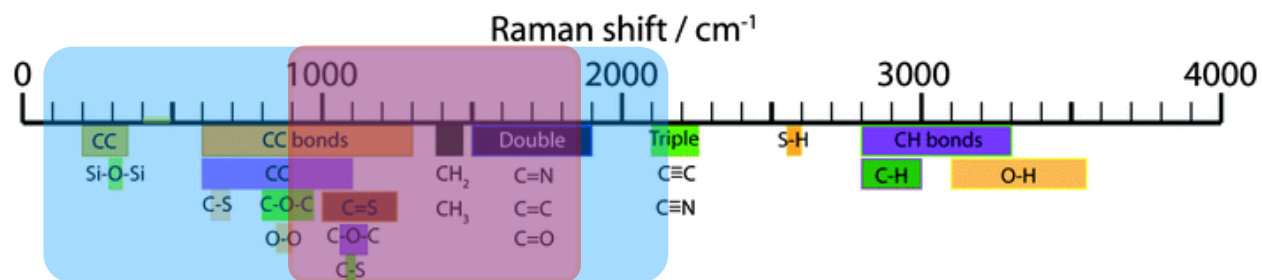


Figure 28: Common Raman shift regions for organic molecules. The blue square represents the range of frequency shifts that are accessible using the low frequency grating in our lab. The red region is the fingerprint region. (adapted from Chrimes et al (156))

theories like DFT. While not exclusive to Raman, it is indeed one of the few spectroscopies where good match between theory and experiment is possible.

Raman spectroscopy can be used for identification of live intact microorganisms and cellular tissue (159). However, due to the multitude of chemical species that are present in a cell, spectra from different species are hard to discern from each other and the use of multivariate analysis (MVA) to analyze such spectra is essential (149; 160). This method has been coupled with microfluidics to discriminate and collect cells in flow cytometry (161).

5.2.2 The Raman effect

Raman spectroscopy is based on the inelastic scattering of photons by molecular vibrations, known as the Raman effect (162). It is a two photon effect, which can be viewed as one photon exciting a molecule to a virtual (superposition of excited states) state and another photon emitting when the molecule relaxes to the excited vibration. However, this is more a model for description of the scattering process since the virtual state is not a steady state of the molecule, and exists only as a superposition of excited states due to a short lived distortion of the electron cloud stimulated by

the oscillating electric field of the light beam (163). Figure 29 illustrates that a molecule can relax with the scatter of another photon with an energy that is shifted from the incident photon energy. At room temperature, molecules are mostly in their ground vibrational state, and due to the lower population of the excited vibrational state, the fraction of incident photons that lose energy to a vibrational mode (Stokes shift) is much higher than the fraction that gain energy from a populated excited vibrational mode (anti-Stokes shift). An overwhelming majority of applications using Raman spectroscopy are focused on Stokes shifted Raman, ours being no exception.

This type of scattering experiment has the minimal requirements of: monochromatic light source for excitation, sample, an energy discriminator for the scattered light, and a suitable detector (see Figure 30). In fact, in 1928, Krishnan and Raman discovered the Raman effect using this basic design. Aided by a few lenses and a blue filter, they used sunlight to excite the sample. The sample was a neat solvent and a yellow filter was used to block the unshifted Rayleigh scattered light and discriminate the Raman scatter with the human eye used as a detector. At the time however, Raman spectroscopy was not feasible as a practical research tool due to its being a feeble effect, as C. V. Raman correctly stated (162).

In a classical treatment, the scattered intensity (I_{stokes}) of a Stokes shifted normal mode is given as,

$$I_{stokes} \propto \left(\frac{\partial \alpha}{\partial Q_i} \right)_0^2 \cdot (\omega_0 - \omega_{Q_i})^4 \cdot E_0^2 \quad (5.1)$$

where the first term on the right hand side is the change in molecular polarizability with change of nuclear coordinate along the normal mode, Q_i being considered. The second term is the difference between the energy of the normal mode (ω_{Q_i}) and the incident light (ω_0) and E_0 is the electric field associated with the incident light. The use of lasers as excitation sources in the late 1960s provided

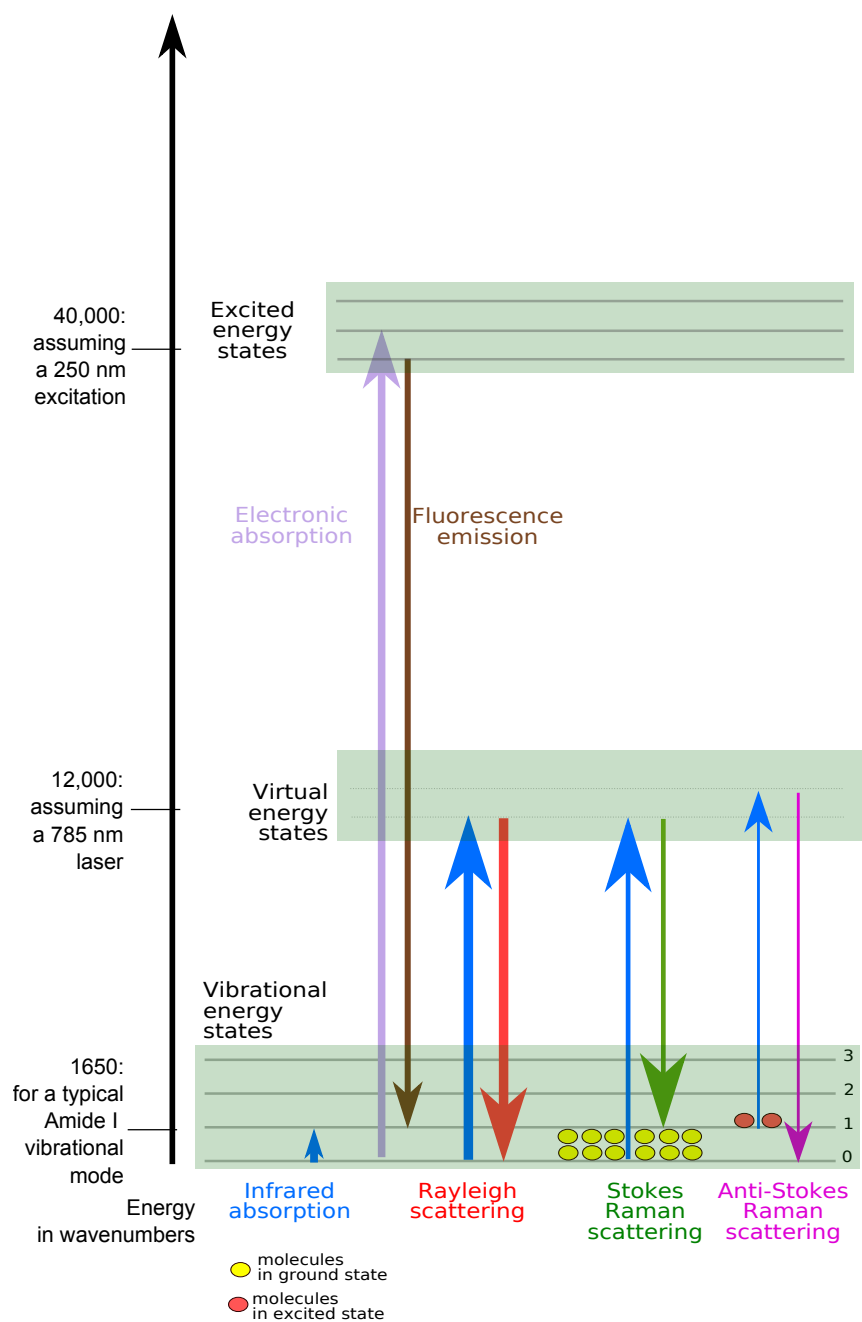


Figure 29: Energy levels associated with scattering and fluorescence. The energy axis values are typical for molecules studied and our instrument parameters (see text for details). Adapted version of original illustration by Moxfyre and used under a Creative Commons Attribution-ShareAlike license.

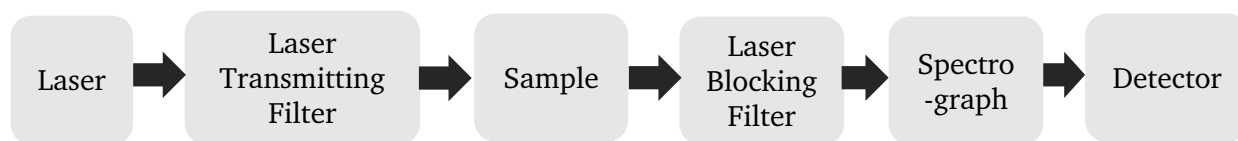


Figure 30: Basic Raman spectroscopy experimental design. The original experiment by Raman and Krishnan in 1928 was similar except they employed sun light as the excitation source and did not discriminate the frequencies of the scattered light beyond blocking the excitation (Rayleigh scatter)

the first revolution in Raman spectroscopy due to the dramatic increase possible in the E_0 term in in Equation 5.1.

5.2.3 Infra-red vs. Raman

Essentially, Raman is vibrational spectroscopy in or near the visible spectral region. Infrared spectroscopy also probes molecular vibrations and it does so with much enhanced sensitivity as absorption can be viewed as 10 orders of magnitude stronger than Raman if they are compared on the basis of relative cross section (see Table XXI). It is then reasonable to justify the need for Raman spectroscopy.

TABLE XXI: Transition cross sections of various processes

Phenomena	Transition cross section per molecule
Absorption	10^{-16} cm^2
Fluorescence	$10^{-18} \text{ cm}^2 \text{ sr}^{-1}$
Rayleigh	$10^{-28} \text{ cm}^2 \text{ sr}^{-1}$
Raman	$10^{-30} \text{ cm}^2 \text{ sr}^{-1}$

The primary reasons for the use and growth of Raman spectroscopy are simplicity and selectivity. Simplicity affects costs and convenience. Raman requires a monochromatic source of light, not a broad band source as in dispersive or interferometric (FT)IR. With the advent of lasers, the problem of a low scattering cross section in Raman can be subverted. Lasers today are relatively small and low cost, and further, the lack of moving parts when used with multichannel detectors makes the entire instrument rugged and portable. It is imperative to mention that as concentration of analyte decreases and its complexity increases, the quality and sophistication of instrumentation required to detect Raman signal increases, as will be apparent in the next chapter.

Convenience arises from ease of sampling and therefore a higher throughput is possible. Many chemical and most biological samples are prepared in aqueous media and often most easily measured in glass vials and cuvettes. Both glass and water show low Raman scattering but high IR absorbance. Samples for Raman, can therefore be studied without much sample preparation (for an exception see Section 5.2.4).

IR and Raman often are viewed as being complementary, since Raman is more sensitive to vibrational modes with a large change in polarizability, while IR is more sensitive to vibrational modes associated with changes in dipole moment. Selectivity can also be enhanced using resonance enhancement, where the certain chromophores of the molecule are excited to real excited states and vibrational modes associated with the chromophore are enhanced (164).

With the help of enhancement mechanisms like surface enhancement (SERS), Raman sensitivity can exceed that of IR. Using patterned surfaces that enhance the local electric field, SERS has been measured for single molecules (165). Tip enhanced Raman spectrometry (TERS) also exploits this enhancement phenomena, where Raman is coupled with atomic force microscopy to gather Raman spectra with high spatial resolution, beyond the diffraction limit (166).

5.2.4 Fluorescence interference in Raman

Fluorescence interference becomes a source of concern if the incident photon excites a molecule to a real excited state rather than a virtual one. Table XXI lists the transition cross sections associated with various light-matter interaction phenomena and shows that fluorescence is a much stronger effect (i.e. larger cross section) than Raman, and the presence of even nanomolar amounts of a fluorophore can completely overwhelm the Raman signal.

The virtual state energy is dependent on the excitation laser frequency while fluorescence energy levels are intrinsic properties of a molecule. Figure 29 illustrates that one way to mitigate fluorescence interference effects on Raman is to use a lower energy excitation frequency, one that does not provide the energy required to reach a real excited state. Our lab adopted the use of near-infrared (NIR) excitation at 785 nm (1.5 eV) (108) for Raman spectra, which is sufficiently low in energy to not excite fluorescence while yet allowing sufficiently sensitive (Si-based CCD detected) Stokes Raman measurements. The Raman signal with 785 nm excitation will be weaker due to its ω^4 dependence, as shown in Equation 5.1. The development of affordable NIR diode lasers in the mid 1990s started a second resurgence of Raman as an accessible (and even portable) research and process analytical tool. This coincided with the availability of sensitive array detectors like charged coupled devices (CCD) (167) which had high signal to noise ratio, ruggedness and other advantages inherent to multi-channel detection (168). All the aforementioned principles are incorporated into the system described in the next chapter.

5.2.5 Raman microscopy

Since Raman scattering is multi-directional, two standard geometries of collecting the scattered light have evolved in the Raman spectroscopy community, 90° excitation and 180° back scattering (Figure 31). For 90° excitation of optically clear solutions, a focused laser passes through the sample

and the profile of its beam waist in the sample is imaged onto the entrance slit of a spectrograph. Such a system was also constructed for routine measurements in our laboratory. A 180° sampling geometry allows for sampling of surfaces, even for poor optical quality samples, and this geometry is amenable to microscopic sampling. Since scattering intensity scales with the number of scattering molecules, it might seem that Raman microscopy at 180° might be less sensitive than conventional 90° Raman. While it is true that the sampling volume is smaller in micro-sampling using 180° back-scattering, this is easily compensated by the intense laser focus and the improved collection efficiency of a high numerical aperture objective. The tight focus also allows for introducing confocality and thus rejecting off-focus light, which is essential when using oil-immersion objectives, as will be explained in Chapter 6.

This also highlights one of the advantages Raman microscopy has over IR: spatial resolution. While infrared radiation at $6\ \mu\text{m}$ is diffraction limited to roughly $3\ \mu\text{m}$, a $785\ \text{nm}$ excitation laser in Raman can be focused down to $\approx 400\ \text{nm}$. Raman spectroscopy coupled with confocal microscopy allows for chemical characterization of sample volumes down to about one femtoliter.

Despite the above improvements, acquiring Raman spectra of a dilute solution of complex biological molecules still remains a non-trivial task. In solvents with low viscosity, like water, a $0.5\ \mu\text{m}$ particle can diffuse out of the laser illuminated focal volume in about one second, and a single biomolecule, such as a protein, much faster (169). To collect sufficient signal in a reasonable time, the analyte needs to be at a concentration such that the population of the focal volume remains effectively constant, or if a larger particle is to be studied, it must be restricted to remain within the laser focal volume. One solution is chemical immobilization or fixation, which may lead to changes in the chemical micro-environment and is not reversible. Additionally, such fixation is not feasible for live cell work or for cases where a locomotion of the cells might be of interest.

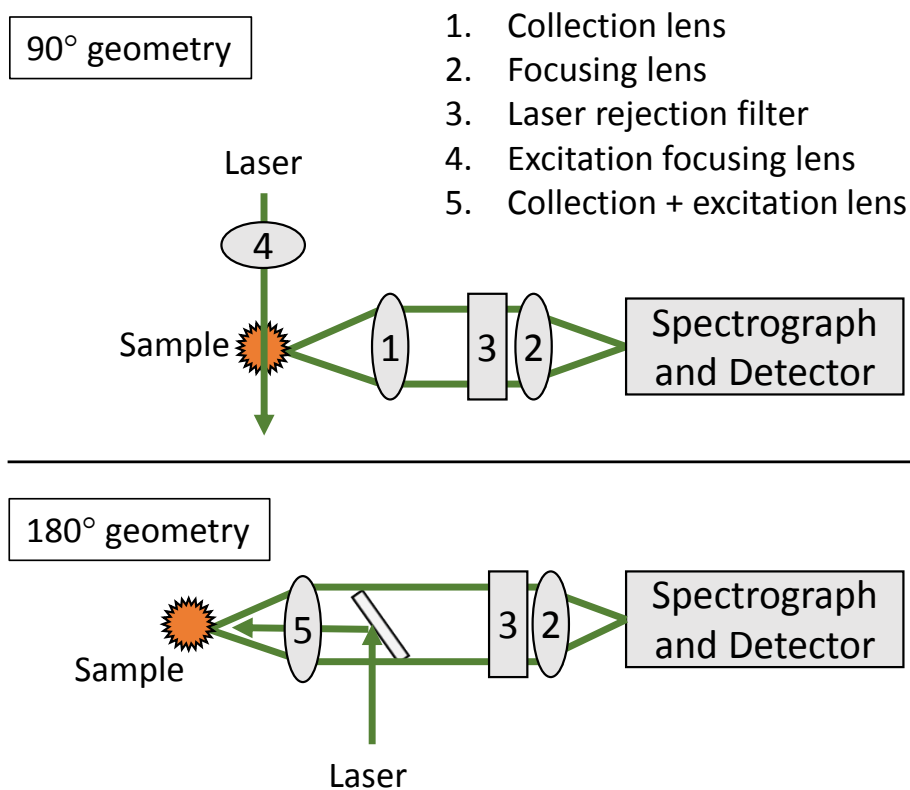


Figure 31: Two common experimental geometries, 90° (top) and 180° (bottom)

One viable method, especially for live cells, is optical fixing, which is immobilization using optical tweezers. Such immobilization affords a relatively non intrusive method. (170).

5.3 Optical Trapping Principle

While the photon momentum associated with light beams has little effect at the macro scale, tightly focused lasers can cause substantial optical pressure on μm sized particles. When a dielectric particle of higher refractive index than its surroundings encounters the focal region of a tightly focused laser, it experiences a potential that makes it “fixed” within the focus. The method of optical trapping was first developed by Arthur Ashkin at Bell labs, who in 1970 noticed that particles in a

laser beam were propelled forward with extremely high acceleration and, in addition, particles that were not in the beam were attracted to it (171). In 1987 he extended that to cells (172) and in 1997 his colleague Steven Chu received the Nobel prize for trapping cold atoms. By 2007 optical traps had even been implemented in undergraduate laboratories (173; 174) and commercial instruments not requiring any assembly are now available (175; 176). Trapping physics is usually described in terms of limiting pictures depending on the relative size of the scatterer to the wavelength of light used and is expanded upon in the next section.

5.3.1 Ray optics approach

A simple case to illustrate trapping, is that of a spherical dielectric particle, the diameter of which is much larger than the wavelength of the trapping laser ($d \gg \lambda_{trap}$). Examples of such cases would be bacteria (172; 177), polystyrene beads or giant unilamellar vesicles (GUV) (158). In such cases, a working intuition can be built on the basis of a ray optics limit.

A ray of light that enters a particle, with a refractive index other than that of the surrounding media, is bent by refraction and exits undergoing a change in direction. This changes the momentum associated with the incident light and, in accordance with Newton's third law, imparts an equal and opposite momentum to the particle.

Figure 32 illustrates that a particle in a laser beam with a Gaussian profile experiences a net force laterally towards the beam center due to the high intensity of the laser there, which results in a higher momentum transfer toward the center. If the beam is very tightly focused, as shown in Figure 32, then slightly below the focus all the lateral forces cancel out, and there is a net force towards the center. This axial gradient force cancels out the forward scattering force to form a trap that is stable in three dimensions.

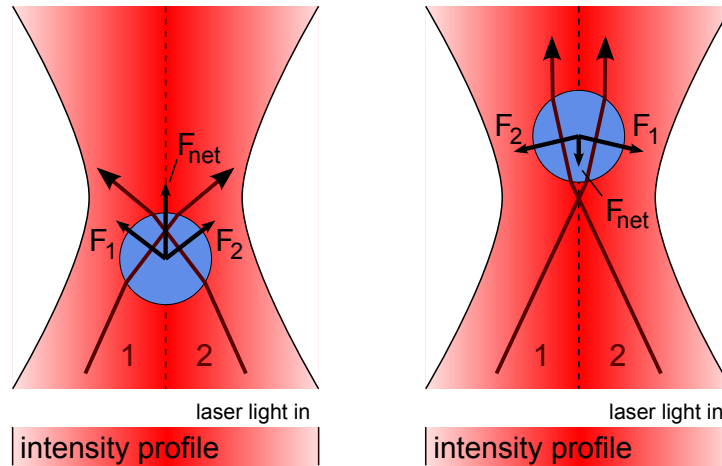


Figure 32: A ray optics picture of optical trapping. Adapted version of original illustration by Roland Koebler and used under a Creative Commons Attribution-ShareAlike license.

5.3.2 Rayleigh approach

If the trapped dielectric particle is much smaller than the laser wavelength used to trap it ($d \ll \lambda_{trap}$), then the particle might be considered as a point dipole (Rayleigh limit). Examples of this include trapping of gold nanorods (178) and nanoparticles (179; 180). Due to the refractive index mismatch between the particle and the media, light is refracted and therefore the momentum associated with light changes. To conserve momentum, the particle will move in the opposite direction. The optical forces in a trap can be resolved into a scattering force (F_{scat}), that pushes the particle away in the axial (propagation) direction and a gradient force (F_{grad}) that pulls the particle to the center of the beam. Figure 33 highlights the optical forces acting on a trapped particle.

The scattering force due to the absorption and scattering of the incident photons, also called the radiation pressure, is given as:

$$\vec{F}_{scat} = \frac{n_m}{c} C_{scat} I \quad (5.2)$$

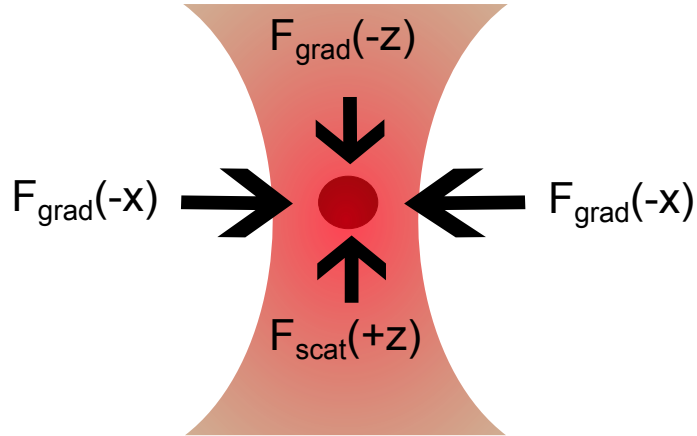


Figure 33: An arbitrary x-z cross section of an optical trap and a trapped particle that is stable in three dimensions. Due to the symmetrical Gaussian TEM₀₀ laser beam, the lateral gradient forces cancel out. The axial gradient force balances out the forward scattering force.

where c is the speed of light, n_m is the refractive index of the medium, I is the intensity of the incident light and C_{scat} is the scattering cross section (or the Rayleigh cross section if $d \ll \lambda$)

$$C_{scat} = \frac{8\pi}{3} \frac{r^6}{\lambda^4} \left(\frac{m^2 - 1}{m^2 + 2} \right)^2 \quad (5.3)$$

where n and r are the refractive index and radius of trapped particle respectively. m is the effective index of refraction, which is the ratio of the refractive index of the particle n to the refractive index of the medium n_m i.e. $m = n/n_m$.

The second force involved in the trap is the gradient force. Due to the gradient of the intensity $\nabla I (= \nabla E^2)$, a point dipole also experiences another force i.e. the Lorentz force (F) given as,

$$\vec{F}_{grad} = \vec{p} \cdot \nabla \vec{E} + \frac{1}{c} \frac{d\vec{p}}{dt} \times \vec{B} \quad (5.4)$$

where \vec{p} is the induced dipole moment, t is time and E and B are the electric and magnetic fields associated with the excitation beam. Conventionally the trapping laser has a Gaussian profile (TEM₀₀), hence this Lorentz force points towards the focus. Also, trapping is usually performed with a continuous wave (CW) laser where

$$\frac{\partial}{\partial t}(\vec{E} \times \vec{B}) = 0 \quad (5.5)$$

therefore the second term in Equation 5.4 averages to zero and the time averaged induced dipole moment \vec{p} relates to the electric field \vec{E} via the polarizability of the trapped particle α ,

$$\vec{p} = \alpha \vec{E} \quad (5.6)$$

and α depends on the relative refractive indices of the particle and the media as

$$\alpha = n_m^2 r^3 \left(\frac{m^2 - 1}{m^2 + 2} \right) \quad (5.7)$$

where n_m and m are the same as in Equation 5.2 and Equation 5.3 respectively.

The time averaged force $\langle \vec{F} \rangle$ is given as,

$$\langle F_{grad}^{\vec{}} \rangle = \frac{\alpha}{2} \nabla \langle \vec{E}^2 \rangle \quad (5.8)$$

and since the square of the electric field is proportional to the intensity of the light ($E^2 = I$),

$$\langle F_{grad}^{\vec{}} \rangle \propto \frac{\alpha}{2} \nabla \langle I \rangle \quad (5.9)$$

For most conventional situations the scattering force dominates the gradient force. However, near the focus of laser the gradient force must be considered. For stable trapping in three dimensions the restraining axial gradient force must balance the forward scattering force. For small particles $F_{grad} > F_{scat}$, due to the r^3 dependence of F_{grad} (Equation 5.7) vs. the r^6 dependence of F_{scat} (Equation 5.3) (169).

The two pictures described above, Rayleigh and ray-optics are sufficient to develop an intuitive understanding of the principle of optical tweezing. Since the size of the trapped particle in our experiment is close to the wavelength of the trapping light ($d \approx \lambda_{trap}$), neither the ray optics nor the Rayleigh picture are completely correct. This intermediate size regime is completely described by Mie theory, which also takes into account the fact that the scattering is not isotropic. Mie theory requires numerical computations, which is beyond the scope of this thesis.

5.3.3 Trap details

Another factor that affects trapping is the refractive index contrast, m , where as before, m is the relative refractive index (n_m i.e. $m = n/n_m$). To maximize the gradient force with respect to the scattering force, m should be in the 1.2-1.3 range. Typical values are shown Table XXII, according to which if we consider water as a solvent ($n_m = 1.32$), polystyrene beads have $m = 1.2$ while *E. coli* in water have $m = 1.05$. This suggests that, all other parameters being equal, trap stiffness for polystyrene is larger than that for *E. coli*, which is what we have experimentally observed.

For trapping in a fluid media we must account for effects due to the media. For a particle to stay trapped, the trap depth (the term “trap depth” here corresponds to the magnitude of the restoring force of the trap in units of force/distance) must be high enough to overcome the escape probability due to fluctuations due to Brownian motion. To maximize the trap depth, the intensity, $\langle I \rangle$, needs to be maximized. If the power of the laser is held constant (which usually is the case when operating

TABLE XXII: Refractive index of materials used in our studies.

Material	Refractive index (η)
Polystyrene bead	1.57
Oil (Cargille DF)	1.51
Glass (BK7)	1.51
Yeast	1.49
Oil (Cargille FF)	1.47
Quartz (Fused)	1.45
<i>E.Coli</i>	1.38
Water	1.32

low power diode lasers at their power limit), high $\langle I \rangle$ can only be achieved by reducing the laser beam waist, w_{trap} , at the focus.

There is a lower limit to the beam waist at the focus, which is governed by the diffraction limit of light. An ideal lens of focal length f focusing a laser beam with diameter, D , and wavelength λ_o causes a trap with waist w_o such that,

$$w_{trap} \geq \frac{1.22f\lambda}{2D} = \frac{1.22\lambda_o}{n_m} \sqrt{\left(\frac{n_m}{NA}\right)^2 - 1} \quad (5.10)$$

NA is the numerical aperture of the lens. A typical achromatic 100 \times , oil-immersion objective, like the one used in our experiment, has a NA of 1.25 and results in a theoretical limiting focal spot size of $w_o = [1.22(0.79)/(1.5)]\sqrt{(1.5/1.25)^2 - 1} = 0.42 \mu\text{m}$ for 785 nm light (173).

Another factor that should be considered is that the maximal gradient force is proportional to the polarizability of the trapped particle, α (179). Therefore while it may require a very high powered laser to trap polystyrene particles smaller than 50 nm, due to their higher amplitude

Brownian fluctuation, similar sized gold spheres have been successfully trapped owing to their higher polarizability (179). Recently, single gold nanorods as small as 18 nm have been trapped, albeit the laser intensity in this case was a few hundred milliwatts at the sample. (180; 178).

5.4 Quantitative measurements

While a well-aligned laser passing through a high NA objective is sufficient to form a trap, it gives no information about the external forces experienced by particle in the trap. For the trap to act as a force transducer it needs to be calibrated.

5.4.1 Position detection

Position detection can be done with video microscopy, but it suffers from very low bandwidth, .i.e. the frame rate for most cameras is much too slow for adequate time resolution of positional information. This method is therefore seldom used, unless a very high frame rate camera (usually with a CMOS sensor) is available.

Another method for position detection, that also provides for force detection, is the use of high bandwidth position sensitive detector like a quadrant diode photodiode detector (QPD). While backscattered laser light from a trapped object is used to acquire chemical information (Raman), the interference of the forward scattered light with the unscattered laser beam is used to measure the optical force exerted by the trap. This method, known as back focal plane interferometry (BFPI), depends upon the analysis of the Brownian motion of the trapped bead to measure forces (181; 174; 182)

In the BFPI method, the unscattered light from the laser and the forward scattered light by the trapped particle are collected by another lens, termed the condenser and interfere at the back focal plane. The image of the back focal plane is projected onto a position sensor using a relay lens. This method is insensitive to the position of the trap in the field of view of the condenser

lens but sensitive only to the displacement of the particle with reference to the optical trap. The displacement of the particle causes a change in the intensity pattern at the back focal plane image which is detected by the QPD.

5.4.2 Force calibration

One method to calculate the force being exerted on the particle is the equipartition method. Figure 34 illustrates that optical traps exert a harmonic force on a trapped particle, $\vec{F} = -\kappa\vec{x}$, where κ denotes the trap stiffness and \vec{x} represents the position of the particle with respect to the center of the trap.

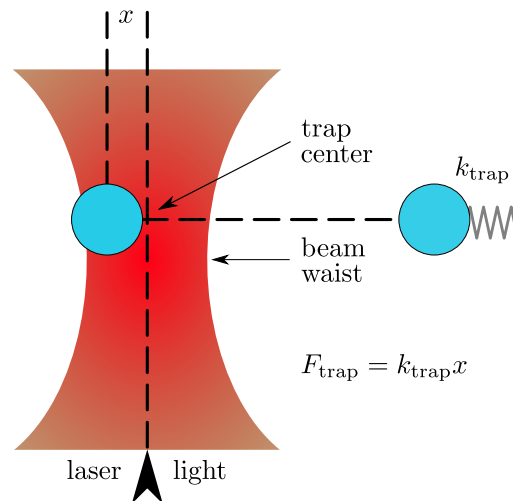


Figure 34: The principle of optical trapping. Adapted version of original illustration by R.Kobler and used under a Creative Commons Attribution-ShareAlike license.

The optical trap acts like a spring with a linear restoring force near its center. According to the equipartition theorem, the energy of a harmonically trapped bead in one dimension is $\frac{1}{2}k_B T$ and

the energy stored in a spring is $\frac{1}{2}\kappa(x - x_o)^2$ where κ is now the spring constant and $(x - x_o)$ is the displacement from center. The variance of the position $\langle x^2 \rangle$ is the time averaged displacement. Setting the energies equal we have,

$$\kappa = \frac{\langle x^2 \rangle}{k_B T} \quad (5.11)$$

Once the positional variance, $\langle x^2 \rangle$, has been ascertained, the trap stiffness κ can be calculated using Equation 5.11.

Another method, one that is considered more powerful, is based on the calculation of the power spectral density of the Brownian motion. In an optical trap, a particle undergoes diminished Brownian motion and the Brownian motion of the particle is given by the Langevin equation,

$$\beta \dot{x}(t) + \alpha x(t) = F(t, T) \quad (5.12)$$

where x is the position of the bead, $\beta = 6\pi\eta r$ is the drag coefficient of the bead, η is the viscosity of the surrounding fluid and r is the bead radius. $F(t, T)$ is a white noise term due to Brownian motion, which is dependent on both time (t) and temperature (T), and $\langle F \rangle_t = 0$. The first term in Equation 5.12 is the drag force and the second term is the trap force.

One solution of the Langevin equation is in the frequency domain. After squaring the Fourier transform of Equation 5.12, the power spectrum is obtained. If the system has been calibrated for detector response, i.e. a conversion from voltage on QPD to displacement (in nm) is performed, then the power spectrum $S_{xx}(f)$ has units of displacement²/frequency (nm²/Hz) and is given as,

$$S_{xx}(f) = \sqrt{\frac{k_B T}{\pi^2 \beta (f_c^2 + f^2)}} \quad (5.13)$$

where f_c is the corner frequency and β is the drag coefficient as before.

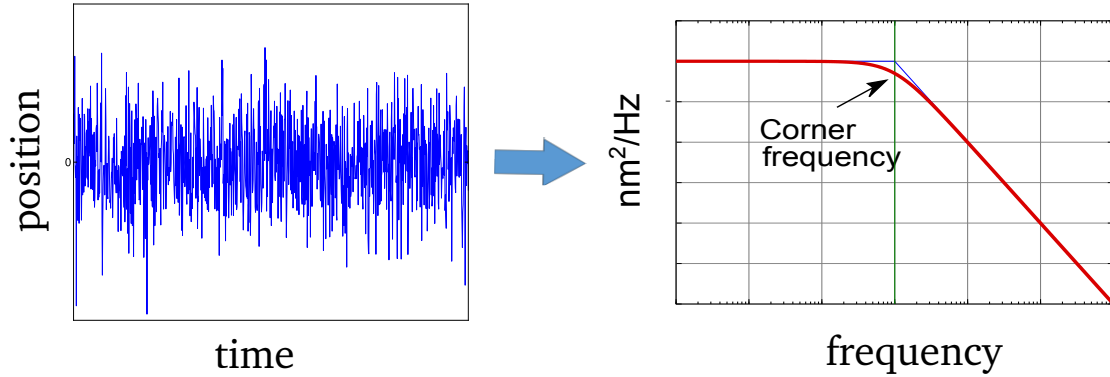


Figure 35: Force detection using the power spectral density method. Positional fluctuations of the trapped particle are detected by the a position sensitive detector. A power spectral density of the positional values in time results in the power spectral density. The corner frequency provides information about the trapping stiffness (see text).

The positional power spectrum, which has a Lorentzian form, has two distinct regions as shown in Figure 35. There is a plateau region comprising the slow frequencies and a region with a linear slope that represents rapid Brownian motion, which has been quenched by the trap (183). The corner frequency f_c , is the -3dB point of the power spectrum, where the signal power falls to 50% of its maximum, and can be related to the trap stiffness κ using,

$$f_c = \frac{\kappa}{2\pi\beta} \quad (5.14)$$

Thus by fitting experimental power spectral density data to Equation 5.13, the trap stiffness can be estimated (see chapter 7).

5.5 Optical Trapping Raman Spectrometry (OTRS)

As mentioned before, the criteria of a tight focus, provides for a natural convergence of the techniques of Raman microscopy and optical trapping. While some work in this direction was done as early as 1984 (184), most of the seminal work has been done in the past decade with applications in organelles (185) and cells (177). These studies were a direct consequence of technological achievements like the development of sensitive Raman detectors.

While both optical trapping and Raman microscopy are now mature, their coupling is a relatively nascent field. A few research groups are involved in developing OTRS and primary among them are the Dholakia group at St.Andrews, the Petrov group at the University of Barcelona, the groups of Chan and Huser at the NSF biophotonics center at UC-Davis, the Popp research group at Jena and the Li group at East Carolina University. Research in these groups primarily focus on single live cell characterization and cell sorting using Raman spectral signatures of individual cells. In addition, the Harris group in Utah uses optically trapped phospholipid vesicles to concentrate analytes for Raman analysis.

Due to the high numerical aperture (NA), the optical power density at the focus is in the MW/cm² range and a near-IR excitation wavelength is preferred for trapping, since absorption by biological components of cells is lower than in the visible (186). While such high power densities could still cause thermal degradation of the sample, since the trapped particle is usually in aqueous media, heat is dissipated into the surroundings without a substantial increase in temperature. Use of 785 nm also avoids absorption by the vibrational excitation of most water overtones in the near IR (187).

In the absence of flow, only a fraction of a milliwatt of laser intensity is required to trap a particle. However, moderate to high power density is essential to collect high signal-to-noise ratio Raman spectra. All Raman active elements in the signal path will contribute to the Raman scattering. This includes the glass cover-slip close to the sample and the immersion oil used with oil immersion lenses. Water immersion objectives can partly alleviate this problem, however they make for weaker traps due to lower numerical aperture (apart from their being substantially more expensive). These and other technical concerns are discussed in the next chapter, where the design and construction of the OTRS is detailed.

CHAPTER 6

DESIGN AND CONSTRUCTION OF A FORCE SENSING OPTICAL TRAPPING RAMAN SPECTROMETER (OTRS)

6.1 Objective

As introduced in the previous chapter, the goal was to design an experiment that would allow for the observation of molecular structural changes in cells while simultaneously measuring applied mechanical force. This translates to a device that is in essence a Raman spectrometer with the added functionality of being able to optical trap (172) cells and particles.

6.2 Design

Figure 36 shows the basic building blocks in our apparatus and provides an overview. Each element in the figure is a distinct and integral aspect of the design, they will be referred to as “channels”. The instrument was prototyped and developed on a passively damped optical air table (Newport). The air table damps any low frequency building vibrations (2-10 Hz) which might affect the trap (188), however the intended purpose of the optical table was primarily to facilitate rapid prototyping. While the field of optical trapping and Raman spectroscopy are independently mature, their integration is still relatively nascent. Therefore, the literature is not abundant with experimental designs that meet all our requirements. A majority of such integrated setups are based around suitably modified research microscopes (189).

When we initially pursued this idea and based our design around an inverted fluorescence microscope (Diaphot TMD, Nikon), we collected low intensity Raman spectra with poor force sensing. Research microscopes are essentially black boxes with multiple lenses and mirrors for

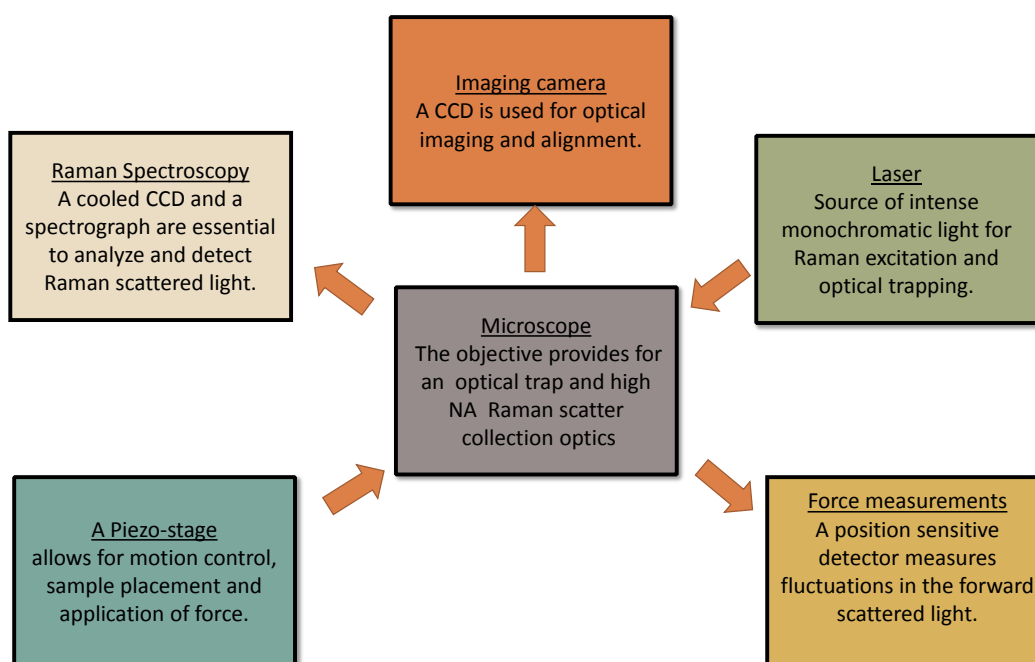


Figure 36: Outline of the basic building blocks of the OTRS. Arrows indicate the flow of information, the details are further expanded in Figure 37.

superior image quality. Our Raman setup is not intended for imaging a large field of view and these optics prove counterproductive, since the Raman scattered light is very low in intensity and optical image quality is not of prime importance. Additionally, microscope optics are coated for the visible and not for the near-IR and minor reflective losses over multiple optical elements lead to more significant signal loss. To maximize signal, our final design eliminated the commercial microscope, and instead we designed an integrated system that gives us control over the internal optical components. Our current design criteria center around minimizing optical elements and maximizing their performance at 785 nm, our choice of excitation wavelength.

6.3 Construction

This section details the construction of the OTRS instrument. A minimalistic “side-on” design was selected instead of the conventional inverted or upright microscope design. All components in this section and its subsections are diagrammatically represented in Figure 37 and listed in Table XXIII. In addition Figure 38 is a 3D CAD representation of the instrument, which gives some perspective on the relative spatial arrangement of optical components of the OTRS.

6.3.1 Microscope

The microscope is the key component around which the entire system is built. Ultimately, it is the numerical aperture (NA) of the objective that governs both the trapping efficiency of the trap and the collection efficiency of the Raman signal. A 100× oil-immersion achromat objective, OBJ1 (Nikon, 1.25 NA, ∞ corrected), is used to tightly focus a collimated laser to create the optical trap. A Nikon achromat objective was chosen due to its longer working distance of 0.23 mm. A Delrin[®] adapter was machined in-house to mount the Nikon objective on a cage mount, while thermally isolating the objective from the rest of the instrument. The objective was threaded onto a cage cube (C6B, Thorlabs) with its optical axis parallel to the optical table, as shown in Figure 38. The center

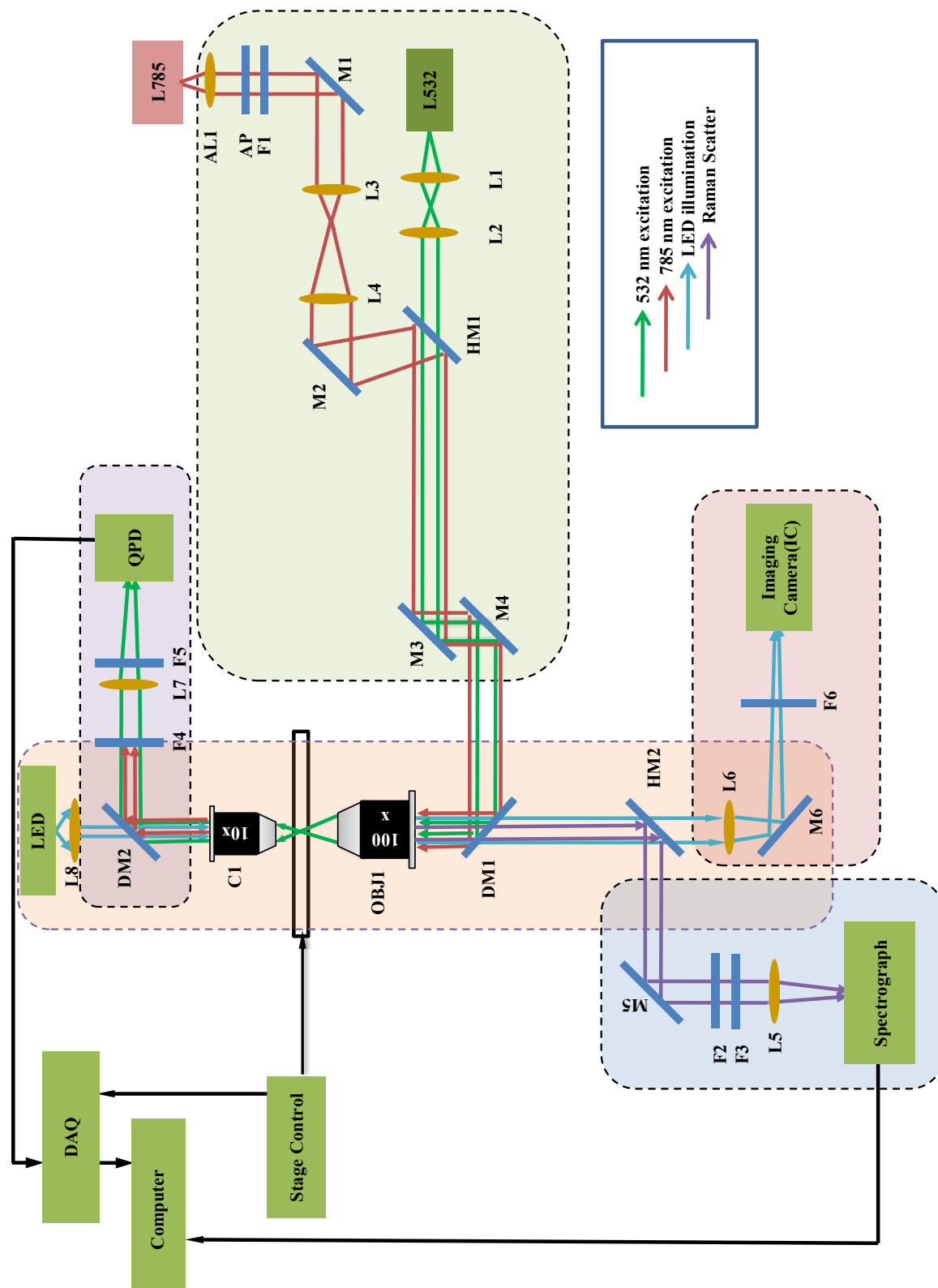


Figure 37: Detailed schematic of the OTRS (See Table XXIII for abbreviations). All optics are labeled, but for clarity, structural components are not displayed. The dashed lines enclose the key building blocks as outlined in Figure 36.

TABLE XXIII: List of parts used in the construction of the OTRS

Part	Description	Part number/ Manufacturer
L785	785 laser diode	L785P090, Thorlabs
AL1	7.5 mm lens, aspherical	A375TM-B, Thorlabs
AP	Anamorphic Prism 2.5x	PS877-B, Thorlabs
F1	785 nm diode bandpass filter	LL01-785, Semrock
M1	Dielectric mirror	BB1-E03, Thorlabs
L3	30 mm lens, achromat doublet	AC254-030-B, Thorlabs
L4	30 mm lens, achromat doublet	AC254-030-B, Thorlabs
M2	Dielectric mirror	BB1-E03, Thorlabs
HM1	Hot mirror	M254H45, Thorlabs
M3	Dielectric mirror	BB2-E02, Thorlabs
M4	Dielectric mirror	BB2-E02, Thorlabs
L532	532 nm DPSS laser	Compass 315M, Coherent
L1	25mm lens, achromat doublet	AC127-025-A, Thorlabs
L2	175 mm lens, plano-convex	LA1229-N-BK7, Thorlabs
DM1	785 nm dichroic beamsplitter	LPD01-785RS-25, Semrock
OBJ1	objective	Nikon 100x, oil, 1.25 NA
HM2	Hot mirror	M254H45, Thorlabs
M5	Dielectric mirror	BB1-E03, Thorlabs
F2	514 nm long pass edge filter	LP02-514RS-25, Semrock

Continued on next page

Table XXIII – continued from previous page

Part	Description	Part number/ Manufacturer
F3	785 nm long pass edge filter	785LP-RU, Semrock
L5	25 mm lens, achromat doublet	AC127-025-B, Thorlabs
SG	Spectrograph	Holospec f/1.8 ,Kaiser
CCD	CCD detector	Newton 920DUBRDD, Andor
L6	200 mm lens, achromat doublet	AC254-200-A, Thorlabs
M6	Mirror, protected aluminium	PF10-03-G01,Thorlabs
F6	505 nm short pass filter	HQ505SP, Chroma
IC	Imaging CCD	DFK41BU02.H, Imaging Source
C1	Condenser, infinity corrected	10x American optical, 0.25 NA
L8	20 mm,Aspheric Condenser Lens	ACL2520-DG6-A, Thorlabs
LED	455 nm LED	Rebel Star, Luxeon
DM2	Hot mirror	FM02, Thorlabs
F4	Neutral density filter, OD=2	NE20B,Thorlabs
L7	40 mm lens, bionvex	LB1027-A,Thorlabs
F5	785 nm Long pass filter	LP02-785RS-25, Semrock
QPD	Quadrant diode detector	QP-50-6-SD2, Pacific Silicon
STAGE	XYZ stage	Ultralign 561D-XYZ, Newport
PICO	Piezomotors	Picomotor, Newfocus
DAQ	DAC card	PCIe-6361, National Instruments

element in the cube is a 785 nm dichroic beamsplitter, DM1 (LPD01-785RS-25, Semrock), which reflects light at 785 nm (and also 10% at 532 nm) laser onto the back aperture of the objective. The objective focuses the beam down to a near diffraction-limited spot in the sample chamber, creating a tight enough focus for optical trapping.

The same objective, OBJ1, simultaneously acts as the primary collection lens for the Raman light (180° backscatter) from the focused spot. Since the microscope objective, OBJ1, is an infinity corrected lens, the light transmitted through the back aperture is collimated. Again, the dichroic mirror DM1, positioned right behind OBJ1, reflects (and rejects) the Rayleigh scattered light from the sample, while allowing the Stokes shifted Raman light (red shifted from 785nm excitation), to be transmitted. The transmitted Raman light then encounters the hot mirror HM2 (M254H45, Thorlabs) which is mounted as the center optic in another cage cube mount (C4B, Thorlabs). The mirror HM2 reflects light longer than 710 nm onto a dielectric mirror, M5 (BB1-E03, Thorlabs).

6.3.2 Raman Channel

Raman scattered light reflected from mirror HM2 is again reflected at 90° by mirror M5, which is mounted in a 90° cage mount (KCB1, Thorlabs). The light is then filtered by a 785 nm long pass filter F3 (785LP-RU, Semrock), which removes any residual Rayleigh scattered light at the laser frequency (785 nm). The light is then focused with a 25 mm achromat doublet, L5 (AC127-025-B) onto the 50 μm entrance slit of the spectrograph. Lens L5 is mounted on a XYZ stage (SM1XY, Thorlabs) to allow for the focus to coincide with the slit of the spectrograph. Mirrors HM2 and M5 form a two mirror system that allows for complete control of the position and propagation of the Raman scattered light incident on lens L5. The dichroic filter F3 has an OD 7 at 785 nm but also 40% transmission at 455 nm, the wavelength which is used for optical illumination (see next section). To prevent the 455 nm light that passes through filter F3 from interfering with the Raman

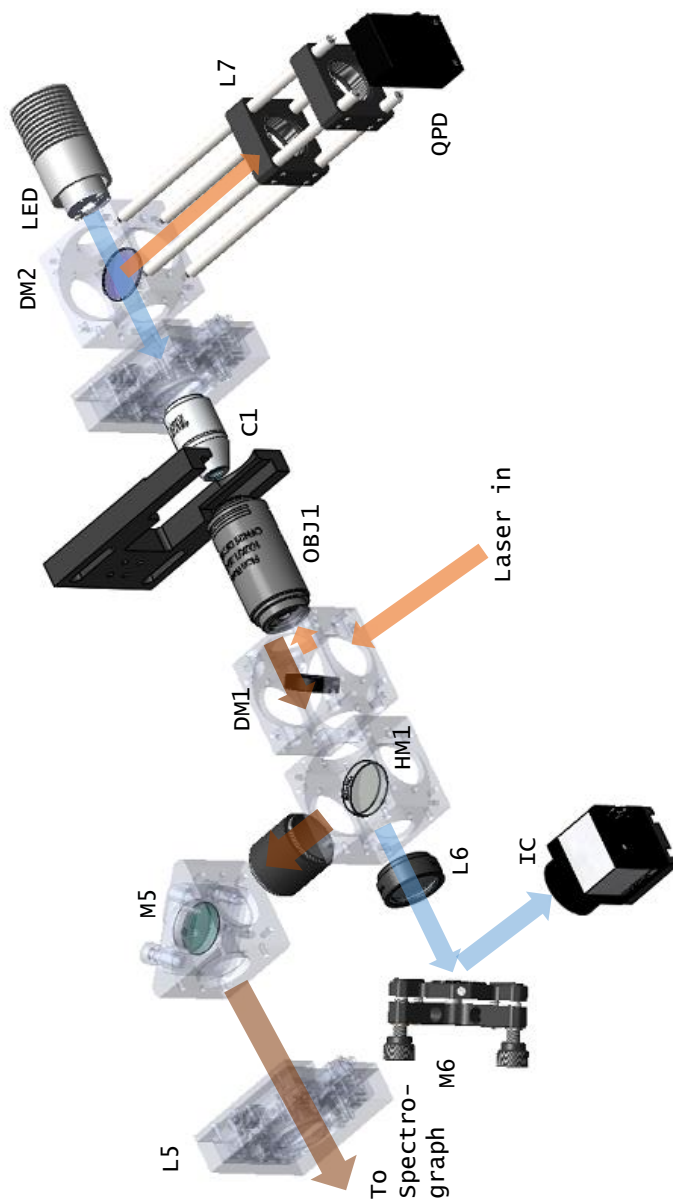


Figure 38: Exploded view of the OTRS core, highlighting the propagation of light along the various channels. Red arrows show the 785 nm excitation laser, blue arrows show the 455 nm illumination light path and dark red arrows show the Raman scattered signal path.

signal (due to second order diffraction from the spectrograph grating), it is blocked using a 532 nm long pass filter, F2 (532LP-RS, Semrock).

The spectrograph used is a f/1.8 transmission type, with a focal length of 85 mm (Holospec, Kaiser Optical Systems). It is fitted with a 1644 groves/mm grating optimized for Raman spectra with 785 nm excitation and scattering in the -200 to 2000 cm^{-1} range (HSG-785-LF, Kaiser). This disperses light onto a CCD detector with 2 cm^{-1} per pixel dispersion (for a pixel size of $26\text{ }\mu\text{m}$). The spectrographic CCD is based on a back thinned and deep depleted silicon chip (Newton DU920N-BRDD, Andor) that has a 90% quantum efficiency(QE) at 785 nm. Using this grating, the 1024×256 pixels on the CCD can record Stokes shifted Raman scatter from the laser line to nearly 1900 cm^{-1} . The detector is cooled thermo-electrically and operated at -75°C to reduce noise. The signal is recorded using software provided by the CCD camera manufacturer (Solis 4.23, Andor), and the camera is controlled by a PC via a USB 2.0 connection.

6.3.3 Illumination and Imaging Channel

Live imaging of the optically trapped sample is crucial to locate a trappable object, as well as optical monitoring of events apart from its general use as an alignment aid. Illumination with a standard incandescent bulb is not useful since they have a strong emission all the way into the IR and interfere with the Raman. An advantageous feature of DM1 is that it has 90% transmission below 500 nm and hence a 1 watt, 455 nm LED is chosen for illumination (Rebel Star, Luxeon). The LED allows for simultaneous collection of the near IR Raman signal while the sample is illuminated using blue light. A homebuilt current controller (Don Rippon, UIC Chemistry electronics shop) is used to drive the LED, which is mounted on a heat-sink and seated in a lens tube (SM1, Thorlabs). The LED output is collimated using an aspherical condenser lens, L8 (ACL2520-DG6-A, Thorlabs). The collimated light passes unreflected through a dichroic mirror DM2 and is focused onto the

sample with a 10× infinity corrected objective, C1 (American Optical), and is then collimated by objective OBJ1. The light is transmitted through both DM1 and HM2 and is focused using a 200 mm achromatic tube lens, L6 (AC254-200-A, Thorlabs) onto a 1/2 inch color CCD (DFK41BU02.H, Imaging Source). A 505 nm short pass filter (ChromaTech) may be inserted into a filter holder between the CCD and L6 if using the 532 nm laser scatter to prevent it from saturating the CCD. This CCD for imaging is mounted on a home built XYZ translation stage.

It should be noted, that the dichroic mirror, DM1, has 85% transmission at 455 nm and less than 1% transmission at 532 nm while still performing its intended purpose with a 10% transmission at 785nm (OD=1) and 95% transmission at 800 nm (238 cm^{-1} Stokes shift from the laser line at 785 nm). This allows for DM1 to transmit blue illumination light, reflect both the 532 nm green and the 785 nm red laser to the objective and allow the Stokes Raman scattered light (excited at 785 nm) to pass through to the spectrograph.

6.3.4 Lasering Channel: Trapping and Raman Excitation

6.3.4.1 785 nm Laser

Initial experiments were carried out with a commercial 785 nm, 1 watt multimode fiber coupled laser (Innovative Photonics). Due to the high power multimodal lasing, it was challenging to tightly focus the light to form a stable trap. A homebuilt system was therefore built using a 785 nm laser diode (L785P090, Thorlabs, or DL7140, Sanyo). The diode is mounted in a holder that provides Peltier cooling (LDC21, Thorlabs). The light is collimated using a aspherical lens AL1 (A375TM-B, Thorlabs). A dual current and temperature driver (SDL800, SDL labs) is used to drive the diode. Diode lasers are spectrally “dirty”, i.e. they have many longitudinal lasing modes. Due to this, side bands from our laser setup had to be removed using a 3 nm band pass filter (Maxline LL01-785, Semrock). The spatial mode of the laser is TEM_{00} but the beam profile is elliptical, as is often

the case with diode lasers. Consequently the beam profile was circularized by inserting an $2.5\times$ anamorphic prism in the beam path (PS877-B, Thorlabs). Since ideal trapping requires overfilling of the back aperture of the objective (188), the beam is expanded $3\times$ using a Keplerian telescope consisting of lenses, L3 and L4. The 785 nm laser beam was then made coaxial with the 532 red laser beam (see below) using a two mirror system: a dielectric mirror M3 (BB1-E03, Thorlabs) and a hot mirror HM1 (M254H45, Thorlabs).

6.3.4.2 532 nm Laser

The ability to incorporate a second laser line in the green region for trapping and Raman excitation was also developed. The original laser trapping experiments using one of our prototype designs were performed using the 514 nm laser line from an argon ion laser (Innova 300, Coherent) as both the trapping and Raman excitation source. The green laser induced strong fluorescence excitation in biological samples and therefore we decided against using it as a Raman excitation source for such samples, and chose to focus on the NIR laser described in the previous section. However, use of a green laser to facilitate a second optical trap was anticipated and it was retained in the overall design. The green laser may also be used as an epi-illumination source (190; 174).

The argon laser was later replaced by a diode pumped, solid state (DPSS) 532 nm laser. The 532 nm laser is a 100 mW single longitudinal mode (SLM) 532 nm DPSS laser (Compass 315M-100, Coherent Laser) and has a TEM_{00} beam profile with excellent short and long term temperature stability. It can be used for Raman excitation, trapping, for monitoring the trapping potential, for fluorescent excitation of appropriate dyes, and as a visual alignment aid. The beam from this green laser was expanded $3\times$ using plano-convex lenses L1 and L2 as Keplerian telescope. The expanded beam passes through the hot mirror (HM1) after which it was made collinear with the 785 nm laser. Dielectric mirrors M2 (BB1-E02, Thorlabs) and M3 (B1-E02, Thorlabs) were then used to

“walk” (191) the beam to the back aperture of the objective OBJ1 via dichroic mirror DM1. Mirrors M2 and M3 are AR coated for reflection in the 400-750 nm region, but have 99% reflectance at 785 nm and therefore their performance is superior to aluminum mirrors.

6.3.5 Force Detection

To monitor the trapping potential and subsequent forces acting on the trap, the method of back focal plane imaging was used. Objective OBJ1 creates a tightly focused spot (the “optical trap”) from the laser beam, that then diverges fast and is collected and collimated by a 10× condenser, C1. This condenser is actually a 10× objective that has a NA of 0.25 and will not collect all the light from the trap. It is, however, sufficient for our needs of monitoring the trap (192), as shown in the next chapter. Higher NA objectives available to us do not have sufficiently long working distances to allow the use of a 1 mm thick microscope slide for the sample cell.

The forward scattered light, which has been collimated by C1, is then reflected by dichroic mirror DM2 onto a neutral density filter (NDF), F4 (ND20B, Thorlabs), with 1% transmission at 785 nm. F4 is followed by a 40 mm lens, L7 (LA1304, Thorlabs), that is mounted on a cage x-y translation mount (CXY1, Thorlabs). Lens L7 projects the image of the trap either onto a quadrant photo detector (QPD, QP-50-6-SD2, Pacific Silicon). Alternatively, a lateral effect position sensor (PSD, PDP90A, Thorlabs) was also substituted for the QPD. Both the position detectors QPD and PSD use home-built power supplies and are mounted onto cage XY translators (CXY1, Thorlabs).

6.3.6 Data Acquisition and Instrument Control

The QPD detector provides three signal channels out, two difference channels for x and y position of the light on the detector and a sum channel that records the total light intensity on the detector. Shielded cable (cat 6) is used to transfer the signals from the QPD to a 16-bit data acquisition (DAQ) card (PCIe-6361, 2 MS/s, National Instruments).

The same DAQ card is used to drive a microscope stage (ULTRAlign 561-XYZ, Newport) via an actuator driver (Picomotor 8801, Newport) and three actuators (Picomotor 8301, Newport), one for each axis. The stage was either driven by digital pulses from the DAQ card using a custom program (LabView, National Instruments) and interface software written by Yang Cui, or by an external controller/ joystick (Picomotor 8620, Newport).

6.3.7 Sample chamber

Quartz was used to construct the sample cell, because glass shows a broad fluorescence peak around 882 nm that overlaps with the 1400 cm^{-1} region for Raman scattering when excited at 785 nm (193). This feature can easily overwhelm the Raman peaks in the $1200\text{-}1600\text{ cm}^{-1}$ region. While quartz also shows a large Raman peak below 400 cm^{-1} , it does not interfere in the spectral region of our interest (158). To construct the cell, a quartz slide was immersed in water and two 1.58 mm holes were drilled with a 1/16" diamond core bit. Tygon tubes with an inner diameter of 0.51 mm (EW-06419-01, Cole Parmer), were then inserted into the holes and sealed using epoxy glue. The outer diameter of these tygon tubes are 1.52 mm, close to a standard drill bit size of 1.58 mm. A quartz cover slip, with 0.17 mm thickness (1015T-AB, SPI supplies), was then attached to the slide using double sided tape (Scotch, 3M) as shown in Figure 39. The double sided tape acts as a convenient $\approx 100\text{ }\mu\text{m}$ spacer for the cell. The two remaining open edges were then sealed using commercially available nail enamel. The sample chamber (excluding the tubing) can retain 2 μl of sample (174). Samples were introduced into the cell using a syringe and a 29 gauge needle attached to the tygon tube. The cell was firmly fixed on to a metal mount using double sided tape and medium binder clamps (72050, Acco brands) and the mount was attached to a XYZ stage. The metal mount was designed and constructed so that it can be thermostatted using a water bath.

The metal mount is thermally isolated from the stage by the insertion of a plastic (Delrin[®]) spacer between the stage and the mount.

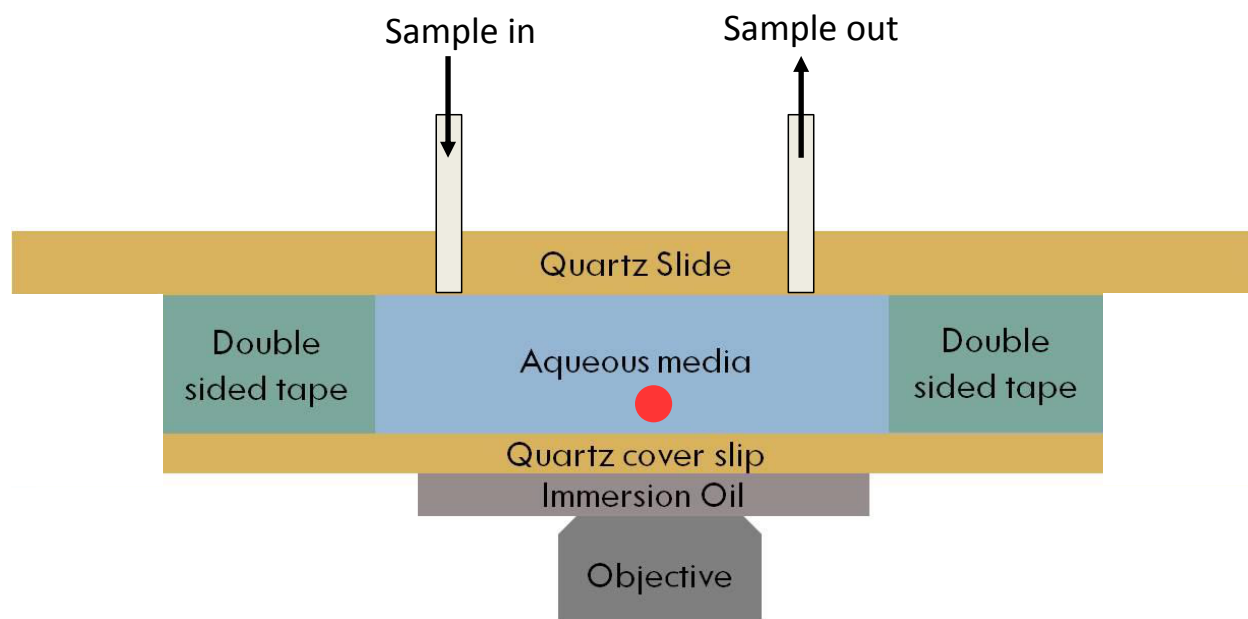


Figure 39: Cross section of the sample chamber (not to scale). A laser is focused into the 0.1 mm sample chamber created by sticking a quartz cover slip (0.17 mm) to a quartz microscope slide (1.0 mm) using double sided tape (0.10 mm).

6.4 Alignment

After the construction of the instrument, the alignment of the instrument was performed using a 100× oil immersion objective with DF immersion oil (Cargille Labs).

6.4.1 Laser

One criteria for a trap is that the trapping laser must be coaxial with the optical axis of the objective (191). For a crude alignment, the objective OBJ1 was removed and an iris (SM1D12D, Thorlabs) was inserted in its place. The iris' aperture was kept slightly smaller than the laser beam size, and mirror M3 was used to center the laser beam on this iris. A second similar iris was placed between objective OBJ1 and condenser C1 and mirror M4 was adjusted to center the laser beam on this iris. The process was reiterated by alternating between adjusting M3 and M4, until the beam was centered on both the irises. The irises were then removed and OBJ1 is threaded back in its position.

An imaging CCD was used for fine tuning of the alignment process. The laser power was attenuated, and a silicon wafer, which was sandwiched in between a glass slide and a quartz cover slip, was then placed on the sample stage. The stage was translated along the optical axis, so that the silicon surface moved through the laser focus point. The focal spot was then imaged onto a CCD. The reflected spot shape was observed and M4 was precisely adjusted until the focal spot shape was symmetric while defocussing the reflected spot by translating the sample along the optical axis.

6.4.2 Raman

The spectrograph is aligned using a 633 nm HeNe laser counter-propagating to the normal 785 nm laser direction, only for the purposes of alignment. An alignment aid was constructed using aluminum sheet with a center hole which covers the grating in the Holospec spectrograph. The spectrograph cover was removed and the aid was placed on the grating. A HeNe laser was aligned to pass through the center of the grating and a 167 μm entrance slit. Focusing lens L5 and dichroic mirror DM1 were removed and mirrors HM2 and M5 were used to steer the HeNe laser beam onto the back aperture of OBJ1. The system was then reassembled and a silicon wafer was placed in

the sample holder. Lens L5 was then inserted and the real time Raman spectrum of silicon was acquired at video rates. Lens L5 was centered and translated along the optical axis until the silicon 521 cm^{-1} Raman peak intensity was maximized and its peak width (FWHM) was minimized. The spectrograph has an adjustable lens to focus the diffracted light from the grating onto the plane of the CCD, which was also adjusted to minimize the measured peak width.

6.4.3 Confocal Raman

Raman spectra from the trap are often contaminated with Raman scatter from the oil, the cover-slip and water in the sample cell which are out of the focal volume but are of larger total volume than the particle in the trap. Given the weak Raman scatter from biological samples, and even less for a single trapped particle or cell, it is essential to reduce this off-focus interference. A confocal design could limit the depth of focus for scattered light that reaches the spectrograph (194; 195; 196). Inserting confocal optics would normally require inserting a pinhole, at least two more lenses and positioning stage mounts for all of them. The reflection loss of the lenses would only impede throughput and this would be contrary to our minimalistic, high throughput design principle.

An alternative pseudo-confocal setup was implemented instead (197). A pinhole can be approximated with two slits, orthogonal to both the direction of propagation and to each other. The $50\text{ }\mu\text{m}$ entrance slit to the spectrograph provides one such “vertical” slit. The stigmatic, imaging spectrograph images the slit onto the CCD with unitary magnification. Therefore, by binning the CCD for only 2 pixels vertically, a “horizontal” slit of $50\text{ }\mu\text{m}$ is approximated. Combined with the spectrometer entrance slit, the net effect is a $50\text{ }\mu\text{m}$ confocal aperture that eliminates most of the off-focus scattered light. This design concept is illustrated in Figure 40.

The confocal aperture has a depth resolution, R_d , given by (198),

$$R_d = \frac{1.4n\lambda}{NA^2} \quad (6.1)$$

where n is the refractive index of the immersion media and λ is the wavelength of light used. For our objective with NA of 1.25 and laser wavelength of 785 nm, R_d is calculated to be 1 μm .

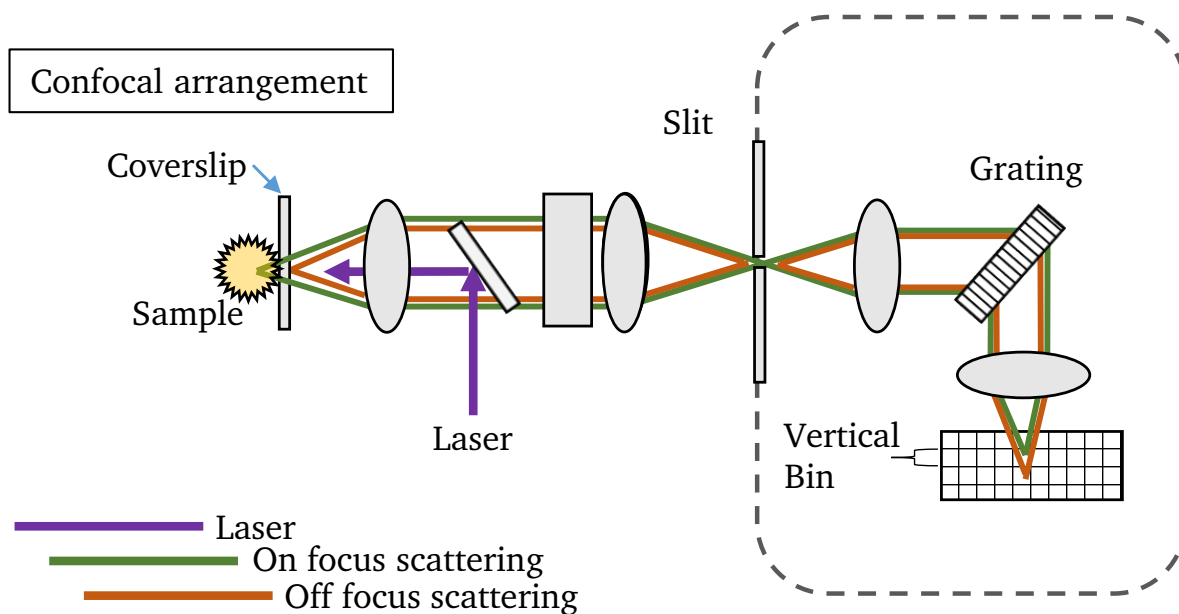


Figure 40: In confocal Raman microscopy, the slit can act as part of a confocal aperture in one dimension, while vertically binning only selected pixels on the CCD completes the confocal design, collectively emulating a square pinhole. Scattered light from above and below the confocal plane (red lines) is rejected in this design.

6.4.4 Force detection

The condenser C1 was mounted on a xyz stage and is translated along the optical axis till the forward transmitted light, is collimated as it comes out the back aperture. F4, F5, L7 and QPD are all mounted on cage plate mounts (CP02, Thorlabs) and then cage rods designed for a 30 mm cage cube system. All optics are auto-centered on the optical axis by use of this mounting design. Dichroic mirror DM2 is a hot mirror and reflects 785 nm light onto lens L7. The QPD is translated along the optical axis until the laser light fills roughly 70% of the QPD area. Lens L7 and QPD are both mounted on separate cage mounted x-y translation stages (CXY1, Thorlabs) and the QPD signal is nulled by adjusting the position of L7 and the QPD.

6.4.5 Force calibration

Figure 41 illustrates the quadrant diode used in our setup. It has four quadrants that are Si-photocurrent detectors. The diode is mounted on a board that performs I-V conversion and amplification. The time series of the voltage signals are digitized and recorded. The signal is post processed using the theory discussed in Chapter 5 and sample results are shown in the next chapter.

6.5 Calibration

6.5.1 Spectral calibration

Raman scattered photons are detected on the CCD as counts vs. the pixel number. To obtain useful chemical information the pixels need to be converted to Raman shifts ($\Delta\tilde{\nu}$) using atomic line lamps or chemical species with known Raman shifts. Calibration was performed using 1 μm polystyrene (PS) latex beads (LB11, Sigma-Aldrich). A 1:50,000 dilution of the PS beads in DI water was introduced into sample chamber. The stage was then translated along the optical axis of the microscope until the cover-slip was in focus, which was monitored by the reflection of the 785 nm

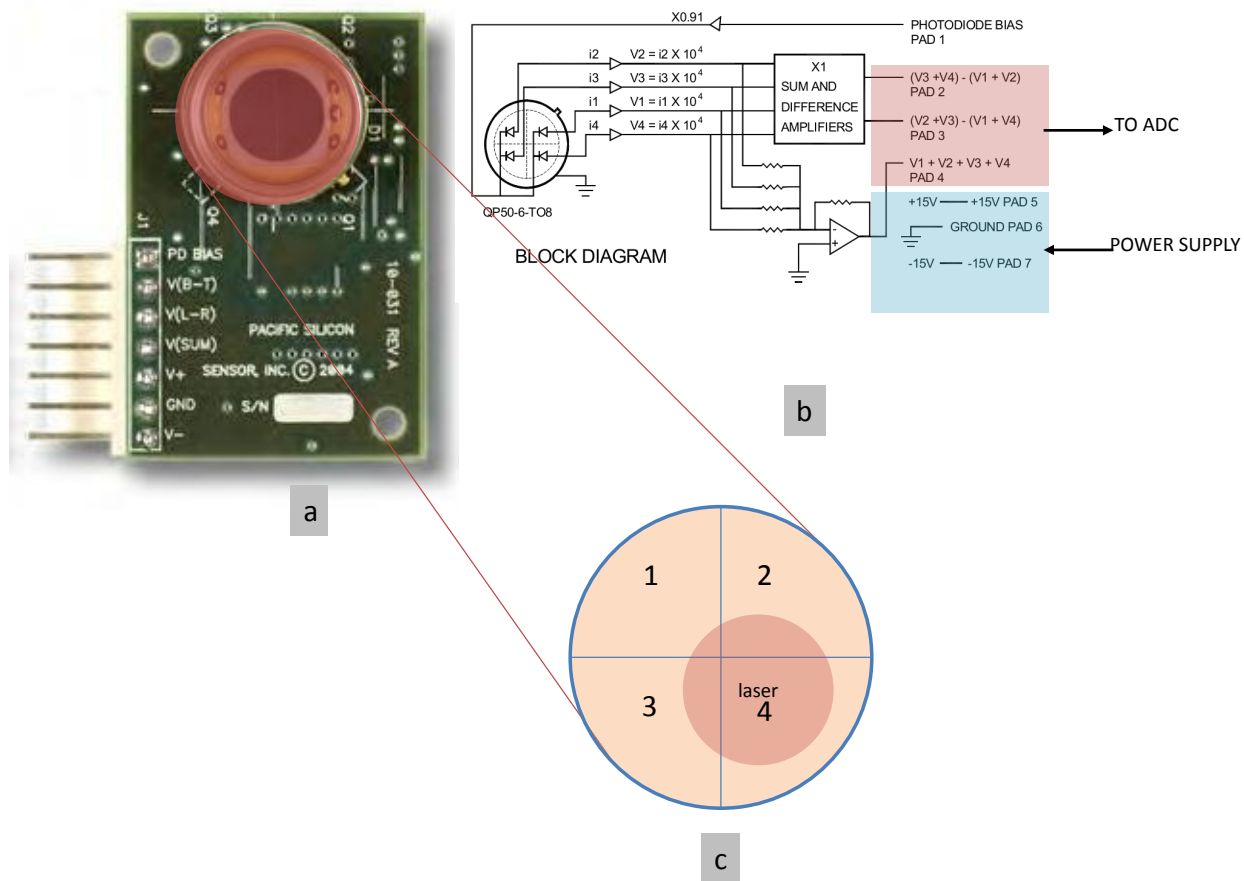


Figure 41: (a) The quadrant diode mounted on math and amplification circuitry. (b) Schematic of all the in and out pins on the QPD. The position detection signals are highlighted in pink. (c) A cartoon representation of the laser spot fluctuation in the quadrant detector. The voltage in each quadrant corresponds to the illuminated area on each quadrant.

laser on a imaging CCD. A bead was captured at the focus of the laser spot and then moved 5 to 10 μm away from the coverslip (deeper into the sample) to reduce the background scatter from the glass (or quartz) surface. If the trap is moved any further into the sample the trap stiffness quickly deteriorates. Polystyrene Raman lines are well known in literature (199) and were used to calibrate the frequency dispersion on the CCD. This calibration was cross validated using the 521 cm^{-1} phonon peak from a silicon wafer glued to a microscope slide. The instrumental linewidth, measured using the ring breathing mode of polystyrene at 1004 cm^{-1} , was determined to be 6 cm^{-1} .

6.5.2 Spectral imaging

The spectrograph has a two dimensional CCD as a detector, but this capability is not used for the purpose of imaging in our experiment. However, in order to diagnose the instrument, a minimal analysis of the spectral imaging capabilities is given here. The Raman spectrum of silicon is collected from a focal spot smaller than $1\text{ }\mu\text{m}$ diameter. The collimated light from the focal spot is imaged onto the slit with lens L5, which is effectively the tube lens for the Raman channel and the magnification is calculated using Equation 6.2.

$$\text{Effective Magnificaton} = \frac{\text{Tube lens focal length}}{\text{Objective front focal length}} \quad (6.2)$$

For the confocal setup, the tube lens L5 has focal length 75 mm and therefore the magnification is $\approx 38\times$.

6.5.3 Image magnification

Our design eliminates an eyepiece and the therefore image magnification is the product of the objective magnification and the monitor magnification. The objective magnification using a 200 mm tube lens is $100\times$. The monitor magnification is calculated to be $41\times$ using a 13 inch image and a

1/2 inch (8 mm × 6.4mm) CCD sensor size. In order to test this a bead of 3 μm diameter was stuck to a coverslip and moved 3 μm along any one axis using a translation stage. The actual measured displacement of the image on the monitor is 12 mm and therefore the effective video magnification is 4000×, in good agreement with the above computation.

6.5.4 Choice of immersion oil

When using an optical trap for Raman spectroscopy, the objective immersion oil needs to be optimized. Due to the side-on nature of our trap the oil needs to have a viscosity that is high enough so that it doesn't flow. The fluorescence from the oil needs to be low and Raman signal must have minimal interference in the region of interest. A few immersion oils from a leading supplier of microscope immersion oil (Cargille Labs) were tested. Type FF, a virtually fluorescence free oil, is very attractive for our application as it has no Raman bands above 1400 cm⁻¹ (200). However, it has an unsuitably low refractive index of 1.48 and very low viscosity at 170 centistokes (cSt). Due to the vertical design of the sample holder, lower viscosity oils tend to bleed away due to gravity. The refractive index of the oil must be close to 1.52 to provide an effective trap (201). Type LDF is another low fluorescence oil that was tested, and, with a viscosity of 500 cSt and refractive index of 1.51, it is more suitable than type FF. Finally, type 37LDF is a grade of immersion oil that is highly viscous even at moderately elevated temperatures such as 37°C and also has a refractive index of 1.51. Immersion oil types LDF and 37LDF were both found suitable for optical trapping.

6.6 Conclusion

The aim of this chapter was to detail the technical aspects of how the OTRS instrument was realized. An instrument design was conceived and constructed, and then reconstructed to optimize various aspects of the experiment. The instrument was finely tuned and the system was calibrated. In

the next chapter the results of testing the system using various model samples and some applications of the OTRS will be discussed.

CHAPTER 7

TESTING AND APPLICATIONS OF THE OTRS

Initial alignment of the OTRS system was performed using a silicon surface as a test surface. The laser was aligned as described in Chapter 6 until the image of the laser spot was symmetric with respect to axial translation of the silicon surface. Figure 42 is an image of a focused spot of a well aligned laser that is imaged onto a CCD with magnification of 100 \times .

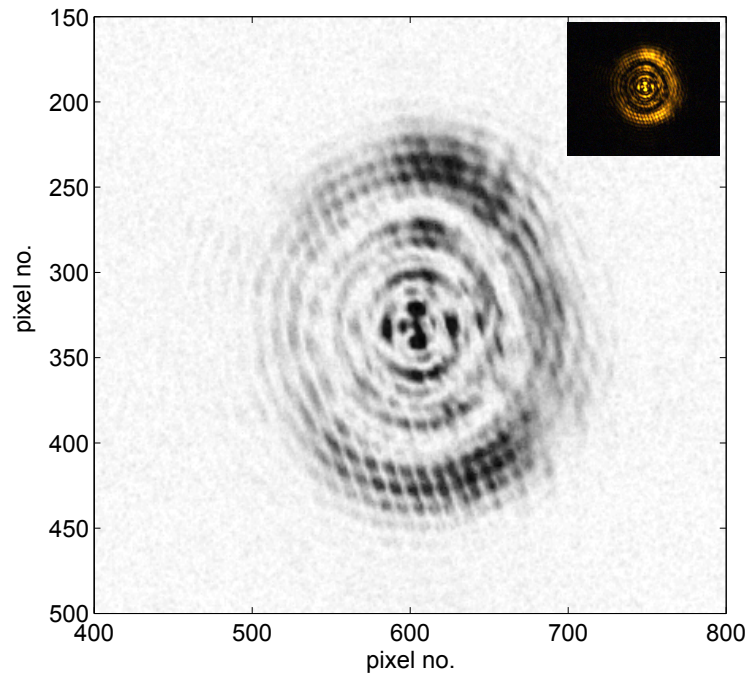


Figure 42: Inverted and grayscale image of the reflection of a well aligned 785 nm trapping laser off the silicon surface on the imaging CCD. The inset shows the original image.

The 521 cm^{-1} Raman peak from silicon, which has a large polarizability (202), was used to optimize the alignment of the optics that couple the microscope to the Raman spectrograph (163). The same Raman peak at 521 cm^{-1} was also monitored for an extended time to monitor power and wavelength stability.

7.1 Polystyrene beads

7.1.1 Raman spectrum

Testing and finer optimization of the OTRS instrument was performed using an optically trapped sample. A standard model system for this is a trapped polystyrene bead (203). Commercially available polystyrene microspheres with average diameters of $3.0\text{ }\mu\text{m}$, $1.0\text{ }\mu\text{m}$ and $0.5\text{ }\mu\text{m}$ were purchased as colloidal suspensions (LB-30, LB-11, LB-5 Sigma-Aldrich). The stock beads were diluted 1:10,000 in deionized water and introduced into a sample chamber using the sampling system described in Chapter 6. Figure 43 shows the confocal Raman spectrum acquired from a $3\text{ }\mu\text{m}$ bead, where the Raman spectrum is dispersed by the grating onto the horizontal pixels. The Raman spectra on different vertical pixels are collected from various positions around the laser focus. Restricting Raman acquisition to selected vertical pixels simulates confocality. Table XXIV is a list of the vibrational mode assignments for the Raman peaks in Figure 43, based upon previous studies by others (204; 199; 205).

Figure 44 shows the intensity of the 1000 cm^{-1} peak, the highest, of polystyrene for each of the CCD tracks in Figure 43. The signal to noise ratio (SNR) for polystyrene was obtained by calculating the ratio of the Raman intensity, in analog-to-digital converter counts (ADC), for the ring bending mode of polystyrene at 1000 cm^{-1} to the standard deviation of the ADC counts in the $1800\text{-}2000\text{ cm}^{-1}$ region which is devoid of any characteristic peaks (199; 206). The track with highest intensity in Figure 44 has a SNR of 66.

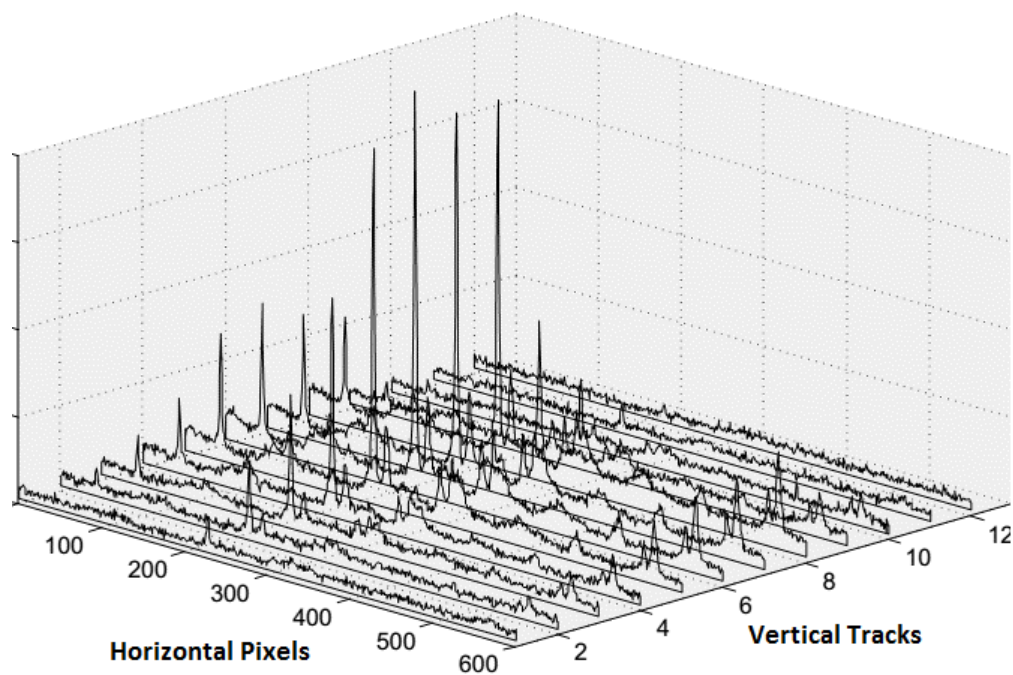


Figure 43: Confocal mode Raman spectrum of trapped polystyrene beads. Each spectrum (track) is obtained by binning 2 vertical pixels.

TABLE XXIV: Characteristic Raman peaks of polystyrene

Raman shift (cm^{-1})	Vibrational normal mode
621	ring deformation
795	ring breathing
1001	ring breathing
1031	CH deformation
1155	C-C stretching
1450	CH ₂ scissoring
1583	ring-skeletal stretching
1602	ring-skeletal stretching

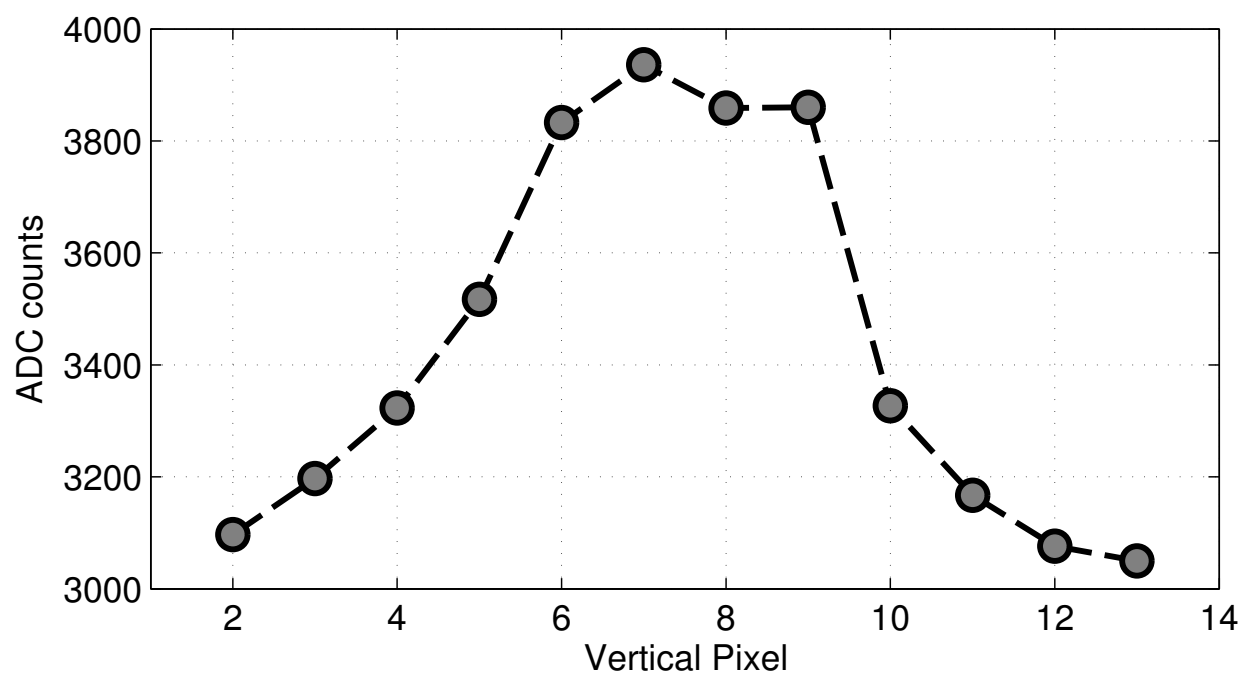


Figure 44: Plot of the intensity of the 1000 cm^{-1} peak of polystyrene for all the CCD tracks in Figure 43.

The trap stiffness for a polystyrene sphere was calculated using the BFPI method outlined in Chapter 5. Figure 45 shows the power spectral density spectrum (PSD) for a polystyrene bead. Using the corner frequency for one of the directions perpendicular to the direction of propagation, the trap stiffness is calculated to be 0.06 pN/nm. This is the maximum trap stiffness possible for our OTRS since the laser is operated at maximum power. Since the trapping laser does not have a perfectly circular intensity distribution, the trapping stiffness is not symmetric in the x and y directions ($\kappa_x \neq \kappa_y$). The trap stiffness in the direction of propagation of light (z), is usually much weaker than perpendicular to the direction of propagation (x,y) (180). Due to the exploratory nature of our project, trapping ability in the axial (z) direction was not studied further.

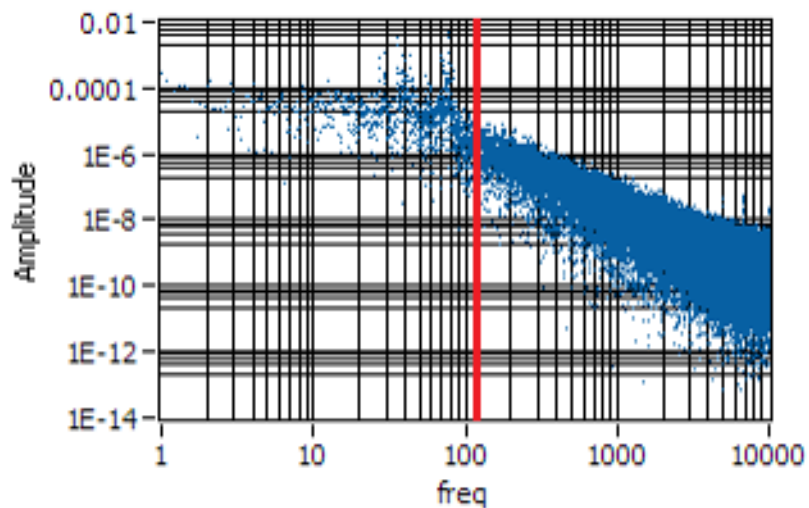


Figure 45: Power spectral density of a trapped polystyrene bead.

7.2 Single cells

As an example of the viability of our system for the study of complex systems, we measured the Raman spectra for both prokaryotic and eukaryotic cells in a laser trap. *E. coli* cells from (BL21-DE3 strain) was used to test the trap for prokaryotic media. The cells were grown using lysogeny broth (LB) as cell growth media. Immediately prior to measurement, the cells were further diluted using fresh LB media. Unlike PS beads dissolved in water, in the case of biological samples in LB media, the background contribution from the media was high and needed to be subtracted. Since LB media contains lipids, sugars and amino acids for cell growth, its Raman spectral signature is similar to that of the cell. Therefore it is essential to carefully subtract the background signal due to the media.

The single cell Raman spectrum and background Raman scattering from the media needed to be acquired in identical conditions. This was realized by first temporarily blocking the laser after acquiring Raman signal from a trapped cell. In the absence of an optical force, cells typically diffuse out of the focal region at a few μm per second in solution (207). After a few seconds the cell diffuses far enough from the optical trap influence so that its probability of recapture by the trap is low. The laser was then unblocked and the Raman spectra of only the media was acquired as a background spectrum. Weighted subtraction of this background was used to correct the Raman spectrum that was acquired with the cell in the trap. A weighted subtraction was required due to the fact that, when trapped, a cell occupies a major part of the Raman focal volume, displacing the media in which it is suspended. Therefore when a cell is in the trapping volume, the Raman contribution from the media is lower than when the cell is not trapped and the focal volume contains just the

media (208). Figure 46 shows the Raman spectra acquired from LB background and Equation 7.1 summarizes the background correction method,

$$Raman_{(cell)} = Raman_{(cell+media)} - [\text{weighing factor} \times Raman_{(media)}] \quad (7.1)$$

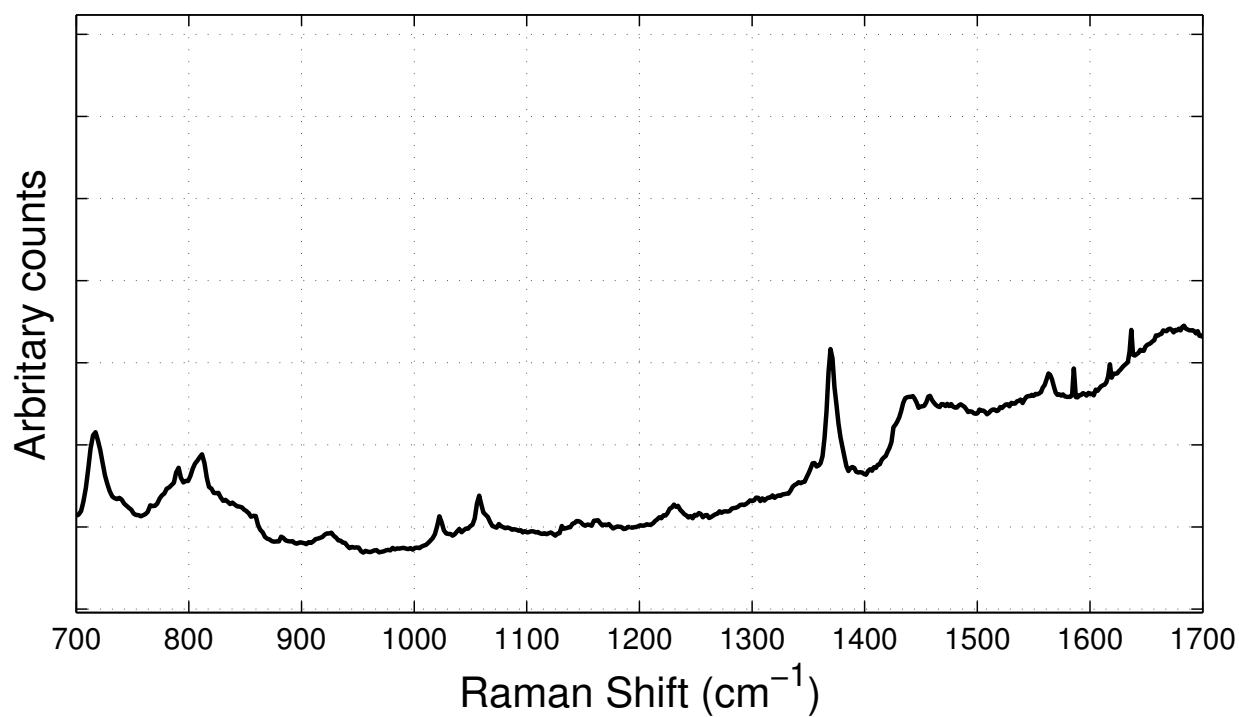


Figure 46: Raman spectra from LB media used as spectral background. The spectrum was acquired with an integration time of 30 s, 15 mW laser power at sample.

Figure 47 shows the Raman signal obtained from *E. coli* using 15 mW (at sample) of 785 nm excitation and an integration time of 30 sec. Raman peak positions matched those available in literature (207) and are listed in Table XXV. High frequency noise in all the single cell spectra has been removed by applying a Savitzky-Golay low pass filter with a 9th order polynomial and a 25 cm^{-1} window (209). The fate of the cell after exposure to the laser was not studied, but near IR light for trapping is known to cause minimal damage to cells like *E. coli* and has been studied previously by others (186).

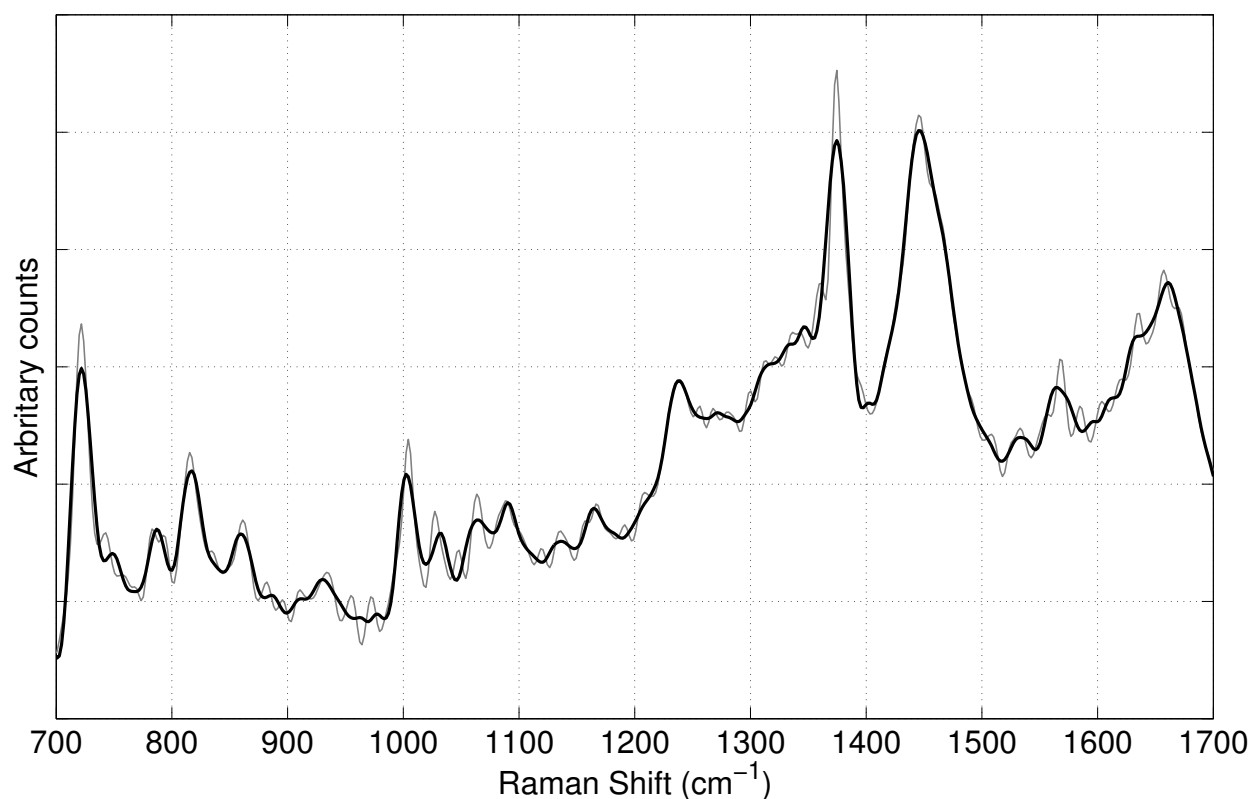


Figure 47: Raman spectra from a single *E. coli* cell. The spectrum was acquired with an integration time of 30 s, 15 mW laser power at sample. Gray lines are the original spectrum and the black line is the spectrum after smoothing.

TABLE XXV: Tentative assignments for the Raman spectrum of a single *E. coli* cell

Raman shift (cm^{-1})	Assignment
721	Nucleic acids
858	Protein (Tyrosine)
1004	Protein (Phenylalanine)
1235	Protein (Amide III)
1338	Nucleic acids
1445	Lipids (Alkyl CH_2 bend, scissor)
1659	Protein (Amide I) and Lipids (Ester $\text{C}=\text{C}$ stretch)

Larger, eukaryotic cells can also be trapped and their Raman spectrum acquired. To demonstrate this *S. cerevisiae* is a standard model system for eukaryotic systems. Commercially available baker's yeast was grown at 37°C , diluted and introduced into the sample cell. Single cell Raman was measured and is shown in Figure 48 with some tentative peak assignments listed in Table XXVI.

7.3 Metal nanoparticles

Since the Raman spectra of single cells showed low signal to noise, it was postulated that SERS enhancement from metallic nanoparticles might increase the SNR. Also a trapped metallic nanoparticle might act as a local probe of structure, since it is known that Raman enhancement is limited to molecular modes of components coupled to or in the vicinity of the nanoparticle (210). While polystyrene beads smaller than 300 nm are hard to trap, metallic particles as small as 18 nm have previously been optically trapped by others (179; 180). Plasmon resonances in metallic nanoparticles aid the trapping mechanism in aggregates of gold nanorods (GNR) (211)

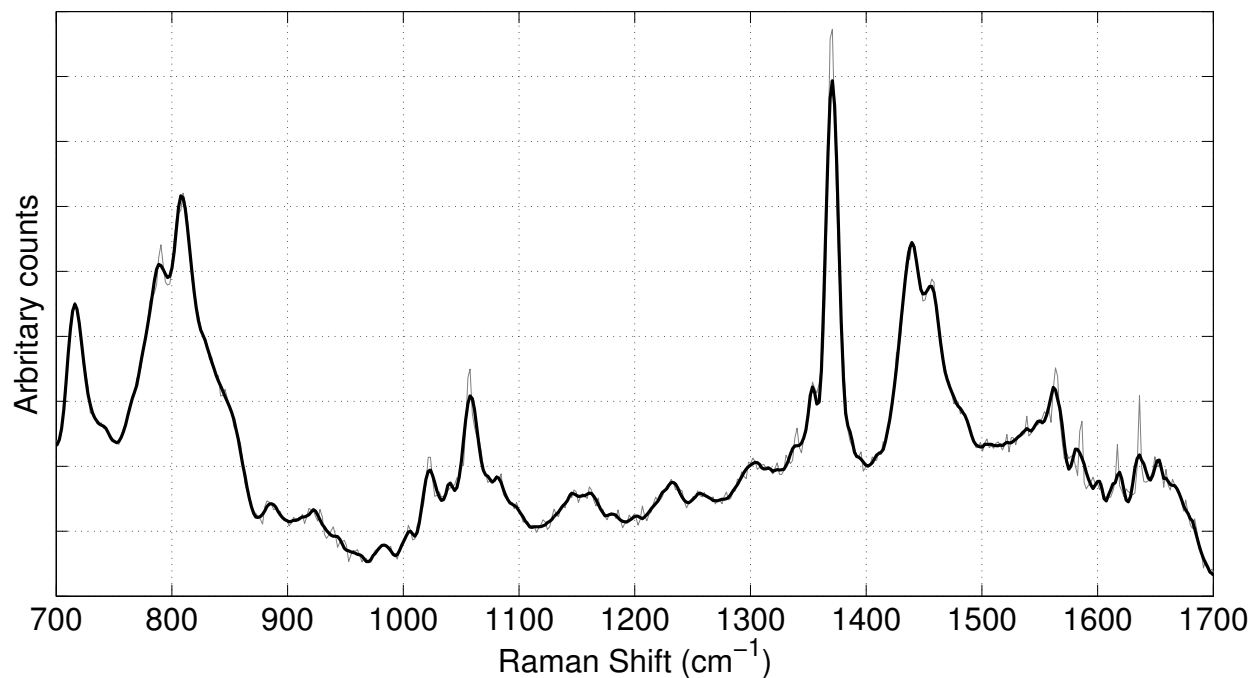


Figure 48: Raman spectra from a single *S. cerevisiae* cell. The spectrum was acquired with an integration time of 30 s, 15mW laser power at sample.

TABLE XXVI: Tentative assignments for the Raman spectrum of a single *S. cerevisiae* cell

Raman shift (cm ⁻¹)	Assignment
712	Lipids
847	Protein (Tyrosine)
920	Nucleic acids
1222	Protein (Amide III)
1440	Lipids

and have been used previously by others for in-vivo SERS imaging and for localized photo-thermal heating (212).

Commercially available bare gold nano rods (GNR) suspended in 100 mM CTAB buffer were purchased (A12-10-780, Nanopartz). The measured UV-vis spectrum (Cary 300, Agilent) of these GNR confirm a surface plasmon peak at 780 nm, close to the Raman excitation and trapping wavelength of 785 nm (see Figure 49). The nanorods are specified by the manufacturer to have a narrow distribution of size with mean axial diameter of 10 nm and length of 38 nm, which was confirmed using dynamic light scattering (DLS).

The GNRs are smaller than the diffraction limit of visible light and thus the microscope images show only diffraction limited images of the GNR. It has been shown by others that to effectively optically trap nanorods, the frequency of the trapping laser should be lower than the plasmon frequency (178). Also the highest SERS enhancement, when using 785 nm excitation, has been shown to occur when the nanoparticle plasmon wavelength is near 750 nm (213).

However, in our instrument, we were not able to optically trap the nanoparticles. It is assumed that this is due to inadequate optical power from the trapping laser. It was noteworthy though, that even at 15 mW of power (at the sample) there was intense heating and bubble formation in the sample chamber (211). Improvements in the OTRS that may enable such trapping are discussed in the next section.

7.4 Possible improvements in the OTRS

Testing the OTRS system highlighted some technical shortcomings in its design. Possible improvements in the instrument by careful selection of modified components are briefly discussed. To manipulate and study gold nanoparticles and other smaller systems the trap strength needs to be increased. One possibility is to increase the intensity of light, which would mean the incorporation

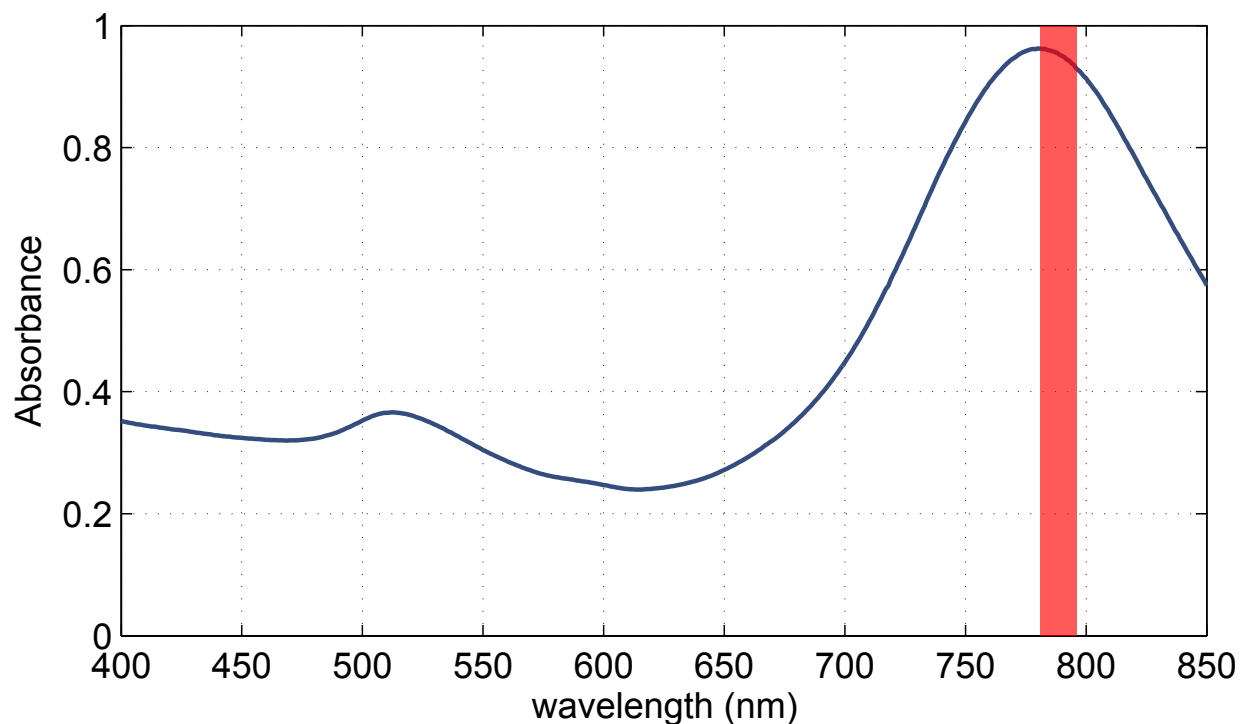


Figure 49: UV-Vis absorption spectrum of bare gold nanorods in CTAB buffer. The peak at 780 nm is the surface plasmon peak and the red stripe indicates the excitation frequency region (780-785 nm).

of a higher powered laser. However, use of higher light intensity would lead to sample heating and a solution to this problem would need to be taken into consideration while designing new experiments (214).

Another factor that might be optimized is the quality and NA of the objective. Regular achromat objectives designed for the visible, like the one we use, have a transmission of only 30% light in the near IR and therefore 70% of the NIR Raman signal is lost due to the internal components of the achromat (204). Consequently, the dominant objectives in optical trapping are ones optimized for the near IR. These objectives also tend to have a higher NA (1.3 - 1.45) and allow for formation

of tighter optical traps. Achromat objectives suffer from large chromatic aberrations in the near IR which is a major problem for NIR Raman. This effect may be illustrated using the amide I band as an example. The amide I, as was discussed previously, is Stokes shifted by 1600-1700 cm^{-1} from the laser excitation wavelength. For Raman excitation using a 785 nm ($12,738 \text{ cm}^{-1}$) excitation source, a 1600 cm^{-1} Stokes shift would place the amide I band at an absolute wavelength of 910 nm ($10,989 \text{ cm}^{-1}$), and the focal spot for 910 nm light is axially offset from that for 785 nm light by a several hundred nanometers. It is quite probable that this chromatic aberration is detrimental to the light collection efficiency in our system. One solution to this problem is the use of a fluorite or apochromatic microscope objective. Both these objectives have internal fluorite optics, which have very low dispersion and hence do not suffer from significant chromatic aberration.

Another change that could enhance our spectral collection would be incorporation of a water immersion objective, instead of the oil immersion one we use. This would eliminate any possibility of interference by Raman bands from the oil and allow trapping deeper into the sample cell to reduce interference from the cover-slip (204). Using a water immersion objective the trap formed will be less stiff than we obtain using oil. This and other factors would need to be taken into account while choosing a microscope objective for the OTRS.

Finally, the use of an electron multiplying CCD (EMCCD) for Raman detection might significantly increase the signal to noise while simultaneously reducing acquisition time. Due to their high gain (up to 1000 \times), EMCCDs have been recently employed to collect biological Raman spectra in milliseconds particularly in Raman based flow cytometry (215). Faster detection with higher gain would enable averaging of Raman spectra and to obtain an increase in the signal to noise.

7.5 Future goals

The OTRS system fulfilled its design goal of coupling force and molecular spectroscopy and was tested on a few model systems. The efforts mentioned in this chapter demonstrate an implementation of simultaneous optical trapping, visual imaging, Raman spectroscopy and optical force detection on biologically relevant samples.

The main application of this OTRS instrument would be to study the effect of perturbation on structural variation at the single cell level. One such application might be to monitor the effect of antibiotic peptides on single living cells. Certainly performing studies with model lipid bilayer vesicles interacting with peptides or proteins will result in simpler spectra for interpretation and offer more control on the structural changes such interactions might induce. The ultimate goal of the OTRS design would be the study of the correlation of the mechanical perturbation of the trapped cell to molecular structure of both the perturbant and cell wall components (lipids and proteins) during the interaction using Raman spectroscopy.

CITED LITERATURE

1. Dashek, W.: Plant cell biology. Enfield NH, Science Publishers, 2006.
2. Pauling, L., Corey, R. B., and Branson, H. R.: The structure of proteins: Two hydrogen-bonded helical configurations of the polypeptide chain. Proc. Natl. Acad. Sci., 37(4):205–211, April 1951.
3. Ramachandran, G., Ramakrishnan, C., and Sasisekharan, V.: Stereochemistry of polypeptide chain configurations. J. Mol. Biol., 7(1):95–99, July 1963.
4. Berman, H. M., Westbrook, J., Feng, Z., Gilliland, G., Bhat, T. N., Weissig, H., Shindyalov, I. N., and Bourne, P. E.: The Protein Data Bank. Nucleic Acids Res., 28(1):235–42, January 2000.
5. Zhou, A. Q., O'Hern, C. S., and Regan, L.: Revisiting the Ramachandran plot from a new angle. Protein Sci., 20(7):1166–71, July 2011.
6. Pace, C. N.: Evaluating contribution of hydrogen bonding and hydrophobic bonding to protein folding. Methods Enzymol., 259:538–54, January 1995.
7. Sheu, S.-Y., Yang, D.-Y., Selzle, H. L., and Schlag, E. W.: Energetics of hydrogen bonds in peptides. Proc. Natl. Acad. Sci. U. S. A., 100(22):12683–7, October 2003.
8. McDonald, I. K. and Thornton, J. M.: Satisfying hydrogen bonding potential in proteins. J. Mol. Biol., 238(5):777–93, May 1994.
9. Silva, R. A., Kubelka, J., Bour, P., Decatur, S. M., and Keiderling, T. A.: Site-specific conformational determination in thermal unfolding studies of helical peptides using vibrational circular dichroism with isotopic substitution. Proc. Natl. Acad. Sci. U. S. A., 97(15):8318–23, July 2000.
10. Kubelka, J., Huang, R., and Keiderling, T. A.: Solvent Effects on IR And VCD Spectra of Helical Peptides: Insights from Ab Initio Spectral Simulations with Explicit Water. J. Phys. Chem. B, 109:8231–8243, 2005.
11. Sean, M. D. and Decatur, S. M.: IR spectroscopy of isotope-labeled helical peptides: Probing the effect of N-acetylation on helix stability. Biopolymers, 54(3):180–185, 2000.
12. Wieczorek, R. and Dannenberg, J. J.: Alpha-helical peptides are not protonated at the N-terminus in the gas phase. J. Am. Chem. Soc., 126(39):12278–9, October 2004.

13. Palma, R.: Energy transfer along alpha-helical proteins. Int. J. Quantum Chem., 44(S19):167–177, March 1992.
14. Barlow, D. and Thornton, J.: Helix geometry in proteins. J. Mol. Biol., 201(3):601–619, June 1988.
15. Fodje, M. N. and Al-Karadaghi, S.: Occurrence, conformational features and amino acid propensities for the pi-helix. Protein Eng. Des. Sel., 15(5):353–358, May 2002.
16. Enkhbayar, P., Hikichi, K., Osaki, M., Kretsinger, R. H., and Matsushima, N.: 3(10)-helices in proteins are parahelices. Proteins, 64(3):691–9, August 2006.
17. Vieira-Pires, R. S. a. and Morais-Cabral, J. a. H.: 3(10) helices in channels and other membrane proteins. J. Gen. Physiol., 136(6):585–92, December 2010.
18. Millhauser, G. L.: Views of Helical Peptides: A Proposal for the Position of 310-Helix along the Thermodynamic Folding Pathway. Biochemistry, 34(12):3873–3877, March 1995.
19. Bezanilla, F.: How membrane proteins sense voltage. Nat. Rev. Mol. Cell Biol., 9(4):323–32, April 2008.
20. Schwaiger, C. S., Bjelkmar, P., Hess, B., and Lindahl, E.: 3(10)-helix conformation facilitates the transition of a voltage sensor S4 segment toward the down state. Biophys. J., 100(6):1446–54, March 2011.
21. Otda, K., Kitagawa, Y., Kimura, S., and Imanishi, Y.: Chain length dependent transition of 3(10)- to alpha-helix of Boc-(Ala-Aib)_n-OMe. Biopolymers, 33(9):1337–1345, September 1993.
22. Vargas, E., Yarov-Yarovoy, V., Khalili-Araghi, F., Catterall, W. A., Klein, M. L., Tarek, M., Lindahl, E., Schulten, K., Perozo, E., Bezanilla, F., and Roux, B.: An emerging consensus on voltage-dependent gating from computational modeling and molecular dynamics simulations. J. Gen. Physiol., 140(6):587–94, December 2012.
23. Swartz, K. J.: Sensing voltage across lipid membranes. Nature, 456(7224):891–7, December 2008.
24. Crisma, M., Formaggio, F., Moretto, A., and Toniolo, C.: Peptide helices based on alpha-amino acids. Biopolymers, 84(1):3–12, January 2006.
25. Karle, I. L. and Balaram, P.: Structural characteristics of .alpha.-helical peptide molecules containing Aib residues. Biochemistry, 29(29):6747–6756, July 1990.

26. Benedetti, E., Bavoso, A., Di Blasio, B., Pavone, V., Pedone, C., Crisma, M., Bonora, G. M., and Toniolo, C.: Linear oligopeptides. 81. Solid-state and solution conformation of homooligo(α -aminoisobutyric acids) from tripeptide to pentapeptide: evidence for a 3₁₀ helix. J. Am. Chem. Soc., 104(9):2437–2444, May 1982.
27. Toniolo, C., Bonora, G. M., Barone, V., Bavoso, A., Benedetti, E., Di Blasio, B., Grimaldi, P., Lelj, F., Pavone, V., and Pedone, C.: Conformation of pleionomers of α -aminoisobutyric acid. Macromolecules, 18(5):895–902, September 1985.
28. Pengo, P., Pasquato, L., Moro, S., Brigo, A., Fogolari, F., Broxterman, Q. B., Kaptein, B., and Scrimin, P.: Quantitative correlation of solvent polarity with the α -/3(10)-helix equilibrium: a heptapeptide behaves as a solvent-driven molecular spring. Angew. Chem. Int. Ed. Engl., 42(29):3388–92, July 2003.
29. Kitagawa, K., Morita, T., and Kimura, S.: A helical molecule that exhibits two lengths in response to an applied potential. Angew. Chem. Int. Ed. Engl., 44(39):6330–3, October 2005.
30. Toniolo, C., Crisma, M., Formaggio, F., and Peggion, C.: Control of peptide conformation by the Thorpe-Ingold effect (C α -tetrasubstitution). Biopolymers, 60(6):396–419, January 2001.
31. Bavoso, A., Benedetti, E., Di Blasio, B., Pavone, V., Pedone, C., Toniolo, C., and Bonora, G. M.: Long polypeptide 3₁₀-helices at atomic resolution. Proc. Natl. Acad. Sci., 83(7):1988–1992, April 1986.
32. Zhang, L. and Hermans, J.: 3₁₀ Helix Versus α -Helix: A Molecular Dynamics Study of Conformational Preferences of Aib and Alanine. J. Am. Chem. Soc., 116(26):11915–11921, December 1994.
33. MacArthur, M. W. and Thornton, J. M.: Influence of proline residues on protein conformation. J. Mol. Biol., 218(2):397–412, March 1991.
34. Li, S. C., Goto, N. K., Williams, K. A., and Deber, C. M.: α -helical, but not β -sheet, propensity of proline is determined by peptide environment. Proc. Natl. Acad. Sci., 93(13):6676–6681, June 1996.
35. von Heijne, G.: Proline kinks in transmembrane α -helices. J. Mol. Biol., 218(3):499–503, April 1991.
36. Cordes, F. S., Bright, J. N., and Sansom, M. S. P.: Proline-induced distortions of transmembrane helices. J. Mol. Biol., 323(5):951–60, November 2002.

37. Horng, J.-C. and Raines, R. T.: Stereoelectronic effects on polyproline conformation. Protein Sci., 15(1):74–83, January 2006.
38. Shi, Z. and Kallenbach, N. R.: Ramachandran redux. Proc. Natl. Acad. Sci. U. S. A., 108(1):3–4, January 2011.
39. Hinderaker, M. P. and Raines, R. T.: An electronic effect on protein structure. Protein Sci., 12(6):1188–94, June 2003.
40. Bartlett, G. J., Choudhary, A., Raines, R. T., and Woolfson, D. N.: n- \rightarrow pi* interactions in proteins. Nat. Chem. Biol., 6(8):615–20, August 2010.
41. Dukor, R. K. and Keiderling, T. A.: Reassessment of the random coil conformation: vibrational CD study of proline oligopeptides and related polypeptides. Biopolymers, 31(14):1747–61, December 1991.
42. Hamburger, J. B., Ferreon, J. C., Whitten, S. T., and Hilser, V. J.: Thermodynamic mechanism and consequences of the polyproline II (PII) structural bias in the denatured states of proteins. Biochemistry, 43(30):9790–9, August 2004.
43. Rath, A., Davidson, A. R., and Deber, C. M.: The structure of "unstructured" regions in peptides and proteins: role of the polyproline II helix in protein folding and recognition. Biopolymers, 80(2-3):179–85, January 2005.
44. Venkatachalam, C. M.: Stereochemical criteria for polypeptides and proteins. V. Conformation of a system of three linked peptide units. Biopolymers, 6(10):1425–36, October 1968.
45. Blanco, F. J., Rivas, G., and Serrano, L.: A short linear peptide that folds into a native stable β -hairpin in aqueous solution. Nat. Struct. Biol., 1(9):584–590, September 1994.
46. Hughes, R. M. and Waters, M. L.: Model systems for beta hairpins and betasheets. Curr. Opin. Struct. Biol., 16(4):514–24, August 2006.
47. Cochran, A. G., Skelton, N. J., and Starovasnik, M. A.: Tryptophan zippers: stable, monomeric beta -hairpins. Proc. Natl. Acad. Sci. U. S. A., 98(10):5578–83, May 2001.
48. McHale, J.: Molecular spectroscopy. Upper Saddle River NJ, Prentice Hall, 1999.
49. Barth, A. and Zscherp, C.: What vibrations tell us about proteins. Q. Rev. Biophys., 35(4):369–430, November 2002.
50. Miyazawa, T.: Perturbation Treatment of the Characteristic Vibrations of Polypeptide Chains in Various Configurations. J. Chem. Phys., 32(6):1647, June 1960.

51. Turner, D. R. and Kubelka, J.: Infrared and vibrational CD spectra of partially solvated alpha-helices: DFT-based simulations with explicit solvent. J. Phys. Chem. B, 111(7):1834–45, February 2007.
52. Brewer, S. H., Song, B., Raleigh, D. P., and Dyer, R. B.: Residue Specific Resolution of Protein Folding Dynamics Using Isotope-Edited Infrared Temperature Jump Spectroscopy. Biochemistry, 46:3279–3285, 2007.
53. Fesinmeyer, R. M., Peterson, E. S., Dyer, R. B., and Andersen, N. H.: Studies of helix fraying and solvation using $^{13}\text{C}'$ isotopomers. Protein Sci., 14(9):2324–32, September 2005.
54. Deflores, L. P., Ganim, Z., Nicodemus, R. A., and Tokmakoff, A.: Amide I-II' 2D IR spectroscopy provides enhanced protein secondary structural sensitivity. J. Am. Chem. Soc., 131(9):3385–91, March 2009.
55. Sen, A. C. and Keiderling, T. A.: Vibrational circular dichroism of polypeptides. II. Solution amide II and deuteration results. Biopolymers, 23(8):1519–32, August 1984.
56. Anderle, G. and Mendelsohn, R.: Thermal denaturation of globular proteins. Fourier transform-infrared studies of the amide III spectral region. Biophys. J., 52(1):69–74, July 1987.
57. Asher, S. A., Ianoul, A., Mix, G., Boyden, M. N., Karnoup, A., Diem, M., and Schweitzer-Stenner, R.: Dihedral ψ Angle Dependence of the Amide III Vibration- A Uniquely Sensitive UV Resonance Raman Secondary Structural Probe. J. Am. Chem. Soc., 123(47):11775–11781, November 2001.
58. Mirkin, N. G. and Krimm, S.: A New Vibrational Spectroscopic Tool for the Determination of Peptide Conformation: The Isotope-Edited C α H α Stretch Mode. J. Phys. Chem. A, 108(50):10923–10924, December 2004.
59. Maekawa, H., De Poli, M., Toniolo, C., and Ge, N.-H.: Couplings between peptide linkages across a 3(10)-helical hydrogen bond revealed by two-dimensional infrared spectroscopy. J. Am. Chem. Soc., 131(6):2042–3, February 2009.
60. Muto, K., Yoshida, R., Yashida, R., Ishii, T., and Handa, T.: Circular dichroism of the backbone and side chains separated from natural circular dichroism of poly-L-tryptophan by the fluorescence detected circular dichroism method. J. Am. Chem. Soc., 108(20):6416–6417, 1986.
61. Kubelka, J. and Keiderling, T. A.: The anomalous infrared amide I intensity distribution in ^{13}C isotopically labeled peptide β -sheets comes from extended, multiple-stranded structures. An ab initio study. J. Am. Chem. Soc., 123:6142–6150, 2001.

62. Keiderling, T. a.: Protein and peptide secondary structure and conformational determination with vibrational circular dichroism. Curr. Opin. Chem. Biol., 6(5):682–8, October 2002.
63. Grdadolnik, J., Mohacek-Grosev, V., Baldwin, R. L., and Avbelj, F.: Populations of the three major backbone conformations in 19 amino acid dipeptides. Proc. Natl. Acad. Sci. U. S. A., 108(5):1794–8, February 2011.
64. Eker, F., Cao, X., Nafie, L., and Schweitzer-Stenner, R.: Tripeptides Adopt Stable Structures in Water. A Combined Polarized Visible Raman, FTIR, and VCD Spectroscopy Study. J. Am. Chem. Soc., 124(48):14330–14341, December 2002.
65. Chi, Z., Chen, X. G., Holtz, J. S. W., and Asher, S. A.: UV Resonance Raman-Selective Amide Vibrational Enhancement- Quantitative Methodology for Determining Protein Secondary Structure. Biochemistry, 37(9):2854–2864, March 1998.
66. Schlamadinger, D. E., Gable, J. E., and Kim, J. E.: Hydrogen bonding and solvent polarity markers in the uv resonance raman spectrum of tryptophan: application to membrane proteins. J. Phys. Chem. B, 113(44):14769–78, November 2009.
67. Takekiyo, T., Wu, L., Yoshimura, Y., Shimizu, A., and Keiderling, T. A.: Relationship between hydrophobic interactions and secondary structure stability for Trpzip beta-hairpin peptides. Biochemistry, 48(7):1543–52, February 2009.
68. Leitner, D. M.: Vibrational Energy Transfer in Helices. Phys. Rev. Lett., 87(18):188102, October 2001.
69. Botan, V., Backus, E. H. G., Pfister, R., Moretto, A., Crisma, M., Toniolo, C., Nguyen, P. H., Stock, G., and Hamm, P.: Energy transport in peptide helices. Proc. Natl. Acad. Sci. U. S. A., 104(31):12749–54, July 2007.
70. Wilson, E. B.: A Method of Obtaining the Expanded Secular Equation for the Vibration Frequencies of a Molecule. J. Chem. Phys., 7(11):1047, November 1939.
71. Hohenberg, P.: Inhomogeneous Electron Gas. Phys. Rev., 136(3B):B864–B871, November 1964.
72. Jensen, F.: Introduction to computational chemistry. Chichester [u.a.], Wiley, 2007.
73. Kohn, W. and Sham, L. J.: Self-Consistent Equations Including Exchange and Correlation Effects. Phys. Rev., 140(4A):A1133–A1138, November 1965.

74. Perdew, J. P. and Wang, Y.: Accurate and simple analytic representation of the electron-gas correlation energy. Phys. Rev. B, 45(23):13244–13249, June 1992.
75. Becke, A. D.: Density-functional exchange-energy approximation with correct asymptotic behavior. Phys. Rev. A, 38(6):3098–3100, September 1988.
76. Kubelka, J., Bour, P., and Keiderling, T. A.: Quantum Mechanical Calculations of Peptide Vibrational Force Fields and Spectral Intensities. In Biol. Biomed. Infrared Spectrosc., eds. A. Barth and P. Haris, Adv. Biomedical Spectroscopy, Vol. 2, pages 178–223. Amsterdam, IOS Press, 2009.
77. Hehre, W. J.: Self-Consistent Molecular-Orbital Methods. I. Use of Gaussian Expansions of Slater-Type Atomic Orbitals. J. Chem. Phys., 51(6):2657, September 1969.
78. Kubelka, J. and Keiderling, T. A.: Ab Initio Calculation of Amide Carbonyl Stretch Vibrational Frequencies in Solution with Modified Basis Sets. 1. N -Methyl Acetamide. J. Phys. Chem. A, 105(48):10922–10928, December 2001.
79. Kim, J., Huang, R., Kubelka, J., Bour, P., and Keiderling, T. A.: Simulation of IR spectra for b-hairpin peptides stabilized by an Aib-Gly turn sequence: correlation between conformational fluctuation and vibrational coupling. J. Phys. Chem. B, 110:23590–23602, 2006.
80. Jensen, J. H.: Molecular Modeling Basics. Taylor & Francis Group, 2010.
81. Nafie, L.: Vibrational optical activity principles and applications. Chichester [England] ;;Syracuse, N.Y. :, Wiley, 2011.
82. Stephens, P. J., Jalkanen, K. J., and Kawiecki, R. W.: Theory of vibrational rotational strengths: comparison of a priori theory and approximate models. J. Am. Chem. Soc., 112(18):6518–6529, August 1990.
83. Rosenfeld, L.: Quantenmechanische Theorie der natürlichen optischen Aktivitat von Flüssigkeiten und Gasen. Zeitschrift fur Phys., 52(3-4):161–174, March 1929.
84. Stephens, P. J., Devlin, F. J., and Pan, J.-j.: Review Article The Determination of the Absolute Configurations of Chiral Molecules Using Vibrational Circular Dichroism (VCD) Spectroscopy. Chirality, 663(August 2007):643–663, 2008.
85. Cheeseman, J., Frisch, M., Devlin, F., and Stephens, P.: Ab initio calculation of atomic axial tensors and vibrational rotational strengths using density functional theory. Chem. Phys. Lett., 252(3-4):211–220, April 1996.

86. Ruud, K., Helgaker, T., Bak, K. L., Jorgensen, P., and Jensen, H. J. A.: Hartree-Fock limit magnetizabilities from London orbitals. J. Chem. Phys., 99(5):3847, September 1993.
87. Tang, J.: Studies in Raman Intensity Theory. J. Chem. Phys., 49(3):1144, August 1968.
88. Barone, V. and Cossi, M.: Quantum Calculation of Molecular Energies and Energy Gradients in Solution by a Conductor Solvent Model. J. Phys. Chem. A, 102(11):1995–2001, March 1998.
89. Klamt, A. and Schuurmann, G.: COSMO: a new approach to dielectric screening in solvents with explicit expressions for the screening energy and its gradient. J. Chem. Soc. Perkin Trans. 2, (5):799, January 1993.
90. Takano, Y. and Houk, K. N.: Benchmarking the Conductor-like Polarizable Continuum Model (CPCM) for Aqueous Solvation Free Energies of Neutral and Ionic Organic Molecules. J. Chem. Theory Comput., 1(1):70–77, January 2005.
91. Svensson, M., Humbel, S., Froese, R. D. J., Matsubara, T., Sieber, S., and Morokuma, K.: ONIOM A Multilayered Integrated MO + MM Method for Geometry Optimizations and Single Point Energy Predictions. A Test for Diels-Alder Reactions and Pt(P(t-Bu)₃)₂ + H₂ Oxidative Addition. J. Phys. Chem., 100(50):19357–19363, January 1996.
92. Kubelka, J., Silva, R. A. G. D., and Keiderling, T. A.: Discrimination between Peptide 3(10) - and α -Helices. Theoretical Analysis of the Impact of α -Methyl Substitution on Experimental Spectra. J. Am. Chem. Soc., 124(19):5325–5332, May 2002.
93. Bour, P., Sopkova, J., Bednarova, L., Malon, P., and Keiderling, T. A.: Transfer of molecular property tensors in cartesian coordinates: A new algorithm for simulation of vibrational spectra. J. Comput. Chem., 18(5):646–659, April 1997.
94. Jacob, C. R., Lubber, S., and Reiher, M.: Analysis of secondary structure effects on the IR and Raman spectra of polypeptides in terms of localized vibrations. J. Phys. Chem. B, 113(18):6558–73, May 2009.
95. Autschbach, J.: Computing chiroptical properties with first-principles theoretical methods: background and illustrative examples. Chirality, 21 Suppl 1:E116–52, January 2009.
96. Runge, E. and Gross, E. K. U.: Density-Functional Theory for Time-Dependent Systems. Phys. Rev. Lett., 52(12):997–1000, March 1984.
97. Foerster, D.: Fast computation of the Kohn-Sham susceptibility of large systems. Phys. Rev. B, 72(7):073106, August 2005.

98. Ullrich, C. A.: Time-dependent density-functional theory beyond the adiabatic approximation: insights from a two-electron model system. *J. Chem. Phys.*, 125(23):234108, December 2006.
99. Marques, M.: Time-dependent density functional theory, 2006.
100. Casida, M. E., Jamorski, C., Casida, K. C., and Salahub, D. R.: Molecular excitation energies to high-lying bound states from time-dependent density-functional response theory: Characterization and correction of the time-dependent local density approximation ionization threshold. *J. Chem. Phys.*, 108(11):4439, March 1998.
101. Frisch, M. J., Trucks, G. W., Schlegel, H. B., Scuseria, G. E., Robb, M. A., Cheeseman, J. R., Scalmani, G., Barone, V., Mennucci, B., Petersson, G. A., Nakatsuji, H., Caricato, M., Li, X., Hratchian, H. P., Izmaylov, A. F., Bloino, J., Zheng, G., Sonnenberg, J. L., Hada, M., Ehara, M., Toyota, K., Fukuda, R., Hasegawa, J., Ishida, M., Nakajima, T., Honda, Y., Kitao, O., Nakai, H., Vreven, T., Montgomery Jr., J. A., Peralta, J. E., Ogliaro, F., Bearpark, M., Heyd, J. J., Brothers, E., Kudin, K. N., Staroverov, V. N., Kobayashi, R., Normand, J., Raghavachari, K., Rendell, A., Burant, J. C., Iyengar, S. S., Tomasi, J., Cossi, M., Rega, N., Millam, J. M., Klene, M., Knox, J. E., Cross, J. B., Bakken, V., Adamo, C., Jaramillo, J., Gomperts, R., Stratmann, R. E., Yazyev, O., Austin, A. J., Cammi, R., Pomelli, C., Ochterski, J. W., Martin, R. L., Morokuma, K., Zakrzewski, V. G., Voth, G. A., Salvador, P., Dannenberg, J. J., Dapprich, S., Daniels, A. D., Farkas, O., Foresman, J. B., Ortiz, J. V., Cioslowski, J., and Fox, D. J.: Gaussian09 Revision D.02.
102. Rappoport, D. and Furche, F.: Analytical time-dependent density functional derivative methods within the RI-J approximation, an approach to excited states of large molecules. *J. Chem. Phys.*, 122(6):064105, March 2005.
103. Huang, R., Kubelka, J., Barber-Armstrong, W., Silva, R. A. G. D., Decatur, S. M., and Keiderling, T. A.: Nature of vibrational coupling in helical peptides: an isotopic labeling study. *J. Am. Chem. Soc.*, 126(8):2346–54, March 2004.
104. Kubelka Jan, Bour Petr, Silva R. A. Gangani D., Decatur Sean M., and Keiderling Timothy A.: *Chirality: Physical Chemistry*, volume 810 of *ACS Symposium Series*. Washington, DC, American Chemical Society, March 2002.
105. Benedetti, E., Di Blasio, B., Pavone, V., Pedone, C., Toniolo, C., and Crisma, M.: Characterization at atomic resolution of peptide helical structures. *Biopolymers*, 32(4):453–6, April 1992.
106. Silva, R. A. G. D., Yasui, S. C., Kubelka, J., Formaggio, F., Crisma, M., Toniolo, C., and Keiderling, T. A.: Discriminating 3(10)- from alpha-helices: vibrational and electronic

- CD and IR absorption study of related Aib-containing oligopeptides. Biopolymers, 65(4):229–43, November 2002.
107. Lakhani, A.: A New Dispersive Vibrational Circular Dichroism Instrument: Development, Testing, and Application. Doctoral dissertation, 2011.
108. Lakhani, A., Roy, A., De Poli, M., Nakaema, M., Formaggio, F., Toniolo, C., and Keiderling, T. A.: Experimental and theoretical spectroscopic study of 3(10)-helical peptides using isotopic labeling to evaluate vibrational coupling. J. Phys. Chem. B, 115(19):6252–64, May 2011.
109. Chi, H., Lakhani, A., Roy, A., Nakaema, M., and Keiderling, T. A.: Inter-residue coupling and equilibrium unfolding of PPII helical peptides. Vibrational spectra enhanced with (13)C isotopic labeling. J. Phys. Chem. B, 114(39):12744–53, October 2010.
110. Tiffany, M. L. and Krimm, S.: New chain conformations of poly(glutamic acid) and polylysine. Biopolymers, 6(9):1379–82, January 1968.
111. Bour, P. and Keiderling, T. A.: Ab initio modeling of amide I coupling in antiparallel beta-sheets and the effect of 13C isotopic labeling on infrared spectra. J. Phys. Chem. B, 109(11):5348–57, March 2005.
112. Torres, J., Kukol, A., Goodman, J. M., and Arkin, I. T.: Site-specific examination of secondary structure and orientation determination in membrane proteins: the peptidic (13)C=(18)O group as a novel infrared probe. Biopolymers, 59(6):396–401, November 2001.
113. Smith, A. W. and Tokmakoff, A.: Probing Local Structural Events in β -Hairpin Unfolding with Transient Nonlinear Infrared Spectroscopy. Angew. Chemie, 119(42):8130–8133, October 2007.
114. Decatur, S. M.: Elucidation of residue-level structure and dynamics of polypeptides via isotope-edited infrared spectroscopy. Acc. Chem. Res., 39(3):169–75, March 2006.
115. Wang, J., Chen, J., and Hochstrasser, R. M.: Local structure of beta-hairpin isotopomers by FTIR, 2D IR, and ab initio theory. J. Phys. Chem. B, 110(14):7545–55, April 2006.
116. Pitera, J. W., Haque, I., and Swope, W. C.: Absence of reptation in the high-temperature folding of the trpzip2 beta-hairpin peptide. J. Chem. Phys., 124(14):141102, April 2006.

117. Snow, C. D., Qiu, L., Du, D., Gai, F., Hagen, S. J., and Pande, V. S.: Trp zipper folding kinetics by molecular dynamics and temperature-jump spectroscopy. Proc. Natl. Acad. Sci. U. S. A., 101(12):4077–82, March 2004.
118. Hauser, K., Ridderbusch, O., Roy, A., Hellerbach, A., Huang, R., and Keiderling, T. A.: Comparison of isotopic substitution methods for equilibrium and t-jump infrared studies of beta-hairpin peptide conformation. J. Phys. Chem. B, 114(35):11628–37, September 2010.
119. Huang, R., Wu, L., McElheny, D., Bour, P., Roy, A., and Keiderling, T. A.: Cross-strand coupling and site-specific unfolding thermodynamics of a trpzip beta-hairpin peptide using ¹³C isotopic labeling and IR spectroscopy. J. Phys. Chem. B, 113(16):5661–74, April 2009.
120. Huang, R., Setnicka, V., Etienne, M. A., Kim, J., Kubelka, J., Hammer, R. P., and Keiderling, T. A.: Cross-strand coupling of a b-hairpin peptide stabilized with an Aib-Gly turn using isotope-edited IR spectroscopy. J. Am. Chem. Soc., 129(44):13592–13603, 2007.
121. Paier, J., Marsman, M., and Kresse, G.: Why does the B3LYP hybrid functional fail for metals? J. Chem. Phys., 127(2):024103, July 2007.
122. Bour, P. and Keiderling, T. A.: Vibrational spectral simulation for peptides of mixed secondary structure: method comparisons with the Trpzip model hairpin. J. Phys. Chem. B, 109(49):23687–97, December 2005.
123. Setnicka, V., Huang, R., Thomas, C. L., Etienne, M. A., Kubelka, J., Hammer, R. P., and Keiderling, T. A.: IR study of cross-strand coupling in a beta-hairpin peptide using isotopic labels. J. Am. Chem. Soc., 127(14):4992–3, April 2005.
124. Kim, Y. S., Liu, L., Axelsen, P. H., and Hochstrasser, R. M.: Two dimensional infrared spectra of isotopically diluted amyloid fibrils from Ab40. Proc. Nat. Acad. Sci. USA, 105:7720–7725, 2008.
125. Kim, J. and Keiderling, T. A.: All-atom molecular dynamics simulations of beta-hairpins stabilized by a tight turn: pronounced heterogeneous folding pathways. J. Phys. Chem. B, 114(25):8494–504, July 2010.
126. Hauser, K., Krejtschi, C., Huang, R., Wu, L., and Keiderling, T. A.: Site-specific relaxation kinetics of a tryptophan zipper hairpin peptide using temperature-jump IR spectroscopy and isotopic labeling. J. Am. Chem. Soc., 130(10):2984–92, March 2008.
127. Wu, L., McElheny, D., Huang, R., and Keiderling, T. A.: Role of tryptophan-tryptophan interactions in Trpzip beta-hairpin formation, structure, and stability. Biochemistry, 48(43):10362–71, November 2009.

128. Wu, L., McElheny, D., Takekiyo, T., and Keiderling, T. A.: Geometry and efficacy of cross-strand Trp/Trp, Trp/Tyr, and Tyr/Tyr aromatic interaction in a beta-hairpin peptide. Biochemistry, 49(22):4705–14, June 2010.
129. Tatko, C. and Waters, M. L.: Selective Aromatic Interactions in Beta-Hairpin Peptides. J. Am. Chem. Soc., 124:9372–9373, 2002.
130. Cochran, A. G., Skelton, N. J., and Starovasnik, M. A.: Correction. Proc. Natl. Acad. Sci., 99(13):9081–9081, June 2002.
131. Rogers, D. M., Besley, N. A., O’Shea, P., and Hirst, J. D.: Modeling the absorption spectrum of tryptophan in proteins. J. Phys. Chem. B, 109(48):23061–9, December 2005.
132. Dedonder-Lardeux, C., Jouvét, C., Perun, S., and Sobolewski, A. L.: External electric field effect on the lowest excited states of indole: ab initio and molecular dynamics study. Phys. Chem. Chem. Phys., 5(22):5118, 2003.
133. Platt, J. R.: Classification of Spectra of Cata-Condensed Hydrocarbons. J. Chem. Phys., 17(5):484–495, 1949.
134. Vivian, J. T. and Callis, P. R.: Mechanisms of tryptophan fluorescence shifts in proteins. Biophys. J., 80(5):2093–2109, May 2001.
135. Robinson, D., Besley, N. A., Lunt, E. A. M., O’Shea, P., and Hirst, J. D.: Electronic Structure of 5-Hydroxyindole: From Gas Phase to Explicit Solvation. J. Phys. Chem. B, 113(8):2535–2541, 2009.
136. Slater, L. S. and Callis, P. R.: Molecular-Orbital Theory of the 1La and 1Lb States of Indole .2. an Ab-Initio Study. J. Phys. Chem., 99(21):8572–8581, May 1995.
137. Grishina, I. B. and Woody, R. W.: Contributions of tryptophan side chains to the circular dichroism of globular proteins: exciton couplets and coupled oscillators. Faraday Discuss., 99(99):245, 1994.
138. Grimme, S. and Parac, M.: Substantial errors from time-dependent density functional theory for the calculation of excited states of large pi systems. Chemphyschem, 4(3):292–295, March 2003.
139. Sebek, J. and Bour, P.: Ab Initio Modeling of the Electronic Circular Dichroism Induced in Porphyrin Chromophores. J. Phys. Chem. A, 112(13):2920–2929, 2008.

140. Mennucci, B. and Tomasi, J.: Continuum solvation models: A new approach to the problem of solute's charge distribution and cavity boundaries. *J. Chem. Phys.*, 106(12):5151–5158, March 1997.
141. Frisch, M. J., Trucks, G. W., Schlegel, H. B., Scuseria, G. E., Robb, M. A., Cheeseman, J. R., Montgomery Jr., J. A., Vreven, T., Kudin, K. N., Burant, J. C., Millam, J. M., Iyengar, S. S., Tomasi, J., Barone, V., Mennucci, B., Cossi, M., Scalmani, G., Rega, N., Petersson, G. A., Nakatsuji, H., Hada, M., Ehara, M., Toyota, K., Fukuda, R., Hasegawa, J., Ishida, M., Nakajima, T., Honda, Y., Kitao, O., Nakai, H., Klene, M., Li, X., Knox, J. E., Hratchian, H. P., Cross, J. B., Bakken, V., Adamo, C., Jaramillo, J., Gomperts, R., Stratmann, R. E., Yazyev, O., Austin, A. J., Cammi, R., Pomelli, C., Ochterski, J. W., Ayala, P. Y., Morokuma, K., Voth, G. A., Salvador, P., Dannenberg, J. J., Zakrzewski, V. G., Dapprich, S., Daniels, A. D., Strain, M. C., Farkas, O., Malick, D. K., Rabuck, A. D., Raghavachari, K., Foresman, J. B., Ortiz, J. V., Cui, Q., Baboul, A. G., Clifford, S., Cioslowski, J., Stefanov, B. B., Liu, G., Liashenko, A., Piskorz, P., Komaromi, I., Martin, R. L., Fox, D. J., Keith, T., Al-Laham, M. A., Peng, C. Y., Nanayakkara, A., Challacombe, M., Gill, P. M. W., Johnson, B., Chen, W., Wong, M. W., Gonzalez, C., and Pople, J. A.: Gaussian 03, Revision D.02.
142. TURBOMOLE V6.5 2013, a development of University of Karlsruhe and Forschungszentrum Karlsruhe GmbH, 1989-2007, TURBOMOLE GmbH, since 2007.
143. Zhong, W., Gulotta, M., Goss, D. J., and Diem, M.: DNA solution conformation via infrared circular dichroism: experimental and theoretical results for B-family polymers. *Biochemistry*, 29(32):7485–7491, 1990.
144. Charney, E.: *The Molecular Basis of Optical Activity*. New York, Wiley, 1979.
145. Rogers, D. M. and Hirst, J. D.: First-principles calculations of protein circular dichroism in the near ultraviolet. *Biochemistry*, 43(34):11092–102, August 2004.
146. Tomasvert, F., Ponce, C. A., Estrada, M. R., Silber, J., Singh, J., and Anunciatta, J.: Experimental and Theoretical-Studies on the Electronic-Spectra of Indole-3-Acetic-Acid and Its Anionic and Protonated Species. *J. Mol. Struct.*, 246(3-4):203–215, June 1991.
147. Albinsson, B. and Norden, B.: Excited-state properties of the indole chromophore: electronic transition moment directions from linear dichroism measurements: effect of methyl and methoxy substituents. *J. Phys. Chem.*, 96(15):6204–6212, 1992.
148. Singh, G. P., Creely, C. M., Volpe, G., Grötsch, H., and Petrov, D.: Real-time detection of hyperosmotic stress response in optically trapped single yeast cells using Raman microspectroscopy. *Anal. Chem.*, 77(8):2564–8, April 2005.

149. Chan, J. W.: Recent advances in laser tweezers Raman spectroscopy (LTRS) for label-free analysis of single cells. J. Biophotonics, 6(1):36–48, January 2013.
150. Lau, A. Y., Lee, L. P., and Chan, J. W.: An integrated optofluidic platform for Raman-activated cell sorting. Lab Chip, 8(7):1116–20, July 2008.
151. Li, M., Xu, J., Romero-Gonzalez, M., Banwart, S. A., Huang, W. E., and Zhou, J.: Single cell Raman spectroscopy for cell sorting and imaging. Curr. Opin. Biotechnol., 23(1):56–63, February 2012.
152. Wolf, I. D.: Micro-Raman spectroscopy to study local mechanical stress in silicon integrated circuits. Semicond. Sci. Technol., 11(2):139–154, February 1996.
153. Tyler, S. W., Selker, J. S., Hausner, M. B., Hatch, C. E., Torgersen, T., Thodal, C. E., and Schladow, S. G.: Environmental temperature sensing using Raman spectra DTS fiber-optic methods. Water Resour. Res., 45(4):1–11, April 2009.
154. Chalmers, J.: Raman spectroscopy in archaeology and art history. Cambridge, Royal Society of Chemistry, 2005.
155. Vandenabeele, P., Edwards, H. G. M., and Jehlička, J.: The role of mobile instrumentation in novel applications of Raman spectroscopy: archaeometry, geosciences, and forensics. Chem. Soc. Rev., 43:2628–2649, January 2014.
156. Chrimes, A. F., Khoshmanesh, K., Stoddart, P. R., Mitchell, A., and Kalantar-Zadeh, K.: Microfluidics and Raman microscopy: current applications and future challenges. Chem. Soc. Rev., 42(13):5880–906, July 2013.
157. Tuma, R.: Raman spectroscopy of proteins: from peptides to large assemblies. J. Raman Spectrosc., 36(4):307–319, April 2005.
158. Wu, H., Volponi, J. V., Oliver, A. E., Parikh, A. N., Simmons, B. A., and Singh, S.: In vivo lipidomics using single-cell Raman spectroscopy. Proc. Natl. Acad. Sci. U. S. A., 108(9):3809–14, March 2011.
159. Teh, S. K., Zheng, W., Ho, K. Y., Teh, M., Yeoh, K. G., and Huang, Z.: Diagnostic potential of near-infrared Raman spectroscopy in the stomach: differentiating dysplasia from normal tissue. Br. J. Cancer, 98(2):457–65, January 2008.
160. Moritz, T. J., Taylor, D. S., Krol, D. M., Fritch, J., and Chan, J. W.: Detection of doxorubicin-induced apoptosis of leukemic T-lymphocytes by laser tweezers Raman spectroscopy. Biomed. Opt. Express, 1(4):1138–1147, January 2010.

161. Li, M., Boardman, D. G., Ward, A., and Huang, W. E.: Single-cell Raman sorting. Methods Mol. Biol., 1096:147–53, January 2014.
162. Raman, C. V. and Krishnan, K. S.: A New Type of Secondary Radiation. Nature, 121:501–502, 1928.
163. McCreery, R.: Raman spectroscopy for chemical analysis. New York, Wiley-Interscience, 2000.
164. Asher, S. A.: UV resonance Raman spectroscopy for analytical, physical, and biophysical chemistry. Part 1. Anal. Chem., 65(2):59A–66A, January 1993.
165. Kneipp, K. and Kneipp, H.: Single molecule Raman scattering. Appl. Spectrosc., 60(12):322A–334A, 2006.
166. Bailo, E. and Deckert, V.: Tip-enhanced Raman spectroscopy of single RNA strands: towards a novel direct-sequencing method. Angew. Chem. Int. Ed. Engl., 47(9):1658–61, January 2008.
167. Adar, F., Delhaye, M., and DaSilva, E.: Evolution of Instrumentation for Detection of the Raman Effect as Driven by Available Technologies and by Developing Applications. J. Chem. Educ., 84(1):50–60, January 2007.
168. Denson, S. C., Pommier, C. J. S., and Denton, M. B.: The Impact of Array Detectors on Raman Spectroscopy. J. Chem. Educ., 84(1):67–74, January 2007.
169. Cherney, D. P. and Harris, J. M.: Confocal Raman microscopy of optical-trapped particles in liquids. Annu. Rev. Anal. Chem., 3:277–97, January 2010.
170. Petrov, D. V.: Raman spectroscopy of optically trapped particles. J. Opt. A Pure Appl. Opt., 9(8):S139–S156, August 2007.
171. Ashkin, A.: Acceleration and Trapping of Particles by Radiation Pressure. Phys. Rev. Lett., 24(4):156–159, January 1970.
172. Ashkin, A., Dziedzic, J. M., and Yamane, T.: Optical trapping and manipulation of single cells using infrared laser beams. Nature, 330(6150):769–71, January 1987.
173. Smith, S. P.: Inexpensive optical tweezers for undergraduate laboratories. Am. J. Phys., 67(1):26–35, January 1999.
174. Appleyard, D. C., Vandermeulen, K. Y., Lee, H., and Lang, M. J.: Optical trapping for undergraduates. Am. J. Phys., 75(1):5–14, January 2007.

175. Piggee, C.: Optical tweezers: not just for physicists anymore. Anal. Chem., 81(1):16–19, January 2009.
176. Matthews, J. N. A.: Commercial optical traps emerge from biophysics labs. Phys. Today, 62(2):26, February 2009.
177. Xie, C., Chen, D., and Li, Y.-q.: Raman sorting and identification of single living microorganisms with optical tweezers. Opt. Lett., 30(14):1800–1802, July 2005.
178. Pelton, M., Liu, M., Kim, H. Y., Smith, G., Guyot-Sionnest, P., and Scherer, N. F.: Optical trapping and alignment of single gold nanorods by using plasmon resonances. Opt. Lett., 31(13):2075–2077, 2006.
179. Svoboda, K. and Block, S. M.: Optical trapping of metallic Rayleigh particles. Opt. Lett., 19(13):930–932, July 1994.
180. Hansen, P. M., Bhatia, V. K. I., Harrit, N., and Oddershede, L.: Expanding the Optical Trapping Range of Gold Nanoparticles. Nano Lett., 5(10):1937–1942, October 2005.
181. Visscher, K., Gross, S., and Block, S.: Construction of multiple-beam optical traps with nanometer-resolution position sensing. IEEE J. Sel. Top. Quantum Electron., 2(4):1066–1076, 1996.
182. Gittes, F. and Schmidt, C. F.: Interference model for back-focal-plane displacement detection in optical tweezers. Opt. Lett., 23(1):7, January 1998.
183. Jauffred, L. and Oddershede, L. B.: Two-photon quantum dot excitation during optical trapping. Nano Lett., 10(5):1927–1930, May 2010.
184. Thurn, R. and Kiefer, W.: Observations of structural resonances in the Raman spectra of optically levitated dielectric microspheres. J. Raman Spectrosc., 15(6):411–413, December 1984.
185. Ajito, K., Morita, M., and Torimitsu, K.: Investigation of the Molecular Extraction Process in Single Subpicoliter Droplets Using a Near-Infrared Laser Raman Trapping System. Anal. Chem., 72(19):4721–4725, October 2000.
186. Neuman, K. C., Chadd, E. H., Liou, G. F., Bergman, K., and Block, S. M.: Characterization of photodamage to Escherichia coli in optical traps. Biophys. J., 77(5):2856–63, November 1999.
187. Celliers, P. M. and Conia, J.: Measurement of Localized Heating in the Focus of an Optical Trap. Appl. Opt., 39(19):3396–3407, July 2000.

188. Neuman, K. C. and Block, S. M.: Optical trapping. Rev. Sci. Instrum., 75(9):2787–809, September 2004.
189. Kong, L., Zhang, P., Wang, G., Yu, J., Setlow, P., and Li, Y.: Characterization of bacterial spore germination using phase-contrast and fluorescence microscopy, Raman spectroscopy and optical tweezers. Nat. Protoc., 6(5):625–39, May 2011.
190. Block, S. M.: Cells: A Laboratory Manual. Vol. 3, Subcellular Localization of Genes and Their Products, Volume 3. In Cells A Lab. Manual. Vol. 3, Subcell. Localization Genes Their Prod. Vol. 3, eds. D. L. Spector, R. D. Goldman, and L. A. Leinwand, chapter 11. Cold Spring Harbor Laboratory Press, 1997.
191. Block, S. M.: Construction of optical tweezers. Cells A Lab. Man., 2:81, 1998.
192. Martínez, I., Roldán, E., Parrondo, J., and Petrov, D.: Effective heating to several thousand kelvins of an optically trapped sphere in a liquid. Phys. Rev. E, 87(3):032159, March 2013.
193. Dochow, S., Krafft, C., Neugebauer, U., Bocklitz, T., Henkel, T., Mayer, G., Albert, J., and Popp, J.: Tumour cell identification by means of Raman spectroscopy in combination with optical traps and microfluidic environments. Lab Chip, 11(8):1484–90, April 2011.
194. Kong, L., Zhang, P., Yu, J., Setlow, P., and Li, Y.-q.: Rapid confocal Raman imaging using a synchro multifoci-scan scheme for dynamic monitoring of single living cells. Appl. Phys. Lett., 98(21):213703, May 2011.
195. Houlne, M. P., Sjoström, C. M., Uibel, R. H., Kleimeyer, J. A., and Harris, J. M.: Confocal Raman Microscopy for Monitoring Chemical Reactions on Single Optically Trapped, Solid-Phase Support Particles. Anal. Chem., 74(17):4311–4319, September 2002.
196. Xie, C. and Li, Y.: Confocal micro-Raman spectroscopy of single biological cells using optical trapping and shifted excitation difference techniques. J. Appl. Phys., 93(5):2982, 2003.
197. Williams, K. P. J., Batchelder, D. N., Kip, B. J., and Pitt, G. D.: Confocal Raman Microspectroscopy Using a Stigmatic Spectrograph and CCD Detector. Appl. Spectrosc., 48(2):232–235, February 1994.
198. Carlsson, K. and Aslund, N.: Confocal imaging for 3-D digital microscopy. Appl. Opt., 26(16):3232–8, August 1987.
199. McCreery, R. L.: Raman Spectroscopy for Chemical Analysis. Meas. Sci. Technol., 12(5):653, 2001.

200. Freebody, N. A., Vaughan, A. S., and Macdonald, A. M.: On optical depth profiling using confocal Raman spectroscopy. Anal. Bioanal. Chem., 396(8):2813–23, April 2010.
201. Reihani, S. N. S. and Oddershede, L. B.: Optimizing immersion media refractive index improves optical trapping by compensating spherical aberrations. Opt. Lett., 32(14):1998, 2007.
202. Aggarwal, R., Farrar, L., Saikin, S., Aspuru-Guzik, A., Stopa, M., and Polla, D.: Measurement of the absolute Raman cross section of the optical phonon in silicon. Solid State Commun., 151(7):553–556, April 2011.
203. Xie, C. and Li, Y.: Raman spectra and optical trapping of highly refractive and nontransparent particles. Appl. Phys. Lett., 81(6):951, August 2002.
204. Jonas, A., Jezek, J., Sery, M., and Zemanek, P.: Raman microspectroscopy of optically trapped micro- and nanoobjects. 16th Polish-Slovak-Czech Opt. Conf. Wave Quantum Asp. Contemp. Opt., pages 714111–8, December 2008.
205. Liang, C. Y. and Krimm, S.: Infrared spectra of high polymers. VI. Polystyrene. J. Polym. Sci., 27(115):241–254, 1958.
206. Alexandrov, T. and Lasch, P.: Segmentation of confocal Raman microspectroscopic imaging data using edge-preserving denoising and clustering. Anal. Chem., 85(12):5676–83, June 2013.
207. Xie, C., Dinno, M. A., and Li, Y.: Near-infrared Raman spectroscopy of single optically trapped biological cells. Opt. Lett., 27(4):249–251, February 2002.
208. Harvey, T. J., Hughes, C., Ward, A. D., Faria, E. C., Henderson, A., Clarke, N. W., Brown, M. D., Snook, R. D., and Gardner, P.: Classification of fixed urological cells using Raman tweezers. J. Biophotonics, 2(1-2):47–69, February 2009.
209. Savitzky, A. and Golay, M. J. E.: Smoothing and Differentiation of Data by Simplified Least Squares Procedures. Anal. Chem., 36(8):1627–1639, July 1964.
210. Talley, C. E., Jackson, J. B., Oubre, C., Grady, N. K., Hollars, C. W., Lane, S. M., Huser, T. R., Nordlander, P., and Halas, N. J.: Surface-enhanced Raman scattering from individual Au nanoparticles and nanoparticle dimer substrates. Nano Lett., 5(8):1569–74, August 2005.
211. Messina, E., Cavallaro, E., Cacciola, A., Saija, R., Borghese, F., Denti, P., Fazio, B., D'Andrea, C., Gucciardi, P. G., Iatii, M. A., Meneghetti, M., Compagnini, G., Amendola, V., and Marago, O. M.: Manipulation and Raman Spectroscopy with Optically Trapped

Metal Nanoparticles Obtained by Pulsed Laser Ablation in Liquids. J. Phys. Chem. C, 115(12):5115–5122, March 2011.

212. von Maltzahn, G., Centrone, A., Park, J.-H., Ramanathan, R., Sailor, M. J., Hatton, T. A., and Bhatia, S. N.: SERS-Coded Gold Nanorods as a Multifunctional Platform for Densely Multiplexed Near-Infrared Imaging and Photothermal Heating. Adv. Mater., 21(31):3175–3180, April 2009.
213. Guillot, N., Shen, H., Fremaux, B., Peron, O., Rinnert, E., Toury, T., and Lamy de la Chapelle, M.: Surface enhanced Raman scattering optimization of gold nanocylinder arrays: Influence of the localized surface plasmon resonance and excitation wavelength. Appl. Phys. Lett., 97(2):023113, July 2010.
214. Seol, Y., Carpenter, A. E., and Perkins, T. T.: Gold nanoparticles: enhanced optical trapping and sensitivity coupled with significant heating. Opt. Lett., 31(16):2429, 2006.
215. Watson, D. A., Brown, L. O., Gaskill, D. F., Naivar, M., Graves, S. W., Doorn, S. K., and Nolan, J. P.: A flow cytometer for the measurement of Raman spectra. Cytometry. A, 73(2):119–28, February 2008.

APPENDICES

Appendix A

PERMISSIONS

Permission for reproduction of published work is attached here. The following articles have been used in parts or in full in this thesis work.

- Reprinted (adapted) with permission from Roy, A., Bour, P., and Keiderling, T. A. (2009) TDDFT modeling of the circular dichroism for a tryptophan zipper peptide with coupled aromatic residues. *Chirality* 21, E163-71. Copyright (2009) John Wiley and Sons.
- Reprinted (adapted) with permission from Lakhani A., Roy A., De Poli M., Nakaema M., Formaggio F., Toniolo C., and Keiderling T. A. (2011) Experimental and theoretical spectroscopic study of 3_{10} -helical peptides using isotopic labeling to evaluate vibrational coupling. *J. Phys. Chem. B* 115, 6252-64. Copyright (2011) American Chemical Society.
- Reprinted (adapted) with permission from Chi H., Lakhani A., Roy A., Nakaema M. and Keiderling, T. A. Inter- residue coupling and equilibrium unfolding of PPII helical peptides. Vibrational spectra enhanced with ^{13}C isotopic labeling. *J. Phys. Chem. B* 114, 12744-53 (2010). Copyright (2010) American Chemical Society.
- Reprinted (adapted) with permission from Hauser K., Ridderbusch O., Roy A., Hellerbach A., Huang R., and Keiderling T. A. (2010) Comparison of isotopic substitution methods for equilibrium and T-jump infrared studies of beta-hairpin peptide conformation. *J. Phys. Chem. B* 114, 11628-37. Copyright (2010) American Chemical Society.
- Reprinted (adapted) with permission from Huang R., Wu L., McElheny D., Bour P., Roy A., and Keiderling T. A. (2009) Cross-strand coupling and site-specific unfolding thermodynamics of a trpzip β -hairpin peptide using ^{13}C isotopic labeling and IR spectroscopy. *J. Phys. Chem. B* 113, 5661-74. Copyright (2009) American Chemical Society.

Appendix A (Continued)

JOHN WILEY AND SONS LICENSE TERMS AND CONDITIONS

May 01, 2014

This is a License Agreement between anjan roy ("You") and John Wiley and Sons ("John Wiley and Sons") provided by Copyright Clearance Center ("CCC"). The license consists of your order details, the terms and conditions provided by John Wiley and Sons, and the payment terms and conditions.

All payments must be made in full to CCC. For payment instructions, please see information listed at the bottom of this form.

License Number	3380500931337
License date	May 01, 2014
Licensed content publisher	John Wiley and Sons
Licensed content publication	Chirality
Licensed content title	TD-DFT modeling of the circular dichroism for a tryptophan zipper peptide with coupled aromatic residues
Licensed copyright line	Copyright © 2009 Wiley-Liss, Inc.
Licensed content author	Anjan Roy,Petr Bouř,Timothy A. Keiderling
Licensed content date	Nov 6, 2009
Start page	E163
End page	E171
Type of use	Dissertation/Thesis
Requestor type	Author of this Wiley article
Format	Print and electronic
Portion	Full article
Will you be translating?	No
Title of your thesis / dissertation	MODELING MOLECULAR SPECTRA OF SELECTED PEPTIDES AND DEVELOPMENT OF AN OPTICAL TRAPPING RAMAN SYSTEM
Expected completion date	May 2014
Expected size (number of pages)	250
Total	0.00 USD
Terms and Conditions	

TERMS AND CONDITIONS

This copyrighted material is owned by or exclusively licensed to John Wiley & Sons, Inc. or one of its group companies (each a "Wiley Company") or handled on behalf of a society with which a Wiley Company has exclusive publishing rights in relation to a particular work (collectively

Appendix A (Continued)



RightsLink®

Home

Account
Info

Help

ACS Publications
MOST TRUSTED. MOST CITED. MOST READ.

Title: Experimental and Theoretical Spectroscopic Study of 310-Helical Peptides Using Isotopic Labeling to Evaluate Vibrational Coupling

Logged in as:
anjan roy

LOGOUT

Author: Ahmed Lakhani, Anjan Roy, Matteo De Poli, Marcelo Nakaema, Fernando Formaggio, Claudio Toniolo, and Timothy A. Keiderling

Publication: The Journal of Physical Chemistry B

Publisher: American Chemical Society

Date: May 1, 2011

Copyright © 2011, American Chemical Society

PERMISSION/LICENSE IS GRANTED FOR YOUR ORDER AT NO CHARGE

This type of permission/license, instead of the standard Terms & Conditions, is sent to you because no fee is being charged for your order. Please note the following:

- Permission is granted for your request in both print and electronic formats, and translations.
- If figures and/or tables were requested, they may be adapted or used in part.
- Please print this page for your records and send a copy of it to your publisher/graduate school.
- Appropriate credit for the requested material should be given as follows: "Reprinted (adapted) with permission from (COMPLETE REFERENCE CITATION). Copyright (YEAR) American Chemical Society." Insert appropriate information in place of the capitalized words.
- One-time permission is granted only for the use specified in your request. No additional uses are granted (such as derivative works or other editions). For any other uses, please submit a new request.

BACK

CLOSE WINDOW

Copyright © 2014 [Copyright Clearance Center, Inc.](#) All Rights Reserved. [Privacy statement.](#)
Comments? We would like to hear from you. E-mail us at customercare@copyright.com

Appendix A (Continued)



RightsLink®

Home

Create Account

Help

ACS Publications
MOST TRUSTED. MOST CITED. MOST READ.

Title: Inter-residue Coupling and Equilibrium Unfolding of PPII Helical Peptides. Vibrational Spectra Enhanced with ¹³C Isotopic Labeling

Author: Heng Chi, Ahmed Lakhani, Anjan Roy, Marcelo Nakaema, and Timothy A. Keiderling

Publication: The Journal of Physical Chemistry B

Publisher: American Chemical Society

Date: Oct 1, 2010

Copyright © 2010, American Chemical Society

User ID
<input type="text"/>
Password
<input type="text"/>
<input type="checkbox"/> Enable Auto Login
<input type="button" value="LOGIN"/>
Forgot Password/User ID?
If you're a copyright.com user , you can login to RightsLink using your copyright.com credentials. Already a RightsLink user or want to learn more?

PERMISSION/LICENSE IS GRANTED FOR YOUR ORDER AT NO CHARGE

This type of permission/license, instead of the standard Terms & Conditions, is sent to you because no fee is being charged for your order. Please note the following:

- Permission is granted for your request in both print and electronic formats, and translations.
- If figures and/or tables were requested, they may be adapted or used in part.
- Please print this page for your records and send a copy of it to your publisher/graduate school.
- Appropriate credit for the requested material should be given as follows: "Reprinted (adapted) with permission from (COMPLETE REFERENCE CITATION). Copyright (YEAR) American Chemical Society." Insert appropriate information in place of the capitalized words.
- One-time permission is granted only for the use specified in your request. No additional uses are granted (such as derivative works or other editions). For any other uses, please submit a new request.

BACK

CLOSE WINDOW

Appendix A (Continued)



RightsLink®

Home

Account
Info

Help

ACS Publications
MOST TRUSTED. MOST CITED. MOST READ.

Title: Comparison of Isotopic Substitution Methods for Equilibrium and T-Jump Infrared Studies of β -Hairpin Peptide Conformation

Author: Karin Hauser, Oliver Ridderbusch, Anjan Roy, Alexandra Hellerbach, Rong Huang, and Timothy A. Keiderling

Publication: The Journal of Physical Chemistry B

Publisher: American Chemical Society

Date: Sep 1, 2010

Copyright © 2010, American Chemical Society

Logged in as:

anjan roy

LOGOUT

PERMISSION/LICENSE IS GRANTED FOR YOUR ORDER AT NO CHARGE

This type of permission/license, instead of the standard Terms & Conditions, is sent to you because no fee is being charged for your order. Please note the following:

- Permission is granted for your request in both print and electronic formats, and translations.
- If figures and/or tables were requested, they may be adapted or used in part.
- Please print this page for your records and send a copy of it to your publisher/graduate school.
- Appropriate credit for the requested material should be given as follows: "Reprinted (adapted) with permission from (COMPLETE REFERENCE CITATION). Copyright (YEAR) American Chemical Society." Insert appropriate information in place of the capitalized words.
- One-time permission is granted only for the use specified in your request. No additional uses are granted (such as derivative works or other editions). For any other uses, please submit a new request.

BACK

CLOSE WINDOW

Copyright © 2014 [Copyright Clearance Center, Inc.](#) All Rights Reserved. [Privacy statement.](#)
Comments? We would like to hear from you. E-mail us at customercare@copyright.com

Appendix A (Continued)



RightsLink®

Home

Account
Info

Help

ACS Publications
MOST TRUSTED. MOST CITED. MOST READ.

Title: Cross-Strand Coupling and Site-Specific Unfolding Thermodynamics of a Trpzip β -Hairpin Peptide Using ^{13}C Isotopic Labeling and IR Spectroscopy

Logged in as:
anjan roy

LOGOUT

Author: Rong Huang, Ling Wu, Dan McElheny, Petr Bouř, Anjan Roy, and Timothy A. Keiderling

Publication: The Journal of Physical Chemistry B

Publisher: American Chemical Society

Date: Apr 1, 2009

Copyright © 2009, American Chemical Society

PERMISSION/LICENSE IS GRANTED FOR YOUR ORDER AT NO CHARGE

This type of permission/license, instead of the standard Terms & Conditions, is sent to you because no fee is being charged for your order. Please note the following:

- Permission is granted for your request in both print and electronic formats, and translations.
- If figures and/or tables were requested, they may be adapted or used in part.
- Please print this page for your records and send a copy of it to your publisher/graduate school.
- Appropriate credit for the requested material should be given as follows: "Reprinted (adapted) with permission from (COMPLETE REFERENCE CITATION). Copyright (YEAR) American Chemical Society." Insert appropriate information in place of the capitalized words.
- One-time permission is granted only for the use specified in your request. No additional uses are granted (such as derivative works or other editions). For any other uses, please submit a new request.

BACK

CLOSE WINDOW

Copyright © 2014 [Copyright Clearance Center, Inc.](#) All Rights Reserved. [Privacy statement.](#)
Comments? We would like to hear from you. E-mail us at customercare@copyright.com

VITA

ANJAN ROY

EDUCATION

- Ph.D. (University of Illinois at Chicago) 2014
- M.S. (University of Illinois at Chicago) 2009
- M.Sc.(University of Delhi, New Delhi) 2004
- B.Sc.(University of Delhi, New Delhi) 2002

EXPERIENCE

- 2005 - 2014, Graduate Student, University of Illinois at Chicago, Chicago, IL,
 - Novel instrument design and development
 - Proposed, designed and developed an Optical Trapping Raman Spectrometer.
 - Constructed microfluidic setups and incorporated cellular mechanical force sensing ability.
 - Constructed conventional Raman spectrometers.
 - Studied Raman of biomolecular systems and calculated structure-spectra correlations.
- 2009 IOCB, Guest Researcher, Czech Academy of Sciences, Prague, Czech Republic.
 - Performed Quantum Mechanical calculations to determine structure and spectral signatures of helical peptides.
- 2004 - 2005, Research Associate, National Institute of Immunology, New Delhi, India.
 - Synthesized small molecule natural products from the Thai curry spice Galangal.

PUBLICATIONS

- Roy, A., Bour, P., and Keiderling, T. A. (2009) TDDFT modeling of the circular dichroism for a tryptophan zipper peptide with coupled aromatic residues. *Chirality* 21, E163-71.
- Lakhani A., Roy A., De Poli M., Nakaema M., Formaggio F., Toniolo C., and Keiderling T. A. (2011) Experimental and theoretical spectroscopic study of 3_{10} -helical peptides using isotopic labeling to evaluate vibrational coupling. *J. Phys. Chem. B* 115, 6252-64.
- Chi H., Lakhani A., Roy A., Nakaema M. and Keiderling, T. A. Inter-residue coupling and equilibrium unfolding of PPII helical peptides. Vibrational spectra enhanced with ^{13}C isotopic labeling. *J. Phys. Chem. B* 114, 12744-53 (2010).
- Hauser K., Ridderbusch O., Roy A., Hellerbach A., Huang R., and Keiderling T. A. (2010) Comparison of isotopic substitution methods for equilibrium and T-jump infrared studies of β -hairpin peptide conformation. *J. Phys. Chem. B* 114, 11628-37.

- Huang R., Wu L., McElheny D., Bour P., Roy A., and Keiderling T. A. (2009) Cross-strand coupling and site-specific unfolding thermodynamics of a trpzip β -hairpin peptide using ^{13}C isotopic labeling and IR spectroscopy. *J. Phys. Chem. B* 113, 5661-74.

PRESENTATIONS

- Anjan Roy and Timothy A. Keiderling, Site-specific conformational studies of selectively isotopic labeled peptides using Raman and IR spectra XXI International Conference on Raman Spectroscopy 2008.
- Anjan Roy and Timothy A. Keiderling Site-specific conformational Raman and IR spectra studies of selectively isotopic labeled peptides, 63rd molecular spectroscopy symposium Ohio state university 2008.
- Heng Chi, Ahmed Lakhani, Anjan Roy, Marcelo Nakaema, Timothy A. Keiderling, Inter-residue coupling and equilibrium unfolding of ^{13}C isotopic labeled PPII helices studied with vibrational spectra, 54th Biophysical meeting 2010.
- Ahmed Lakhani, Anjan Roy, Marcelo Nakaema, Claudio Toniolo and Timothy A. Keiderling, experimental and theoretical spectroscopic studies of 3_{10} -helicalpeptides using isotopic labeling, 54th Biophysical meeting 2010.
- Anjan Roy, Marcelo Nakaema and Timothy A Keiderling, Optical trapping Raman spectroscopy of protein and membrane interaction, XXII International Conference on Raman Spectroscopy (ICORS) 2010.
- Ahmed Lakhani, Anjan Roy, Marcelo Nakaema, Claudio Toniolo and Timothy A. Keiderling, Raman scattering investigation of 3_{10} -helical peptides using isotopic labeling XXII ICORS 2010.
- Chi Heng, Ahmed Lakhani, Anjan Roy, Marcelo Nakaema and Timothy A. Keiderling Inter-residue coupling of model PPII helices using ^{13}C isotopic labeling investigated by vibrational spectroscopy XXII ICORS 2010.
- Anjan Roy, Marcelo Nakaema, and Timothy A Keiderling Optical trapping Raman spectroscopy of protein and membrane interaction, 55th Biophysical meeting 2011.